

# An investigation of the proton structure in the space-like domain and feasibility studies of the proton electromagnetic form factor measurement in the time-like region

Dissertation

zur Erlangung des Grades  
"Doktor der Naturwissenschaften"

am Fachbereich Physik, Mathematik und Informatik  
der Johannes Gutenberg-Universität  
in Mainz

von  
Dmitry A. Khanefit  
geb. in Kemerovo (Russland)

Mainz, den 17. Juli 2017



# Abstract

The proton electromagnetic form factors (FF) in the space-like region ( $q^2 < 0$ ) have been measured for multiple decades using electron–proton scattering and Rosenbluth separation method. Recently developed polarization transfer technique resulted in a different value of extracted FF. It was suggested that the previously unaccounted hard two-photon exchange (TPE) effect, can be responsible for the discrepancy. The OLYMPUS experiment performed a high precision measurement of the TPE contribution via measurement of the positron to electron elastic scattering cross section ratio  $\sigma_{e^+p}/\sigma_{e^-p}$ . It was performed at DESY using 2 GeV  $e^\pm$  beams and the BLAST spectrometer. A crucial part of the experiment was precise measurement of the integrated luminosity. The symmetric Møller/Bhabha luminosity monitors, which were designed and built in Mainz, used Møller and Bhabha processes for luminosity measurements. The analysis of the collected SYMB data is presented in this work.

In the time-like region, where  $q^2 > 0$ , form factor data is scarce and only the ratio of electric to magnetic form factor have been measured so far. The  $\bar{\text{P}}\text{ANDA}$  experiment will be able to measure individual electric and magnetic time-like FF. Extensive feasibility studies of the proton form factor measurement have been performed using PandaRoot simulation framework. This include the signal  $\bar{p}p \rightarrow e^+e^-$  selection, the main background  $\bar{p}p \rightarrow \pi^+\pi^-$  suppression, and investigation of possible sources of systematic uncertainties in the  $q^2$  range between 5.4 GeV<sup>2</sup> and 13.9 GeV<sup>2</sup>. The estimated statistical and systematic accuracy of the proton FF extraction at  $\bar{\text{P}}\text{ANDA}$  is 2%-57%.



# Zusammenfassung

Die elektromagnetischen Formfaktoren (FF) des Protons im raumartigen Bereich ( $q^2 < 0$ ) waren seit einigen Jahrzehnten Gegenstand zahlreicher Messungen unter Verwendung elastischer Elektron-Proton Streuung sowie der Rosenbluth-Separations-Methode. Die mit Hilfe der kürzlich entwickelten Polarisations-Transfer-Methode extrahierten Werte unterscheiden sich deutlich von bereits existierenden Werten. Einen möglichen Erklärungsversuch sollte der zu diesem Zeitpunkt unbekannt Effekt des Zwei-Photon-Austauschs (TPE) liefern. Das OLYMPUS-Experiment führte dazu Hochpräzisionsmessungen zur Bestimmung des TPE Beitrags zu den FF mittels elastischer  $e^\pm$ - $p$  Streuung durch. Das Verhältnis der Wirkungsquerschnitte  $\sigma_{e^+p}/\sigma_{e^-p}$  erlaubte sodann eine direkte Bestimmung des TPE Beitrags. Die Messung wurde am DESY unter Verwendung eines 2 GeV  $e^\pm$  Strahls und des BLAST Spektrometers durchgeführt. Eine entscheidende Rolle spielte dabei die präzise Bestimmung der integrierten Luminosität. Der symmetrische Møller/Bhabha-Luminositätsmonitor (SYMB), welcher in Mainz entworfen und gebaut wurde, verwendete Møller- und Bhabhastreueung zur Luminositätsmessung. Die Analyse der gewonnenen SYMB Daten wird in dieser Arbeit vorgestellt.

Im zeitartigen Bereich ( $q^2 > 0$ ) sind die elektromagnetischen FF des Protons bislang nur wenig bekannt. Bereits existierende Messdaten verfügen über geringe Statistik und erlaubten in der Vergangenheit lediglich die Bestimmung des Verhältnisses aus elektrischem und magnetischem FF. Das  $\bar{P}$ ANDA-Experiment wird in der Lage sein, die Werte des elektrischen und magnetischen FF im zeitartigen Bereich einzeln zu bestimmen. Unter Verwendung der Simulationssoftware PandaRoot wurden ausführliche Machbarkeitsstudien zur Messung der FF des Protons an  $\bar{P}$ ANDA durchgeführt. Diese beinhalten unter anderem die Selektion von Signalereignissen des Prozesses  $\bar{p}p \rightarrow e^+e^-$ , die Unterdrückung des wichtigsten Untergrundprozesses  $\bar{p}p \rightarrow \pi^+\pi^-$  und die Untersuchung möglicher Quellen von systematischen Ungenauigkeiten im Bereich zwischen  $q^2 = 5.4 \text{ GeV}^2$  und  $13.9 \text{ GeV}^2$ . Die statistischen und systematischen Genauigkeiten der zeitartigen elektromagnetischen FF des Protons bei  $\bar{P}$ ANDA werden auf 2%-57% geschätzt.



# Contents

<b>I</b>	<b>Foundations</b>	<b>12</b>
1	Introduction	13
2	Discovery of the Proton Structure	18
2.1	Structured Proton . . . . .	18
2.2	Dirac and Pauli Proton Form Factors . . . . .	18
2.3	Sachs Proton Form Factors . . . . .	19
2.4	Physical Interpretation . . . . .	20
3	Proton Form Factors Measurements	22
3.1	Space-like Form Factor Puzzle . . . . .	22
3.1.1	Rosenbluth Separation . . . . .	22
3.1.2	Recoil Proton Polarization . . . . .	26
3.1.3	Two-photon Exchange . . . . .	28
3.2	Time-like Form Factors . . . . .	32
<b>II</b>	<b>Experiments</b>	<b>38</b>
4	OLYMPUS Experiment	39
4.1	Physics Goal . . . . .	39
4.2	Experiment Overview . . . . .	40
4.2.1	DORIS Electron/Positron Beams . . . . .	40
4.2.2	Hydrogen Target . . . . .	42
4.2.3	Magnet System . . . . .	44

4.2.4	Drift Chambers . . . . .	44
4.2.5	Time of Flight Detectors . . . . .	45
4.3	Luminosity Measurement . . . . .	46
4.3.1	12° Luminosity Monitors . . . . .	46
4.3.2	Symmetric Møller/Bhabha Luminosity Monitor . . . . .	48
4.3.3	Slow Control . . . . .	50
4.4	Operation . . . . .	50
4.5	Data Analysis and Simulation Software . . . . .	52
<b>5</b>	<b><math>\bar{\text{P}}\text{ANDA}</math> experiment</b>	<b>54</b>
5.1	Physics program . . . . .	54
5.2	$\bar{\text{P}}\text{ANDA}$ detector . . . . .	55
5.2.1	Target spectrometer . . . . .	55
5.2.2	Forward spectrometer . . . . .	58
5.2.3	Luminosity Detector . . . . .	59
5.3	High Energy Storage Ring . . . . .	59
5.4	PandaRoot simulation framework . . . . .	59
<b>III</b>	<b>Symmetric Møller/Bhabha Monitor</b>	<b>62</b>
<b>6</b>	<b>SYMB Physics Processes</b>	<b>63</b>
6.1	Kinematics . . . . .	63
6.1.1	Scattering Processes . . . . .	63
6.1.2	Lepton Annihilation Process . . . . .	64
6.2	Cross Sections . . . . .	65
6.2.1	Møller Scattering . . . . .	66
6.2.2	Bhabha Scattering . . . . .	67
6.2.3	Electron-positron Annihilation . . . . .	68
<b>7</b>	<b>The SYMB Detector System</b>	<b>70</b>
7.1	Detector Construction . . . . .	70
7.1.1	PbF <sub>2</sub> Crystals . . . . .	70

7.1.2	Magnetic shielding . . . . .	71
7.1.3	Collimators . . . . .	71
7.1.4	Readout Electronics . . . . .	72
7.2	Detector Characterization . . . . .	73
7.2.1	Photomultiplier Gain Calibration . . . . .	73
7.2.2	Energy Calibration and Energy Resolution . . . . .	76
7.3	SYMB Operation during the Experiment . . . . .	79
7.3.1	The Energy Spectra . . . . .	79
7.3.2	Stability . . . . .	82
7.3.3	Sensitivity to Beam Parameters . . . . .	83
7.4	Simulation of SYMB Events . . . . .	83
7.4.1	Event Generators . . . . .	83
7.4.2	Simulation of the Detector Response . . . . .	85
<b>8</b>	<b>Luminosity Measurement with SYMB</b>	<b>87</b>
8.1	Luminosity Determination . . . . .	87
8.1.1	Data Division . . . . .	89
8.1.2	Results . . . . .	90
8.2	Extraction of the Event Number . . . . .	91
8.3	Systematic Uncertainties . . . . .	104
8.3.1	Beam Emittance . . . . .	104
8.3.2	Beam Position and Slope . . . . .	106
8.3.3	Detector Alignment . . . . .	112
8.3.4	Magnetic Field . . . . .	118
8.3.5	Other Sources of the Discrepancy . . . . .	121
8.4	Results from Different Time Periods . . . . .	124
8.5	Conclusion . . . . .	126
<b>IV</b>	<b>Form Factors at <math>\overline{\text{PANDA}}</math></b>	<b>130</b>
<b>9</b>	<b>Feasibility Study of <math> G_E </math> and <math> G_M </math> Extraction</b>	<b>131</b>
9.1	Kinematics . . . . .	131

9.2	Signal Simulation . . . . .	133
9.2.1	Signal Event Generator . . . . .	133
9.2.2	Simulation Parameters . . . . .	134
9.3	Background Study . . . . .	136
9.3.1	Background Simulation . . . . .	137
9.4	Particle Identification . . . . .	138
9.4.1	Particle Identification Probabilities . . . . .	138
9.4.2	Detector Response . . . . .	139
9.4.3	Kinematic Cuts . . . . .	140
9.5	Extraction of Form Factors . . . . .	140
9.5.1	Event Selection . . . . .	140
9.5.2	Determination of the Signal Efficiency . . . . .	141
9.5.3	Extraction of the Form Factor Ratio . . . . .	142
9.5.4	Individual Extraction of $ G_E $ and $ G_M $ . . . . .	143
9.5.5	Results . . . . .	143
9.6	Systematic Uncertainties . . . . .	143
9.6.1	Luminosity Measurement . . . . .	144
9.6.2	Detector Alignment . . . . .	144
9.6.3	Pion Background . . . . .	145
9.6.4	Two-photon Exchange Contribution . . . . .	145
9.6.5	Contribution to Form Factors . . . . .	146
9.7	Comparison to Other Feasibility Studies . . . . .	146
9.8	Competitiveness of the $\bar{P}$ ANDA Experiment . . . . .	147
<b>10</b>	<b>Backward Endcap Calorimeter Performance Studies</b>	<b>159</b>
10.1	Geometry Description . . . . .	160
10.2	Simulation Settings . . . . .	161
10.3	Event Selection . . . . .	164
10.4	Energy Resolution and Efficiency Determination . . . . .	165
10.5	Results . . . . .	166
<b>A</b>	<b>SYMB Calibration</b>	<b>173</b>

<b>B</b>	<b>Response of the EMC and STT detectors at <math>\bar{P}</math>ANDA</b>	<b>178</b>
<b>C</b>	<b>Backward EMC efficiency and energy resolution</b>	<b>181</b>

**Part I**

**Foundations**

# Chapter 1

## Introduction

More than two centuries ago William Prout, who was an English chemist, physician, and natural theologian, suggested that all chemical elements consist of hydrogen atoms. The idea was based on the fact that the atomic weights of all known elements seemed to be whole multiples of the atomic weight of hydrogen. This led to a hypothesis that the hydrogen atom is the only basic construction block of all other elements. Prout named it protyle, from Greek  $\text{prōt}$  - first and  $\text{hylē}$  - substance, *i.e.*, base substance which makes up all other elements.

Even though Prout's hypothesis was disproved when a more accurate atomic weights measurement have been performed, it predicted masses of individual isotopes with an error less or equal 1%.

In 1917 Ernest Rutherford, who was influenced by the Prout's idea, experimentally proved the existence of protons. Rutherford studied the interaction of  $\alpha$  particles with different gases, *i.e.*, hydrogen and nitrogen. A beam of  $\alpha$  particles being shot into hydrogen knocked out particles of 1 unit positive charge (hydrogen nuclei). The same  $\alpha$  particle beam when shot through nitrogen also produced hydrogen nuclei. Rutherford realized that the positive charge of any nucleus is equal to an integer number of hydrogen nuclei. It was clear that hydrogen nucleus plays a fundamental role as a building block of matter. In the 1920 hydrogen nucleus was given the name proton to differentiate it from the neutral hydrogen atom.

The next major advance happened in the nineteen fifties. Elastic electron-proton

scattering experiments performed by Robert Hofstadter showed that proton charge and magnetic moment are not consistent with those of a point-like particle [1,2]. Hofstadter observed that the elastic electron-proton scattering cross section is not compatible with the hypothesis of a point-like proton. In 1961 Hofstadter won the Nobel Prize in Physics for his groundbreaking studies of electron-nucleus scattering and discoveries of the structure of the nucleons. At the same, advances have also been made in the theory of electron-nucleus scattering. Marshall Rosenbluth developed a proton model [3] which was widely accepted. The deviation from the point-charge and point-magnetic moment was explained by a virtual meson cloud with a neutron in its center.

During the next decades many, new measurements of proton electromagnetic form factors (FFs) have been performed around the world. New experiments provided more precise results in an extended kinematic range. In addition, the ratio of the electric  $G_E$  to magnetic  $G_M$  FFs was measured not only in the space-like (SL) domain [4–11] where the four-momentum transfer is negative  $Q^2 \equiv -q^2 < 0$  but also in the time-like (TL) domain [12–16] where  $Q^2 > 0$ . These form factors parameterize the finite-size structure of the proton. The measurements were performed with lepton colliders using electron-positron annihilation into a proton-antiproton pair. Unfortunately, the TL data lacks in statistics and precision in comparison to the SL data. Due to the low available statistics only the form factor (FF) ratio  $G_E/G_M$  have been measured in the TL region. The  $\bar{\text{P}}\text{ANDA}$  experiment at Facility for Antiproton and Ion Research (FAIR) in Darmstadt will expand the FFs measurements to the higher  $Q^2$  region and perform an individual extraction of  $G_E$  and  $G_M$  using  $\bar{p}p \rightarrow e^+e^-$  and  $\bar{p}p \rightarrow \mu^+\mu^-$  reactions.

With an advent of polarized beams and polarized targets, a new type of experiment became possible. Proton FFs can be determined by scattering a polarized electron beam from an unpolarized proton target and measuring the polarization of the recoil proton. First results of experiments that used the polarization transfer method came as a big surprise. The FF ratio  $G_E/G_M$  extracted using polarization method was different from that determined with the Rosenbluth technique [17–24]. The results of the former one showed smaller values of the proton FF ratio. In fact, it was demonstrated that the ratio decreases with the increase of the four-momentum transfer  $Q^2$ .

The most probable source of the discrepancy is considered to be QED radiative correc-

tions. The Rosenbluth separation technique is strongly affected by the radiative corrections in contrast to the polarization transfer method. Two hard photon exchange, which was previously neglected, is believed to be the cause of the discrepancy. The OLYMPUS experiment [25] aims to resolve the experimental discrepancy in the determination of the ratio of the proton electric to magnetic FF  $G_E/G_M$ , extracted using Rosenbluth separation method and polarization transfer technique.

The thesis has two physics topic: the feasibility study of the proton TL electromagnetic FFs with the  $\bar{P}$ ANDA experiment [26] and the luminosity measurement at the OLYMPUS experiment.

# Thesis Overview

The thesis covers two projects: the already completed OLYMPUS experiment and the future  $\bar{\text{P}}\text{ANDA}$  experiment at FAIR.

Chapter 2 gives a brief historical overview of the discovery of proton structure and introduces theoretical foundations of proton electromagnetic form factor measurements in space-like and time-like kinematic domains, relevant for the OLYMPUS and  $\bar{\text{P}}\text{ANDA}$  experiments.

Chapter 3 describes different techniques which are used to extract space-like and time-like proton form factors. Results of numerous experiments on space-like proton form factors are presented. The discrepancy between different measurement methods serves as the motivation of the OLYMPUS experiment. Scarce data available in the time-like domain promote the  $\bar{\text{P}}\text{ANDA}$  experiment as an excellent opportunity to expand our knowledge and perform one of the first individual measurements of electric and magnetic proton form factors.

Chapters 4 and 5 shortly present the main elements of OLYMPUS and  $\bar{\text{P}}\text{ANDA}$  detectors, including operation and data collection performance of the OLYMPUS experiment and those expected to be achieved in the  $\bar{\text{P}}\text{ANDA}$  experiment. Additionally, Monte Carlo frameworks used to simulate processes of interest for both experiments are introduced.

The following four chapters are devoted to the OLYMPUS experiment and are focused on the SYmmetric Møller/Bhabha (SYMB) luminosity monitor, one out of three ways used to determine the relative integrated luminosity.

Chapter 6 gives an overview of Møller, Bhabha and annihilation processes detected by the SYMB luminosity monitor.

Chapter 7 introduces different sides of the SYMB detector system. First, a detailed description of the mechanical design and readout electronics is given. Second, results of the SYMB detectors characterization during the test beam at the DESY testing facility are presented. That includes gain and energy calibrations, and determination of the energy resolution. Then, the performance during data taking is shown. In addition, a more detailed description of the SYMB related simulation software is given. Event generator of signal processes is, propagation and digitization procedures are presented.

Chapter 8 presents a method of luminosity determination with the SYMB detectors

including data and event selection procedures, and extraction of the relative electron to positron integrated luminosity. In addition, a detailed study of numerous possible systematical uncertainties is given. Finally, the conclusions are drawn based on the analysis results.

The next two chapters are dedicated to proton form factor measurements at the  $\bar{\text{P}}\text{ANDA}$  experiment and the Monte Carlo study of the backward end cap calorimeter performance which is an essential part of the  $\bar{\text{P}}\text{ANDA}$  electromagnetic calorimeter.

Chapter 9 gives a short overview of the antiproton-proton annihilation into a lepton pair process which will be used for the space like proton form factor measurements. Procedure of the signal and background event production is presented including description of the event generators, kinematic constraints and energy ranges. A detailed description and motivation of the signal selection and the background suppression methods are given. Results of this work are presented and compared to similar studies done by other people. Finally, the competitiveness of the  $\bar{\text{P}}\text{ANDA}$  experiment with existing and future facilities is discussed.

Chapter 10 describes the simplified geometry of the backward end cap calorimeter used in the  $\bar{\text{P}}\text{ANDA}$  simulation framework. The energy resolution and efficiency study with photons are presented. Multiple different photon energies and incident angles are considered. Additionally, different configurations of other detectors placed between the target and the backward end cap calorimeter are investigated.

# Chapter 2

## Discovery of the Proton Structure

### 2.1 Structured Proton

In 1933 [27] Stern and his colleagues performed the first measurement of the proton magnetic momentum. To their surprise, the measurement yielded the magnetic moment which was around 2.5 times larger than it was expected from a point-like spin-1/2 particles. It was the first evidence of a nonpoint-like structure of the proton.

Twenty years later, Hofstadter measured the differential cross section of the elastic electron-proton scattering [1]. The tree-level diagram of the electron-proton scattering is shown in Fig. 2.1. The results of the experiment are schematically shown in Fig. 2.2. Together with the experimental curve, the Mott curve, the point-charge and point-magnetic moment curve are drawn. The fact that the experimental curve lies between the Mott curve and the point-charge, point-magnetic moment curve was the direct evidence of the proton having a "structure factor" or form factor and of its finite size.

### 2.2 Dirac and Pauli Proton Form Factors

The FFs were first introduced by Clementel [28] as  $F_1$  and  $F_2$ , functions that depend on the  $Q^2$ .  $F_1$  is associated with the deviation from a point-like charge (Dirac FF) and  $F_2$  with the deviation from a point-like magnetic moment (Pauli FF). Subsequently, these FFs were also employed by Hofstadter and his colleagues [2, 29, 30]. The Rosenbluth

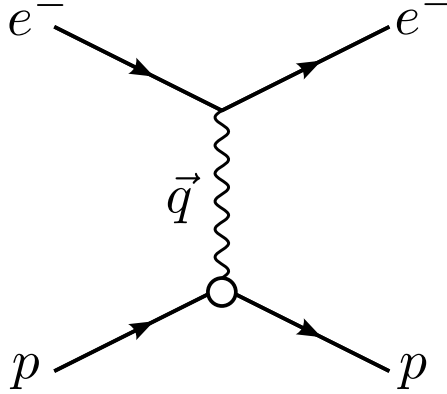


**Figure 2.1:** Tree-level diagram of the elastic electron-proton scattering.

parameterization of the elastic electron-proton scattering in term of  $F_1$  and  $F_2$  can be written in the following form [29]:

$$\sigma(\theta) = \sigma_{Mott} \{ F_1^2(Q^2) + \tau [2(F_1(Q^2) + \mu F_2(Q^2))^2 \tan^2 \frac{\theta}{2} + \mu^2 F_2^2(Q^2)] \}, \quad (2.1)$$

where

$$\sigma_{Mott} = \left( \frac{Ze^2}{2E} \right) \frac{\cos^2 \frac{\theta}{2}}{\sin^4 \frac{\theta}{2}} \quad (2.2)$$

is the Mott cross section,  $Ze$  is the charge of the target nuclei,  $E$  and  $\theta$  are the incident electron energy and the scattering angle in the laboratory (lab.) frame respectively, and  $\tau = Q^2/4m_p^2$ . Where  $m_p$  is the proton mass,  $\mu$  is the proton magnetic moment.

## 2.3 Sachs Proton Form Factors

In "modern" experimental and theoretical physics, it is more common to refer to the proton FFs in the form of electric  $G_E$  and magnetic  $G_M$  FFs [31]. The electric and magnetic proton FFs are linear combinations of the Dirac and Pauli FFs defined in the following way:

$$G_E = F_1 - \frac{Q^2}{4m_p^2} F_2, \text{ and } G_M = F_1 + F_2. \quad (2.3)$$

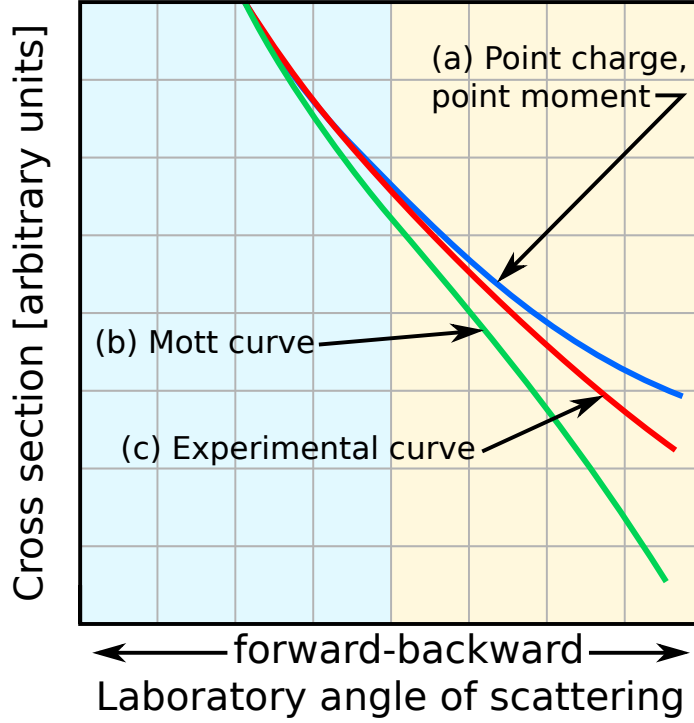


**Figure 2.2:** Curve (a) shows the theoretical curve for a point-like proton with the point-charge and point-magnetic moment. Curve (b) shows the Mott curve for a spinless point proton. Curve (c) shows experimental results.

The Rosenbluth cross section for elastic electron-proton scattering can be rewritten as follows [3]:

$$\frac{d\sigma}{d\Omega} = \left( \frac{d\sigma}{d\Omega} \right)_{Mott} \frac{1}{(1 + \tau)} \left[ G_E^2(Q^2) + \frac{\tau}{\varepsilon} G_M^2(Q^2) \right] \quad (2.4)$$

where  $\varepsilon = 1/[1 + 2(1 + \tau) \tan^2(\theta/2)]$  is related to the virtual photon polarization, which at fixed  $Q^2$  is a function of  $\theta$  alone. Nowadays,  $G_E$  and  $G_M$  are called Sachs' FFs.

## 2.4 Physical Interpretation

Depending on whether we consider the SL or the TL region, the interpretation of the proton electromagnetic FFs can be different.

In the SL region, where  $Q^2 < 0$ , the proton FFs can be interpreted within the Breit frame. In the Breit frame,  $G_E$  and  $G_M$  are the Fourier transforms of the spatial charge and magnetization distributions of the proton.

There is no widely accepted interpretation of the TL proton FFs. In the TL region we deal with two interacting hadrons (proton-antiproton), therefore one can assume that FFs may describe the dynamics of quarks and their interaction inside and between two hadrons<sup>1</sup>.

---

<sup>1</sup>Inspired by Yue. Ma.

# Chapter 3

## Proton Form Factors Measurements

### 3.1 Space-like Form Factor Puzzle

In this section two different methods of proton FFs measurement are described, namely: the Rosenbluth separation and the recoil polarization technique. As it was already mentioned, these two methods yielded different results for the proton FF ratio. The cause of the discrepancy and a way to reconcile the data is presented.

#### 3.1.1 Rosenbluth Separation

For a long time, the only way to measure proton FFs was the Rosenbluth separation method, which allowed individual determination of  $G_E$  and  $G_M$ . In the SL domain, proton electromagnetic can be measured via elastic electron-proton scattering. In this case, the Rosenbluth elastic electron-proton cross section (Eq. (2.4)) can be rewritten in the following way:

$$\sigma_{red} = \frac{\varepsilon(1 + \tau)}{\tau} \frac{\sigma_{exp}}{\sigma_{Mott}} = G_M^2(Q^2) + \frac{\varepsilon}{\tau} G_E^2(Q^2) \quad (3.1)$$

where  $\sigma_{exp}$  is the experimentally measured cross section. Measuring the reduced cross section at the same  $Q^2$ , but for a number of different  $\varepsilon$  values, makes the independent determination of  $G_E$  and  $G_M$  possible. Fig. 3.1 illustrates the concept of the Rosenbluth separation method. Reduced cross section as a function of  $\varepsilon$  is fitted using the following

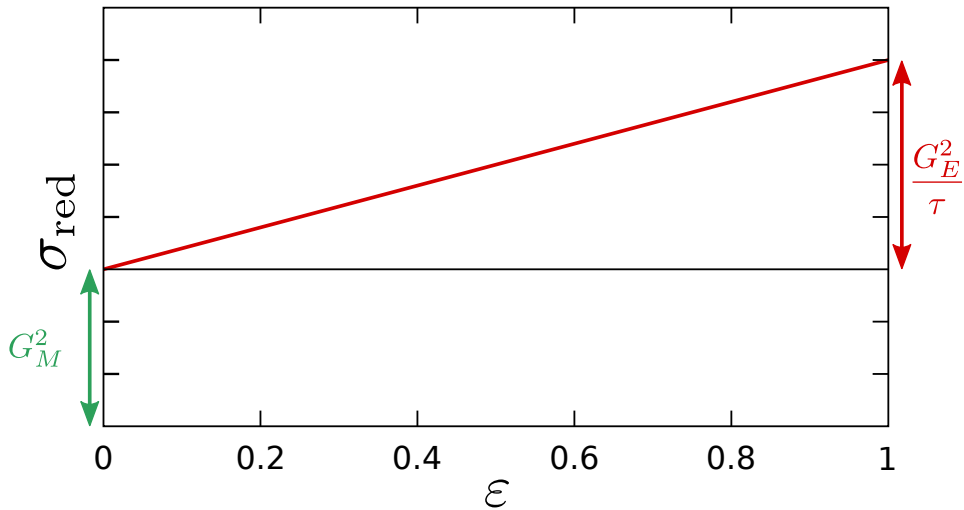


**Figure 3.1:** The principle of the Rosenbluth separation method. Points represent data, the line is a fit.

linear function:

$$\sigma_{red} = a + \epsilon b \quad (3.2)$$

where  $a = G_M^2$  and  $b = G_E^2/\tau$ . The fit gives  $G_M^2$  as the intercept and  $G_E^2/\tau$  as the slope of the fit line.

Figs. 3.2 and 3.3 show a selection of experiments which measured the electric [4–11,32] and the magnetic [4–11] proton FFs in the SL region. The results are shown as the ratios  $G_E/G_D$  and  $G_M/(\mu_p G_D)$ , assuming  $G_E = G_D$  and  $G_M = \mu_p G_D$ , where  $\mu_p$  is the proton magnetic moment and  $G_D$  is the dipole FF given by [33]:

$$G_D = \frac{1}{(1 + Q^2/0.71\text{GeV}^2)^2} \quad (3.3)$$

As can be seen in Fig. 3.2, all experiments are consistent with each other and  $G_E/G_D$  is approximately equal to unity up to  $Q^2 = 1 \text{ (GeV}/c)^2$ . At higher  $Q^2$ , both the measured values and the error bars significantly deviate between different experiments and are not comparable with the unity anymore. This is caused by the fact that  $G_E^2$  is multiplied by  $1/\tau$ , which suppresses the  $G_E^2$  contribution to the cross section. The effect is stronger at higher  $Q^2$ .

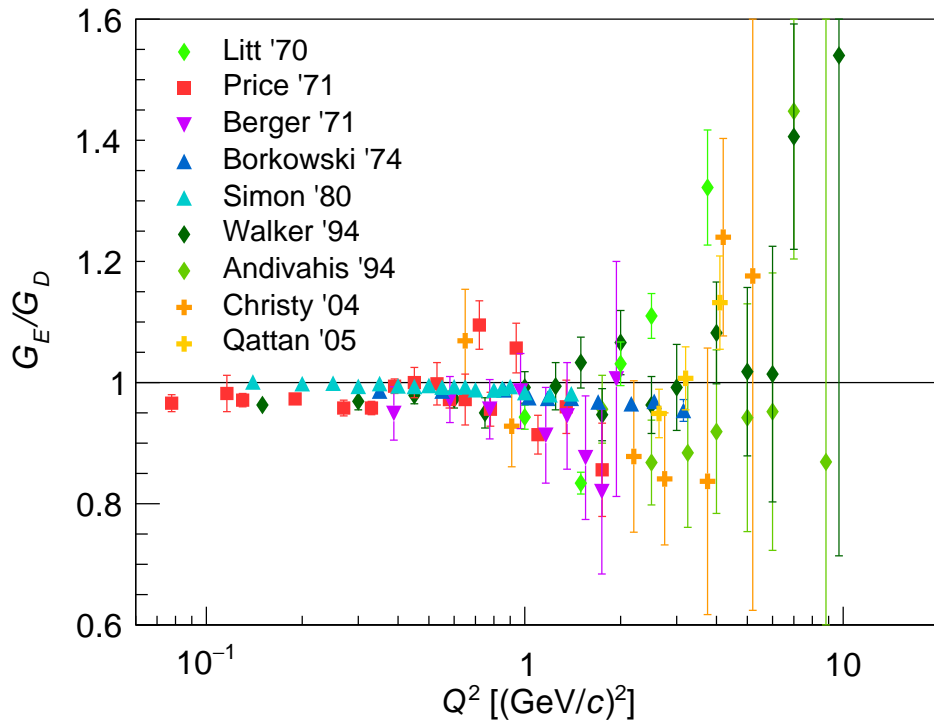


**Figure 3.2:** Normalized proton electric FF determined using Rosenbluth separation method.

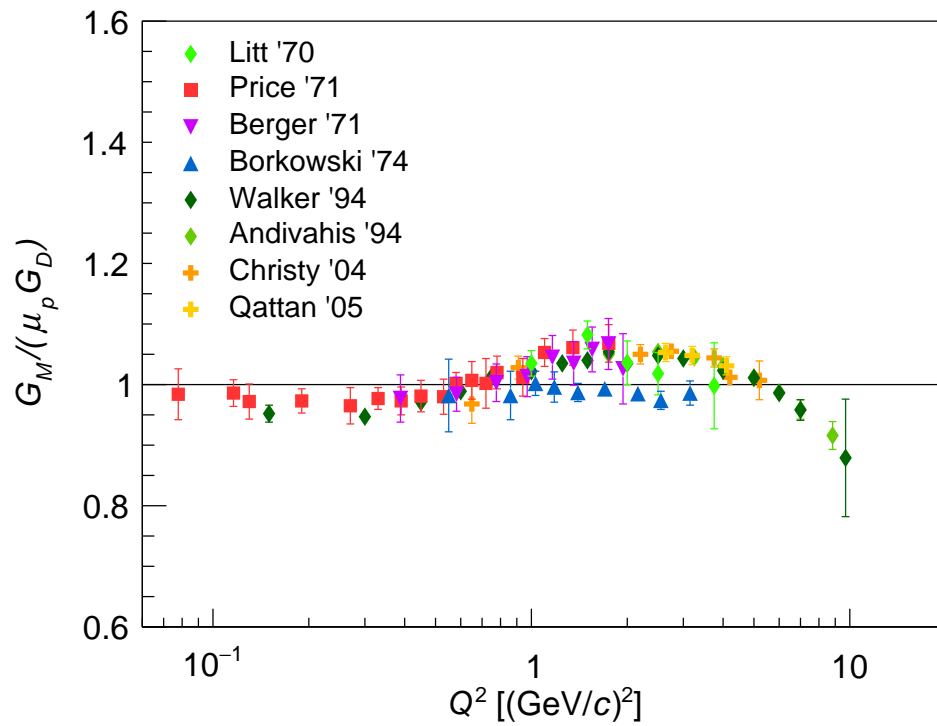


**Figure 3.3:** Normalized proton magnetic FF determined using Rosenbluth separation method.

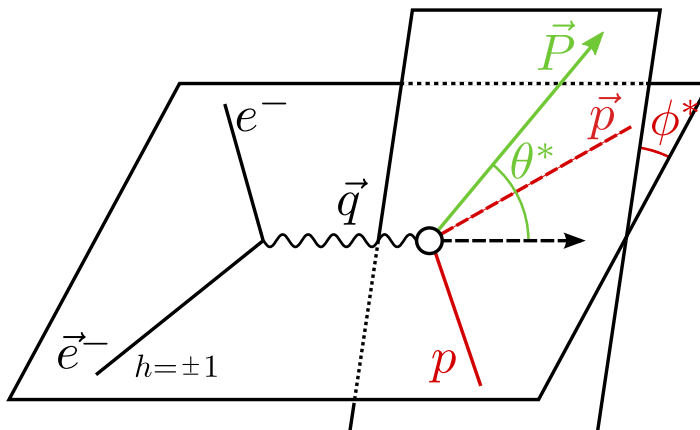


**Figure 3.4:** Tree-level diagram of the electron to proton polarization transfer technique electron-proton scattering.

### 3.1.2 Recoil Proton Polarization

In the 1990s, with the advance of polarized beams and polarized targets a new type of experiments for the proton electromagnetic FF measurements became possible.

As it was shown in the previous section, the separation of  $G_E$  becomes difficult at  $Q^2$  values above 1 (GeV/c)<sup>2</sup>. As a consequence, a number of theoretical work emerged proposing experiments with polarization observables [34–36]. In polarization transfer experiments ( $\vec{e}p \rightarrow e\vec{p}$ ) the recoil proton is detected in coincidence with the scattered electron. Measuring the transverse and the longitudinal components of the proton polarization, the proton electromagnetic FF ratio can be measured in the following way [37]:

$$R \equiv \frac{G_E}{G_M} = -\frac{P_t E_e - E'_e}{P_l 2m_p} \tan\left(\frac{\theta_e}{2}\right), \quad (3.4)$$

where  $E_e(E'_e)$  is the energy of the incident (scattered) electron,  $\theta_e$  is the electron scattering angle in the lab. frame, and  $P_t(P_l)$  is the transverse (longitudinal) component of the recoil proton polarization. Fig. 3.4 shows a tree-level diagram of the electron-proton scattering with the polarization transfer from the incident electron to the recoil proton.

Another method employs a polarized electron beam and a polarized proton target (see Fig. 3.4). In this case the cross section asymmetry between even and odd combinations of beam and target spins is measured. In the one-photon exchange approximation, the

elastic electron-proton scattering, with longitudinally polarized electrons and polarized protons, with respect to the electron beam helicity has the form [38]:

$$A_{phys} = - \frac{2\sqrt{\tau(1+\tau)} \tan(\theta_e/2)}{G_E^2 + \frac{\tau}{\varepsilon} G_M^2} \times \left[ \sin \theta^* \cos \phi^* G_M G_E + \sqrt{\tau[1 + (1+\tau) \tan^2(\theta_e/2)]} \cos \theta^* G_M^2 \right] \quad (3.5)$$

where  $\theta^*$  and  $\phi^*$  are the polar and azimuthal angles of the target polarization in the lab. frame. They are defined relative to the three-momentum transfer vector of the virtual photon as shown in Fig. 3.4. The experimentally measured asymmetry

$$A_{exp} = P_b P_t A_{phys}, \quad (3.6)$$

is affected by the electron beam  $P_b$  and target  $P_t$  polarizations. In order to extract FFs from the Eq. (3.5), the target polarization must be perpendicular to the momentum transfer vector  $\vec{q}$  and within the reaction plane, with  $\theta^* = \pi/2$  and  $\phi^* = 0^\circ$  or  $180^\circ$ . Then Eq. (3.5) can be rewritten as:

$$A_{exp}^\perp = \frac{-2\sqrt{\tau(1+\tau)} \tan(\theta_e/2) \frac{G_E}{G_M}}{\left(\frac{G_E}{G_M}\right)^2 + \frac{\tau}{\varepsilon}}, \quad (3.7)$$

As the FF ratio  $(G_E/G_M)^2$  in the denominator is small, the asymmetry  $A_{exp}^\perp$  can be considered proportional to the FF ratio  $(G_E/G_M)$  in the nominator.

Fig. 3.5 shows a comparison between the FF ratio measured with unpolarized [4–6, 8–11, 39] and polarized [17–24] experiments. It can be seen, that polarized experiments yield more precise results, especially at the higher  $Q^2$ . While the Rosenbluth and the recoil polarization techniques yield consistent results up to  $Q^2 = 1 \text{ (GeV}/c)^2$ , the latter method shows a linear decrease of the FF ratio at higher  $Q^2$ . Assuming that the polarized experiments are correct, this  $Q^2$  dependency is a clear signal that electric and magnetic distributions in the proton are different.

The striking discrepancy between the two methods led to an increased activity in the field. Many experimental and theoretical attempts have been made to explain the

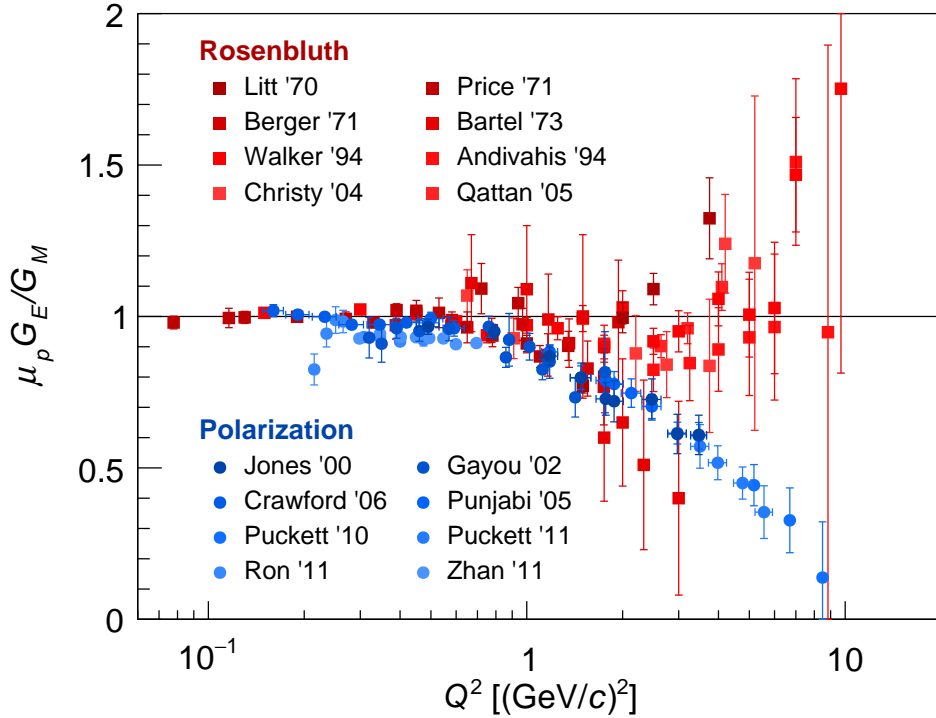


**Figure 3.5:** Ratio of proton electric to magnetic FFs extracted using Rosenbluth separation (red squares) and polarization transfer data (blue circles).

difference and to reconcile the data. The previously unaccounted two-photon exchange (TPE) contribution is expected to be the cause of the discrepancy. As explained in Sec. 3.1.3, its effect on the Rosenbluth separation and polarization transfer technique is different.

### 3.1.3 Two-photon Exchange

The TPE contribution, which was previously neglected, is considered to be the key to the discrepancy in the FF ratio measurements. Fig. 3.6 shows the two diagrams contributing to the TPE. A systematic difference between small- and large-angle scattering, introduced by the TPE, can lead to different  $G_E/G_M$  values. It was analytically shown that the TPE affects the Rosenbluth separation by a few percent [40], while corrections for the polarization transfer method are on the level of 1% [41]. Therefore, correcting the

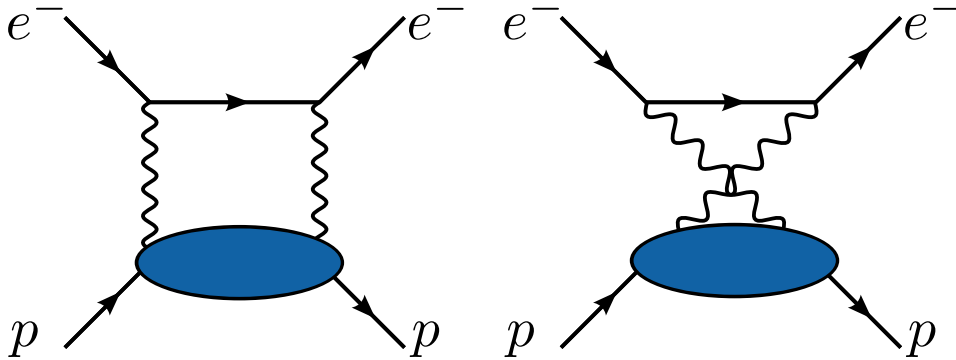


**Figure 3.6:** Box and crossed box TPE contributions to the elastic electron-proton scattering.

Rosenbluth data could resolve the discrepancy.

Fig. 3.7, taken from Ref. [42], illustrates the effect of TPE corrections applied to cross section data. The measured cross section is affected by the TPE contribution. Correcting for the TPE modifies the slope thus changing the  $G_E/G_M$  ratio. Fig. 3.8 shows how TPE correction may reconcile the Rosenbluth and polarization transfer methods [42, 43].

The theoretical approach to the estimation of the TPE is complicated as the complete knowledge of the intermediate hadronic states is needed [40,43]. Therefore any calculation strongly depends on a model.

Experimentally, the size of the two-photon exchange can be directly determined by measuring the elastic scattering cross section ratio  $\sigma_{e^+p}/\sigma_{e^-p}$ . In the one-photon exchange approximation, the cross section ratio  $\sigma_{e^-p}/\sigma_{e^+p}$  is equal to 1 as there is no asymmetry between electrons and positrons. The interference term between the one-  $\mathcal{M}_{1\gamma}$  and two-photon  $\mathcal{M}_{2\gamma}$  exchange amplitudes has the opposite sign for electrons and positrons. The cross section ratio, in terms of these amplitudes, can be written at leading order in  $\alpha$  as

$$\frac{\sigma_{e^+p}}{\sigma_{e^-p}} = \frac{|\mathcal{M}_{1\gamma}|^2 + 2\mathcal{R}(\mathcal{M}_{1\gamma}\mathcal{M}_{2\gamma})}{|\mathcal{M}_{1\gamma}|^2 - 2\mathcal{R}(\mathcal{M}_{1\gamma}\mathcal{M}_{2\gamma})}. \quad (3.8)$$

In the sixties a number of experiments [44–50] measured  $\sigma_{e^+p}/\sigma_{e^-p}$  but the results, as can be seen in Fig. 3.9, are not precise enough for the determination of the TPE contribution at the level of few percent. Theoretical predictions also give different results depending on the model [40, 43, 51, 52].

Until recently, no other attempts were made to measure  $\sigma_{e^+p}/\sigma_{e^-p}$  as its effect was

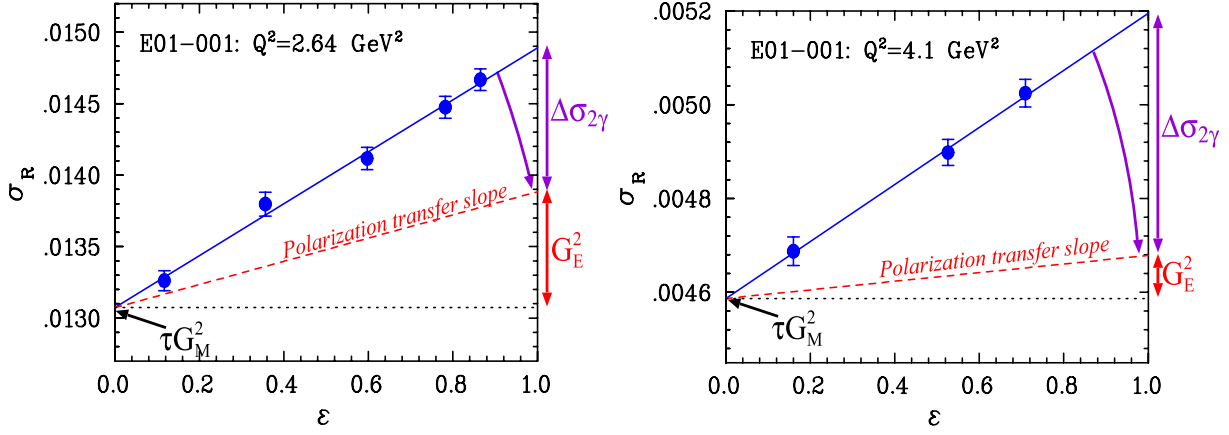


**Figure 3.7:** Reduced cross section as a function of  $\varepsilon$  as predicted from the polarization transfer results from  $G_E/G_M$  (red dashed line) and as measured by the Jefferson Lab experiment E01-001 [10] (circles; blue solid line is best fit).

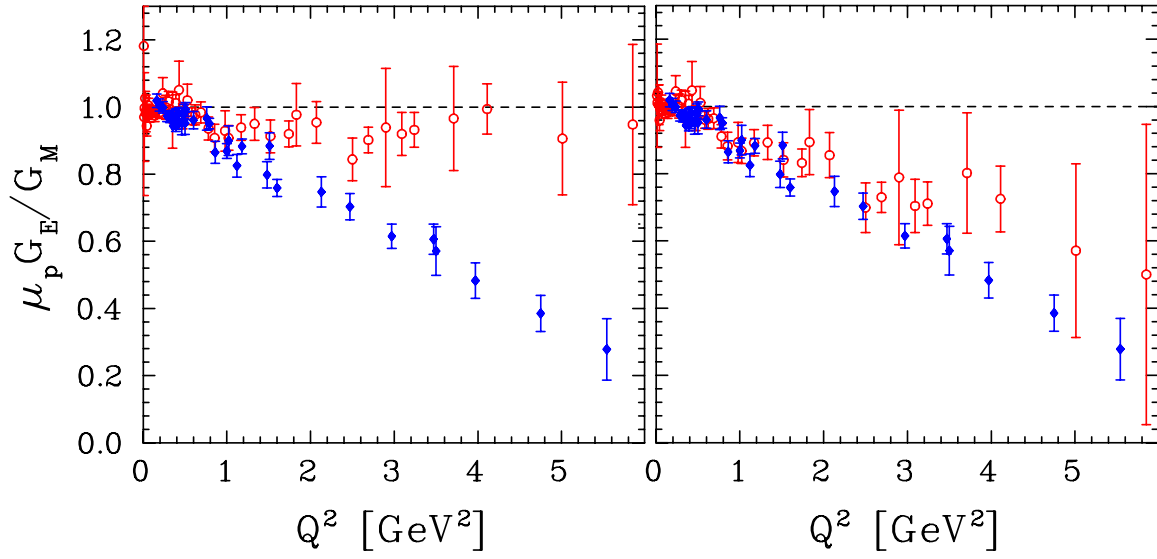


**Figure 3.8:** Comparison of polarization measurements (filled diamonds) and Rosenbluth separations (open circles) without (left) and with the TPE correction (right) from Re. [43].

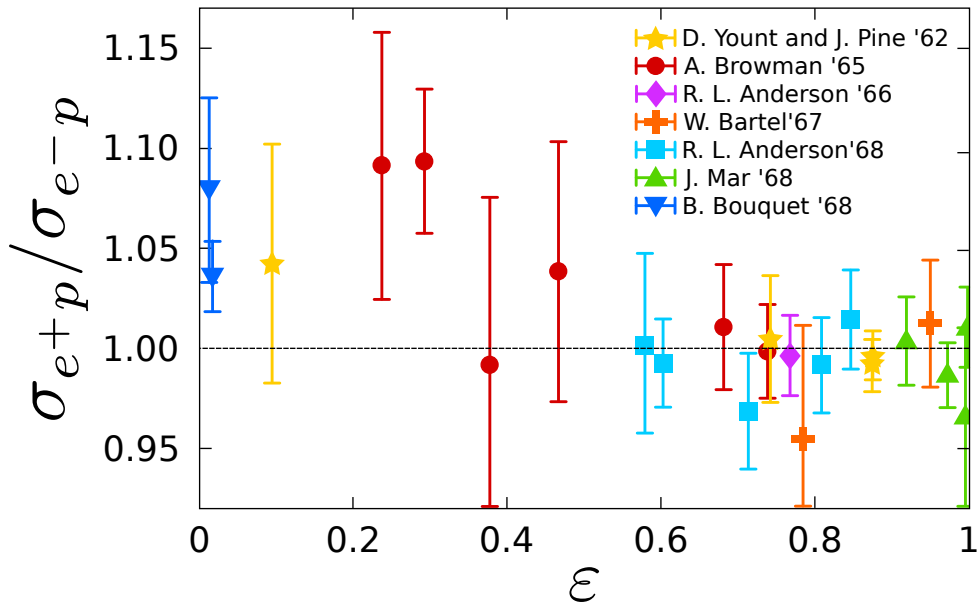


**Figure 3.9:** The ratio of the positron-proton to electron-proton scattering cross section as a function of  $\epsilon$  from Ref. [44–50].

considered negligible. When the need for new and precise data has become evident a series of new experiments was prepared: CLAS at JLab (Newport News), VEPP-3 (Novosibirsk), and OLYMPUS at DESY (Hamburg).

The CLAS experiment [53] measured the elastic scattering cross sections  $\sigma_{e^+p}$  and  $\sigma_{e^-p}$  simultaneously. A mixed beam of electrons and positrons was produced using the primary accelerator electron beam. First, bremsstrahlung photons were produced by hitting a radiator with the primary beam. Second, the photons struck a converter to produce electron-positron pairs. Thanks to the mixed beam and the experimental setup the electron and positron luminosities were equal. The measurement was performed at  $Q^2 = 0.85$  and  $1.45 \text{ GeV}^2$ . A set of photon blockers and collimators were used to fix the maximum and minimum lepton energy.

The VEPP-3 experiment [54] employed alternated electron and positron beams with energies of  $1.0 \text{ GeV}$  and  $1.6 \text{ GeV}$ . The luminosity was measured using elastic lepton-proton scattering detected at small energies  $Q^2 \approx 0.1 (\text{GeV}/c)^2$  and forward angles  $\epsilon > 0.9$  with an assumption that the TPE effect is negligible at these kinematic settings. The data

were collected in the  $Q^2$  range from 0.830 to 1.51 GeV<sup>2</sup>.

The CLAS and VEPP-3 experiments have completed the data analysis and their results [53,54] are presented in Fig. 3.10. Both experiments showed deviation from  $\sigma_{e^+p}/\sigma_{e^-p} = 1$ . The data points lie above one, while values below one are expected from point-like proton [42]. At the same time, the results are consistent with the hadronic calculations [43,55].

## 3.2 Time-like Form Factors

TL proton FFs can be measured via lepton or proton annihilation processes, *i.e.*,  $\bar{p}p \rightarrow e^+e^-$  and  $e^+e^- \rightarrow \bar{p}p$ . The former process will be studied at the  $\bar{P}$ ANDA experiment which is described in details in chapter 5. Let us consider the  $\bar{P}$ ANDA scenario which will employ an antiproton beam and a proton target. Zichichi [56] derived the cross section for  $\bar{p}p \rightarrow e^+e^-$  reaction, which has the following form:

$$\frac{d\sigma}{d\cos\theta} = \frac{\pi\alpha^2}{2\beta s} \left[ |G_M|^2(1 + \cos^2\theta) + \frac{|G_E|^2}{\tau}(1 - \cos^2\theta) \right], \quad (3.9)$$

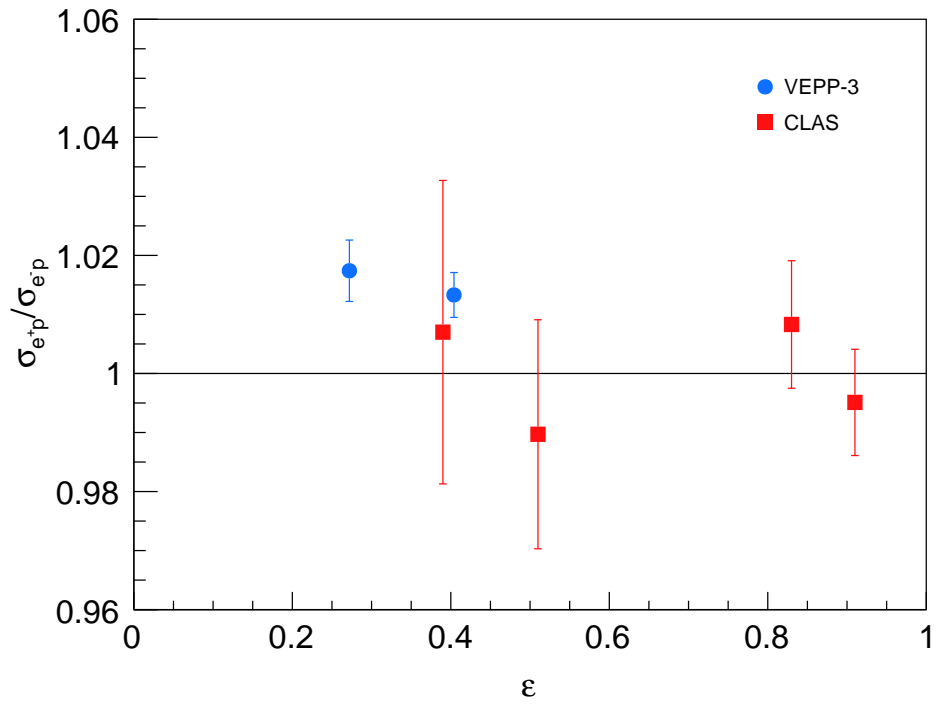
where  $\theta$  is the angle of the outgoing electron in the antiproton-proton center-of-mass frame (c.m.). A measurement of this differential cross section over a wide range of  $\cos\theta$  makes possible not only the determination of the FF ratio  $R$ , but also an independent extraction of the moduli of the proton electromagnetic FF  $G_E$  and  $G_M$ . Fig. 3.11 illustrates the concept of the method. The measured  $\bar{p}p \rightarrow e^+e^-$  cross section as a function of  $\cos\theta$  in the  $\bar{p}p$  c.m. system is fitted using Eq. (3.9). Values of  $G_E$  and  $G_M$  can then be directly extracted from the fit.

It should be noted that for the cross section measurement precise knowledge of the luminosity is crucial. The luminosity uncertainty directly affects that of the cross section and, as a consequence, the uncertainty of  $G_E$  and  $G_M$ . Without luminosity measurement, the angular distribution of the events can be fitted using a modified version of Eq. (3.9):

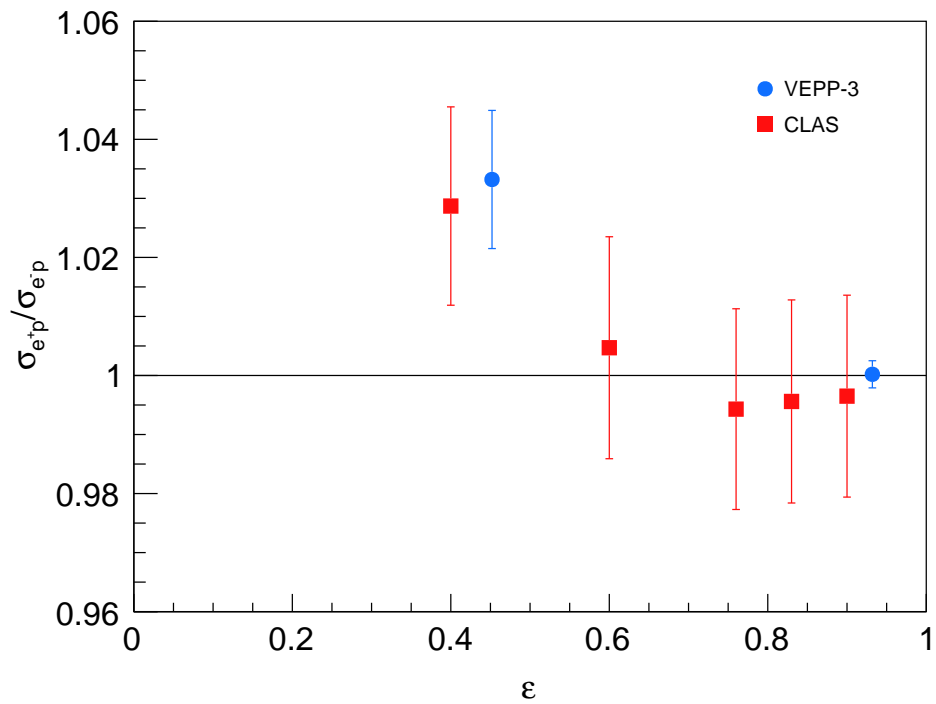
$$\frac{d\sigma}{d\cos\theta} = \frac{\pi\alpha^2}{2\beta s} |G_M|^2 \left[ (1 + \cos^2\theta) + \frac{R^2}{\tau}(1 - \cos^2\theta) \right], \quad (3.10)$$

with the FF ratio  $R$  being the only fit parameter.

Figs. 3.12a and 3.12b illustrate the modulus of the TL magnetic form factor  $|G_M|$  extracted under assumption that  $|G_E| = |G_M|$  from Refs. [12–14,57–64] and the measured



(a)



(b)

**Figure 3.10:** The ratio of positron-proton to electron-proton scattering cross section as a function of  $\epsilon$  at CLAS energies of  $Q^2 \approx 0.85 \text{ (GeV}/c)^2$  (a) and  $1.45 \text{ (GeV}/c)^2$  (b).

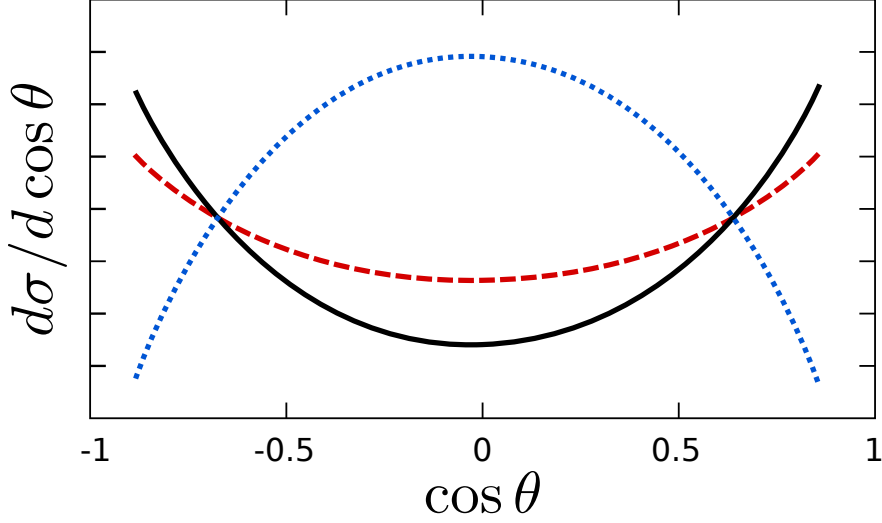


**Figure 3.11:** The concept of the Rosenbluth separation method for determining the TL proton electromagnetic FFs from the differential  $\bar{p}p \rightarrow e^+e^-$  cross section for  $GE/GM = 0$  (red dashed line),  $GE/GM = 0$  (black solid line), and  $GE/GM = 3$  (blue dotted line).

FF ratio from Refs. [12–16]. The  $Q^2$  range where  $\bar{P}$ ANDA is expected to measure proton FFs is shown as a cyan band. The kinematic reach of the  $\bar{P}$ ANDA experiment lies between  $5.1 \text{ (GeV}/c)^2$  and  $30.0 \text{ (GeV}/c)^2$  but since the annihilation cross section decreases with  $Q^2$  the upper limit at  $Q^2 \approx 15 \text{ (GeV}/c)^2$  for the determination of the FF ratio with a statistical uncertainty of around 50% taken the allocated measuring time. The extraction of  $|G_M|$  will be possible up to a  $Q^2 = 22 \text{ (GeV}/c)^2$  by measuring the total cross section.

Theory offers a number of parameterizations of the proton FFs [65–70]. The existing data on the TL effective FF defined as:

$$F_p = (|G_M|^2 + \frac{\tau}{2}|G_E|^2)/(1 + \frac{\tau}{2}), \quad (3.11)$$

are well reproduced by the function proposed in Ref. [33]:

$$|G_{E,M}| = \frac{A}{1 + q^2/m_a^2} G_D, \quad (3.12)$$

where the numerator  $A = 22.5$  is a constant extracted from the fit to the TL data and  $m_a^2 = 3.6 \text{ (GeV}/c)^2$ .

It is clear that the existing measurements are not conclusive. Although multiple measurements have been performed, most of them are limited by the statistics. Most experiments measured  $G_E$  only as shown in Fig. 3.12a. The measurement of the FF ratio are lacking precision and consistency between experiments as shown in Fig. 3.12b. The LEAR and BaBar experiments measured the FF ratio at lower  $q^2$  but their results are inconsistent. At  $q^2 > 5 \text{ (GeV}/c)^2$  the data are very scarce and the precision is very low. While more data are expected to come from BESIII [71], the  $\overline{\text{PANDA}}$  experiment will be able to provide more high precision data in the expanded kinematic range of up to  $q^2 = 15 \text{ (GeV}/c)^2$ . Detailed feasibility study of the proton TL electromagnetic FF with the  $\overline{\text{PANDA}}$  experiment is presented in chapter 9.

In addition, the  $\overline{\text{PANDA}}$  experiment will be capable of measuring the proton electromagnetic FFs in the so-called unphysical region. The unphysical region is the energy range between  $Q^2 = 0 \text{ (GeV}/c)^2$  and  $Q^2 = 4m_p^2$ , *i.e.*, electron-positron production threshold via antiproton-proton annihilation. Through the emission of a neutral pion by the proton or the antiproton, the energy of a virtual photon, which subsequently decays into an electron-positron pair, is decreased. Thus, this process effectively decreases  $Q^2$  below the  $4m_p^2$  threshold. Fig. 3.13 shows two possible diagrams of the  $\bar{p}p \rightarrow e^+e^-\pi^0$  reaction.

The electron-positron pair in the  $\bar{p}p \rightarrow e^+e^-\pi^0$  carries the same information about proton form factors as in the  $\bar{p}p \rightarrow e^+e^-$ . From the experimental point of view, this process requires the detection and identification not only of the lepton pair but also the result of the  $\pi^0$  decay, *i.e.*, two additional photons. It was already shown in Ref. [72] that the  $\overline{\text{PANDA}}$  detection and PID capabilities are sufficient for successful measurement of this process.

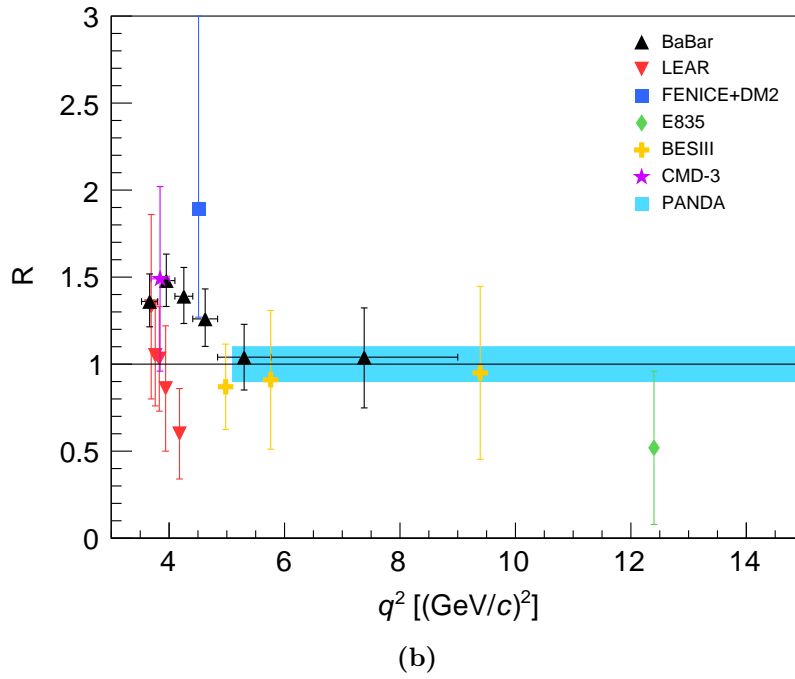
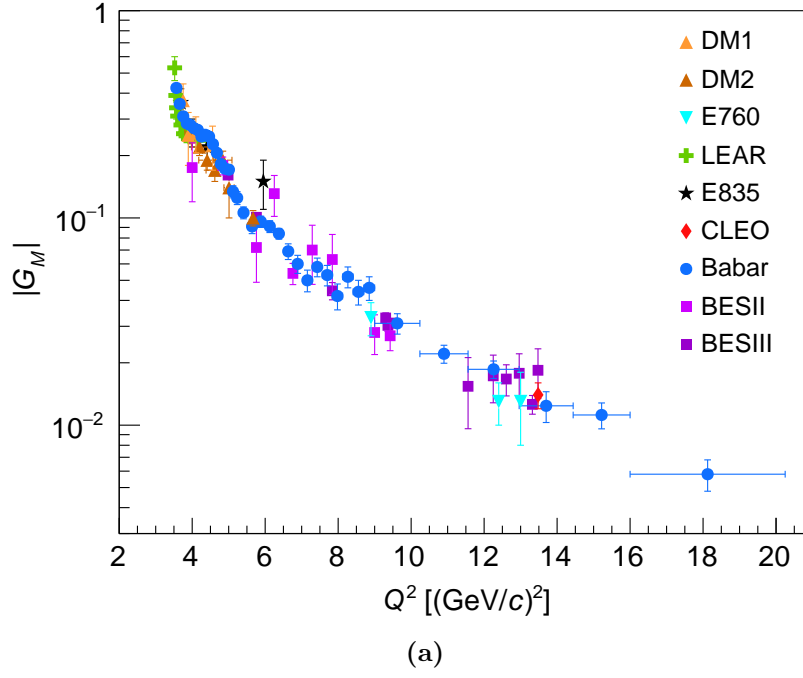


**Figure 3.12:** The modulus of the time-like magnetic form factor  $|G_M|$  (a) extracted with the hypothesis  $G_E/G_M = 1$  [12–14,57–64] and the measured FF ratio (b) [12–16], with the kinematic region where  $\bar{\text{PANDA}}$  is expected to measure proton FFs.

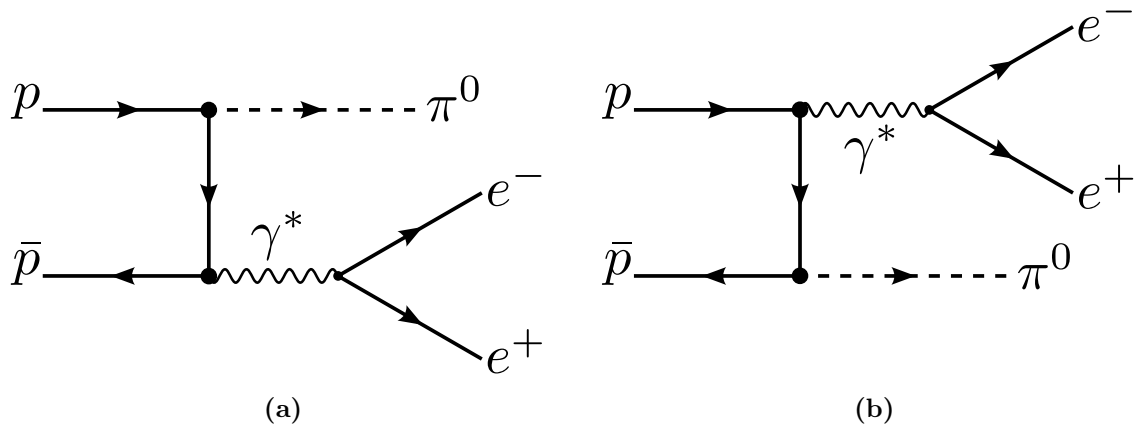


**Figure 3.13:** Feynman graphs for  $\bar{p}p \rightarrow e^+e^-\pi^0$  with a single nucleon exchange in the  $u$ -channel (a) and  $t$ -channel (b).

# Part II

## Experiments

# Chapter 4

## OLYMPUS Experiment

The OLYMPUS experiment involved over 55 people from all around the world. It took a decade to realize the initial idea: prepare a proposal, assemble and build detectors, collect and analyze the data. The experimental setup consisted of the existing BLAST [73] spectrometer, which was transported from the MIT-Bates Research and Engineering Center, as well as newly designed target and luminosity monitors. The whole setup was assembled at the DORIS III (hereinafter DORIS) storage ring at the Deutsches Elektronen-Synchrotron (DESY), Hamburg, Germany.

### 4.1 Physics Goal

The OLYMPUS experiment [25] aims to resolve the experimental discrepancy in the determination of the ratio of the proton electric to magnetic form factor,  $R = G_E/G_M$ , extracted using the Rosenbluth separation method and polarization transfer technique. This discrepancy could be explained by a two-photon exchange contribution in lepton-hadron scattering. A measurement of the elastic scattering cross section ratio  $\sigma_{e+p}/\sigma_{e-p}$  will make possible a direct measurement of the two-photon exchange amplitude, as explained in Sec. 3.1.3.

## 4.2 Experiment Overview

The OLYMPUS detector, shown in Fig. 4.1, was based on a toroidal magnet. The role of the magnetic field was to bend the track of charged particles, which enabled their charge and momentum to be determined. In addition, it allowed to remove low energy charged particles from the tracking detectors. The tracking was performed with two drift chambers placed symmetrically on either side of the beam pipe. The trigger for most of OLYMPUS detectors was provided by the time of flight (TOF) detector.

The luminosity was measured using three independent systems: 1) The 12° degree monitors were built from multi-wire proportional chambers (MWPC) and gas electron multipliers (GEM). Three pairs of MWPC and GEM were placed symmetrically in each sector; 2) The Symmetric Møller/Bhabha (SYMB) luminosity monitor consisted of two identical Cherenkov calorimeters; 3) Additionally, the luminosity was estimated using the slow control system data, *i.e.*, beam current, target density, and the measurement time.

The toroidal magnet, drift chambers, time of flight detectors, support frames and most of the readout and control electronics were originally part of the BLAST spectrometer [73] at MIT-Bates.

### 4.2.1 DORIS Electron/Positron Beams

The DORIS storage ring was built in 1974 as an electron-electron and electron-positron collider with energies between 3.5 and 5 GeV per beam. In 1993 it was modified to operate as a dedicated source for synchrotron radiation.

The OLYMPUS detector was located at the site of the former ARGUS experiment. In order to accommodate the OLYMPUS detector and provide the necessary beam conditions a number of modifications was made to the DORIS storage ring<sup>1</sup>:

- A number of tweaks were performed in order to provide 2.01 GeV electron and positron beams with the required parameters.
- Several RF cavities had to be moved further upstream from the detector area.

---

<sup>1</sup>The DORIS storage ring continued its operation as the synchrotron radiation source between the two OLYMPUS data taking periods.

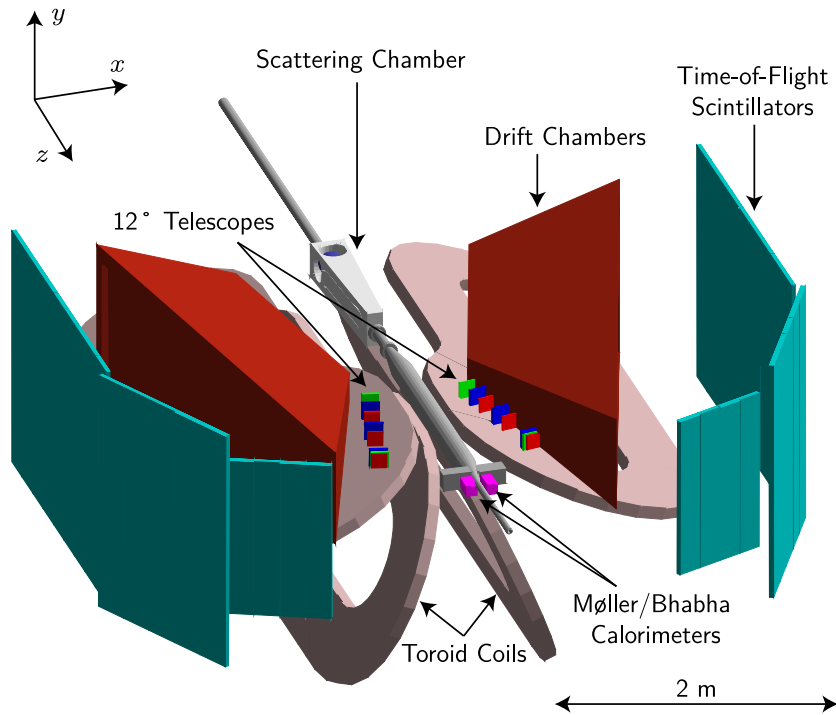


**Figure 4.1:** A solid-model representation of the OLYMPUS detector with the top four magnet coils removed to show the instrumented horizontal sectors.

- Two additional quadrupole magnets were installed on either side of the OLYMPUS detector to reduce the beam size in the interaction region without affecting the beam profile during synchrotron runs.
- Extra target cooling was installed to prevent overheating during synchrotron radiation production.

Thanks to the operation in top-up mode, it was possible to utilize higher target density together with a high average beam current. This also allowed to minimize beam current fluctuations.

The beam position, slope, current, and a number of other parameters were continuously monitored and recorded by the accelerator systems for subsequent use in the OLYMPUS data analysis.

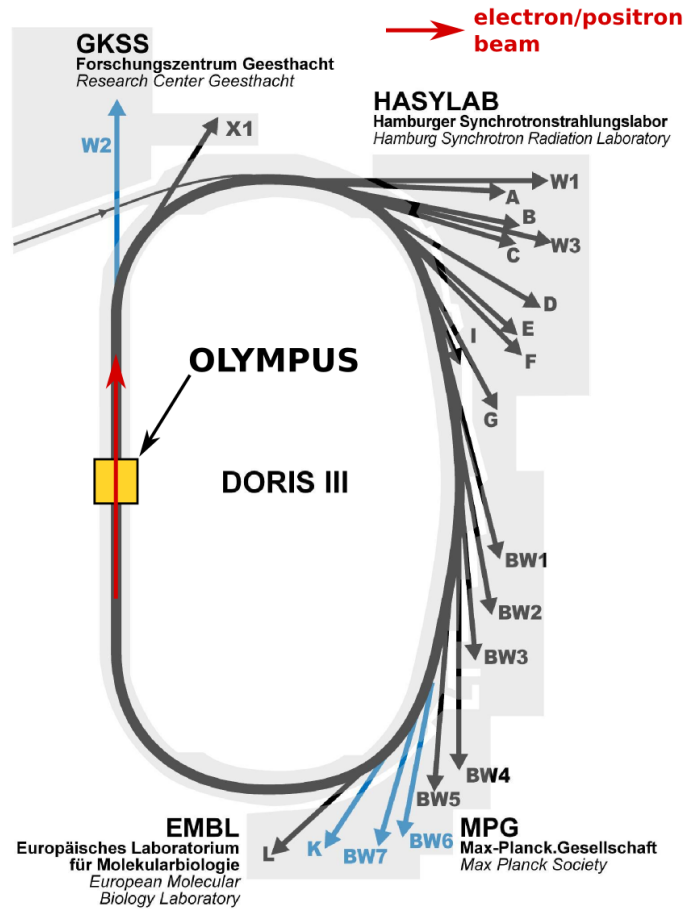


**Figure 4.2:** Overview of the DORIS electron/positron storage ring with the OLYMPUS experiment and multiple synchrotron light beamlines.

### 4.2.2 Hydrogen Target

At the OLYMPUS experiment an extended hydrogen target, shown in Fig. 4.3, was used [74]. Due to the high beam currents the target cell consisted of an open-ended, elliptical cylinder (27 mm horizontal  $\times$  9 mm vertical  $\times$  600 mm long) made of aluminum. The wall thickness was 0.075 mm. The choice was motivated by the DORIS beam profile and the size was approximately  $10\sigma$  of the nominal horizontal and vertical beam size in the interaction region. The beam horizontal and vertical size at target ( $1\sigma$ ) was 0.55 mm and 0.09 mm, respectively.

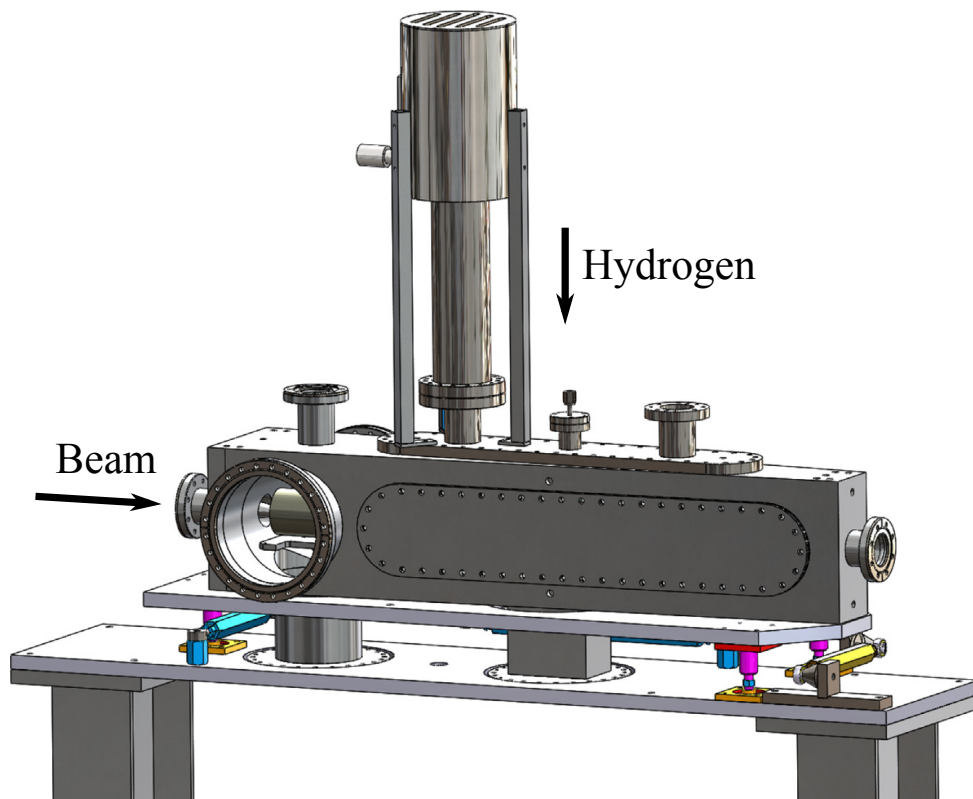


**Figure 4.3:** CAD model of the OLYMPUS target.

In the center of the target cell was an opening through which the hydrogen gas was injected. The maximum gas density was in the center of the cell and linearly decreased towards its ends. A system of six magnetic levitation turbomolecular pumps was used to pump the gas from the part of the beam line located inside the OLYMPUS spectrometer.

Three wakefield suppressors were installed to prevent heating of the target cell. This permitted to keep the target cooled down to 50 K during synchrotron operation and around 70 K during OLYMPUS data taking.

### 4.2.3 Magnet System

The magnet consisted of eight copper coils placed around the beam line and the target. The eight coils divided the space around the interaction region in eight sectors. Two sectors in the horizontal plane were occupied by detectors.

Each coil consisted of 26 turns of 1.5 in square copper tubes, arranged into two layers of 13 turns each. A circular hole, 0.8 in in diameter, inside the tubes served as a channel for cooling water. The coils had a complicated shape to increase the field in the forward, high momentum, direction and to have a more uniform field at large scattering angles.

The magnet was operated at 5000 A that yielded a field up to 0.28 T. The coil position was adjusted to minimize the field along the beam line. An integrated field smaller than 0.005 T m was achieved.

### 4.2.4 Drift Chambers

Two identical drift chambers were located in the two horizontal sectors. The drift chambers provided momentum measurement, charge, polar and azimuthal scattering angle and vertex position determination of outgoing charged particles. Each sector was equipped with three drift chambers (inner, middle, outer) joined together into a single gas volume, as shown in Fig. 4.4. The geometrical acceptance of the drift chambers was from  $20^\circ$  to  $80^\circ$  in polar angle and  $\pm 15^\circ$  in azimuth. The drift field was created by approximately 10,000 wires. 954 of these wires were used to read out the signal produced by charged particles.

Each chamber comprised of two super-layers of drift cells with 20 mm separation

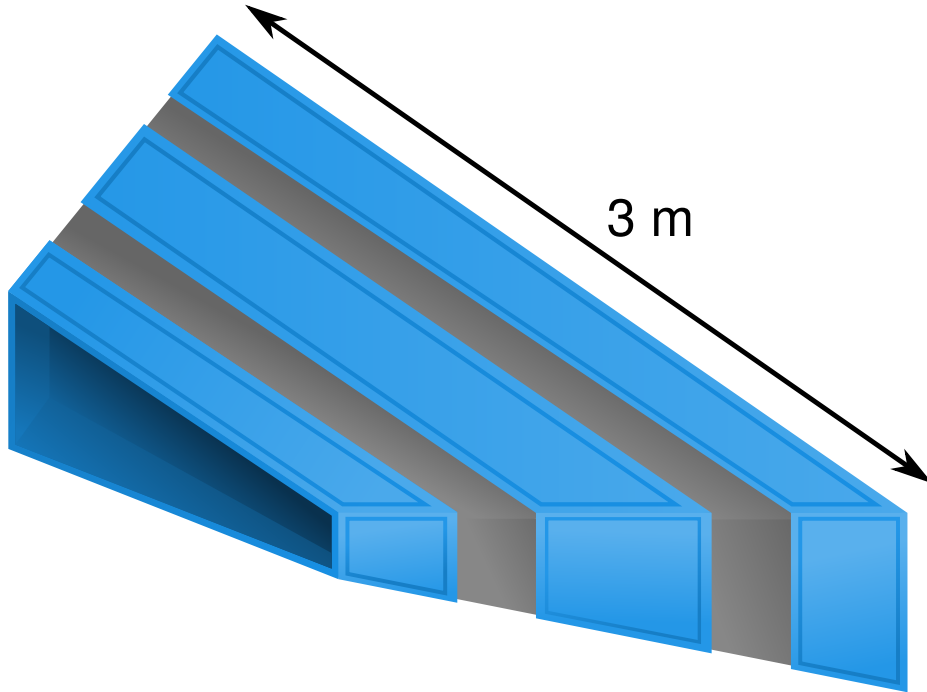


**Figure 4.4:** Three drift chambers (blue) joined together into a single gas volume.

between the super-layers. Drift cells consisted of three sense wires staggered  $\pm 0.5$  mm from the center line. This helped to determine whether a charged particle flew on the right or on the left of the drift cell. Each drift cell was  $78 \times 40$  mm<sup>2</sup>. During the data taking the drift chambers were filled with an Ar:CO<sub>2</sub>:C<sub>2</sub>H<sub>6</sub>O gas mixture (87.4:9.7:2.9).

#### 4.2.5 Time of Flight Detectors

The TOF detectors consisted of 36 vertical scintillator bars. Each sector had 18 bars located behind the drift chambers. The signals were read out with photo-multiplier tubes (PMT) attached to both ends. The four most-forward bars on each side were 119.4 cm high, 17.8 cm wide, and 2.54 cm thick. The remaining 14 bars on each side were 180.0 cm high, 26.2 cm wide, and 2.54 cm thick. The TOF detectors covered the whole acceptance of the drift chambers. The bars were arranged in three planar sections (4, 5, and 9

bars) oriented with their normal approximately pointing toward the target. The two bars covering most-backward angles in each sector were added for the OLYMPUS experiment to increase the acceptance at large polar angles.

The TOF detector provided a readout trigger for most OLYMPUS detectors. The main trigger logic of the experiment required at least one top-bottom coincidence in both sectors.

The active volume of the TOF bars was made from Bicron BC-408 plastic scintillators. The choice was motivated by the fast response time (0.9 ns rise time) and long attenuation length (210 mm).

After the data taking, during the cosmic ray runs, the efficiencies for top/bottom coincidences were measured. The efficiency was found to be on the level of 96-99% for signals coming from the center of each bar.

## 4.3 Luminosity Measurement

The physics goal of the OLYMPUS experiment called for the precise and accurate measurement of the ratio of the integrated luminosities of electron and positron beams. Multiple independent luminosity monitors were operated in parallel to the main spectrometer during data taking.

### 4.3.1 12° Luminosity Monitors

The 12° luminosity monitors, shown in Fig. 4.5, measured elastically scattered electrons and positrons in coincidence with the recoil proton detected in the drift chamber. It comprised of three GEM detectors paired with three MWPCs. The scattering angle of 12° was chosen based on the existing data which point toward the fact that the TPE effect might be negligible at small scattering angles [44–50]. Theory also predicts smaller TPE contributions at forward scattering angles [40, 43, 51, 52]. The designed statistical precision of the system is better than 1% after one hour of data taking.

A trigger signal was provided by two scintillator tiles (120 mm × 120 mm × 4 mm). The read out was triggered by a coincidence signal from two tiles on one side and a TOF signal from back angles the opposite side. For an independent triggering an addition set

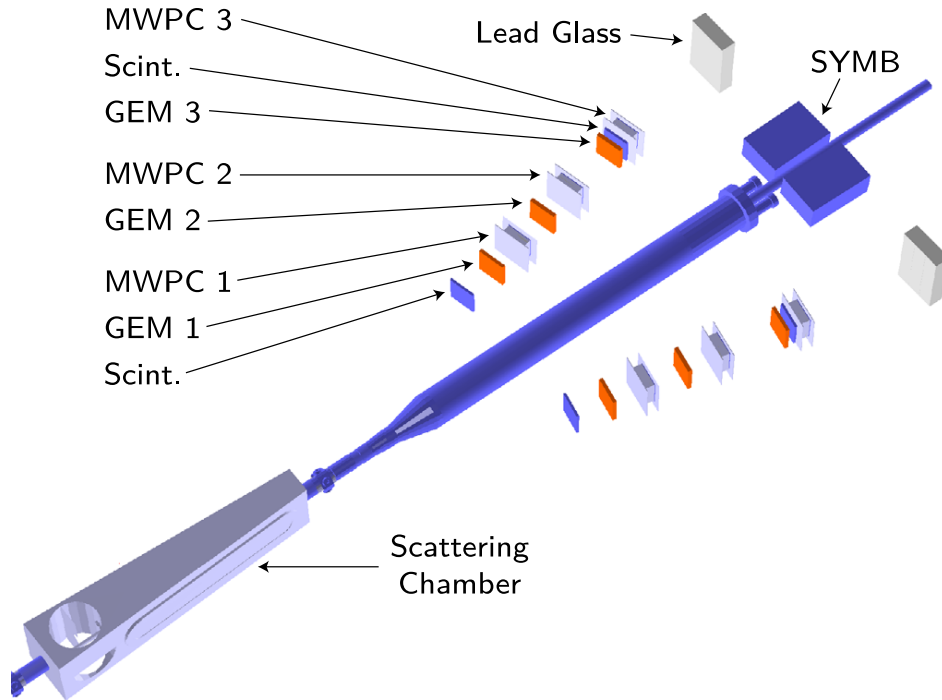


**Figure 4.5:** The layout of the 12° degree monitor consisting from three MWPC and GEM stations and symmetric Møller/Bhabha calorimeters placed symmetrically in each sector.

of lead glass calorimeters were installed behind each 12° monitor. Thus, the efficiency of the tile trigger could be continuously measured throughout data taking. The efficiency of the two scintillator tiles was determined to  $> 99\%$ .

### Gas Electron Multiplier Detectors

GEM detectors were designed at the MIT-Bates Linear Accelerator Center and built at Hampton University. INFN Rome and INFN Genoa designed and constructed the front-end and readout electronics. In total six identical GEM modules were built. Every GEM detector consisted of three GEM foils and a cathode foils stacked together, a readout board, and two pressure volume foils which surrounded the gas volume. A mixture of Ar:CO<sub>2</sub> in a ratio of 7:3 was used. Each GEM detector had 250 channels for the vertical and 250 for the horizontal coordinate. The GEM's active area was approximately 10 cm

$\times 10$  cm in size.

The spatial resolution of the GEM detector was  $70 \mu\text{m}$  and the individual efficiency was around 95%.

### Multi-Wire Proportional Chambers

MWPC and their readout electronics were designed and manufactured at the Petersburg Nuclear Physics Institute [75]. As with GEM detectors, six identical chambers were built. Each MWPC detector ( $180 \text{ mm} \times 180 \text{ mm} \times 50 \text{ mm}$ , with  $112 \text{ mm} \times 112 \text{ mm}$  of an active area) was assembled from three planes of anode sense wires alternated with cathode wire planes. The MWPC was filled with an  $\text{Ar}:\text{CO}_2:\text{CF}_4$  gas mixture in a ratio of 65:30:5.

During data taking the efficiency of each individual chamber of around 99% was observed.

### 4.3.2 Symmetric Møller/Bhabha Luminosity Monitor

The Symmetric Møller/Bhabha [76] luminosity monitor measured the coincidence rate of the electron-electron and electron-positron scattering events at symmetric angles. At the operation beam energy of 2.01 GeV, the angle is  $1.29^\circ$ . Fig. 4.6 illustrates an event where a lepton pair is detected by the SYMB monitor. The SYMB consisted of two identical Cherenkov calorimeters placed symmetrically with respect to the beam line. Each calorimeter comprised of  $3 \times 3$  array of  $\text{PbF}_2$  crystals with a lead collimator set in front of it. A collimator protected the detector from rescattered background particles, possible damage during the beam tuning, and assured that most of the events come from the Møller/Bhabha scattering. The Cherenkov light from each  $\text{PbF}_2$  crystal was gathered by photomultiplier tubes (PMTs). Due to the very high cross section of Møller and Bhabha processes the statistical uncertainty was negligible after few minutes of data taking.

Fig. 4.5 illustrates the layout of the  $12^\circ$  degree and the SYMB calorimeters.

The SYMB detector collected data in three modes: Coincidence, Left Master (LM), and Right Master (RM). In the coincidence mode both SYMB monitors should pass

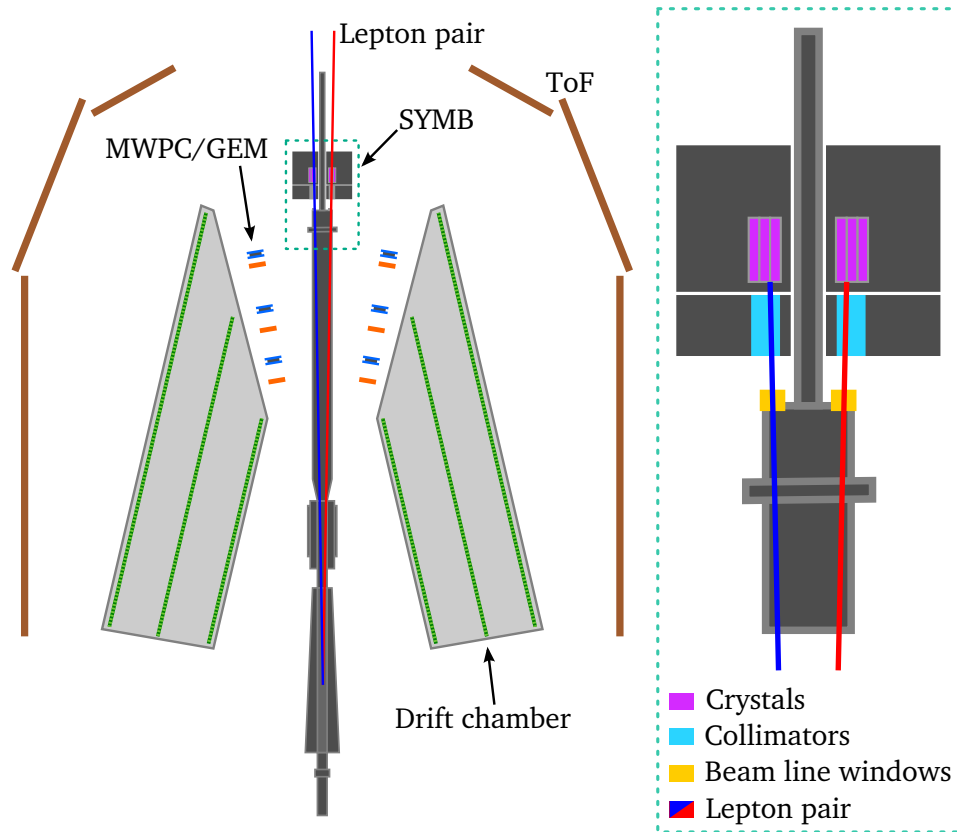


**Figure 4.6:** Kinematics of the lepton-lepton scattering detected by the SYMB monitors. Two leptons emitted from the target area at symmetric angle of  $\approx 1.29^\circ$  pass through the beam line window and deposit their energy in the SYMB calorimeters.

through a "Local Maximum" veto. The veto accepts an event when the signal from the central crystal has the highest amplitude. In the Master-Slave modes, the left or the right sector is considered as the master and the other one as the slave. Any event with a signal that passes the veto in the master detector is recorded independently of the signal registered on the slave detector. In addition, in order to be recorded the signal had to exceed a certain threshold.

### 4.3.3 Slow Control

The slow control system allowed for an online luminosity determination via measurement of the beam current, gas flow to the target, and target cell temperature. The product of the beam current and target density, corrected for the dead time, was used to estimate the integrated luminosity.

$$\mathcal{L} = I \cdot \rho \cdot \Delta t \quad (4.1)$$

where  $I$  is the beam current,  $\rho$  is the target density, and  $\Delta t$  is the measurement time.

The beam current was measured with a high precision DC transformers. The target gas distribution used was determined using a standalone Monte Carlo simulation based on the molecular flow model of hydrogen molecules within the target system [77]. The temperature of the target cell was monitored by seven Pt100 temperature sensors. The sensors were positioned along the length of the cell so that the temperature uniformity could be monitored. The wires for the sensors were fed through the ports in the top of the scattering chamber.

## 4.4 Operation

The OLYMPUS experiment was carried out at DESY Hamburg, Germany using 2.01 GeV electron and positron beams at the DORIS storage ring incident on an internal hydrogen gas target. The beam species were typically changed every 24 h.

The data was collected in two periods: January 2012 - February 2012 and October 2012 - January 2013. In the first data taking period DORIS was manually refilled when the beam current dropped below 50 mA from the initial 65 mA. The high voltage of

various detectors was decreased during refills to avoid possible damage. The target gas density was lower than designed due to an unknown at that time gas leak. It was found due to a discrepancy between the calculated slow control luminosity and the luminosity given by the SYMB monitors. Thus, the total integrated luminosity collected during the first run was significantly lower than expected. In order to have a better control over systematic uncertainties data were collected for both beam species using negative and positive toroid polarities.

Between the two periods a number of changes were performed to improve the DORIS beam injection process. As before, the beam was manually filled to 65 mA and then allowed to decrease to a minimum of 58 mA. At this point the beam was automatically refilled (top-up mode). The high voltage was not lowered during the refill but the DAQ system was stopped for the duration of injection pulses.

Thanks to the DORIS improvements, during the second run the average beam current was higher which allowed to reach the designed integrated luminosity of  $4.5 \text{ fb}^{-1}$ . Thus, providing enough data for the SYMB luminosity determination with better negligible statistical uncertainties. At the same time, it was not possible to run with a negative magnet polarity due to a large amount of background being pushed into the drift chambers. Therefore, only a small number of runs were taken with the negative magnet polarity in conjunction with the lower beam current and target flow. Fig. 4.8 illustrates how the collected luminosity is distributed between the beam species and magnet polarities.

The integrated luminosity delivered to the experiment is shown in Fig. 4.7. In total, approximately  $4.5 \text{ fb}^{-1}$  of data was collected. During the first run the target gas density was lower than the design value due to a gas leak caused by an improper connection between the target and the gas supply system. Consequently, the majority of data, around 90%, was collected during the second period. A typical data taking run had a length of around 20 minutes.

In addition, a series of empty target runs, runs with different, including zero, magnetic field strengths, and other test runs were taken for background monitoring, detector calibrations, and testing.

At the end of data taking, a survey of all of the detectors' positions and of the magnetic field in the regions relevant for tracking were performed.

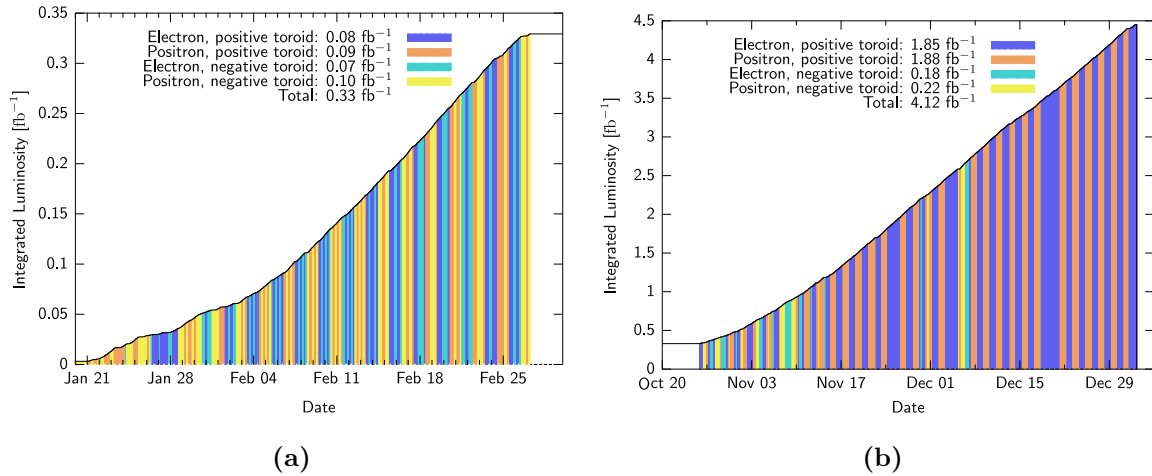


**Figure 4.7:** Integrated luminosity collected during two data taking periods for using electron and positron beams with positive and negative magnet polarities.

## 4.5 Data Analysis and Simulation Software

The OLYMPUS Monte Carlo contains a detailed description of the OLYMPUS detector. The Monte Carlo software is closely tied to the collected experimental data, slow control information, and the beam parameters provided by the DORIS storage ring. First, an experimental run and an event generator have to be chosen. The event generator produces initial state (primary) particles. The  $z$ -vertex is calculated based on the target density distribution, while  $x$ - and  $y$ -vertices are set based on the beam parameters, *e.g.*, the beam offset, slope, etc., for the given run. In general, all relevant parameters are taken from the corresponding experimental run. The polar and azimuthal angles of the generated primary particles are modified according to the beam parameters in the given run. Next, the primary particles are propagated through the OLYMPUS detector. During the propagation step, various physical processes are simulated, including the production of secondary particles using Geant4 simulation toolkit [78]. The signals produced in sensitive volumes of the OLYMPUS detector are digitized and stored in a format identical to that of the experimental data. This allows to analyze simulated and experimental data using the same software and compare them easily.

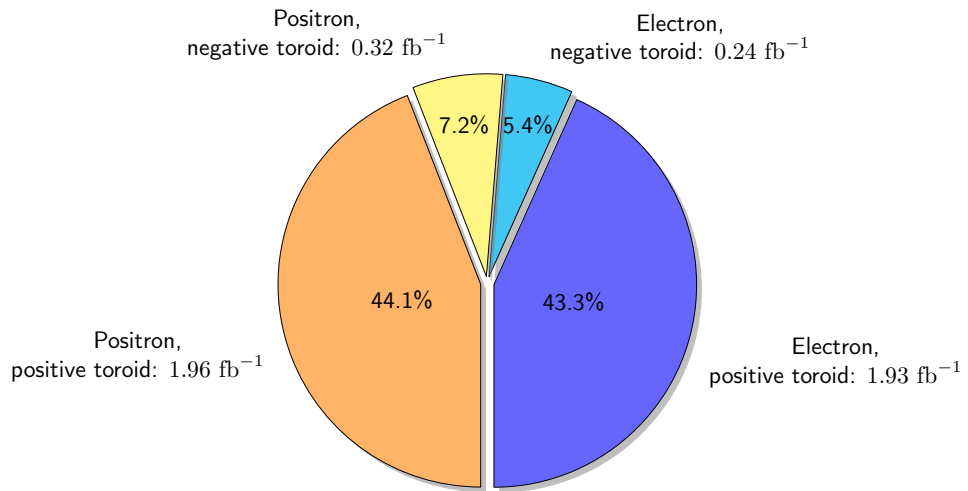


**Figure 4.8:** Integrated luminosity distribution for different beam and magnet settings.

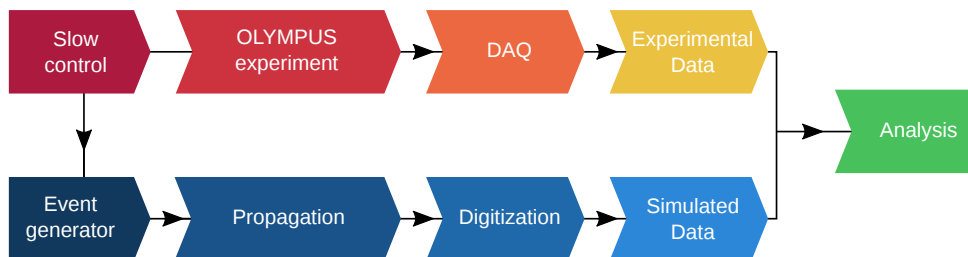


**Figure 4.9:** The simulation and the data analysis procedure in the OLYMPUS Monte Carlo.

# Chapter 5

## $\bar{\text{P}}\text{ANDA}$ experiment

The  $\bar{\text{P}}\text{ANDA}$  experiment has a rich physics program thanks to high-intensity antiproton beams. Numerous measurements will be performed in different areas of hadron physics. A short list of  $\bar{\text{P}}\text{ANDA}$  physics goals and main detector systems are presented below.

### 5.1 Physics program

Study of baryon spectroscopy and understanding of the strong quantum chromodynamics (QCD) is one of the primary goals. Many predicted states [79] like (multi-) strange and charmed baryons which haven't been experimentally observed will be searched at  $\bar{\text{P}}\text{ANDA}$ .

Another key topic is charmonium spectroscopy, it is an important tool for the understanding of strong interactions. While all charmonium states below the open charm threshold are known, their masses, width, and branching ratios are not completely measured. Moreover, the data above the threshold is scarce. The  $\bar{\text{P}}\text{ANDA}$  experiment will allow precision determination of mass, width, decay branches below and above the threshold, as well as measurements of the quark-confining potential.  $\bar{\text{P}}\text{ANDA}$  will also provide unique measurements for states with spin  $\geq 2$  together with the narrow,  $< 10$  MeV, states.

The hadron structure of the proton can also be studied at the  $\bar{\text{P}}\text{ANDA}$  experiment.

The antiproton-proton annihilation into a lepton pair will allow precise measurements of the proton FF ratio as well as an individual determination of  $|G_E|$  and  $|G_M|$  in a wide kinematic range. Moreover, the extraction of the proton FFs will be possible in the unphysical region. Transition distribution amplitudes, universal objects that describe the transition between different particles will be accessible via  $\bar{p}p \rightarrow e^+e^-\pi^0$ .

In addition, a study of hypernuclei systems, in which  $u$  or  $d$  quarks are replaced by strange quarks, with the  $\bar{\text{P}}\text{ANDA}$  detector are planned [80]. An ample production of  $\Xi$ -hyperons with a dedicated target will enable high-precision  $\gamma$ -spectroscopy of double strange system and therefore making possible to explore the hyperon-hyperon interaction for the first time. Comparison ordinary nuclei and hypernuclei may also reveal new information about nuclear physics.

## 5.2 $\bar{\text{P}}\text{ANDA}$ detector

The  $\bar{\text{P}}\text{ANDA}$  detector [81] is designed to study a wide range of final states produced by an antiproton beam, with momentum between 1.5 GeV/ $c$  to 15 GeV/ $c$ , colliding with a proton target. It provides a nearly  $4\pi$  solid angle acceptance, high tracking resolution, time-of-flight measurements, particle identification capabilities, and precise calorimetry in order to fulfill all requirements of the broad physics program. The detector consists of two parts: the target spectrometer and the forward spectrometer equipped with tracking and particle identification detectors.

### 5.2.1 Target spectrometer

The target spectrometer (TS) has almost symmetric design and surrounds the interaction point where either a cluster jet target or a pellet target will be installed [82]. The important characteristics of the target are the homogeneity and spatial confinement, it should provide a primary vertex point independent of the vertex detectors.

At the core of the TS, the micro vertex detector (MVD) will be placed [83]. Its main purpose is to determine the position of second vertices from charmed and strange hadrons. The track curvature in the magnetic field gives particle momentum. It will contribute to the track reconstruction in a combination with the straw tube tracker (STT) and gas

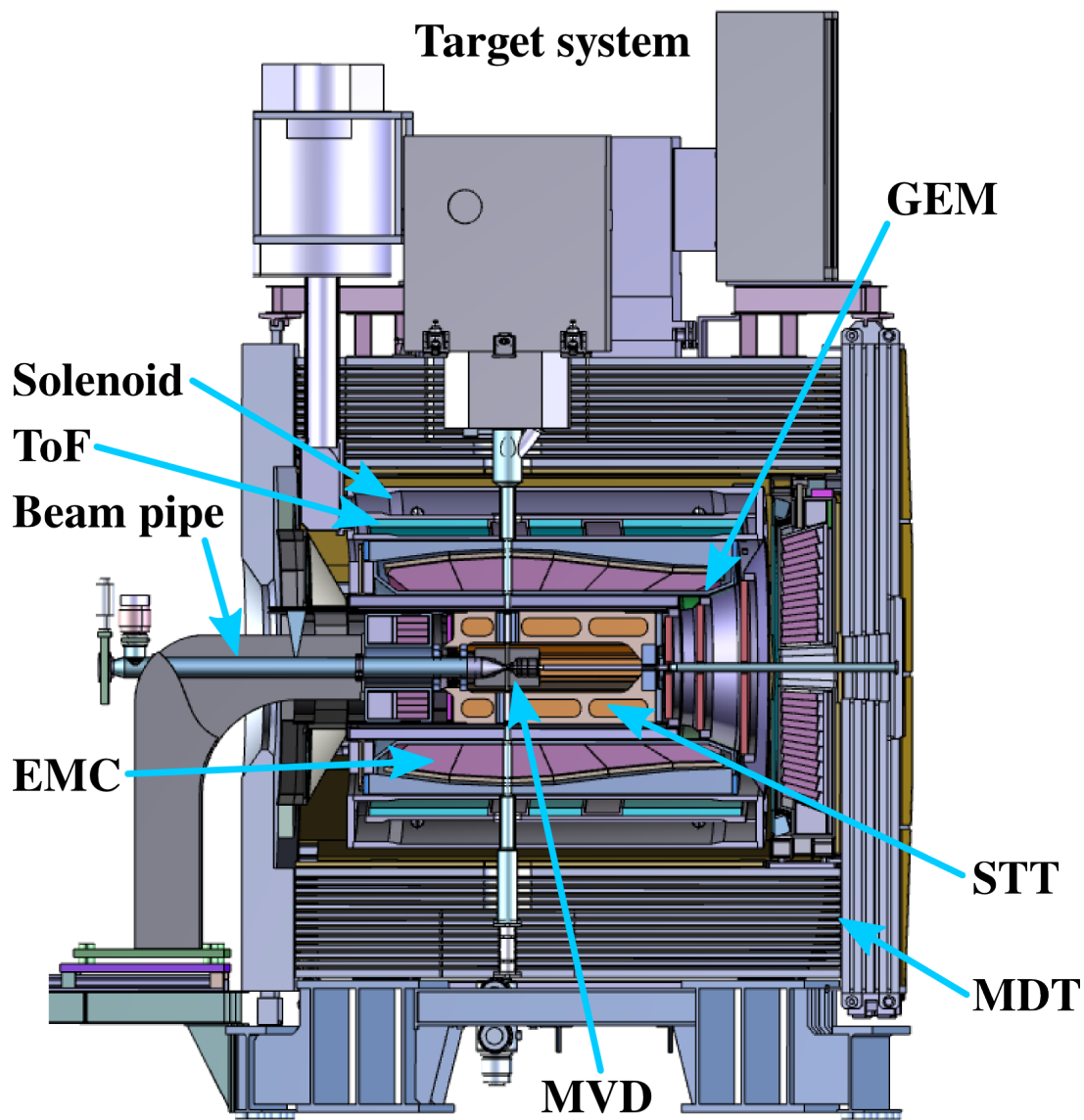


Figure 5.1: Overview of the  $\bar{P}$ ANDA target spectrometer.

electron multiplier (GEM) stations. Together with the measured transverse momentum and energy loss the MVD will be used for low energy kaon and proton identification. The MVD geometrical acceptance will cover polar angles from  $3^\circ$  to  $150^\circ$  and full azimuthal range excluding a hole necessary for the target.

The straw tube tracker [84] encloses the MVD. Its main task is the precise spatial reconstruction of the trajectories of charged particles in the magnetic field in a broad momentum range from about  $100 \text{ MeV}/c$  up to  $8 \text{ GeV}/c$  and the measurement of the energy loss for particle identification (PID). The STT will cover polar angles from  $10^\circ$  to  $140^\circ$  and full azimuthal range with an exception of a gap needed for the target.

Three gas electron multiplier [81] planar stations will be placed downstream next to the STT. Their aim is to provide tracking at forward angles below  $22^\circ$  which are not covered by the STT. The combined information from the MVD, STT, and GEM will be used for the tracking and momentum measurement.

The detection of internally reflected Cherenkov (DIRC) light with Cherenkov detectors [85] will provide PID information. The DIRC will consist of two parts: the barrel DIRC and the forward end cap DIRC. Together they will cover polar angles between  $5^\circ$  and  $140^\circ$ .

Electron and photon energies from  $10 \text{ MeV}$  up to  $14.6 \text{ GeV}$  will be measured with the electromagnetic calorimeter (EMC) [86]. It will be especially effective in electron-pion separation and essential for the neutral PID. The barrel EMC together with the forward and backward end caps will cover polar angles between approximately  $10^\circ$  and  $165^\circ$ .

The time-of-flight (TOF) [87] detector will be employed for precise time measurements of particle tracks to avoid event mixing at high collision rates. Additionally, the PID of slow charged particles will be possible. It covers large polar angle range between  $22^\circ$  and  $140^\circ$ .

In the outer shell, the muon detector (MDT) [88] is located. It will be able to measure muons within a wide momentum range, from below  $1 \text{ GeV}/c$  up to  $10 \text{ GeV}/c$ . It will cover polar angles from  $5^\circ$  to  $125^\circ$ .

The whole detector assembly will be enclosed with a superconducting solenoid magnet [89]. The flux return yoke of the magnet will serve as range system for muon detection.

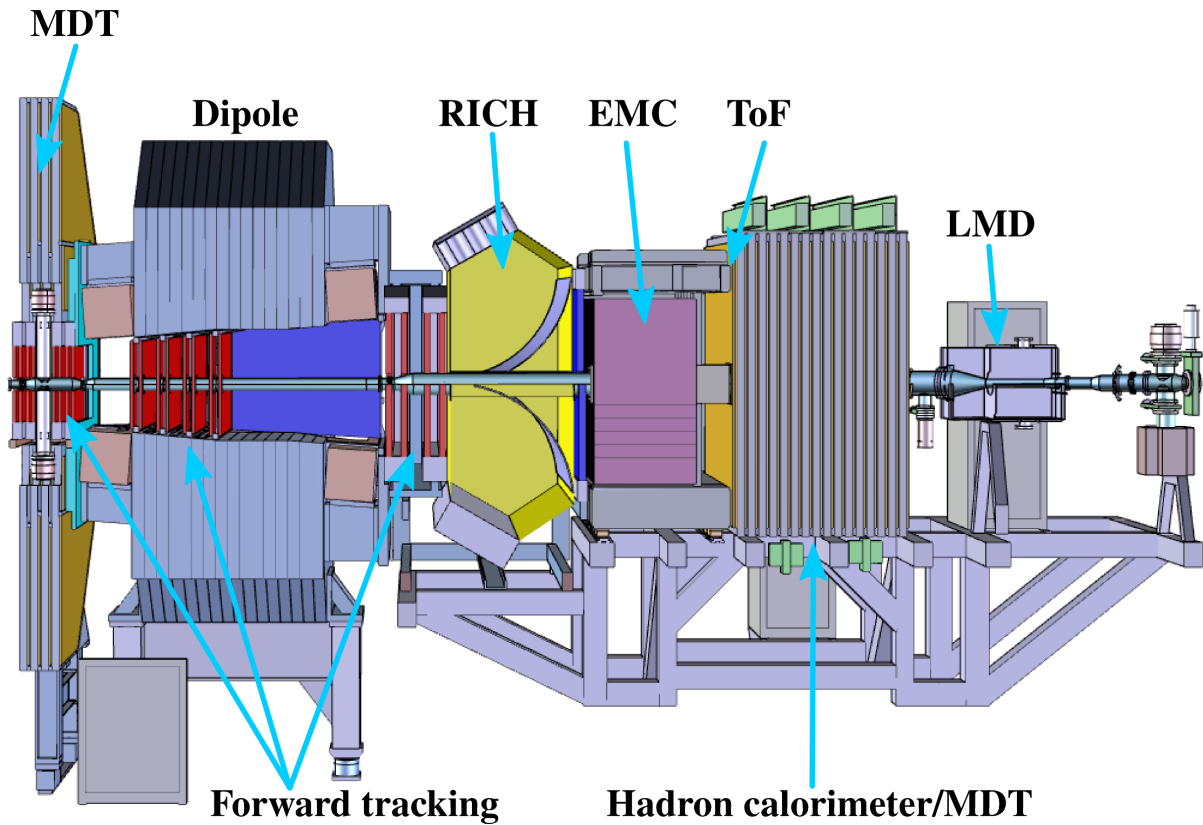


Figure 5.2: Overview of the  $\bar{\text{P}}\text{ANDA}$  forward spectrometer.

### 5.2.2 Forward spectrometer

The forward spectrometer (FS) will detect particles emitted in vertical and horizontal angles between  $\pm 5^\circ$  and  $\pm 10^\circ$ , respectively. It will feature a dipole magnet which, together with a set of wire chambers, will provide particle tracking. The PID will be realized with a combination of Cherenkov detectors (RICH), forward EMC, ToF wall, and a muon detector. The forward muon detector will also serve as a hadron calorimeter.

To summarize, the  $\bar{\text{P}}\text{ANDA}$  detector geometrical acceptance will have almost  $2\pi$  azimuthal and, approximately,  $1^\circ - 165^\circ$  polar angles. It will have an excellent tracking and PID capabilities for charged and neutral particles in a kinematic range from MeVs to GeVs.

### 5.2.3 Luminosity Detector

Precise luminosity measurement is essential for the determination of the cross section for physical processes. The requirements for the  $\bar{\text{P}}\text{ANDA}$  luminosity detector (LMD) [90] is to determine the absolute time-integrated luminosity for a single run with a systematic uncertainty of 5% or better. The relative time-integrated luminosity between runs needs to be measured with an uncertainty of 1% or better. The LMD will also measure instantaneous luminosity during the data taking.

The elastic antiproton-proton scattering will be used as the reference channel for the luminosity determination. is the antiproton-proton elastic scattering, where scattered antiprotons will be detected in the LMD.

## 5.3 High Energy Storage Ring

The high energy storage ring (HESR), illustrated in Fig. 5.3 will provide an antiproton beams between 1.5 GeV/ $c$  and 15 GeV/ $c$  and will operate in two modes: high-luminosity mode with the beam intensities up to  $10^{11}$ , and high-resolution mode with a momentum spread down to a few times  $10^{-5}$ , respectively. In order to meet the experimental requirements, the electron and stochastic cooling techniques will be utilized. Electron cooling will be used for beam momentum between 1.5 GeV/ $c$  and 8.9 GeV/ $c$  while stochastic cooling will be applied for beam momentum between 8.9 GeV/ $c$  and 15 GeV/ $c$ .

## 5.4 PandaRoot simulation framework

The PandaRoot [91] is the  $\bar{\text{P}}\text{ANDA}$  simulation framework based on the ROOT framework [92]. It contains a detailed description of the  $\bar{\text{P}}\text{ANDA}$  detector, including passive materials, *e.g.*, support structures, readout electronics, etc. The full simulation chain consists of following steps: event generator, propagation, digitization, hit reconstruction, particle identification, and data analysis. Fig. 5.4 shows the standard simulation and the data analysis procedure in PandaRoot. First, an event generator produces final state particles. Then they are propagated through the  $\bar{\text{P}}\text{ANDA}$  detector. The propagation is done with Geant4 [78, 93] which simulates the passage of particles through matter and

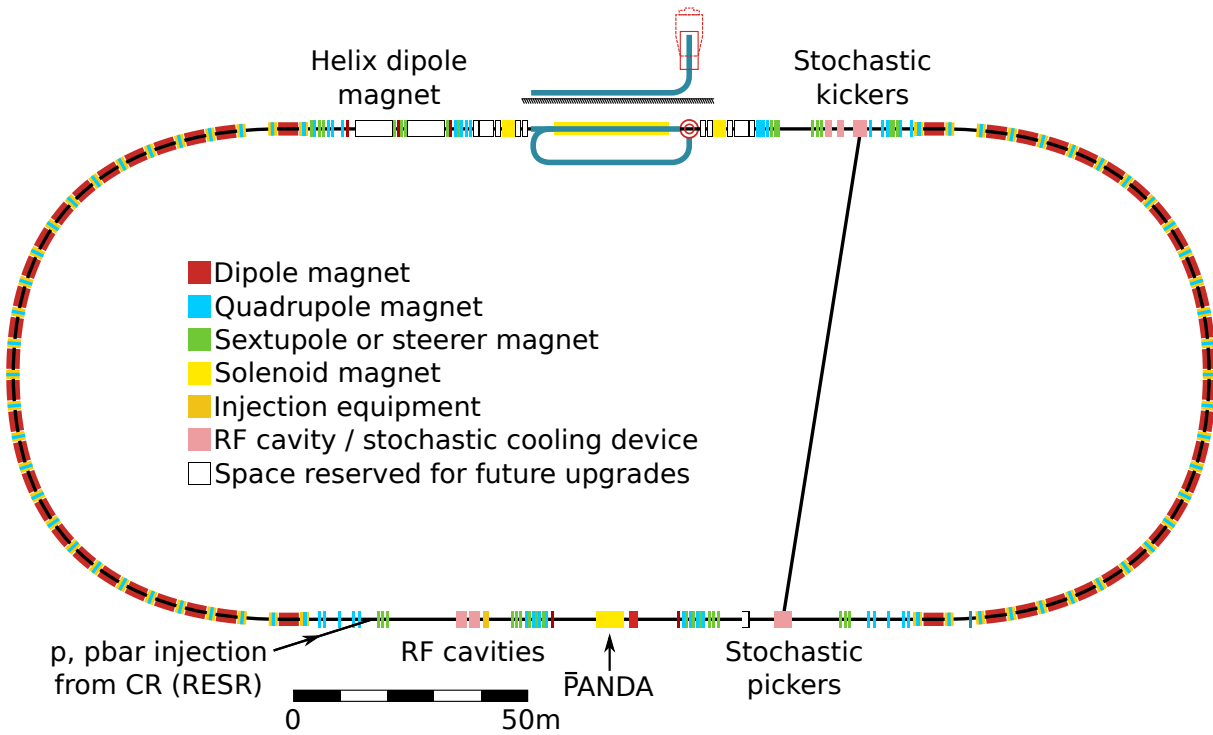


**Figure 5.3:** Layout of the HESR. The beam is injected from the left into the lower straight section. The location of the  $\bar{\text{P}}\text{ANDA}$  detector is indicated with an arrow.

interactions with it. At this stage, particle produces signals in its active elements. Next, the signal is digitized which emulates read out electronics. The data then goes through hit reconstruction and PID algorithms. The results of the simulation can be analyzed just like the experimental data, where details depend on the physical goal of the experiment.

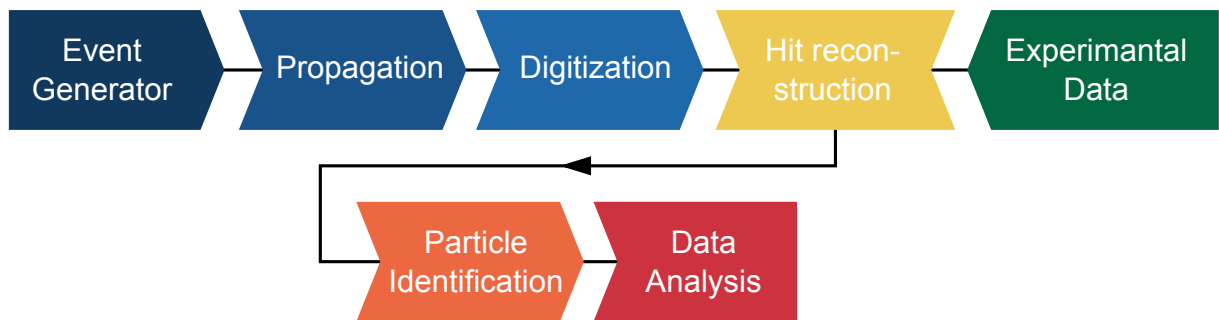


**Figure 5.4:** Standard analysis chain in PandaRoot.

## **Part III**

# **Symmetric Møller/Bhabha Monitor**

# Chapter 6

## SYMB Physics Processes

The SYMB detector measured Møller and Bhabha elastic scattering as well as annihilation when the positron beam was used. In this chapter the kinematics and cross section of these processes is discussed.

### 6.1 Kinematics

#### 6.1.1 Scattering Processes

Let us consider the electron-electron (positron-electron) scattering, where an incident electron (positron) beam with an energy  $E_1$  and a momentum  $\vec{p}_1$  is scattered off an atomic electron at rest, *i.e.*,  $E_2 = m$  and  $\vec{p}_2 = 0$ , where  $m$  is the electron mass. The scattering kinematics is illustrated in Fig. 6.1. Considering pure elastic interaction, the energy and momentum of the scattered  $(E'_1, \vec{p}'_1)$  and recoil  $(E'_2, \vec{p}'_2)$  particles can be constraint by defining the scattering polar angle  $\theta_1$ . Denoting the polar angle of the recoil electron as  $\theta_2$  we can write the following equations for the four-momentum conservation:

$$\vec{p}_1 + \vec{p}_2 = \vec{p}'_1 + \vec{p}'_2, \quad (6.1)$$

considering that  $p_2 = 0$  in the above equation can be rewritten as:

$$p_1 = p'_1 \cos \theta_1 + p'_2 \cos \theta_2, \quad (6.2)$$

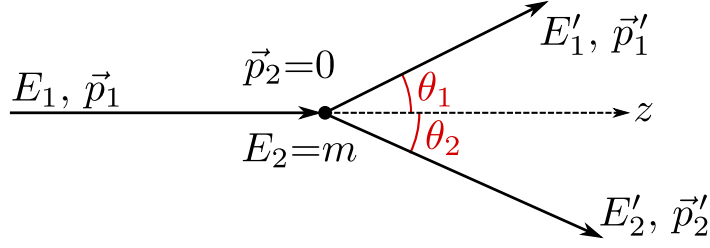


**Figure 6.1:** Elastic scattering in the lab. frame.

The final state kinematics can be constrained by fixing the polar angle  $\theta_1$  of the scattered lepton. As both Møller and Bhabha processes have two-particles with identical mass in the final state, the energy dependence on the polar angle is given by:

$$E_1' = m \left[ \frac{E_1 + m + (E_1 - m) \cos^2 \theta_1}{E_1 + m - (E_1 - m) \cos^2 \theta_1} \right], \quad (6.3)$$

$$E_2' = E_1 + m - E_1'.$$

Knowing the energy of the outgoing particles their momenta can be also calculated:

$$p_1' = \sqrt{E_1'^2 - m^2}, \quad (6.4)$$

$$p_2' = \sqrt{E_2'^2 - m^2}.$$

Finally, using Eq. (6.2) the angle of the recoil lepton results into:

$$\theta_2 = \arccos \left( \frac{p_1 - p_1' \cos \theta_1}{p_2'} \right) \quad (6.5)$$

### 6.1.2 Lepton Annihilation Process

In case of a positron beam, in addition to Bhabha scattering, an annihilation of the beam positron and an atomic electron may occur. In the annihilation a pair of photons is produced. The photons' kinematics is similar to that of Møller or Bhabha scattering with the difference of the photon mass being zero. Therefore, the energy of both photons

has the following form:

$$E'_1 = m \left[ \frac{E_1 + m}{E_1 + m - \sqrt{E_1^2 - m^2} \cos \theta_1} \right]. \quad (6.6)$$

$$E'_2 = E_1 - E'_1.$$

The momenta of the photons is equal to their energy, *i.e.*,

$$p'_1 = E'_1, \quad (6.7)$$

$$p'_2 = E'_2.$$

Thus, the polar angle of the second photon can be calculated using Eq. (6.5).

## 6.2 Cross Sections

Realistic simulation of the SYMB signal reactions needs cross sections implemented in the event generator. For cross section calculations Mandelstam variables are useful:

$$s = (p_1 + p_2)^2, \quad (6.8)$$

$$t = (p_1 - p'_1)^2,$$

$$u = (p_1 - p'_2)^2.$$

The sum of the Mandelstam variables depends on the type of the process and can be written as:

$$s + t + u = 4m^2, \quad (6.9)$$

in case of electron-electron and electron-positron scattering, and

$$s + t + u = 2m^2, \quad (6.10)$$

for electron-positron annihilation.

The relative energy transfer from the beam to the atomic electron in the laboratory is given by:

$$w = \frac{E_1 - E'_1}{E_1 - m}. \quad (6.11)$$

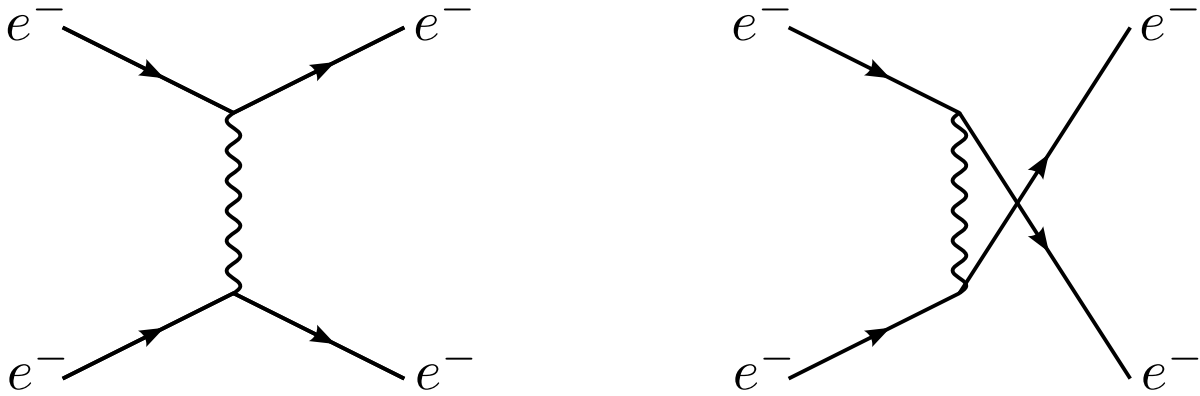


**Figure 6.2:** Electron-electron elastic scattering leading-order diagrams for t-channel (left) and u-channel (right).

### 6.2.1 Møller Scattering

Ch. Møller was the first to calculate elastic electron-electron scattering in 1932 [94]. Using the same notation for the initial and final state particles as in chapter 6 the following set of equations can be written for Møller scattering:

$$\begin{aligned}
 s &= 2m(E_1 + m), \\
 t &= 2m^2 - E_1 E'_1 + p_1 p'_1 \cos \theta_1, \\
 u &= 4m^2 - s - t.
 \end{aligned}
 \tag{6.12}$$

At the tree level there are two contributing Feynman diagrams as shown in Fig. 6.2. Both diagrams t-channel and u-channel together with their interference contribute to the differential cross section [95]:

$$\begin{aligned}
 \frac{d\sigma}{dw} &= \frac{4\pi\alpha^2}{s} \left\{ \frac{1}{t^2} \left[ \frac{u^2 + s^2}{2} + 4m^2(t - m^2) \right] + \frac{1}{u^2} \left[ \frac{s^2 + t^2}{2} + 4m^2(u - m^2) \right] \right. \\
 &\quad \left. + \frac{4}{tu} \left( \frac{s}{2} - m^2 \right) \left( \frac{s}{2} - 3m^2 \right) \right\}.
 \end{aligned}
 \tag{6.13}$$

Due to the indistinguishability of the final state electrons, the cross section has to be multiplied with a statistical factor of 1/2 to avoid double counting.

Dependence of the Møller cross section on the scattered lepton polar angle is given by:

$$\frac{d\sigma}{d\theta_1} = \frac{d\sigma}{dw} \frac{dw}{d\theta_1}.
 \tag{6.14}$$

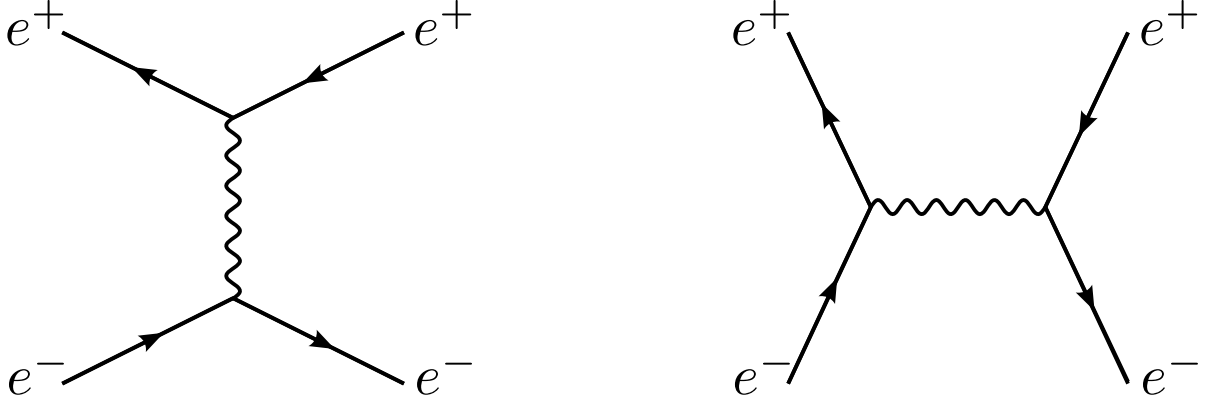


**Figure 6.3:** Positron-electron elastic scattering leading-order diagrams for t-channel (left) and s-channel (right).

Plugging  $E'_1$  which depends on  $\theta$  from Eq. (6.3) into Eq. (6.11) and taking its derivative we get the following expression:

$$\frac{dw}{d\theta_1} = \frac{4m \cos \theta_1 \sin \theta_1 (E_1 + m)}{(E_1 + m - (E_1 - m) \cos^2 \theta_1)^2}. \quad (6.15)$$

### 6.2.2 Bhabha Scattering

The electron-positron cross section was for the first time calculated by H. J. Bhabha in 1935 [96]. The Mandelstam variable for Bhabha scattering are the same as for Møller scattering, defined in Eq. (6.12). Two leading-order diagrams, shown in Fig. 6.3, contribute to the Bhabha cross section. In the t-channel primary leptons exchange a virtual photon while in s-channel they shortly annihilate into a virtual photon which consequently produce an electron-positron pair. Taking their interference term into account the unpolarized Bhabha scattering cross section can be written in the following form [95]:

$$\frac{d\sigma}{dw} = \frac{4\pi\alpha^2}{s} \left\{ \frac{1}{t^2} \left[ \frac{u^2 + s^2}{2} + 4m^2(t - m^2) \right] + \frac{1}{s^2} \left[ \frac{u^2 + t^2}{2} + 4m^2(s - m^2) \right] + \frac{4}{ts} \left( \frac{u}{2} - m^2 \right) \left( \frac{u}{2} - 3m^2 \right) \right\}. \quad (6.16)$$

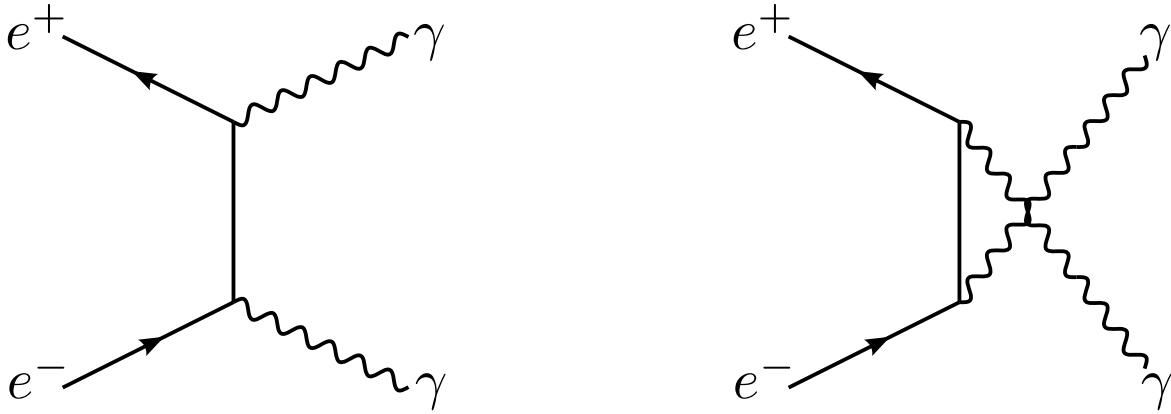


**Figure 6.4:** Electron-positron annihilation leading-order diagrams for t-channel (left) and u-channel (right).

### 6.2.3 Electron-positron Annihilation

The product of the electro-positron annihilation is a pair photons. In this case, due to the photon zero mass, the Mandelstam variables are different from those in Bhabha (Møller) scattering and can be written as:

$$\begin{aligned}
 s &= 2m(E_1 + m), \\
 t &= m^2 - 2(E_1 E'_1 - p_1 p'_1 \cos \theta_1), \\
 u &= 2m^2 - s - t.
 \end{aligned}
 \tag{6.17}$$

The energy transfer also has a different form, because the photons are massless,

$$\frac{d\sigma}{d\theta_1} = \frac{m(E_1 + m)p_1 \sin \theta_1}{(E_1 - m)(E_1 + m - p_1 \cos \theta_1)^2}.
 \tag{6.18}$$

Fig. 6.4 illustrates the two positron-electron annihilation diagrams contributing at the leading order. The differential annihilation cross section can be calculated similarly to the scattering [95]:

$$\begin{aligned}
 \frac{d\sigma}{dw} = \frac{8\pi\alpha^2}{s} \left\{ - \left( \frac{m^2}{u - m^2} + \frac{m^2}{t - m^2} \right)^2 - \left( \frac{m^2}{u - m^2} + \frac{m^2}{t - m^2} \right) \right. \\
 \left. + \frac{1}{4} \left( \frac{u - m^2}{t - m^2} + \frac{t - m^2}{u - m^2} \right) \right\}.
 \end{aligned}
 \tag{6.19}$$

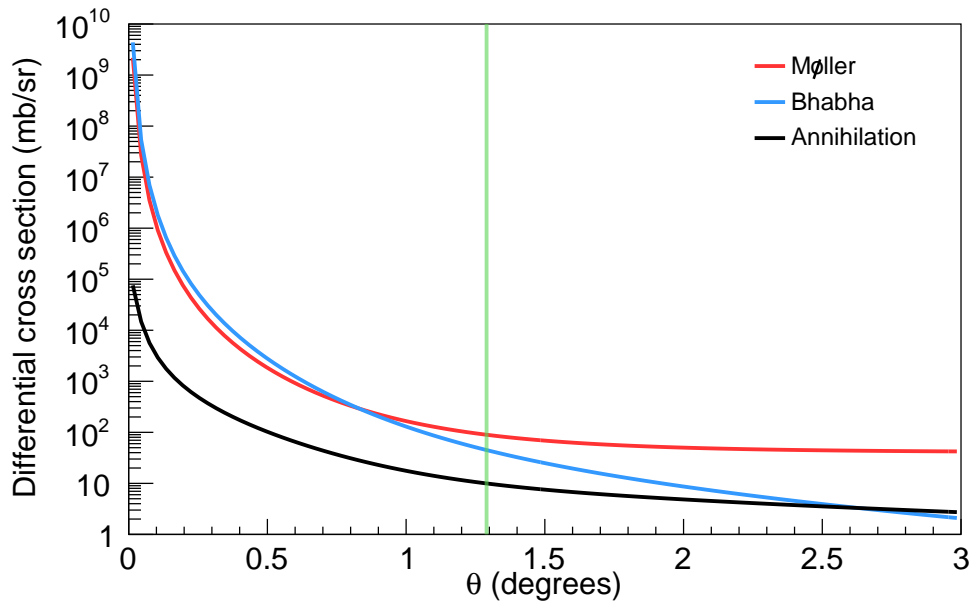


**Figure 6.5:** Elastic scattering and annihilation differential cross sections as a function of the scattering angle in the lab. frame. For a beam energy of 2.01 GeV the green line marks the symmetric scattering angle of  $1.29^\circ$  at this beam energy.

As in the case of Møller scattering, the annihilation cross section has to be multiplied with a statistical factor of  $1/2$  due to the indistinguishability of the final state photons.

Fig. 6.5 shows the differential cross sections for all described processes as a function of the scattering angle in the lab. frame. For a beam energy of 2.01 GeV at the symmetric scattering angle of  $1.29^\circ$  the Møller cross section is larger than the sum of Bhabha and Annihilation cross sections by a factor of 1.63.

# Chapter 7

## The SYMB Detector System

### 7.1 Detector Construction

The SYMB detector system [76] consisted of two identical luminosity monitors which were designed and built in Mainz. Each monitor had 9 lead fluoride ( $\text{PbF}_2$ ) crystals arranged in a  $3 \times 3$  array. The crystals were placed inside a magnetic shielding box (mu-metal box) together with PMTs glued to every crystal and voltage dividers to protect them from the magnetic field of the toroid. In addition, two lead collimators were installed between the target and crystals just outside of the mu-metal box. Both SYMB detectors were fixed on a support tables which could be moved from the working position further away from the beam pipe in order to avoid possible radiation damage during DORIS injections. Thanks to the stable injections it was not necessary to move the detectors away throughout data taking.

#### 7.1.1 $\text{PbF}_2$ Crystals

The crystals used in the SYMB detectors were taken from the A4 experiment a MAMI in Mainz [97]. These were spare crystals which have never been used in the experiment. They have a different length that varied between 150.0 mm and 185.4 mm, each slightly tapered from its front (upstream) face to its back (downstream) face. The faces had a trapezoid shape with an area of around  $670 \text{ mm}^2$  for the front and  $900 \text{ mm}^2$  for the back. Taking the crystals' radiation length of 9.34 mm and Molière radius of 21.24 mm [98],

every monitor could contain more than 95% of the energy of an electromagnetic shower caused by a 1 GeV electron, positron or photon [99].

The planned integrated luminosity of the OLYMPUS experiment was  $4 \text{ fb}^{-1}$ . Considering the collimator acceptance, energy of the lepton beam, the size and density of the crystals it was estimated that the total absorbed dose due to signal events throughout data taking should not exceed 25 Gy. What, according to Ref. [100], could cause only minor deterioration of the  $\text{PbF}_2$  crystals.

Each crystal was wrapped with Millipore paper to improve internal reflection at the faces and then tightly bound in two  $3 \times 3$  arrays with foil and tape.

### 7.1.2 Magnetic shielding

The SYMB detectors were located in the immediate vicinity of the OLYMPUS toroid magnet. Therefore, it was necessary to shield the PMTs from the magnetic field which, as was shown by its survey, had a strength of around  $10^{-3} \text{ T}$  in the SYMB area. Two custom mu-metal boxes were designed and built in Mainz. The crystal-PMTs assembly together with voltage dividers were placed inside these mu-metal boxes. As simulations have shown, a thickness of 3 mm reduced the magnetic field to a negligible value.

### 7.1.3 Collimators

In order to protect the front of the SYMB monitors from beam halo and bremsstrahlung from the beam pipe two lead collimators, each measuring  $200 \text{ mm} \times 100 \text{ mm} \times 120 \text{ mm}$ , were used. A cylindrical aperture 20.5 mm wide were drilled in both collimators to allow leptons to reach the crystals. Although the thickness of 100 mm was sufficient to stop any 1 GeV lepton, in cases where the primary particle hit the collimator close to its opening a shower of secondaries could escape the collimator and reach the crystals. Later in the analysis these events were accepted as they essentially represent signal events even though the energy deposited in such cases could have been significantly smaller in comparison to the direct impact on the crystals. This effect is illustrated in Fig. 7.8 in Sec. 7.3.1.

### 7.1.4 Readout Electronics

Electronics for the SYMB readout were also adapted from the A4 experiment [101,102]. The signal readout scheme is shown in Fig. 7.1. The signal from all nine crystals in each detector were sent to both a sum builder and a "Local Maximum" (LV) veto. The veto determined whether to accept an event or not based on the energy distribution between crystals in the array. It was accepted only if the central crystal's signal had a highest amplitude in comparison to the rest of the array. Then the sum of all nine signals had to pass through a threshold set by a constant fraction discriminator (CFD). After that, it was forwarded to three histogramming cards which saved the data in form of two-dimensional histograms. Data was stored in three different modes: 1) Coincidence mode required that central crystals of both detectors had a highest signal amplitude in comparison to other crystals; 2) Left Master and 3) Right Master modes required that only the central crystal in the left (right) detector had a highest signal amplitude. All three modes also require to pass their corresponding veto and CFD threshold.

In the coincidence mode the histogramming card allowed to record events with energies up to about 1.2 GeV. If an event had higher energy it was saved in the overflow bin. Due to special attenuators the Left master and Right master modes had the energy dynamic range twice as big what allowed to detect elastic lepton-proton scattering when a lepton was scattered within the acceptance of the SYMB detectors as well as double lepton-proton or a combination of lepton-proton and lepton-lepton. More details are given in Sec. 7.3.1.

Considering the kinematics of Møller, Bhabha and annihilation processes, the coincidence mode provided almost exclusive detection of signal events only.

The total dead time of the readout electronics was about 5 ns due to the use of a fast first-in-first-out buffer. Thus, an achievable histogramming rate was much higher than the typical event rate of about 5 kHz. Thanks to the Cherenkov nature of the material which has no slow component in its light output, the signal from PbF<sub>2</sub> crystals has a fast rise time of the order of 5 ns and the full pulse width was within a 20 ns window. As the beam consisted of lepton bunches 24 ps in length and about 100 ns apart, it allowed select events from exactly one bunch.

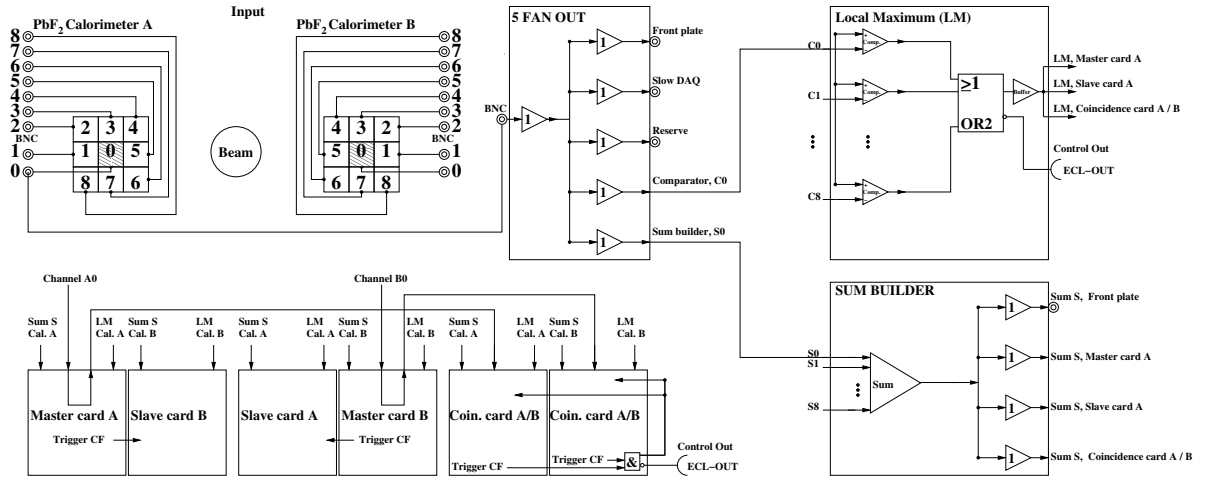


Figure 7.1: SYMB signal readout scheme which was used for data collection.

## 7.2 Detector Characterization

Before the beginning of the OLYMPUS experiment, the SYMB detector was set up in the Test Area 22 at DESY where electron and positron beams with energies from 1 to 6 GeV were available for the detector calibration. The PMTs gain was studied and an energy calibration was performed along with a determination of the energy resolution.

### 7.2.1 Photomultiplier Gain Calibration

In order to guarantee the same signal from each crystal for a given amount of deposited energy, all PMTs needed to be calibrated. All PMTs were glued to the crystals and the detector was fully assembled before the final calibration was performed. Thus, the influence of the glue on the light transmission, tolerance in the crystal alignment, quality of the material of each individual crystal, crystals' wrapping with a reflective foil, *etc.*, were taken into account during the calibration. The only variable that needed to be adjusted was high voltage of the PMTs. It was later assumed that the results of the calibration will stay valid over the whole data taking period. The high voltage (HV) of the central crystal in each module was set to a certain value, which was taken from the provided documentation, while those of the outer crystals were adjusted to produce the

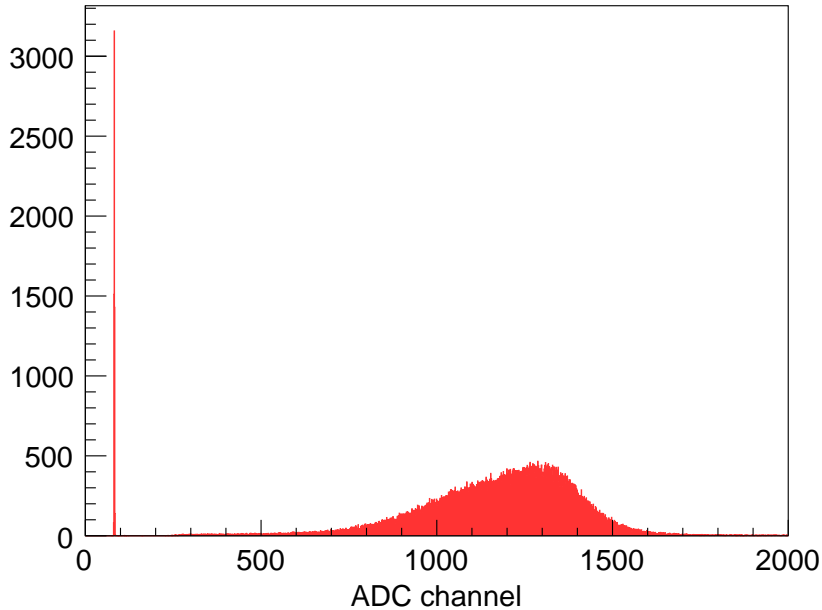


**Figure 7.2:** Energy spectrum for one of the outer crystals taken at HV=1388.9V with a thin pedestal peak on the left and a broad signal distribution on the right.

same effective gain as was seen in the central crystal.

The gain calibration was performed using a 2 GeV positron beam hitting the center of the front face of a crystal at  $90^\circ$ . The energy spectra were taken for each of the outer crystals at different values of HV. Fig. 7.2 shows an energy spectrum for one of the outer crystals taken at HV=1388.9V. On the left, a thin pedestal peak is visible while the signal has a broad distribution on the right part of the figure.

The following procedure was used to find peak positions. First, a Gaussian filter is applied to the energy spectra to smooth out its fluctuations. Then, a derivative is taken from the smoothed out histogram and its zero-crossing under the signal distribution determines the position of the peaks. Results of the filtering and derivation applied to Fig. 7.2 are shown in Fig. 7.3.

An exponential function was fitted to the measured peak positions. In this way, the PMTs response to the 2 GeV positron beam as a function of HV was found. Fig. 7.4 shows results of the peak finding and the fit for one of the outer crystals. This allowed to

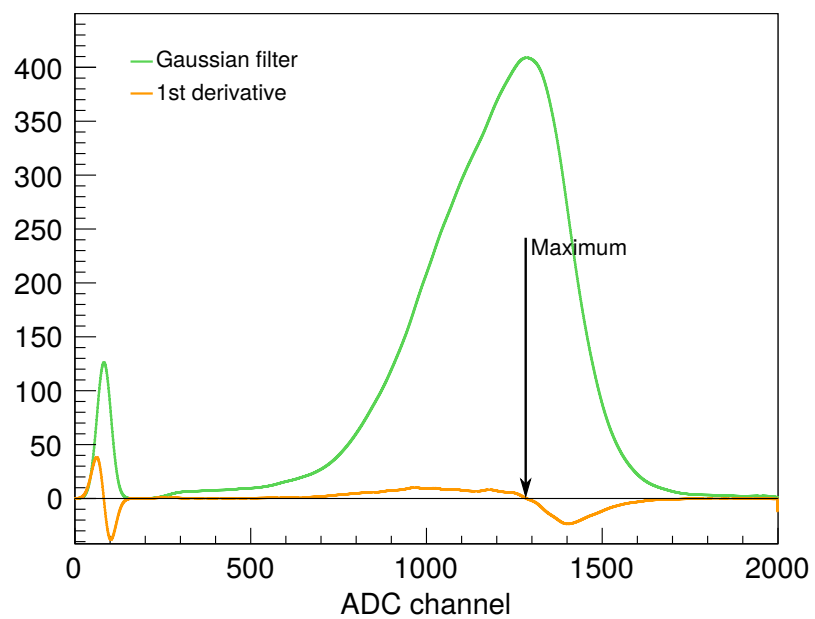


**Figure 7.3:** Effect of the Gaussian filter applied to the energy spectrum and its first derivative. The peak position is found as the zero-crossing of the first derivative under the signal distribution.

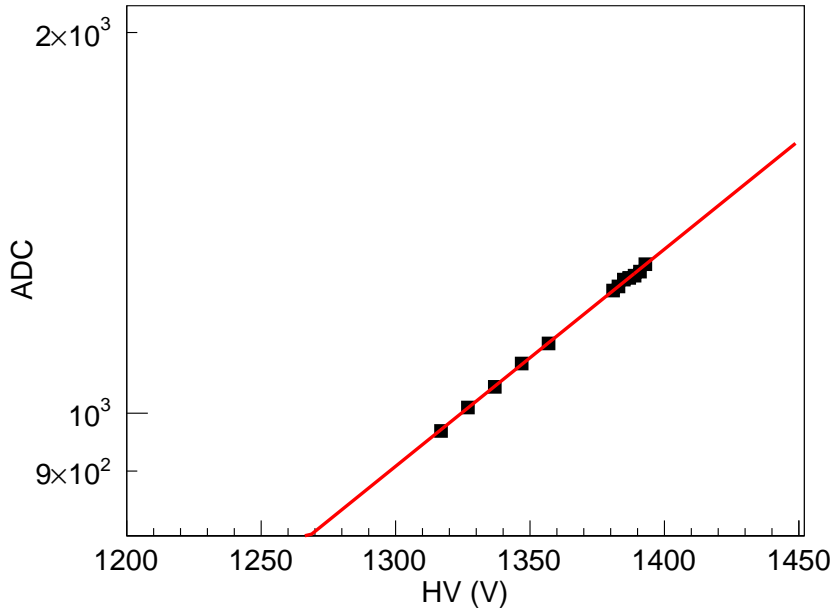


**Figure 7.4:** ADC peak positions as a function of HV (squares) for one of the outer crystals and an exponential fit (line).

adjust the HV of the outer crystals to match the signal of the central one for the same beam energy. Figures with results for other crystals can be found in Appendix A.

## 7.2.2 Energy Calibration and Energy Resolution

Once the PMT gains were calibrated in order to have the same signal in each crystal at a given deposited energy, the signal from nine crystals in each SYMB detector could be summed to have a measurement of the deposited energy in the  $3 \times 3$  array which corresponds on average to 95% of the incoming particle energy.

An additional calibration of each individual SYMB calorimeter was performed in order to assure the same total signal in response to a lepton beam of the same energy. Applying the HV settings from Sec. 7.2.1, each detector in turn was placed so that the test beam was coaxial with the central crystal while the beam energy was varied in the range of 1 to 2 GeV in steps of 0.2 GeV. The relative beam energy spread was constant and equal to 3.2% during the test beam.

Fig. 7.5 shows a typical pedestal-corrected energy spectrum from the left-sector de-

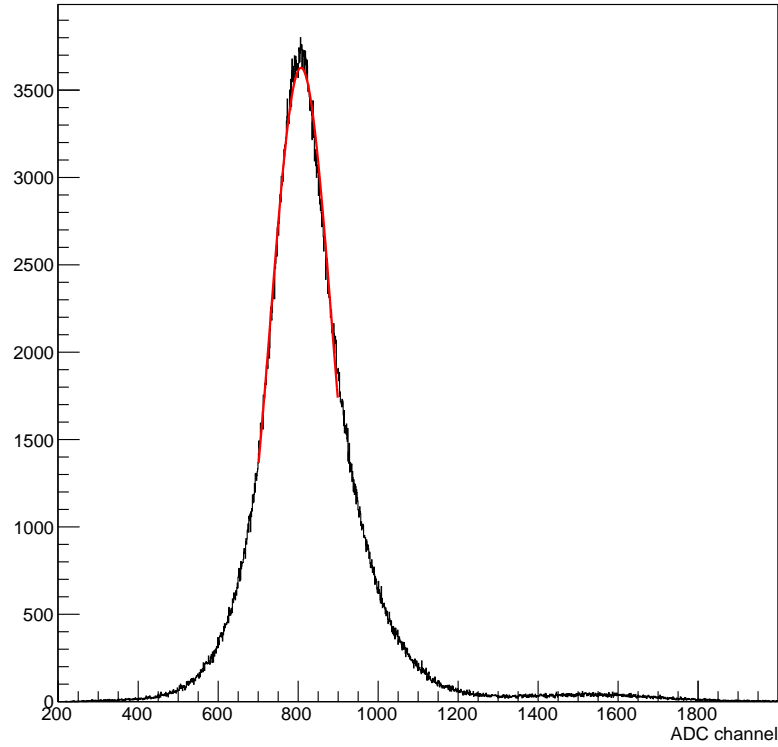


**Figure 7.5:** Typical pedestal-corrected energy spectrum (black) fitted with a Gaussian function (red).

tector for a 1 GeV electron beam, together with a Gaussian fit. The second smaller peak around ADC channel 1500, caused by pile-up events, is visible. Using the results of the fit to each spectrum, a relationship between the ADC signal and the beam energy was determined. Fig. 7.6 shows the results for both SYMB detectors, together with individual linear fits for electron and positron beams.

The same data was used for the energy resolution determination defined as  $\Delta E/E = \sigma/\mu$ . Where  $\sigma$  is the standard deviation of the Gaussian fit and  $\mu$  is its peak position (See Fig. 7.5). The next step was to fit the obtained energy resolution with the following function [103, 104]:

$$\frac{\Delta E}{E} = \sqrt{\left(\frac{a}{E}\right)^2 + \left(\frac{b}{\sqrt{E}}\right)^2} + c^2 \quad (7.1)$$

where  $a$  represents the electronic noise and all other energy independent fluctuations,  $b$

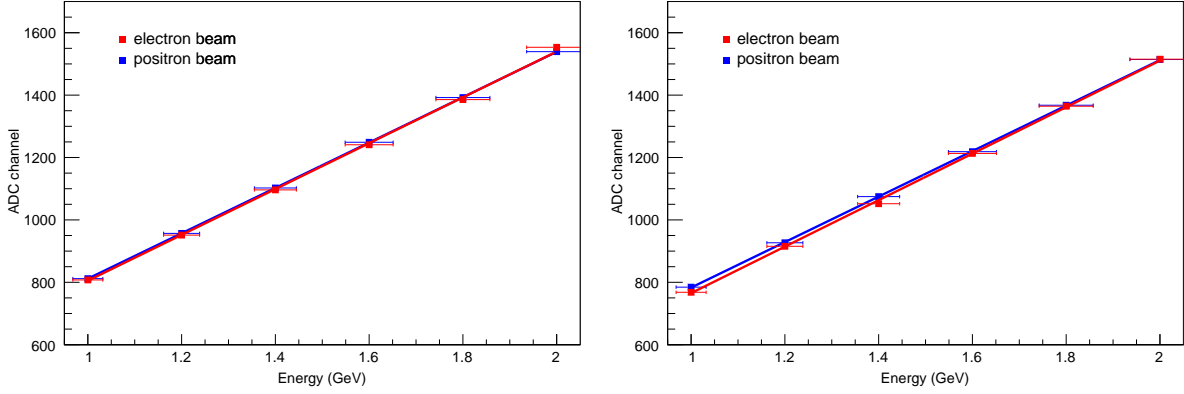


**Figure 7.6:** Energy calibration of the left (left) and right (right) detectors at various beam energies (squares) and fits (lines).

Parameter	LD, $e^+$	LD, $e^-$	RD, $e^+$	RD, $e^-$
$a$ [GeV]	$0.070 \pm 0.037$	$0.073 \pm 0.035$	$0.077 \pm 0.008$	$0.071 \pm 0.035$
$b$ [ $\sqrt{\text{GeV}}$ ]	$0.057 \pm 0.021$	$0.050 \pm 0.023$	$0.055 \pm 0.007$	$0.057 \pm 0.020$
$c$ [%]	$2.9 \pm 0.006$	$3.3 \pm 0.008$	$2.5 \pm 0.007$	$2.9 \pm 0.005$

**Table 7.1:** Summary of the energy resolution fit results for each SYMB detector (LD - left detector, RD - right detector) and test beam species.

is the statistical fluctuations in the number of detected photons, and  $c$  parameterizes the electromagnetic shower fluctuations on the side boundaries of the crystal arrays.

Fig. 7.7 shows the measured energy resolution  $\Delta E/E$  of each calorimeter as a function of the incoming particle energy and the fit for both electron and positron beams. In addition, parameter  $a$  was obtained from pedestal measurements. Table 7.1 summarizes the fit results. The value of  $a$  obtained from the fit and from the pedestal measurements ( $a=0.005$ ) are very different. This can be explained by the fact that the SYMB calibration was performed simultaneously with that of the MWPC and GEM detectors. They were located between the aperture of the beam pipe in the test hall. Taken that the distance between the aperture and the SYMB detectors was around 6 meters it is safe to assume that the effect of the additional material could affect the energy of the incoming particles as well as their trajectories.

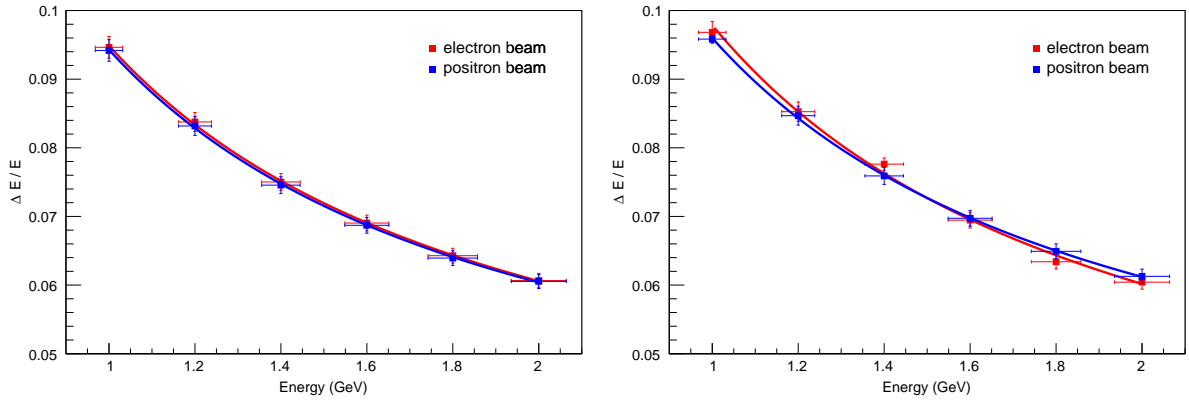


**Figure 7.7:** Energy resolution of the left (left) and right (right) detectors at various beam energies (squares) and fits (lines).

### 7.3 SYMB Operation during the Experiment

For data taking, the SYMB detector was moved into the DORIS beam line together with the whole OLYMPUS apparatus. The detector settings were adjusted according to the calibration results obtained during its commissioning in the test area. Additionally, new readout electronics, employing 8-bit ADCs, were installed for data taking.

In the middle of the first run, the HV was decreased what made possible detection of elastic lepton-proton scattering. During the shutdown, between the first and second runs, HV was set back to nominal values and four 6 dB attenuators were installed to modify the signal in the master-slave modes as it was explained in Sec. 7.1.4. This effectively doubled the dynamic range of recorded signal amplitudes what allowed for the detection of positrons from the elastic lepton-proton scattering throughout the remainder of data taking.

#### 7.3.1 The Energy Spectra

Fig. 7.8 illustrates a typical histogram of the SYMB signal in the coincidence mode, with energy shown for both the left and right sectors. The original 8-bit ADC spectrum was converted to the units of energy (GeV). The offset, visible as the white area to the left and below the spectrum, is due to the negative pedestal values of each ADC. A red

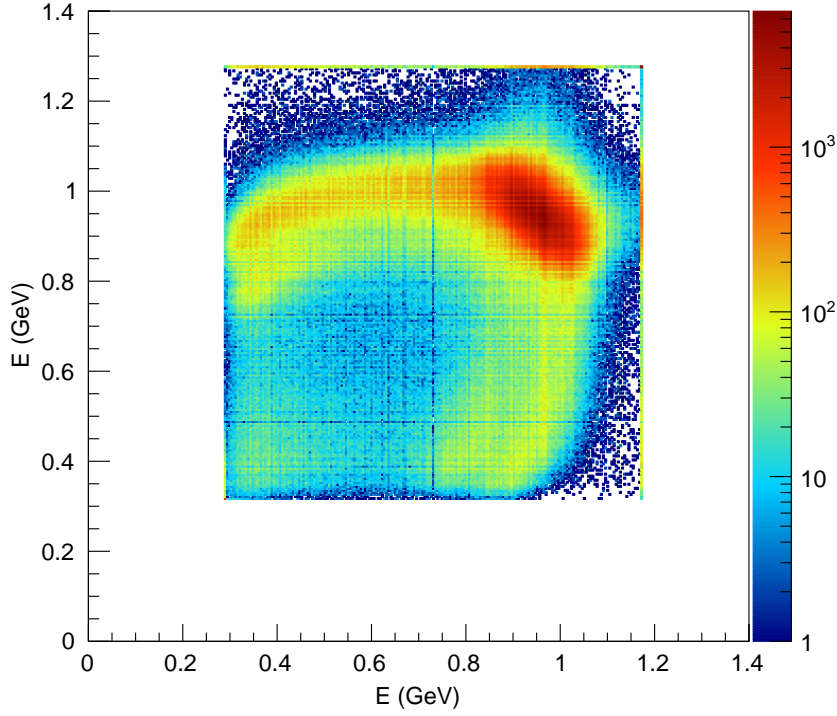


**Figure 7.8:** Typical SYMB data recorded over 20 minutes of beam time by the detector in coincidence mode.

elliptical area visible in the upper right corner (at  $\sim 1$  GeV on each axis) represents the coincidence events in which both primary leptons went through the collimator and deposited most of their energy in the crystals. The area position at  $\sim 1$  GeV can be explained by the symmetric placement of the SYMB detectors at  $1.29^\circ$  which, at the beam energy of 2.01 GeV, is the symmetric scattering angle of Møller and Bhabha processes. Thus, each particle scattered at  $1.29^\circ$  carries the same energy of  $\sim 1$  GeV. Horizontal and vertical band appear when one lepton loses part of its energy due to a collision with a collimator, while the second one directly hits the calorimeter.

The bending of the bands at lower energies is due to the signal pulse cut caused by the electronics time gate, hence the decreased output signal. As soon as a signal from one of the detectors crosses a certain threshold, the electronics start to readout the signal for a set time gate. If one signal reaches the threshold later than another one its readout time

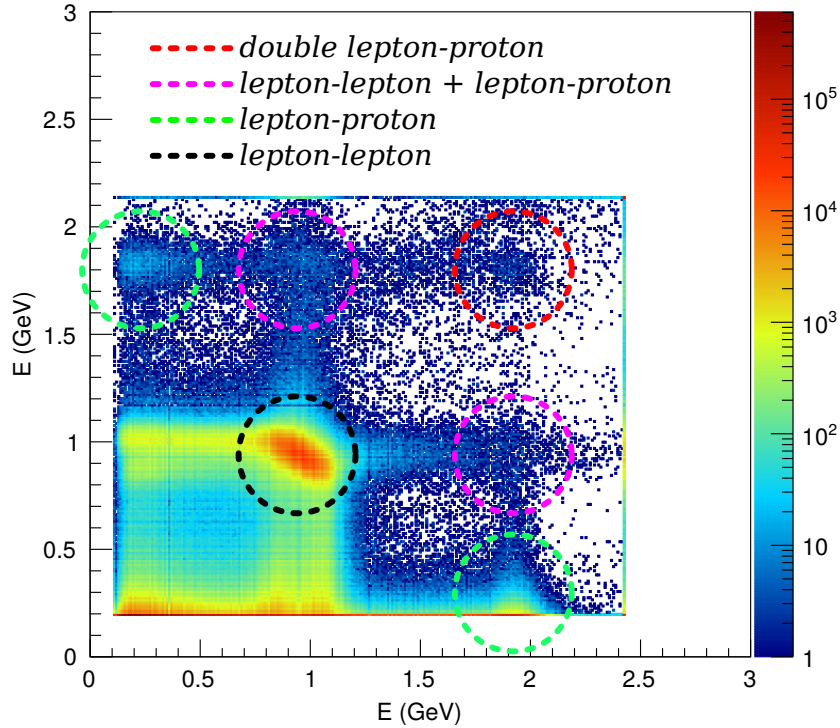


**Figure 7.9:** Typical SYMB data recorded over 20 minutes of beam time by the detector in right-master left-slave mode.

will be shorter, *i.e.*, smaller signal value will be recorded. This effect has no substantial effect on the data analysis.

The signal produced in master-slave modes during the second data taking period is shown in Fig. 7.9. As it was already mentioned, the dynamic range of these modes was approximately twice as big as that of the coincidence mode. This enabled detection of elastic lepton-proton, lepton-lepton with lepton-proton, and double lepton-proton scattering.

The spectra in the coincidence and master-slave modes shown in Fig. 7.9 exhibit an effect of differential nonlinearities in the readout electronics. The ADC bin widths, converted to energy, are not identical. Therefore, thin lines of one bin width containing more or fewer events than the neighbor bins can be seen. The differential nonlinearities have negligible effect and are corrected for in the analysis.

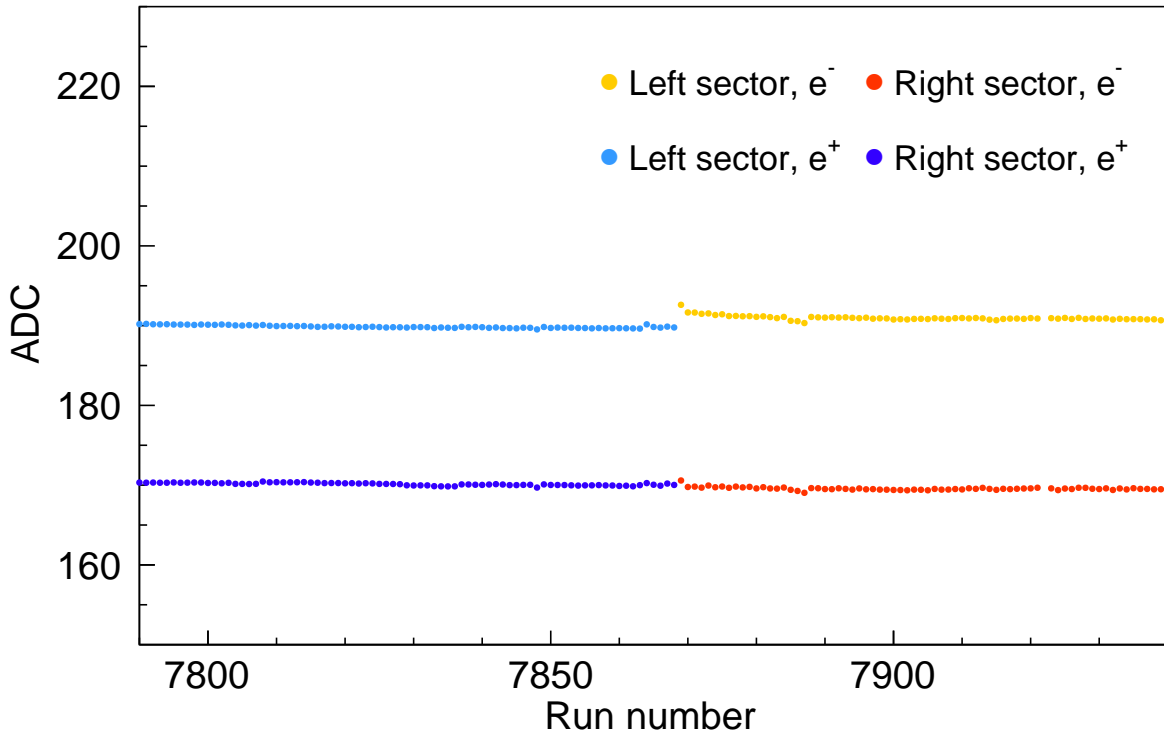


**Figure 7.10:** Positions of the coincidence peaks in the left and right sectors for the both beam species over about two days of data collection. Difference in the ADC peak position between left and right sectors comes from different ADC offsets.

### 7.3.2 Stability

Fig. 7.10 shows the stability of the coincidence peak positions in the ADC channels over about two days of data taking. The difference between the left and right sectors is due to different ADC offsets. An interesting phenomenon can be seen when the beam species are switched, *i.e.*, the ADC peak positions move up by a few ADC channels for a short period of time. This can be explained by crystal regeneration during the beam species switching which took around one hour. This effect had no influence on the measured cross section.

### 7.3.3 Sensitivity to Beam Parameters

Several beam position and beam slope scans were performed during the second period of data taking. During each scan, the beam position or slope at the target center was changed along the vertical or the horizontal axis while being fixed along the other one. The cross sections, *i.e.*, SYMB events normalized by the slow control luminosity, measured in one of the scans are shown in Fig. 7.11. This beam scan show no strong dependence of the cross section on the beam position and slope.

The results of the shown beam scan were used to optimize the beam position and slope to maximize count rates and minimize background in the main spectrometer as well as to study systematic effects on the SYMB detectors (See Sec. 8.3).

## 7.4 Simulation of SYMB Events

In this section, we expand on the OLYMPUS Monte Carlo which was previously introduced in Sec. 4.5. Detailed description of the SYMB signal event generator and the simulation of the detector response is presented.

### 7.4.1 Event Generators

Realistic event generation is a key for precise luminosity determination. The kinematics and Born-level cross sections of Møller, Bhabha, and annihilation processes were described in Chapter 6. Even though the Born-level cross section describes the collected data very well, an accurate measurement of the expectedly small two-photon exchange contribution required to take into account other radiative effects.

A small group within the collaboration developed an event generator which included next-to-leading-order radiative corrections to Møller and Bhabha scattering processes and lepton pair annihilation. The first two are described in Ref. [105].

As an input, the event generator requires the cutoff energy to separate soft- and hard-photon modes and an angular range within which the final state particles are generated. In soft-photon mode, events are described by elastic electron-electron kinematics with modified cross section. In the hard-photon mode, in addition to the two primary leptons,

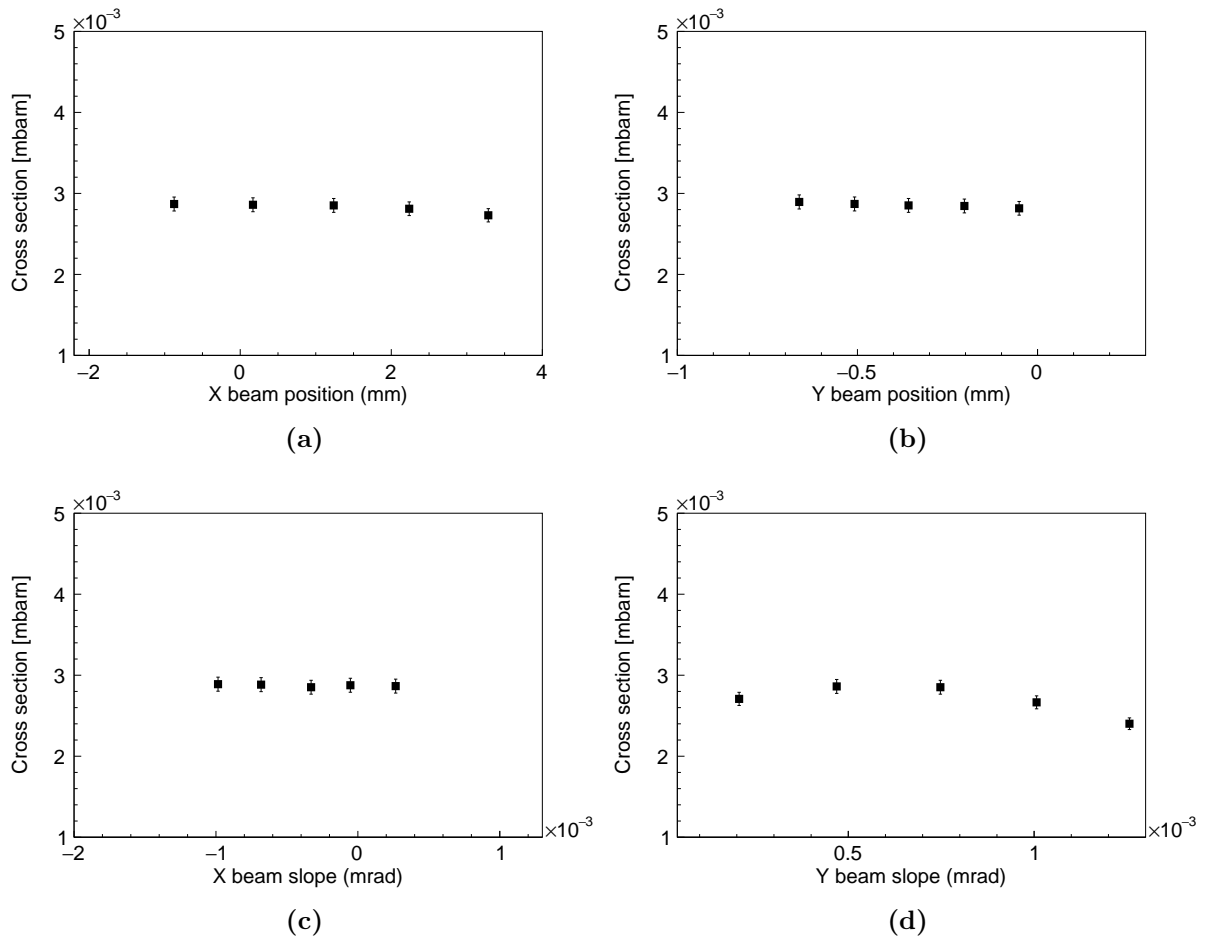


**Figure 7.11:** Cross section, SYMB events normalized by the slow control luminosity, measured during beam position (a, b) and slope (c, d) scans along the horizontal and vertical axes. Most error bars are smaller than markers.

a single bremsstrahlung photon is produced. The angular range was chosen to cover the geometrical acceptance of the SYMB detectors.

## 7.4.2 Simulation of the Detector Response

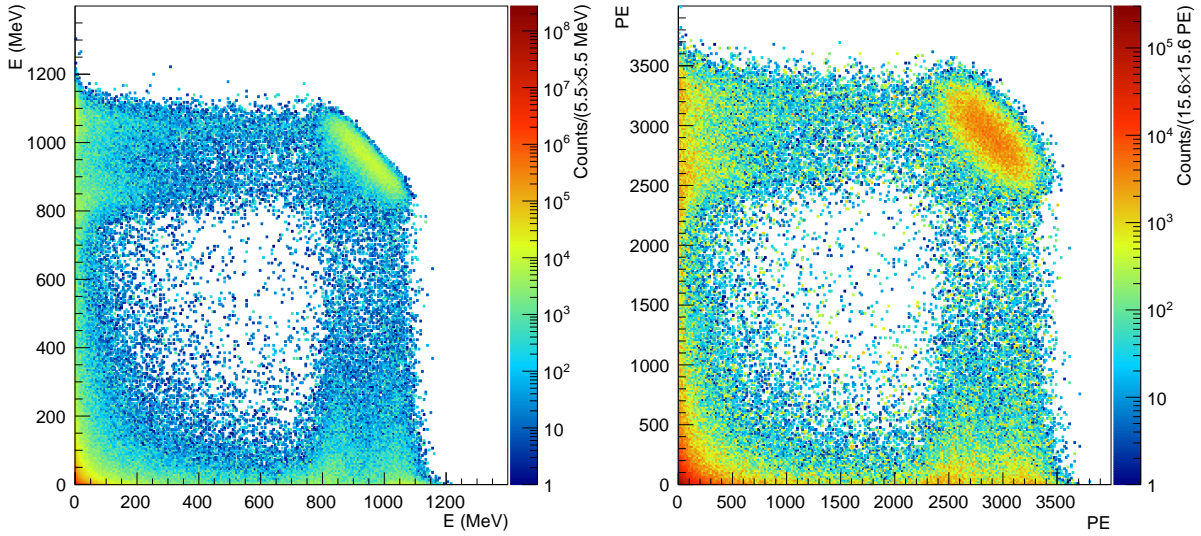
In the OLYMPUS simulation software the SYMB detectors are represented by the lead collimators, part of the mu-metal box located between the target and the front face of the crystals, crystals themselves, and the wrapping around the crystals. The rest is omitted as it had no influence on the simulation.

As primary particles travel from the target cell towards the SYMB detectors, their path and momentum can be affected by multiple factors. Among them are the magnetic field, exit windows of the beam pipe, and collimators. The magnetic field could change the particle trajectories, while interaction with the beam pipe and collimators leads to the production of secondary particles and energy losses. Fig. 7.12a illustrates energy deposited in the left detector versus that in the right detector.

Energy spectra are digitized in order to convert simulated data to the format identical to that of experimental data. The SYMB detectors were built from pure  $\text{PbF}_2$  Cherenkov calorimeters and most of its signal came in a form of Cherenkov light (photons). The propagation and tracking of every single photon produced in the detector would be very time consuming due to extensive computational requirements. An alternative approach, based on Ref. [106], was applied to decrease the simulation time.

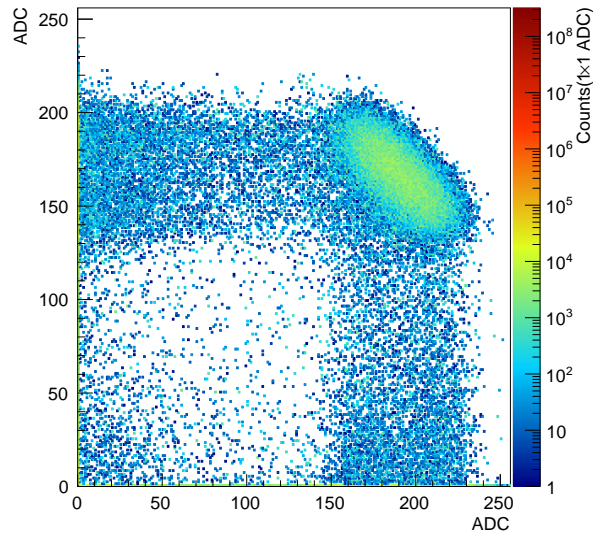
First, a number of Cherenkov photons detected by the PMTs, based on the total energy deposited in a single crystal, is estimated. It is done using parameterization based on data obtained with similar crystals used in the A4 experiment, Mainz. Fig. 7.12b shows results of the energy to photoelectron conversion.

Second, photoelectron spectra are converted into a digital ADC signal using a linear function. Transformation parameters are determined from experimental data for each run individually. Fig. 7.12c shows the final ADC spectrum which is saved in the format identical to that of experimental data. Thus, simulated data is ready to be analyzed using the same analysis routines as experimental data.



(a)

(b)



(c)

**Figure 7.12:** SYMB digitization process of Monte Carlo data, left sector versus right: (a) energy deposition, (b) number of photoelectrons produced, and (c) ADC signal for Møller scattering.

# Chapter 8

## Luminosity Measurement with SYMB

### 8.1 Luminosity Determination

The quantity directly measured by the SYMB detector was a number of events  $N$  which is defined as:

$$N = \sigma \mathcal{L}, \quad (8.1)$$

where  $\sigma$  is the cross section of the detected process and  $\mathcal{L}$  is the time integrated luminosity. Even though cross sections of elastic electron-electron and electron-positron scattering are well known and their radiative corrections can be precisely calculated, the complex geometrical acceptance of the SYMB detector, as shown in Fig. 8.1, makes the calculation of the total cross section and the efficiency determination very difficult. As can be seen, cross section significantly changes its value across collimators and due to the asymmetric scattering kinematics not all events that hit left calorimeter are detected in the right one, *i.e.*, these events are not recorded in the coincidence mode.

As it was shortly discussed in Sec. 4.5, the OLYMPUS Monte Carlo software is an integral part of the data analysis and determination of the luminosity. For each data run an individual Monte Carlo simulation is performed. Data run is an experimental data collected and recorded within one small time interval, typically around 20 minutes long. The number of events in the simulation is normalized to the slow control integrated

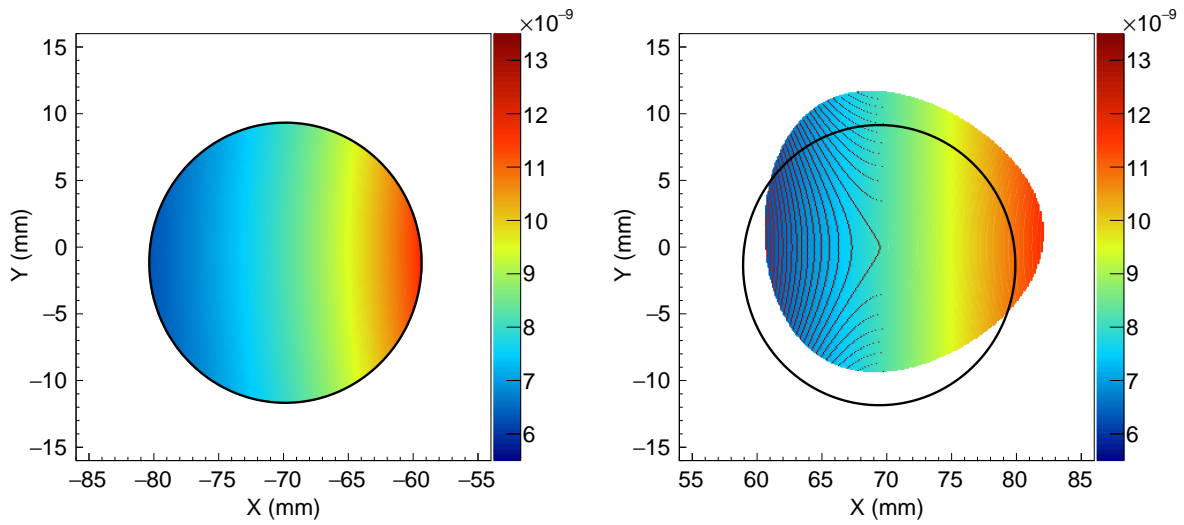


**Figure 8.1:** Event, normalized by the cross section, impact position in the SYMB detectors. Assuming that one particle hits the left collimator (left) the impact position of the second one (right) was calculated using the two-body scattering kinematics. The non linear change of cross section across collimators and non symmetric scattering angles lead to the event loss in the coincidence mode and complicate the acceptance determination. Black circles are the apertures of the collimators.

luminosity for the corresponding data run. Therefore, the ratio of data events to simulated events can be related to the SYMB and slow control luminosity in the following way (assuming proper determination of  $\sigma$ ):

$$R_{D/S}^{e^\pm} = \frac{N_{Data}^{e^\pm}}{N_{Sim}^{e^\pm}} = \frac{\mathcal{L}_{SYMB}^{e^\pm}}{\mathcal{L}_{SC}^{e^\pm}}, \quad (8.2)$$

where  $N_{Data}^{e^\pm}$  is the number of events in the data run,  $N_{Sim}^{e^\pm}$  is the number events in the corresponding simulated run,  $\mathcal{L}_{SYMB}^{e^\pm}$  and  $\mathcal{L}_{SC}^{e^\pm}$  are the SYMB luminosity and slow control luminosity, respectively.

Run-by-run based simulation allows to minimize possible uncertainty due to changing with time experimental conditions, *e.g.*, the beam position in the target region, beam slope, gas flow and so on. All these factors may have influenced the response of the SYMB detectors.

As the main goal of the experiment is to measure the relative electron-proton to positron-proton elastic cross section ratio, only the relative integrated luminosity is needed. Thus, the relative integrated luminosity can be defined as

$$R_{Asym}^{e^\pm} = \frac{R_{D/S}^{e^+}}{R_{D/S}^{e^-}} \quad (8.3)$$

It was expected that  $R_{D/S}^{e^+}$  and  $R_{D/S}^{e^-}$  may deviate from the unity due to possible systematic uncertainty in the determination of the slow control luminosity but both of them should be the same within their error margins, *i.e.*,  $R_{Asym}^{e^\pm}$  should be equal to one within its error margins. A deviation from unity would be a sign of a dependence of luminosity measurements on the beam species.

### 8.1.1 Data Division

Signal selection procedure was a first step in the luminosity determination. Thanks to the coincidence mode operation and very high signal cross sections the whole coincidence spectrum, as shown in Fig. 7.8, was considered to be virtually background free. With an exception of overflow, may contain lepton-proton events, and underflow, may contain noise, bins. Therefore, a *box* cut, which includes all but overflow and underflow bins, was applied to the whole data set.

For an in-depth analysis of different selection methods and a motivation for the one that was chosen in the analysis the reader is invited to see Sec. 8.2.

It must be noted here, that the SYMB detector response was very sensitive to the operation conditions, especially to the beam position and slope as they directly affected the angular acceptance of the SYMB collimators. Again, a thorough investigation of the influence of the beam parameters on the SYMB detectors is presented in following Secs. 8.3.1 and 8.3.2.

Concerning the beam parameter, there were two important events throughout data taking. First, a beam scan was performed, during which the position and slope of the beam were varied in vertical and horizontal planes. The results of the scan were used to find a new setting which would increase count rates in the OLYMPUS detector. After the beam scan was completed, new values for the vertical beam position and slope were set.

Second, at some point the beam orbit became unstable in the horizontal plane. It took few days for the accelerator team to tune the beam settings and restore its stability. The side effect of the beam tuning was a new horizontal position of the electron beam.

Therefore, the data was divided into three sets. The first set contains data from the beginning of the second data taking period till the beam position/slope scan. The second set starts right after the beam scan and continues to the point where the beam orbit became unstable. Set 3 starts after the beam tuning with the both horizontal and vertical beam position and slope being different for electron and positron beams and goes till the end of data taking.

Fig. 8.2 shows how  $R_{D/S}$  have been affected by new beam settings after the beam scan. As can be seen, the data to simulation ratio increased during the first positron running period after the beam scan and stayed at the higher than before scan level. The electron data, after the beam scan, also have visibly higher average data to simulation ratio. The spread of data points among runs is also significantly smaller for both beam species.

### 8.1.2 Results

The *box* selection method (explained in Sec. 8.2) was applied to every data set and the data to simulation ratio was extracted by projecting the data on the  $Y$  axis and fitting a Gaussian to it. Fig. 8.3 shows  $R_{D/S}$  values for all three data sets. Although the

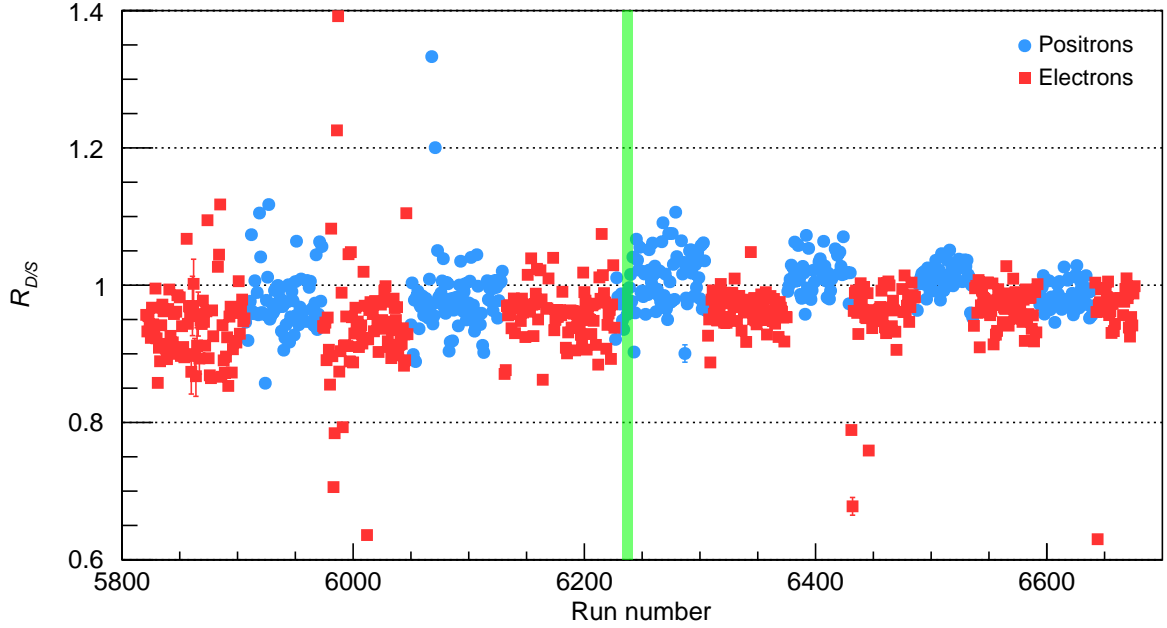


**Figure 8.2:** Data to simulation ratio versus run number. The green line marks the beam scan.

$R_{D/S}$  values are different for different sets, the biggest problem is the discrepancy between electron and positron data. As can be seen in Fig. 8.4, the asymmetry or the deviation from unity of the relative integrated luminosity between electrons and positrons is twice as big in second and third sets in comparison to the first one.

Figs. 8.5 to 8.7 show data to simulation ratio versus run number for all three data sets and corresponding histograms and fits which were used for  $R_{D/S}$  determination.

## 8.2 Extraction of the Event Number

The event number had to be extracted from two dimensional SYMB energy spectra by selecting a specific region of the histogram. An example of these spectra was previously shown in Fig. 7.8 in Sec. 7.3.1. Two different approaches to event selection were considered:

- Box - fixed in size and position rectangular area. In total, eight boxes of different sizes were tested.

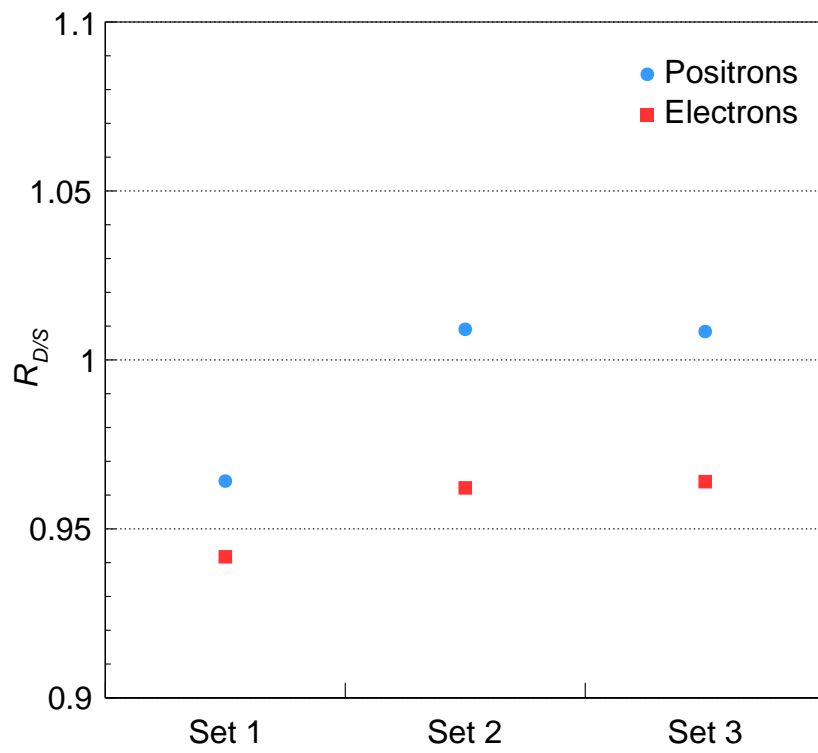


**Figure 8.3:** Data to simulation ratio extracted from each data set.

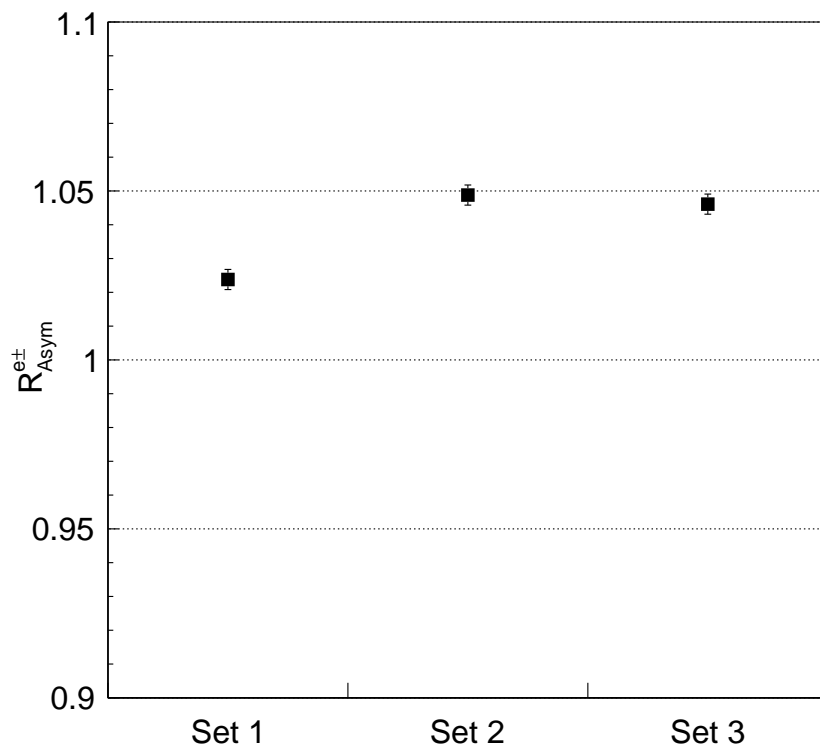


**Figure 8.4:** Asymmetry extracted from each data set.

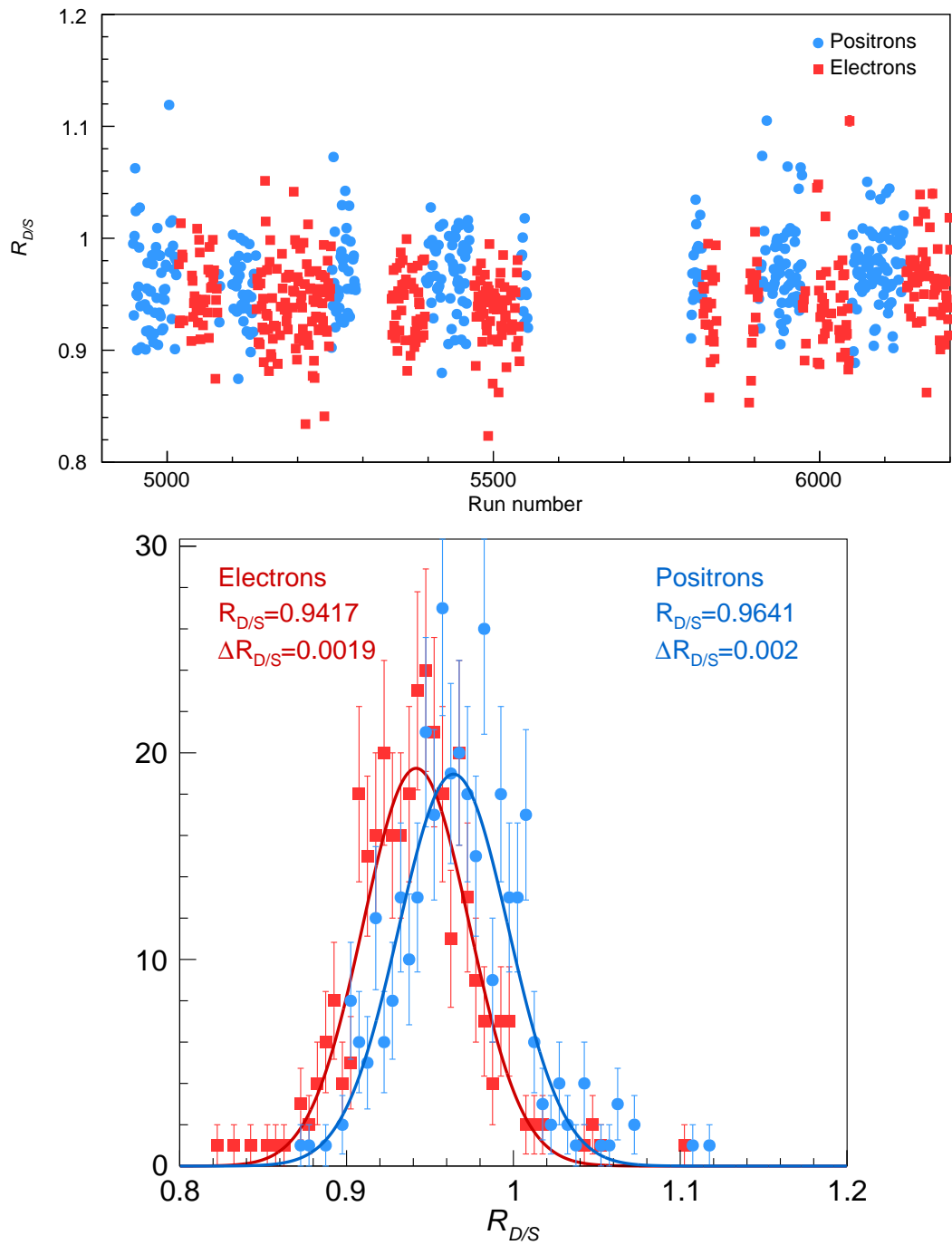


**Figure 8.5:** Results for set 1. Data to simulation ratio versus run number (top). Projected and fitted data points from the top figure (bottom).

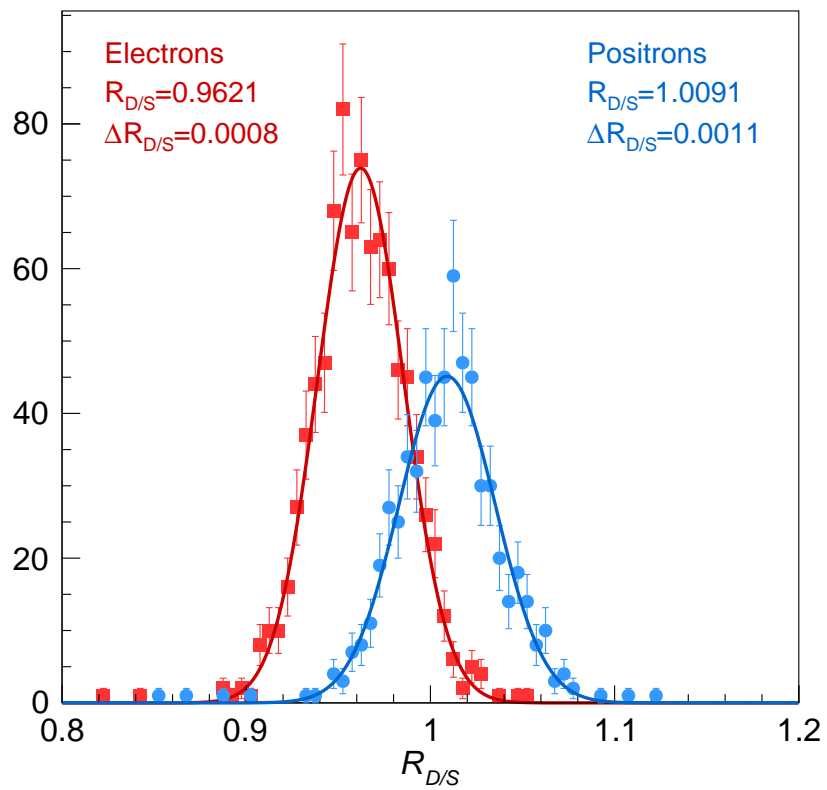
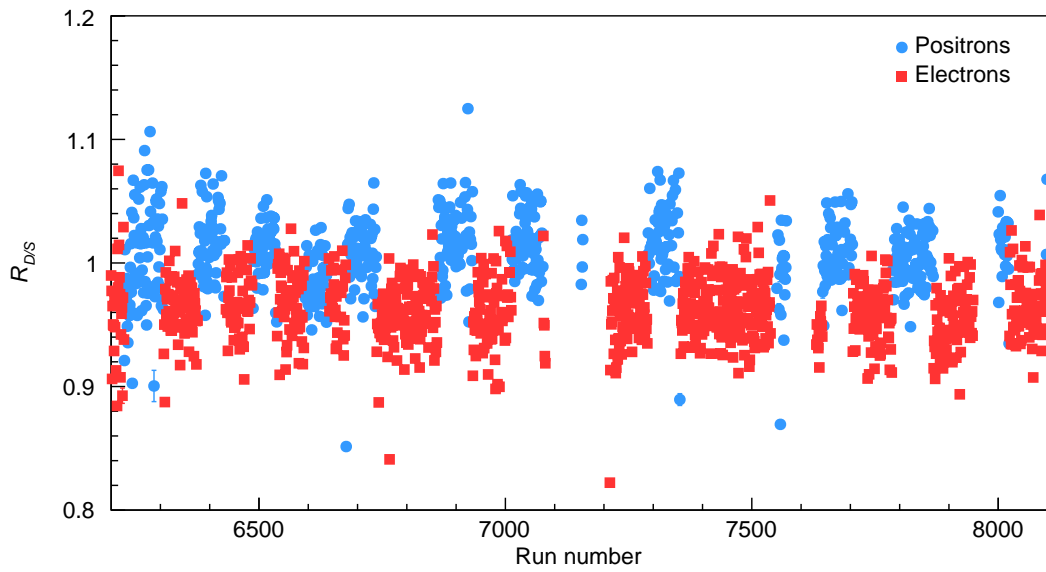


**Figure 8.6:** Results for set 2. Data to simulation ratio versus run number (top). Projected and fitted data points from the top figure (bottom).

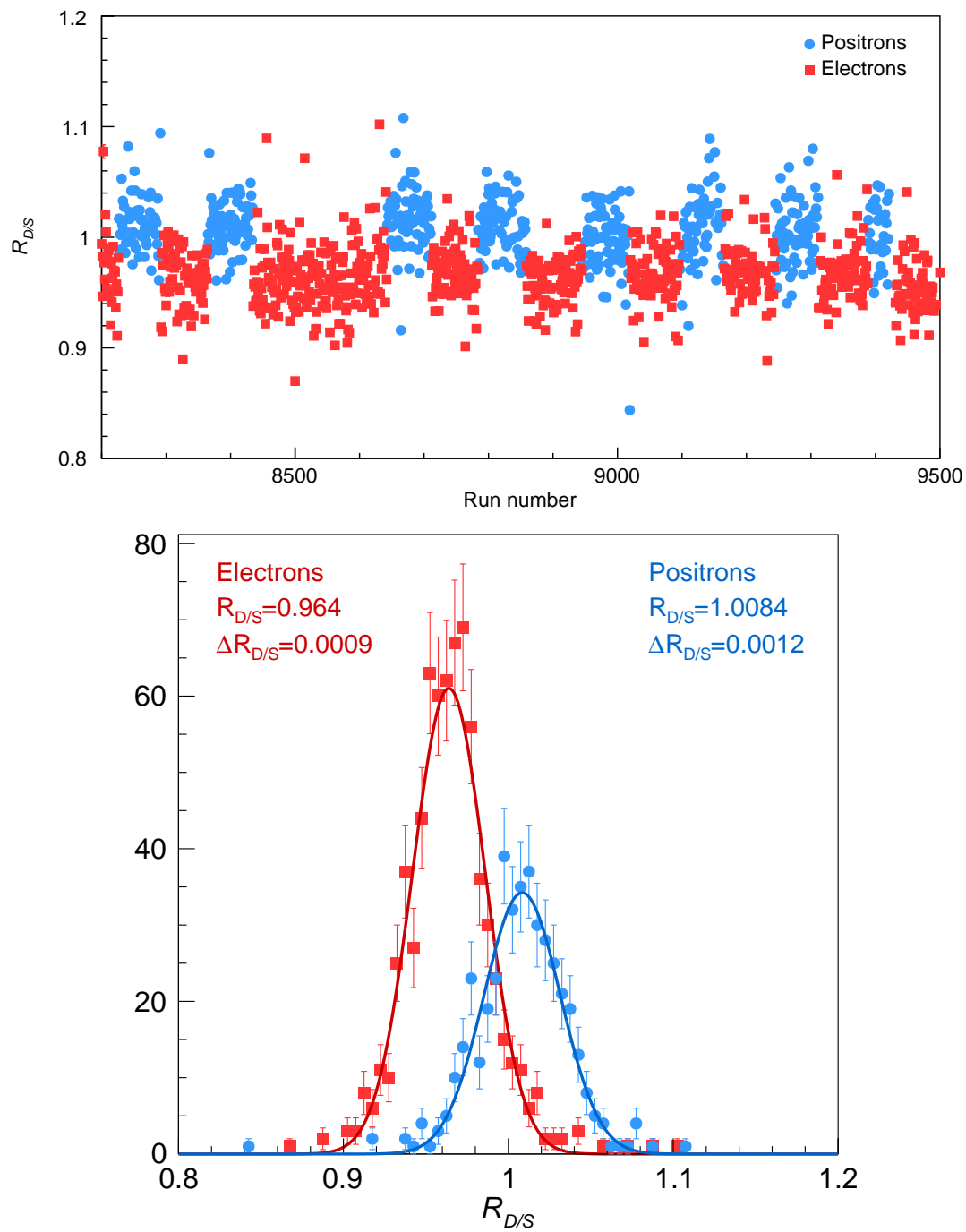


**Figure 8.7:** Results for set 3. Data to simulation ratio versus run number (top). Projected and fitted data points from the top figure (bottom).

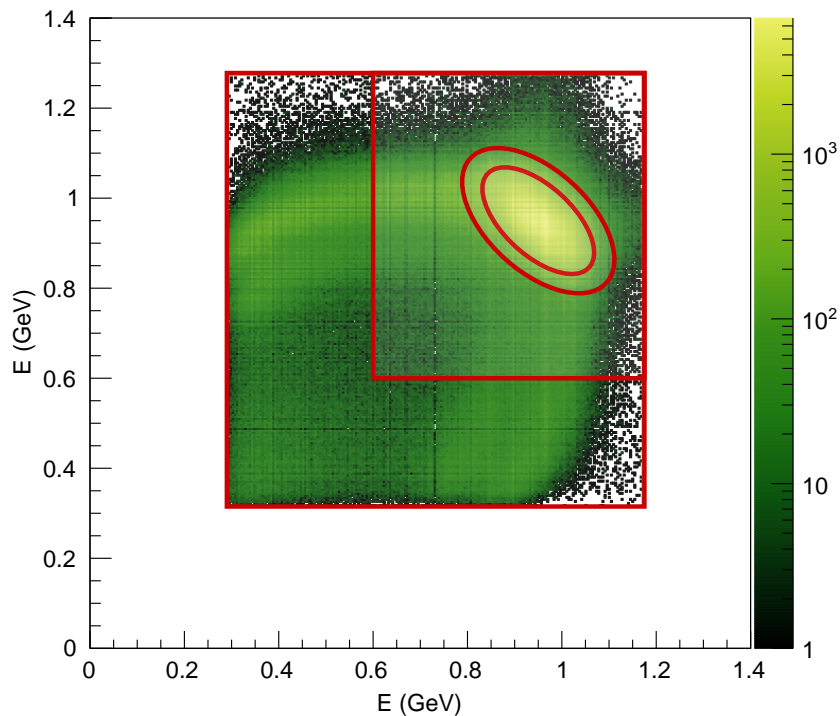


**Figure 8.8:** SYMB coincidence data and an example of four selections areas: two fixed boxes covering biggest part of the spectrum and two elliptical cuts centered on the coincidence region.

- Ellipse - dynamically built and positioned elliptical area centered around the coincidence peak. Two ellipse sizes were studied.

Fig. 8.8 illustrates a few selection areas. Two boxes have fixed size and position relative to the coincidence peak and are independent from the beam species. Due to the fact that the SYMB detector experienced radiation damage during data taking, the coincidence peak position is slightly different from run to run. Fig. 8.9 demonstrates two data samples: one collected in November 2012 and another one in December 2012. In the latter one, the coincidence area is located further away from the top right corner, *i.e.*, the whole spectra moved toward lower ADC values within its dynamic range. This drift caused some entries to go into the underflow bins while others migrated from the overflow bins into the spectrum. Therefore, the box selection methods are affected by the spectrum drift.

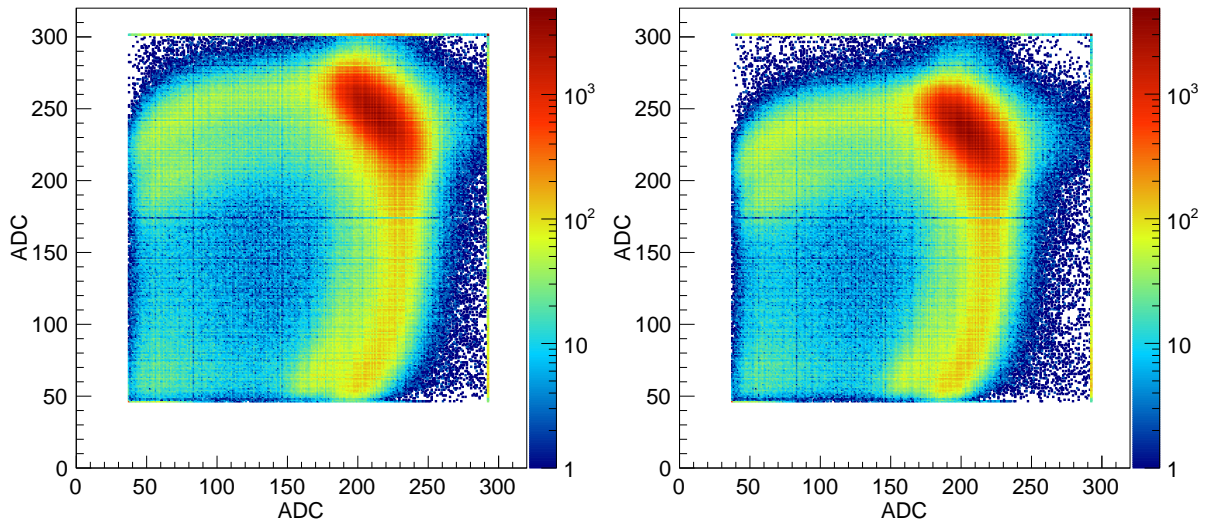


**Figure 8.9:** Subset of the SYMB data collected in one November 2012 run (left) and in one December 2012 run (right). The data were collected 44 days apart.

Additionally, Fig. 8.10 shows the dynamic of the coincidence area center as it changes over the data taking period. As can be seen, both left and right SYMB detectors shows similar signal decrease for electron and positron beams. In total the ADC signal has decreased by approximately 7% and 10% for the left and right sector, respectively.

The dynamic elliptical cuts which follow the center of the coincidence area are unaffected by the drift. The ellipses are constructed in the following way: 1) projections of the SYMB coincidence spectrum on  $X$  and  $Y$  axes are created; 2) Novosibirsk function [107] is fitted to the projections to find their peak position as shown in Figs. 8.11a and 8.11b; 3) the original SYMB spectra is rotated by  $-45^\circ$  as shown in Fig. 8.11c; 4) similar to the first step, two projections on  $X$  and  $Y$  axes are created; 5) Gaussian function is fitted to these projections as shown in Figs. 8.11d and 8.11e; 6) the fit  $\sigma$  parameters are used to set major and minor semi-axes of the ellipses. Two cuts,  $3\sigma$  and  $5\sigma$  were used to set a size of two elliptical selection areas. The former one corresponds to ellipse semi-axes being equal to  $3\sigma$  (small ellipse) while the latter one corresponds to  $5\sigma$  (big ellipse) long semi-axes. The result of the selection is shown in Fig. 8.12. This procedure is performed for each single run, thus it provides individual elliptical selection for each run.

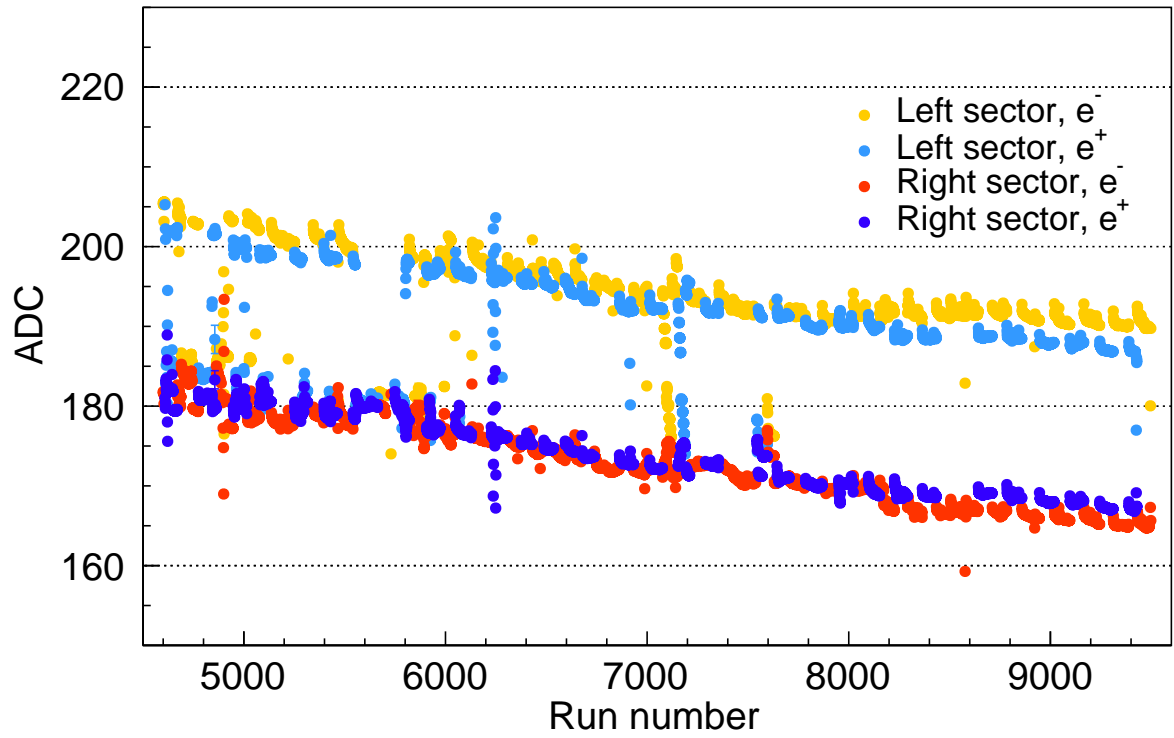


**Figure 8.10:** The center of the coincidence area versus run number or approximately 2200 hours of data taking. Three region around runs 4600, 4900, and 6200 where data points aligned in vertical lines corresponds to the beam scan runs. The beam position and slope along  $X$  and  $Y$  axes were scanned to optimize counting rates. The next two similar structures around runs 7100-7200 and 7500-7600 were caused by the magnetic field scan. The magnet current values were changed between -6730 A and 6730 A. The effect of the magnetic field on  $R_{D/S}$  is discussed in Sec. 8.3.4.

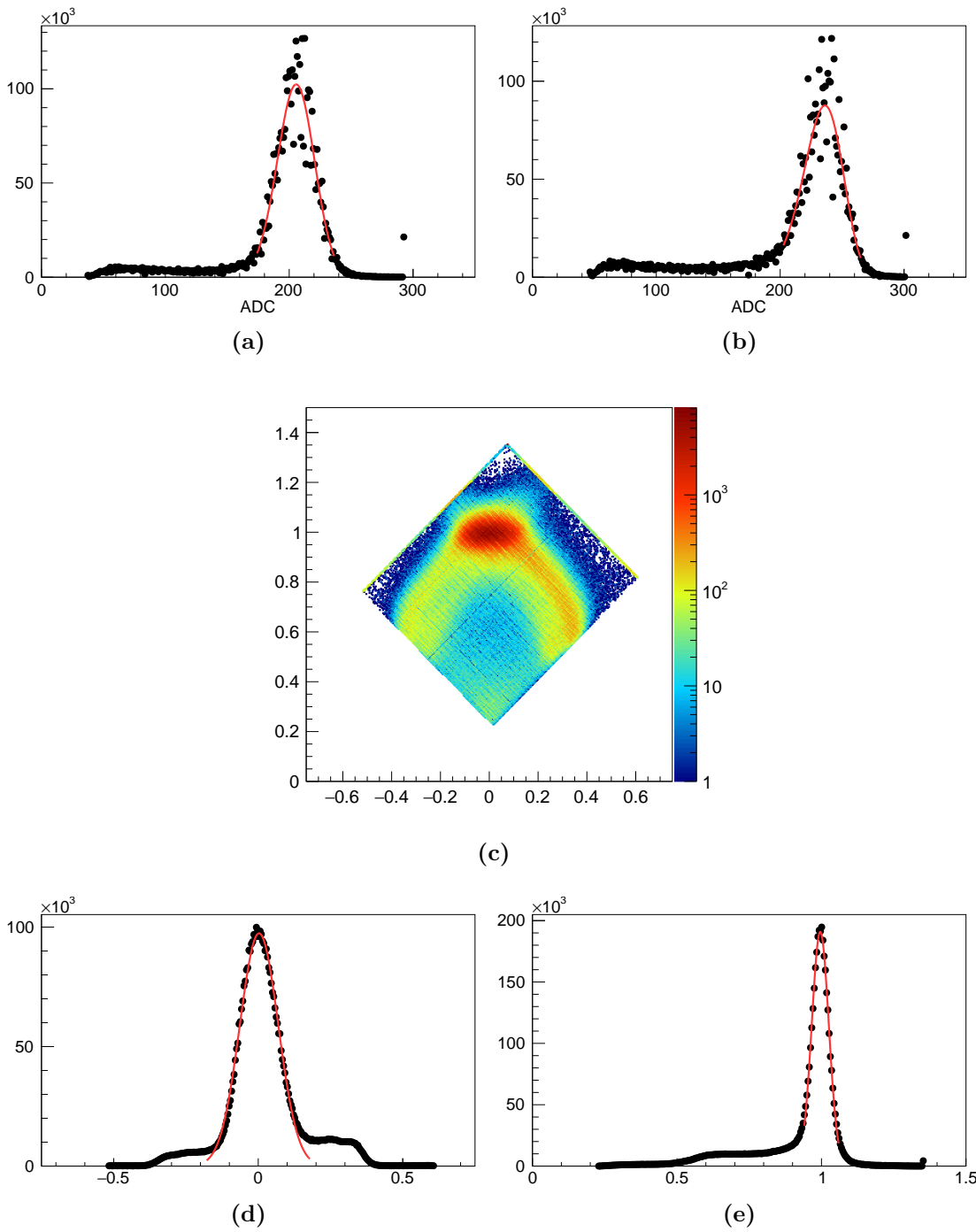


**Figure 8.11:** SYMB data (points) projected on the  $X$  axis (a) and on the  $Y$  axis (b) and the Novosibirsk fit (line). SYMB data rotated by  $-45^\circ$  and transformed so that the coincidence peak area is centered at (0,1) (c). Rotated and transformed SYMB data (points) projected on the  $X$  axis (d) and on the  $Y$  axis (e) and the Gaussian fit (line).

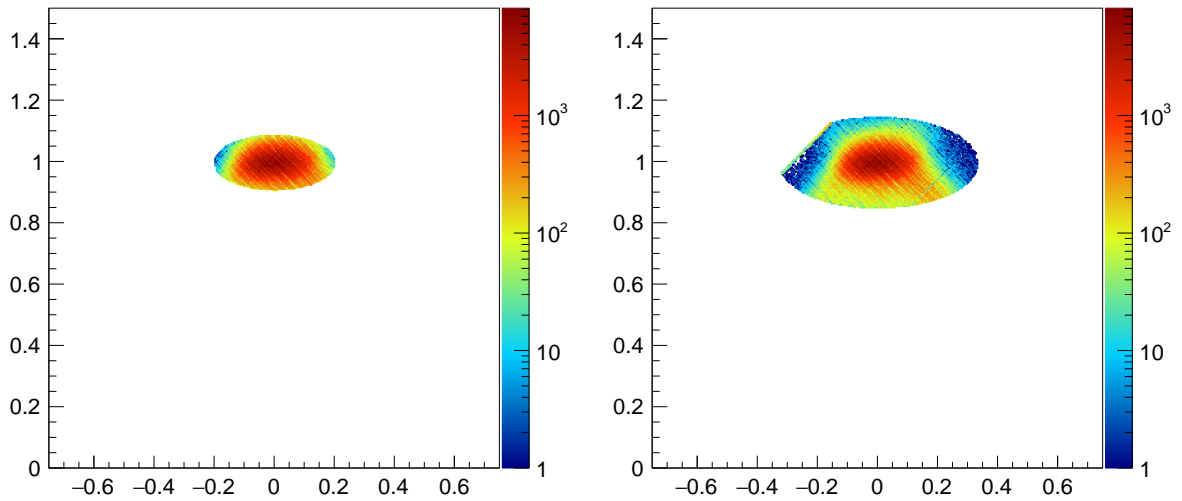


**Figure 8.12:** SYMB data selected using  $3\sigma$  (left) and  $5\sigma$  (right) elliptical cuts. The small ellipse essentially covers the very core of the coincidence area, while the big ellipse extends up to the overflow bin, visible as green line in the left part of the figure, and beyond.

The data to simulation ratio  $R_{D/S}$  was determined for each selection method in the same way as in Sec. 8.1.2. Fig. 8.13 shows results for the two box and two elliptical cuts applied to electron and positron data. The fit results clearly demonstrate that the choice of the selection method affects  $R_{D/S}$ . For example, the difference between the box 1 and box 5 is about 3% for positrons and 2% for electrons, while the difference between two elliptical selections is about 3% and 4% for positrons and electrons, respectively.

Selection results are summarized in Fig. 8.14. A significant difference between electron and positron  $R_{D/S}$  can be observed. Depending on the selection method the data to simulation event ratio fluctuates by up to 5% for both electrons and positrons. Nevertheless, the interspecies asymmetry changes very little with the applied selection method, due to the correlation between electrons and positrons fluctuations, with the only exception being box 8 where asymmetry deviates by  $\sim 3\%$  with respect to other cuts. Thus, it can be said that the selection procedure has a very small effect on the  $R_{Asym}$  and can not be the reason of the interspecies discrepancy.

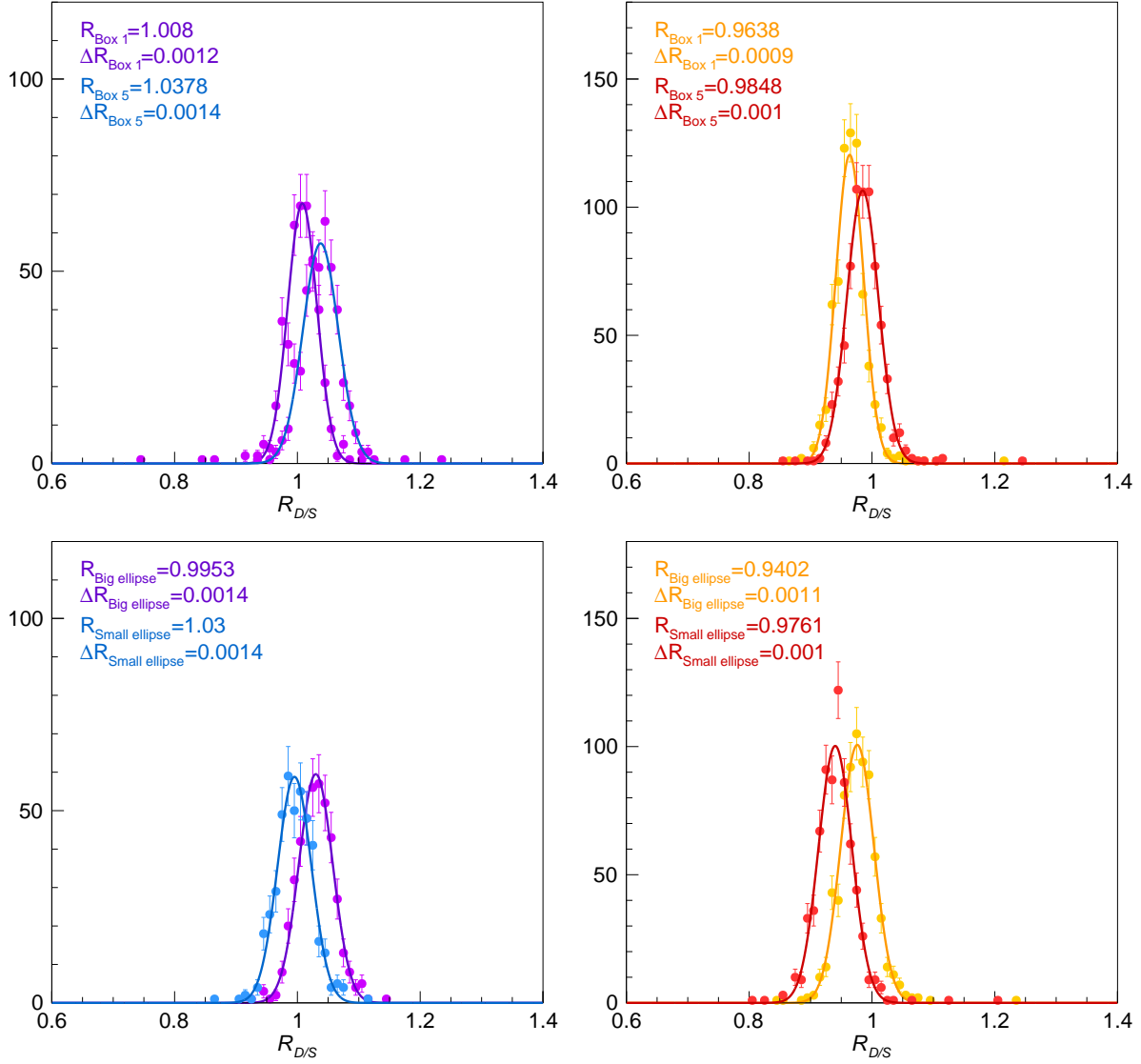


**Figure 8.13:** Data to simulation events ratio  $R_{D/S}^{e^\pm}$  for electrons (red and orange circles) and positron (blue and violet circles) beams and Gaussian fits (lines) for two box selection methods (top row) and two elliptical ones (bottom row).

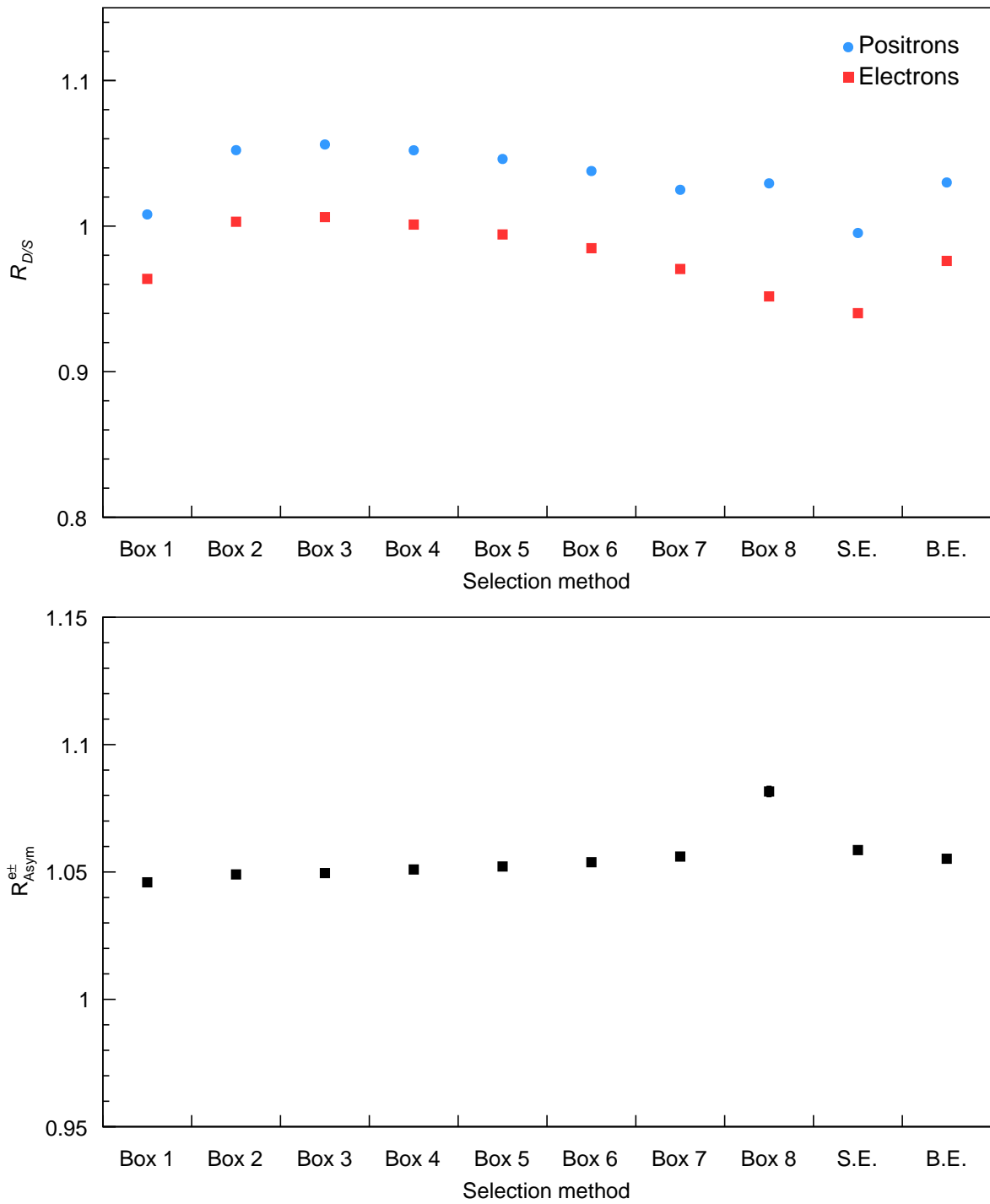


**Figure 8.14:** Data to simulation events ratio for electrons and positrons (top) and positron-electron asymmetry for all selection methods (bottom).

## 8.3 Systematic Uncertainties

In this chapter a number of the most significant systematic uncertainties are discussed. The beam parameters - emittance, position, and slope can have a noticeable impact on SYMB counting rates. It was previously shown in Fig. 8.1 that the variation of signal cross sections across the SYMB geometrical acceptance can not be neglected. Similarly, the position of the detectors themselves affects geometrical acceptance. Finally, the effect of the magnetic field and a number of other parameters will be studied.

### 8.3.1 Beam Emittance

Beam emittance characterizes how beam particles distributed in the position and momentum phase space. Smaller emittance means smaller beam width, momentum and angular spread of beam particles.

At first, it was assumed that the beam emittance had a negligible effect on the SYMB counting rate during the experiment. With a discovery of the interspecies discrepancy it was necessary to take into account effects which could potentially affect the results of the simulation. The horizontal beam emittance data extracted from the DORIS database<sup>1</sup> is shown in Fig. 8.15. The vertical emittance was considered to be 20 times smaller than the horizontal one. Multiple emittance readings were made during each run what is reflected by the visible vertical spread.

An example of the horizontal emittance distribution within one run and the deviation from the mean for the whole data set are shown in Fig. 8.16. The applied Gaussian fit shows that in the particular run the standard deviation of the beam emittance was  $\sim 1.9\%$ . In general, most runs had deviation smaller than few percent what can be seen in Fig. 8.16 (right). To simplify the simulation process, run averaged emittance values, also shown in Fig. 8.16, were used. As can be seen, the run averaged horizontal emittance provides a good approximation of emittance fluctuations throughout data taking.

To investigate how strongly the analysis results are affected by the fluctuating beam emittance the data set 3 (presented in Sec. 8.1.1) was simulated with the emittance set to 80% and 120% of the nominal value. Beam emittance deviation of  $\pm 20\%$  was chosen

---

<sup>1</sup>Thanks to J. Bernauer

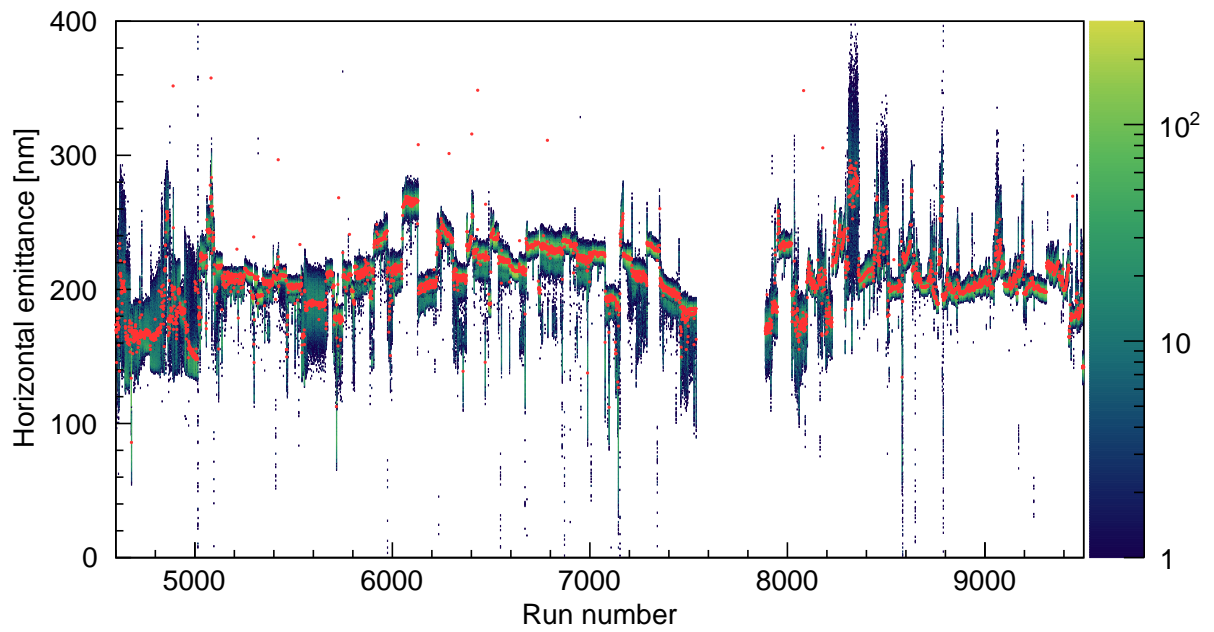


**Figure 8.15:** Horizontal beam emittance throughout data taking (black-green gradient) and run averaged (red dots) used in the OLYMPUS Monte Carlo.

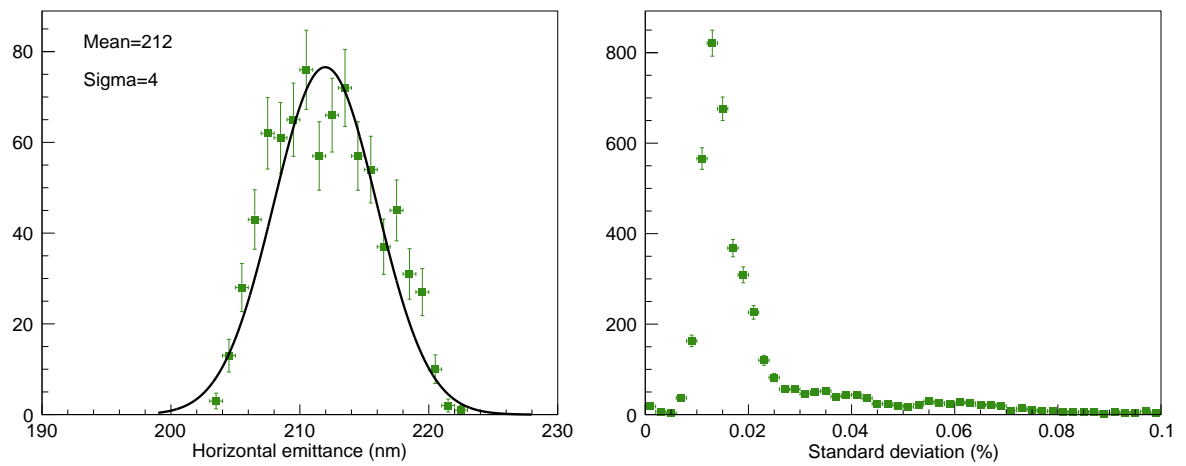


**Figure 8.16:** Left: horizontal emittance distribution within one run (points) and the Gaussian fit (line). Right: standard deviation from the mean across the whole data set.

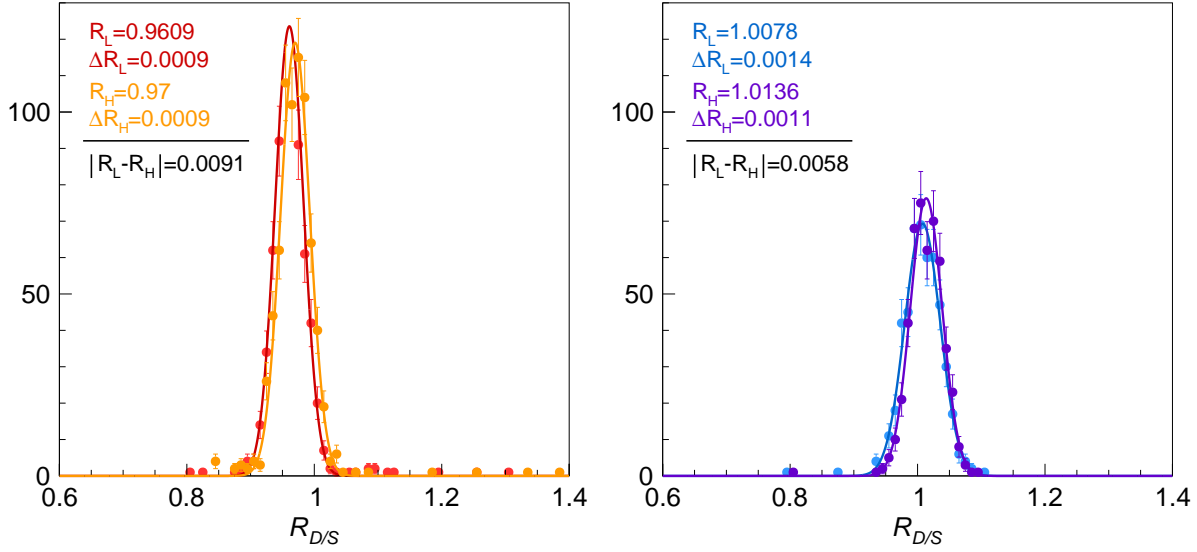


**Figure 8.17:** Data to simulation events ratio for electron (left) and positron (right) beams and the Gaussian fits (lines). Subscripts L and H denote emittance settings of  $0.8 \times$  nominal and  $1.2 \times$  nominal, respectively.

as its influence on the data to simulation event ratio  $R_{D/S}$  was expected to be very small. The results, shown in Fig. 8.17, demonstrate deviation between the two beam emittance settings to be around 0.91% for electrons and 0.58% for positrons.

The real emittance fluctuations from the available DORIS emittance data (see Figs. 8.15 and 8.16) are smaller by a factor of 10 than the difference between low (80%) and high (120%) settings which have been used in this study. Therefore, the effect of the emittance on  $R_{D/S}$  can be taken as 0.1% or less.

### 8.3.2 Beam Position and Slope

As it was already mentioned, the beam position and slope were constantly monitored during data taking. The beam position was defined as beam transverse coordinates along  $X$  and  $Y$  axes at the center of the target cell and the slope as the angle between the beam and the  $Z$  axis. Fig. 8.18 shows beam position and slope in both horizontal ( $X$ ) and vertical ( $Y$ ) planes as it was recorded by the beam position monitors (BPM) at the beginning of each run. Evidently, apart of few regions, the beam was very stable

throughout data taking.

To study the influence of the beam position its slope along  $X$  and  $Y$  axes were set to zero, then the beam was moved around  $(X, Y) = (0, 0)$  from -1 mm to 1 mm in vertical and horizontal directions in steps of 0.1 mm.  $X$  and  $Y$  represent the horizontal and vertical beam position, respectively. The coincidence events were normalized to unity at  $(X, Y) = (0, 0)$ . Fig. 8.19 shows how normalized events change depending on the beam position. The horizontal beam movement shows very little effect on the SYMB events in comparison to that of the vertical displacement. Small fluctuations along the  $X$  axis at fixed  $Y$  value is caused by the statistical fluctuations in the simulation. A shift of one millimeter in the vertical direction changes the SYMB event rate by approximately 7%.

Fig. 8.20 shows integrated counts for an extended scan along the  $Y$  axis from -3 mm to 3 mm with the horizontal position being fixed  $X = 0$ . Starting at  $Y = -3$  mm the number of counts rises until the maximum at  $Y = 1.6$  with an average 10% change in counts per millimeter, followed by a steeper decline with an approximately 14% counts decrease per millimeter. The position of the maximum is not at  $Y = 0$  because the vertical position of the left and right apertures' centers was around  $Y = 1.96$  mm and  $Y = 1.48$  mm, respectively. Thus, the maximum is located between these two points.

In addition, a series of simulations was performed to test whether the OLYMPUS Monte Carlo reproduces the SYMB signal seen in the data. Fig. 8.21 shows the cross section determined from the experimental data and corresponding simulation based on one of the scans. All figures, with the exception of Fig. 8.21d, show no significant dependence of the cross section on the beam position or slope. Therefore, it can be assumed that the recorded beam parameters in the simulation either match those in the real experiment or the error is not big enough to expose itself. Fig. 8.21d shows cross section dependence on the vertical beam slope and the corresponding polynomial fits. The fit results indicate that the maximum simulated and data cross sections are reached at different vertical beam slopes, *i.e.*,  $Y_{slope}^{Sim} = 0.78 \times 10^3$  mrad and  $Y_{slope}^{Data} = 0.59 \times 10^3$  mrad, respectively. That may be a sign that the recorded data does not exactly match the real situation during data taking.

Thus, the quality of the beam itself was considered to be good enough for the purpose of the experiment. On the other hand, the position of the BPMs themselves was known

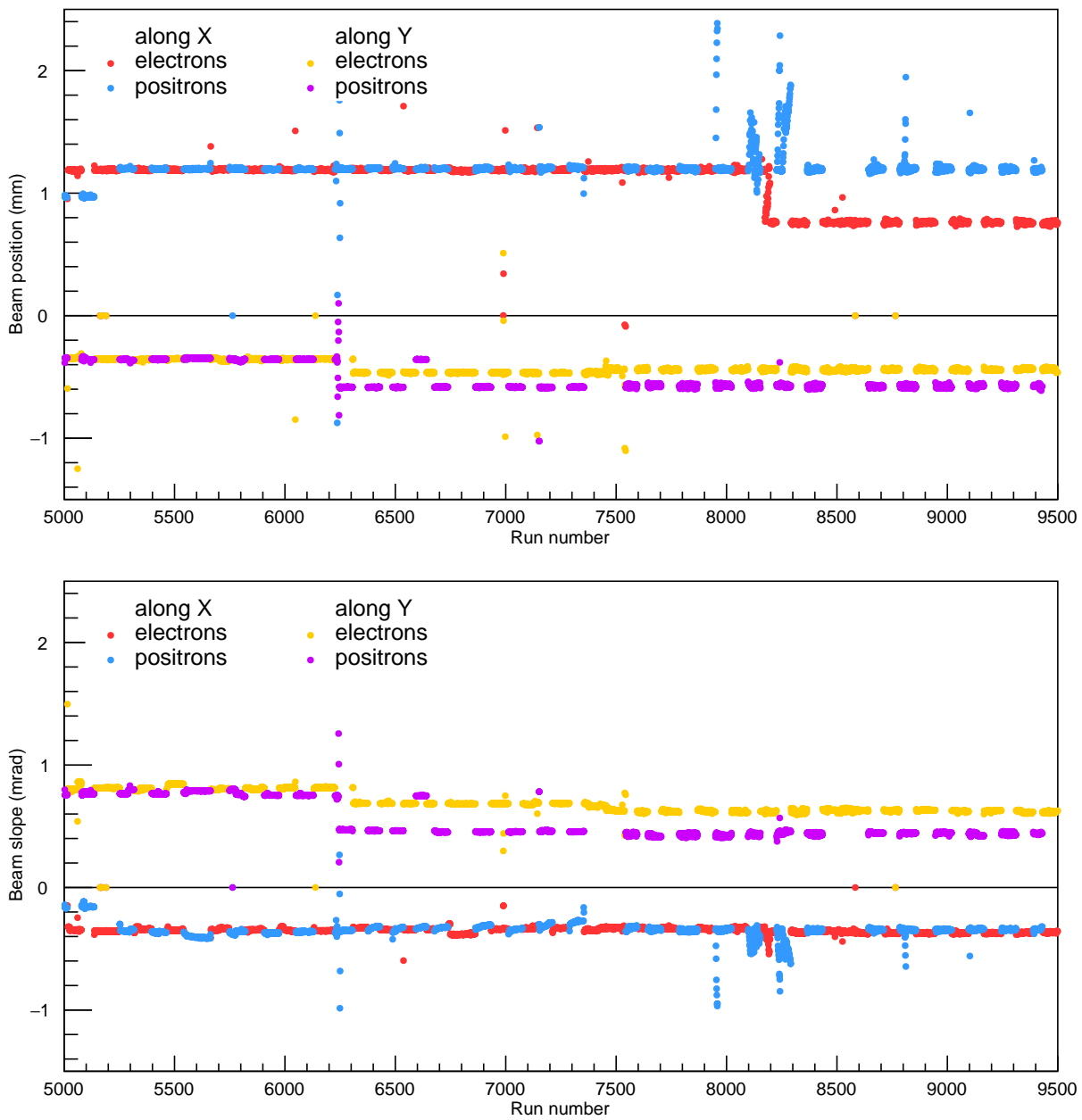


**Figure 8.18:** Beam position and slope as a function of run number throughout data taking. Beam position and slope scan is visible around run 6230 which divides set 1 and 2. Beam instabilities which occurred between 8100 and 8300 separate sets 2 and 3.

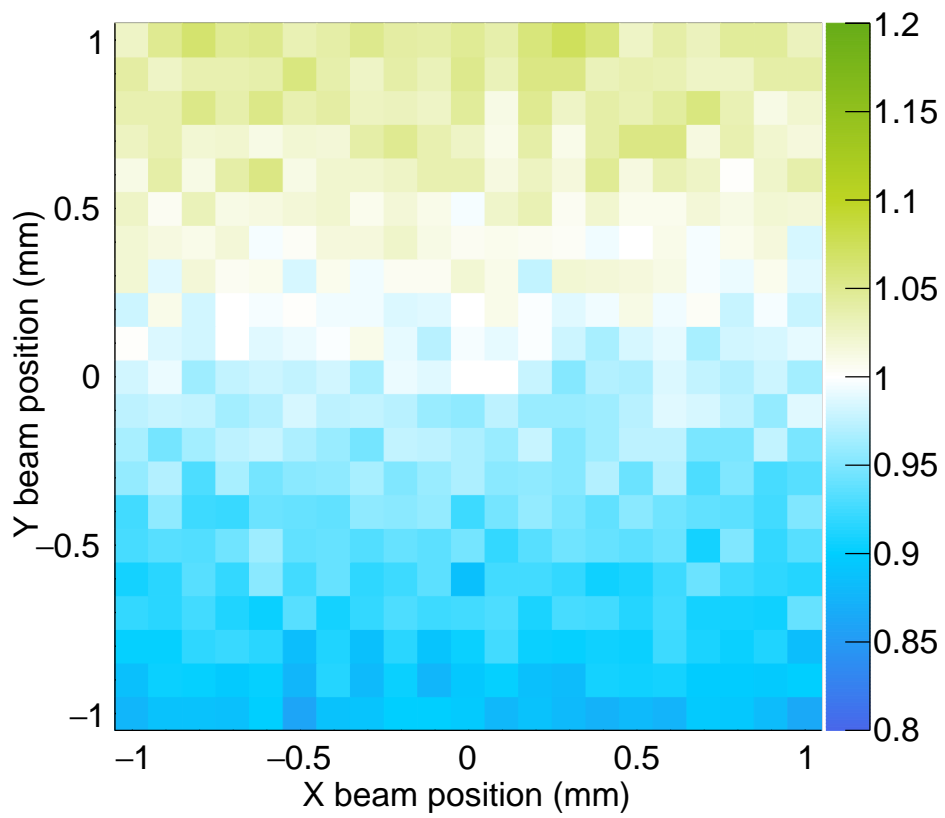


**Figure 8.19:** Normalized SYMB events as a function of the beam position.

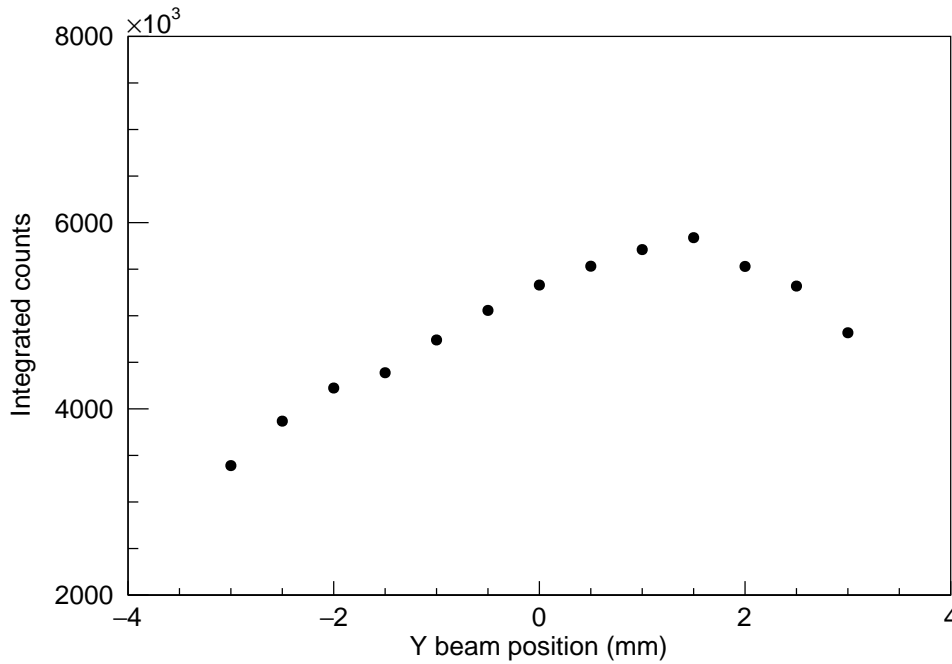


**Figure 8.20:** Integrated SYMB events as a function of the  $Y$  beam position.

with a precision of around 0.2 mm. Uncertainty in the BPMs position can be directly translated into beam position and slope uncertainty. For example, if the survey had an error in measured position of one or both BPMs, their position in the simulation would be different from that in the experiment. Thus, a systematic error in the simulated beam position or beam slope or both would appear.

To quantify the uncertainty, a series of simulations were performed with an offset of  $\pm 0.2$  mm applied to the beam position provided by the BPMs along  $X$  and  $Y$  axes. Table 8.1 summarizes the results. The added offset has a different effect on the electron and position data to simulation event ratio. At some settings the change is smaller than 0.1% while at others it goes as high as 3.5% in comparison to the nominal beam position. The interspecies asymmetry decreases to a minimum around 1.5% or goes up to 6% depending on the beam offset configuration.

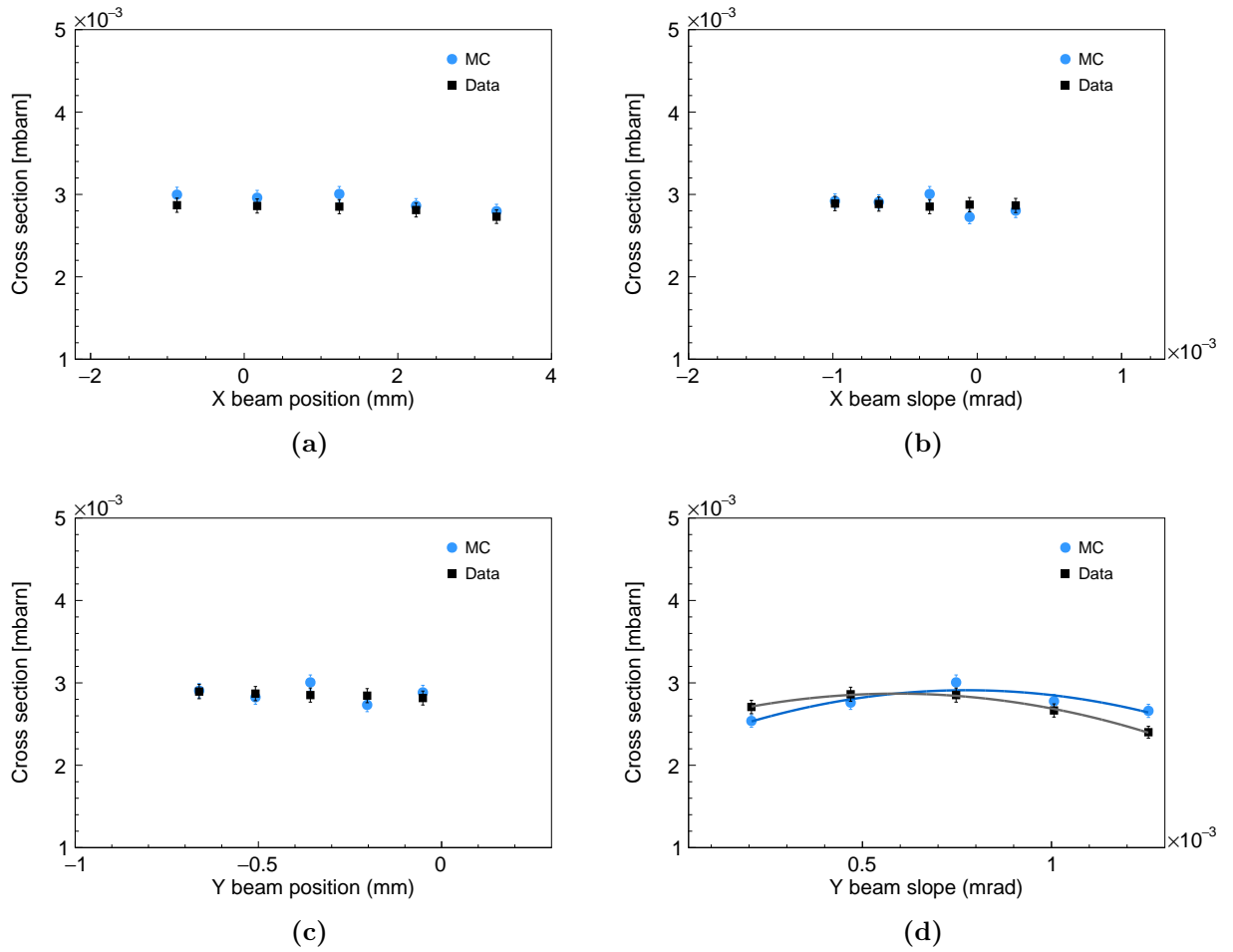


**Figure 8.21:** Comparison of the simulated (blue circles) and measured (black squares) cross section during the November beam position and slope scan with positron beam. The line in (d) is polynomial fit.

$X$ Offset (mm)	$R_{D/S}^{e^+}$	$R_{D/S}^{e^-}$	$R_{Asym}$
-0.2	$0.993 \pm 0.001$	$0.978 \pm 0.001$	$1.016 \pm 0.002$
0.0	$1.009 \pm 0.001$	$0.964 \pm 0.001$	$1.047 \pm 0.002$
+0.2	$1.012 \pm 0.001$	$0.999 \pm 0.001$	$1.014 \pm 0.002$
$Y$ Offset (mm)	$R_{D/S}^{e^+}$	$R_{D/S}^{e^-}$	$R_{Asym}$
-0.2	$1.026 \pm 0.001$	$0.969 \pm 0.001$	$1.060 \pm 0.002$
0.0	$1.001 \pm 0.001$	$0.964 \pm 0.001$	$1.047 \pm 0.002$
+0.2	$1.009 \pm 0.001$	$0.964 \pm 0.001$	$1.038 \pm 0.002$

**Table 8.1:** The influence of the beam offset on the data to simulation ratio and interspecies asymmetry

### 8.3.3 Detector Alignment

As the beam position, the detector alignment is critical for the correct luminosity determination. The difference between the experimental detector placement and the one in the simulation may cause the interspecies discrepancy. A series of studies was performed where each SYMB detector was individually displaced around its nominal position in horizontal ( $X$ ) and vertical ( $Y$ ) directions by  $\pm 1$  mm and  $\pm 2$  mm and along the beam pipe ( $Z$ ) by  $\pm 1$  mm.

Fig. 8.22 (left) shows  $R_{D/S}$  dependence on the offset of the left and right SYMB detectors along the  $X$  axis for electron and positron beams. Moving the left SYMB detector to the left from its nominal position decreases  $R_{D/S}$  for the both beam species while moving it to the right increases it. As shown in Fig. 8.22 (right), the opposite effect is observed when the right SYMB detector is displaced. A polynomial fit was applied to calculate maximum  $R_{D/S}$  deviation at  $\pm 0.5$  mm which is the precision of the detectors' survey.

The interspecies discrepancy changes with the detector position as well. As Table 8.2 shows, the discrepancy decreases when either of two detectors is moved closer to the beam pipe and increases if moved farther away from it.

Fig. 8.23 shows  $R_{D/S}$  dependence on the offset of the left and right SYMB detectors along the  $Y$  axis for electron and positron beams. Displacement of either of two detectors

$R_{Asym}$		
$X$ Offset (mm)	Left detector	Right detector
-2	$1.059 \pm 0.002$	$1.039 \pm 0.002$
-1	$1.054 \pm 0.002$	$1.044 \pm 0.002$
0	$1.051 \pm 0.004$	$1.051 \pm 0.004$
1	$1.042 \pm 0.002$	$1.052 \pm 0.002$
2	$1.036 \pm 0.002$	$1.056 \pm 0.002$
$Y$ Offset (mm)	Left detector	Right detector
-2	$1.005 \pm 0.002$	$1.002 \pm 0.002$
-1	$1.027 \pm 0.002$	$1.025 \pm 0.002$
0	$1.051 \pm 0.004$	$1.051 \pm 0.004$
1	$1.067 \pm 0.002$	$1.068 \pm 0.002$
2	$1.082 \pm 0.002$	$1.082 \pm 0.002$
$Z$ Offset (mm)	Left detector	Right detector
-1	$1.047 \pm 0.002$	$1.048 \pm 0.002$
0	$1.051 \pm 0.004$	$1.051 \pm 0.004$
1	$1.047 \pm 0.002$	$1.048 \pm 0.002$

**Table 8.2:** The interspecies discrepancy dependence on the SYMB position along  $X$ ,  $Y$ , and  $Z$  axes. Zero offset means nominal position as during data taking.

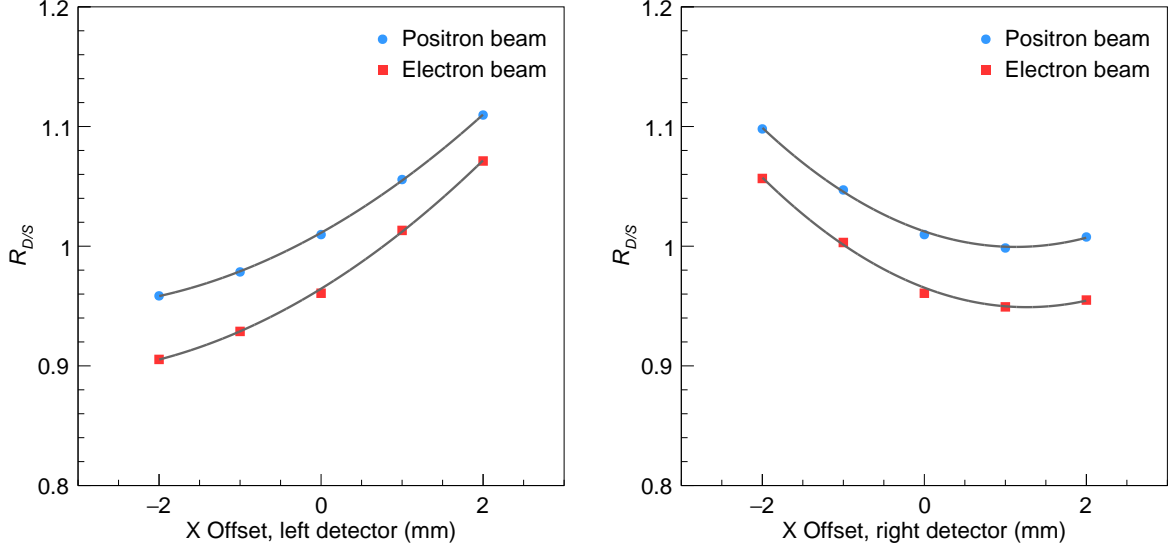


**Figure 8.22:** Dependence of  $R_{D/S}$  on the offset of the left and right SYMB detectors along the  $X$  axis for electron (red squares) and positron (blue circles) beams, and the polynomial fit (gray lines).

produces a similar effect. Shift up from the nominal position not only increases  $R_{D/S}$  of the positron and electron data sets but also makes bigger the interspecies discrepancy. On the other hand, moving either of two detectors down decreases  $R_{D/S}$  of the positron data but have an opposite effect on the electron data which shows small increase. Shifting the left or right detector by -2 mm reduces the difference between electrons and positrons to 0.5% and 0.2%, respectively.

The results of applying an offset along the beam are shown in Fig. 8.24 and Table 8.2. Apparently, the SYMB position along the  $Z$  axis has a very small effect on the data to simulation count ratio for both electron and positron beams.

To summarize, a displacement of 0.5 mm along any axis affects  $R_{D/S}^{e^\pm}$  by up to 2% and  $R_{Asym}^{e^\pm}$  by up to 1%. Exact values of the interspecies discrepancy are shown in Table 8.2.

In addition, an effect of rotation of both detectors have been investigated in a similar manner. Each detector was individually rotated about  $X$ ,  $Y$ , or  $Z$  axis by  $\pm 1$  degree. Results are shown in Figs. 8.25 to 8.27 and summarized in Table 8.3. Although a rotation by  $1^\circ$  about  $X$  or  $Y$  axis does significantly affect the data to simulation event ratio, the interspecies discrepancy changes very little. In the best case it goes down to 3.6%. The

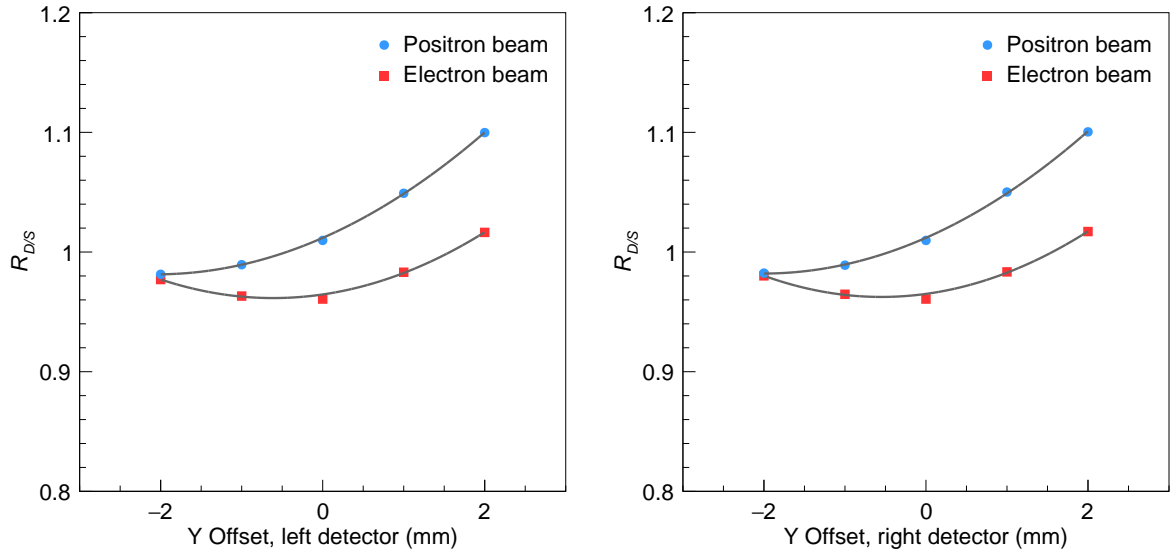


**Figure 8.23:** Dependence of  $R_{D/S}$  on the offset of the left and right SYMB detectors along the Y axis for electron (red squares) and positron (blue circles) beams, and the polynomial fit (gray lines).

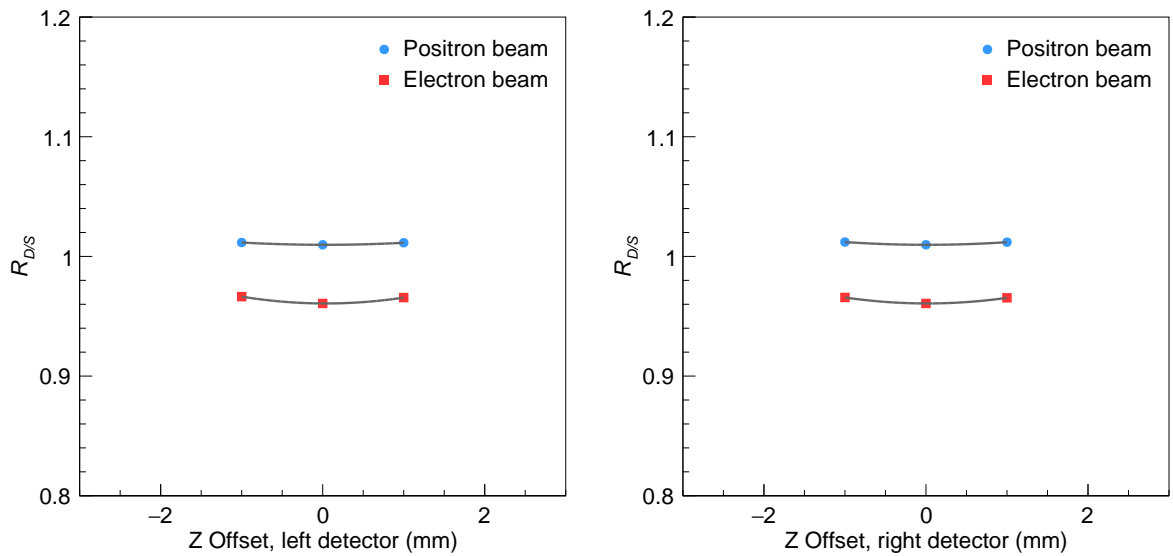


**Figure 8.24:** Dependence of  $R_{D/S}$  on the offset of the left and right SYMB detectors along the Z axis for electron (red squares) and positron (blue circles) beams, and the polynomial fit (gray lines)

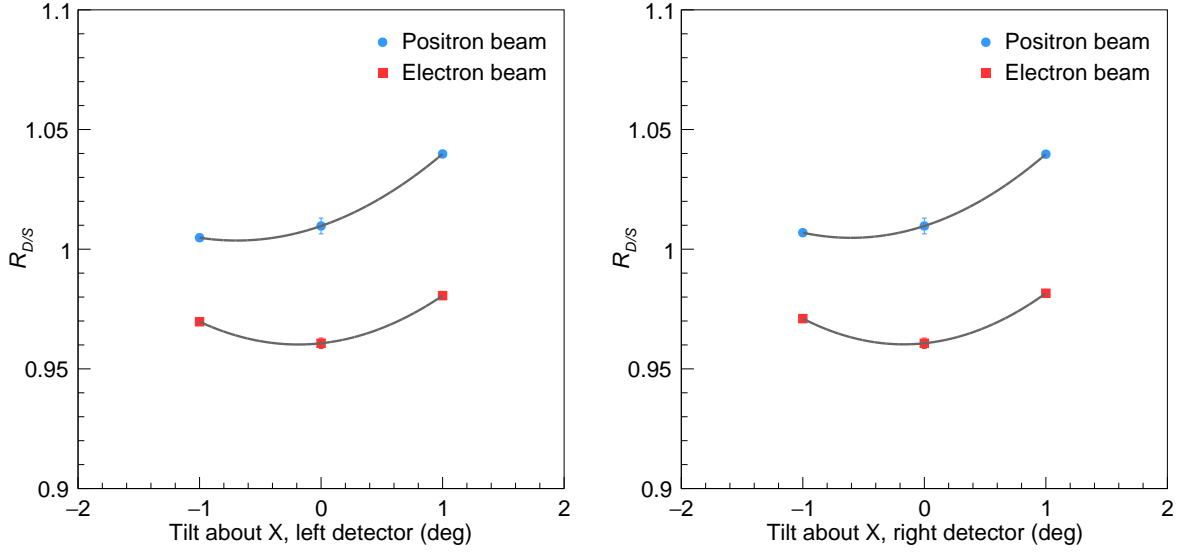


**Figure 8.25:** Data to simulation ratio dependence on the tilt of the left and right SYMB detectors about the  $X$  axis for electron (red squares) and positron (blue circles) beams, and the polynomial fit (gray lines).

rotation about the  $Z$  axis, similar to the displacement along it, has a very little effect on the asymmetry.

These studies have shown that rotating any detector about any axis has a maximum effect of 0.7% and 0.6% on  $R_{D/S}^{e^\pm}$  and  $R_{Asym}^{e^\pm}$ , respectively.

In an attempt to reconcile the electron and positron data to simulation ratio the position and rotation of the SYMB detectors were adjusted in a more realistic way based on the results shown before. Three sets of adjustments, shown in Table 8.4, were applied to the SYMB detectors. Results, also shown in Table 8.4, demonstrate that it is possible to eliminate the interspecies discrepancy in a multiple ways.

Although it is very tempting to accept one of the found solutions as an explanations for the interspecies discrepancy, it is very unlikely that such a big mistakes were done during the detector survey assuming that the position and rotation of the SYMB detectors was measured with a precision better than 0.5 mm and  $0.2^\circ$ , respective. Additionally, as the discrepancy between electrons and positrons can be eliminated by a multiple different adjustments and it's impossible to justify choosing one over others.

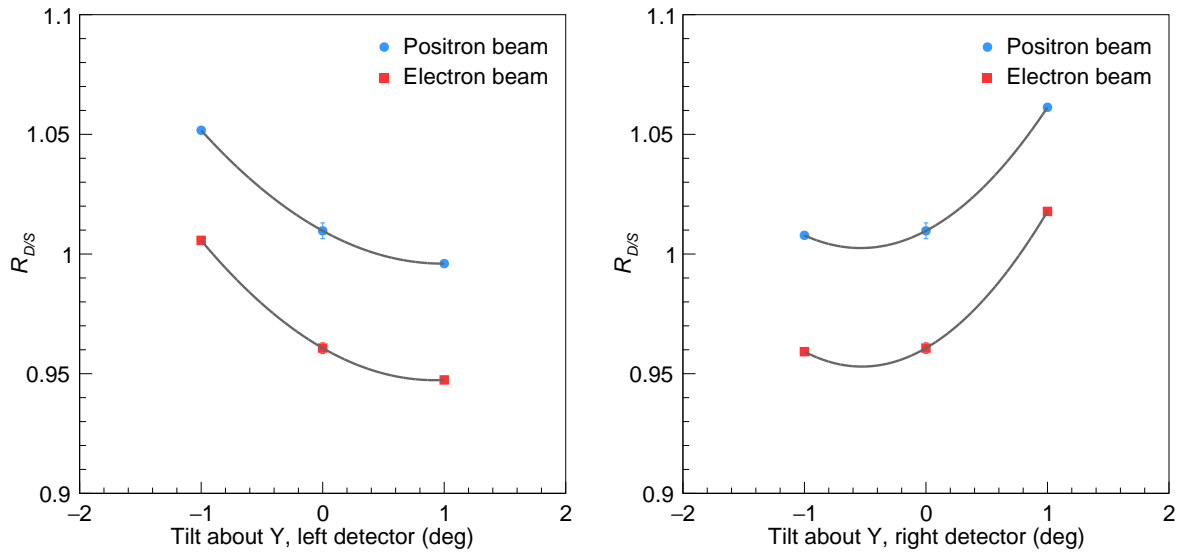


**Figure 8.26:** Data to simulation ratio dependence on the tilt of the left and right SYMB detectors about the  $Y$  axis for electron (red squares) and positron (blue circles) beams, and the polynomial fit (gray lines).

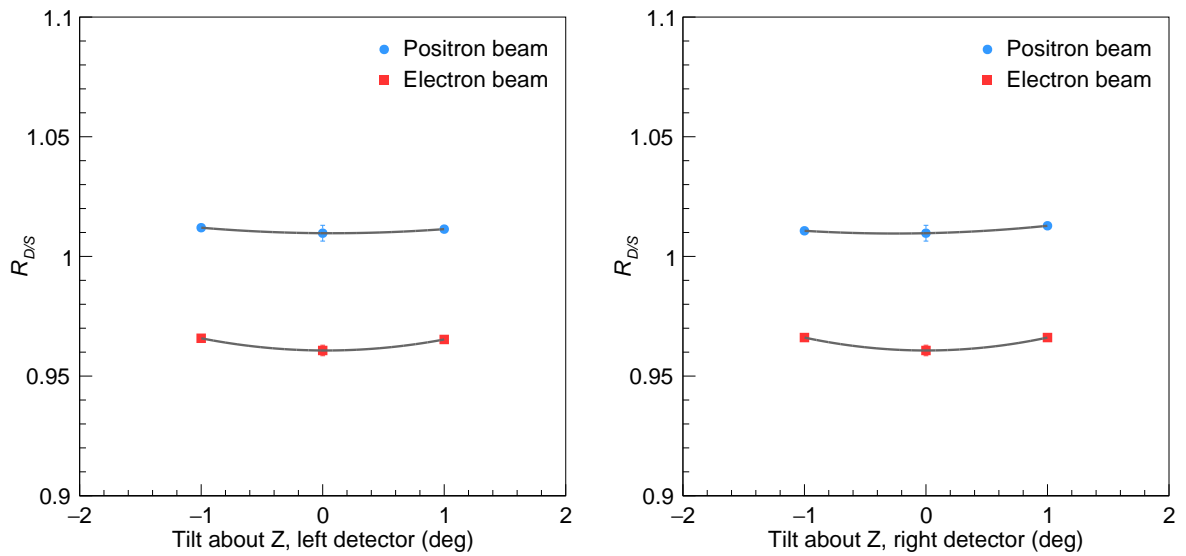


**Figure 8.27:** Data to simulation ratio dependence on the tilt of the left and right SYMB detectors about the  $Z$  axis for electron (red squares) and positron (blue circles) beams, and the polynomial fit (gray lines).

$R_{Asym}$		
$X$ Rotation (deg)	Left detector	Right detector
-1	$1.036 \pm 0.002$	$1.037 \pm 0.002$
0	$1.051 \pm 0.004$	$1.051 \pm 0.004$
1	$1.060 \pm 0.002$	$1.059 \pm 0.002$
$Y$ Rotation (deg)	Left detector	Right detector
-1	$1.046 \pm 0.002$	$1.051 \pm 0.002$
0	$1.051 \pm 0.004$	$1.051 \pm 0.004$
1	$1.051 \pm 0.002$	$1.043 \pm 0.002$
$Z$ Rotation (deg)	Left detector	Right detector
-1	$1.048 \pm 0.002$	$1.046 \pm 0.002$
0	$1.051 \pm 0.004$	$1.051 \pm 0.004$
1	$1.048 \pm 0.002$	$1.048 \pm 0.002$

**Table 8.3:** The interspecies discrepancy dependence on the rotation of the SYMB detectors about  $X$ ,  $Y$ , and  $Z$  axes. Zero rotation means nominal tilt as during data taking.

### 8.3.4 Magnetic Field

The survey of the magnetic field has shown that a residual field of approximately  $10^{-3}$  T were present in the region where products of Møller and Bhabha scattering passed on the way to the SYMB detectors. Therefore, it was important to study the effect of the magnetic field on the SYMB response. The nominal magnet current value used during data taking was 5000 A. To study the effect of the magnetic field a small subset of data was collected with different magnet current settings. As shown in Table 8.5, different current values from 2000 A to 6730 A were used including positive and negative field polarities. Additionally, the data were taken with electron and positron beams as their positions and slopes were not identical, *i.e.*, electrons and positrons were affected different by the magnetic field.

Monte Carlo simulations were performed using the data set 3. In addition, the data set 3 was simulated with the magnet current set to zero. This allows to see how good the simulation can reproduce the data, how electrons and positrons are affected by the mag-

Adjustment 1	Left detector	Right detector	$R_{D/S}^{e^+}$	$R_{D/S}^{e^-}$	$R_{Asym}$
Shift along $X$ (mm)	+0.5	-0.5	1.065	1.046	1.018
Shift along $Y$ (mm)	-0.5	-0.5	$\pm 0.002$	$\pm 0.004$	$\pm 0.004$
Rotate about $Y$ (deg)	-0.5	+0.5			
Adjustment 2	Left detector	Right detector	$R_{D/S}^{e^+}$	$R_{D/S}^{e^-}$	$R_{Asym}$
Shift along $X$ (mm)	+0.5	-0.5	1.058	1.051	1.007
Shift along $Y$ (mm)	-0.7	-0.7	$\pm 0.005$	$\pm 0.002$	$\pm 0.005$
Rotate about $Y$ (deg)	-0.5	+0.5			
Adjustment 3	Left detector	Right detector	$R_{D/S}^{e^+}$	$R_{D/S}^{e^-}$	$R_{Asym}$
Shift along $Y$ (mm)	-1.0	-1.0	1.058	1.051	1.007
Rotate about $X$ (deg)	-0.5	-0.5	$\pm 0.005$	$\pm 0.002$	$\pm 0.004$

**Table 8.4:** Position and rotation adjustments applied to the SYMB detectors and their effect on the data to simulation ratio and asymmetry.

current (A)	
negative field	positive field
-6730	6730
-5900	5900
-5000	5000
-4000	4000
-3000	3000
-2000	2000

**Table 8.5:** List of magnet current settings used during magnetic field scans.

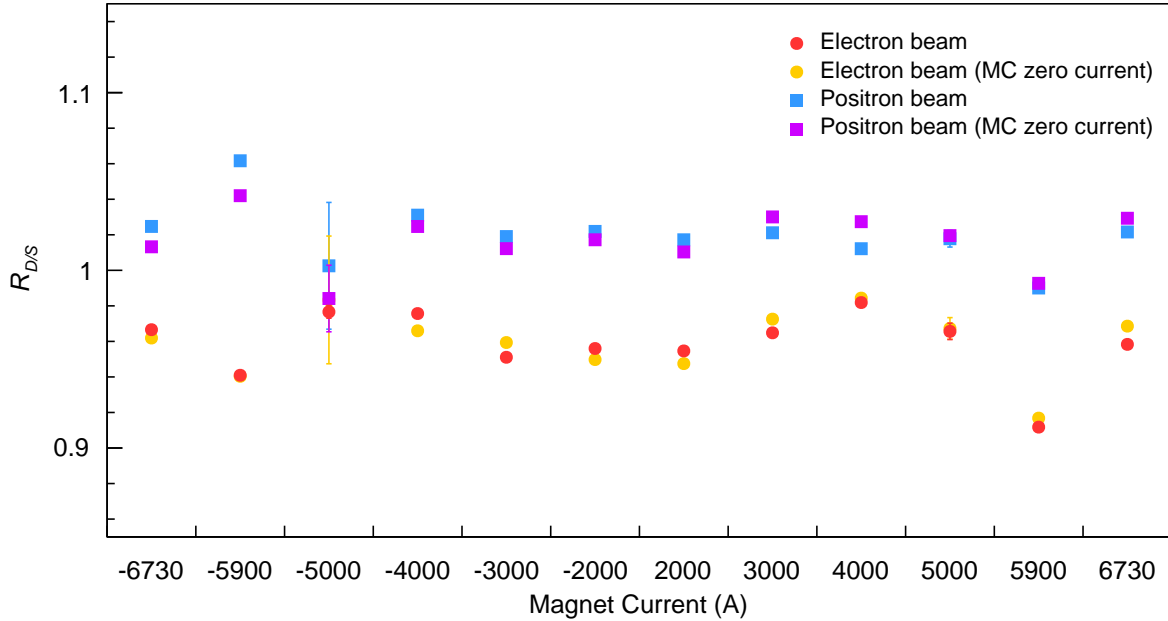


**Figure 8.28:** Data to simulation events ratio for electrons (red and orange circles) and positrons (blue and violet squares) determined at different magnet current settings and polarities.

netic field, and whether the data to simulation events ratio is influenced by the magnetic field. It should be noted that for all magnet current settings, except for  $I = \pm 5000$ , only few runs are available. Therefore, the data to simulation event ratio  $R_{D/S}$  was determined as an arithmetic average from a number of runs.

Results of the simulation is shown in Fig. 8.28. Small fluctuations of  $R_{D/S}$  can be observed for different magnetic fields. The electron-positron discrepancy fluctuates by few percent depending on the magnetic field, with few points demonstrating much bigger deviations. The ratio  $R_{D/S}$  significantly increases for positrons and decreases for electrons at  $I = -5900$ , while at  $I = 5900$  both beam species show smaller  $R_{D/S}$  than average. Another deviation is seen at  $I = -5000$  where the interspecies difference between electrons and positrons is at its minimum of 2%. At the same time, a the comparison between the nominal current simulations and zero current simulations shows, for the most data points, very small difference of about 0.7%. At the standard data taking current of 5000 A this difference is  $\sim 0.3\%$  for positrons,  $\sim 0.6\%$  for electrons, and 0.3% for asymmetry.

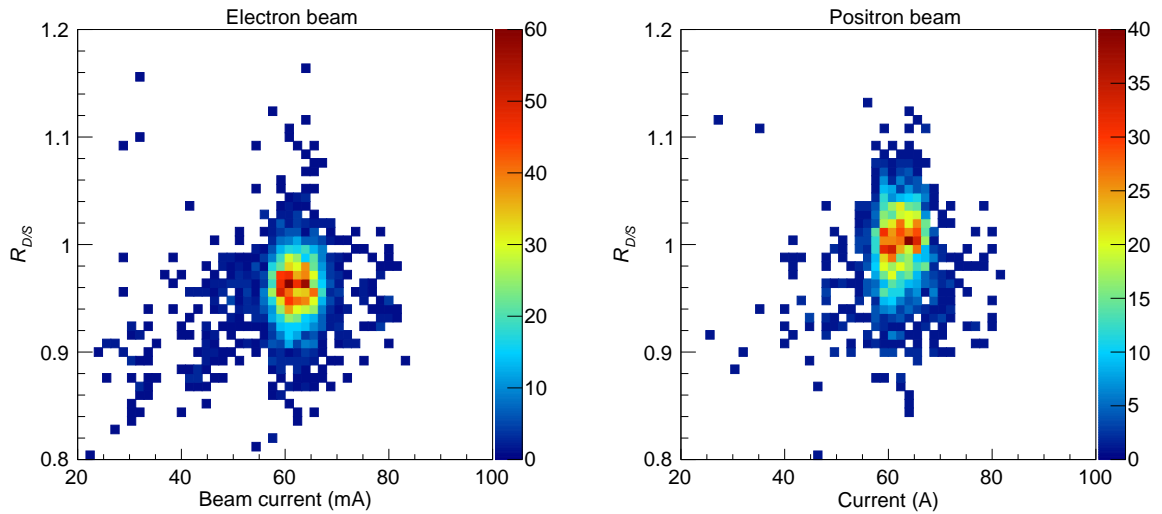


**Figure 8.29:** Dependence of  $R_{D/S}$  on the beam current calculated individually for each run.

### 8.3.5 Other Sources of the Discrepancy

#### Beam current

The influence of the beam current on  $R_{D/S}$  is shown in Fig. 8.29. As it was mentioned in Sec. 4.4, the beam current was kept mostly between 58 mA 65 mA during data taking for both beam species. The interspecies discrepancy is present through the full beam current. Although the difference between beam current during electron and positron runs could be an additional factor toward different count rates, the data show very stable beam current for both beam species.

#### Target Gas Flow

Similarly to the beam current, the gas flow during data taking could influence the results as it also affect count rates. Fig. 8.30 shows the  $R_{D/S}$  dependence on the gas flow. During the second run, the target was typically operated with a flow of 0.5-0.6 sccm depending on the beam quality. Electron data were collected mainly at three different gas flow settings: 0.50, 0.55, and 0.60 sccm, while most of positron data were collected at 0.50 and 0.60 sccm.

A subset of data where running conditions were stable was selected and divided into

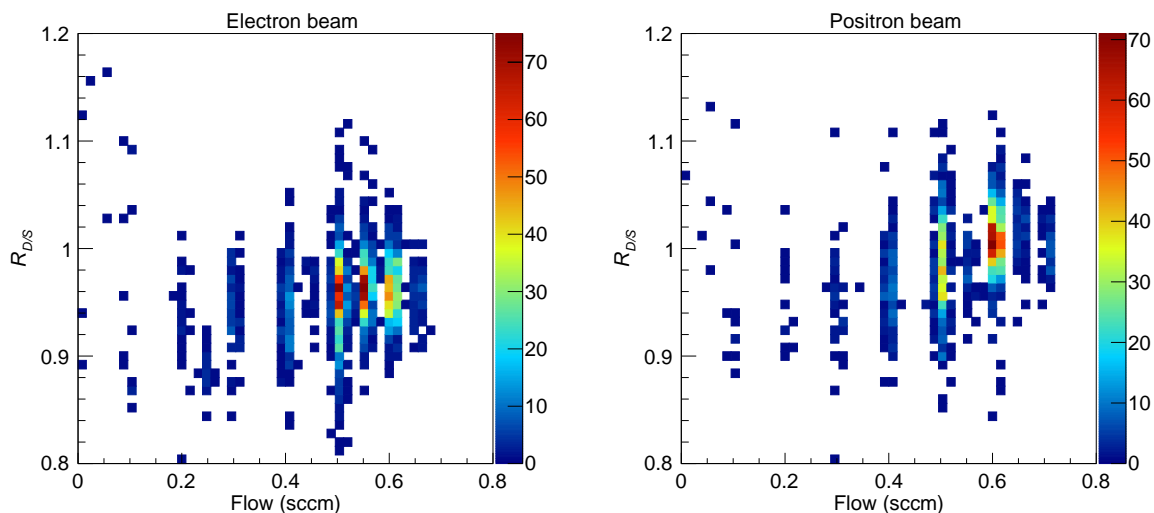


**Figure 8.30:** Dependence of  $R_{D/S}$  on the target gas flow determined for each run individually.

three samples depending on the gas flow. Fig. 8.31 shows that  $R_{D/S}$  is independent from the gas flow. This, in turn, is a sign that the SYMB detectors haven't been affected by different count rates.

## Event Generator

The event generator [105] which was used in this work has an uncertainty of about 1% in calculated cross sections. The source of the uncertainty are the dependence on the chosen model, this difference goes up to 1% between different theoretical models.

## Readout Electronics Effects

As it was briefly mentioned in Sec. 7.1.4, the SYMB readout electronics during the calibration with the test beam and during the data collection itself were different. This happened because the histogramming cards were not ready at the time of the calibration. This could mean that the electronics which was used in the experiment could have unknown effects or bugs which could affect the data acquisition.

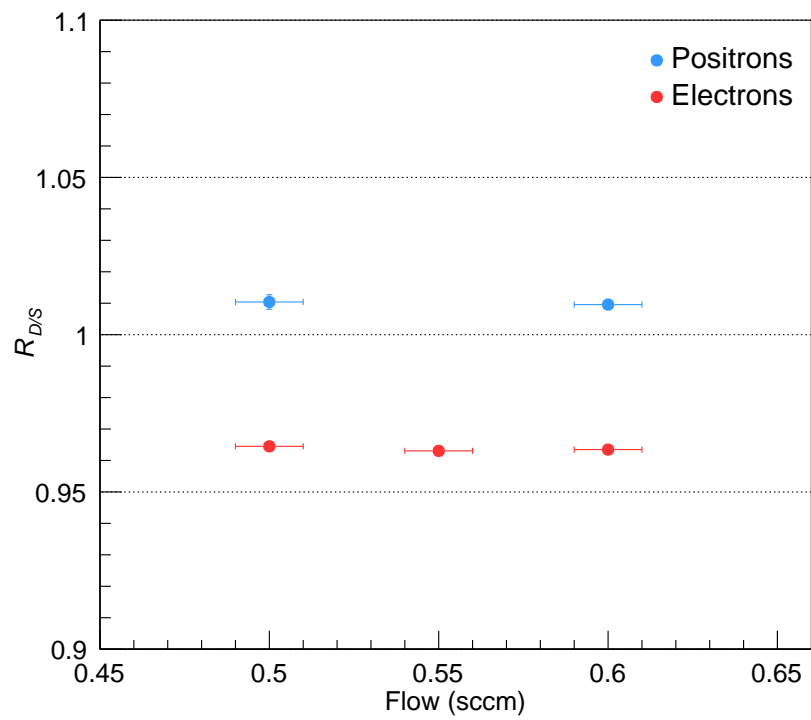


**Figure 8.31:** Dependence of  $R_{D/S}$  on the target gas flow determined from different data samples taken with three specific gas flow settings.

## Crystal Position

Although the survey of the magnetic shielding boxes and collimators were performed multiple times. The position of the crystals inside the boxes were not precisely measured. It was assumed that the central crystal in each box was aligned at the center of the collimators' aperture. Slight misalignments could affect signal collection efficiency.

## 8.4 Results from Different Time Periods

To have a better understanding of how the data to simulation changes with time the data was divided into 24 electron and 24 positron smaller sets. Each set contains data collected within one consecutive, approximately 24 hours long, period of time. Each set contains, in average, 70 runs. Figs. 8.32 and 8.33 show data to simulation ratio and asymmetry for each small set of data. The beam scan, marked by the green line, clearly divides the data in two parts. Before the beam scan,  $R_{D/S}$  is significantly smaller and shows bigger fluctuations from set to set. After the beam scan,  $R_{D/S}$  increases, especially for positron beams. In addition, one can see that electron and positron sets 10 show very similar data to simulation ratio due to the positron  $R_{D/S}$  being much smaller than that of the rest of postscan data. An analysis of slow control data pointed toward the vertical beam position. During the positron set 10, the vertical position and slope of the beam were different in comparison to the rest of postscan data. In fact, for unknown reason, it was set to the same value as before the scan, which is different from the postscan nominal position by approximately 0.2 mm.

As can be seen in Fig. 8.32, the positron prescan data to simulation ratio matches that of electron after scan data. Therefore, if the BPM had a beam charge dependent systematic uncertainty it could be the cause of the data to simulation discrepancy between electron and positron beams. Fig. 8.21d, shown in Sec. 8.3.2, supports this theory that there might be a difference between the vertical beam slope in the real experiment and the one in the simulation. The beam position monitors were calibrated after data taking and their precision was measured to be better than 0.1 mm.

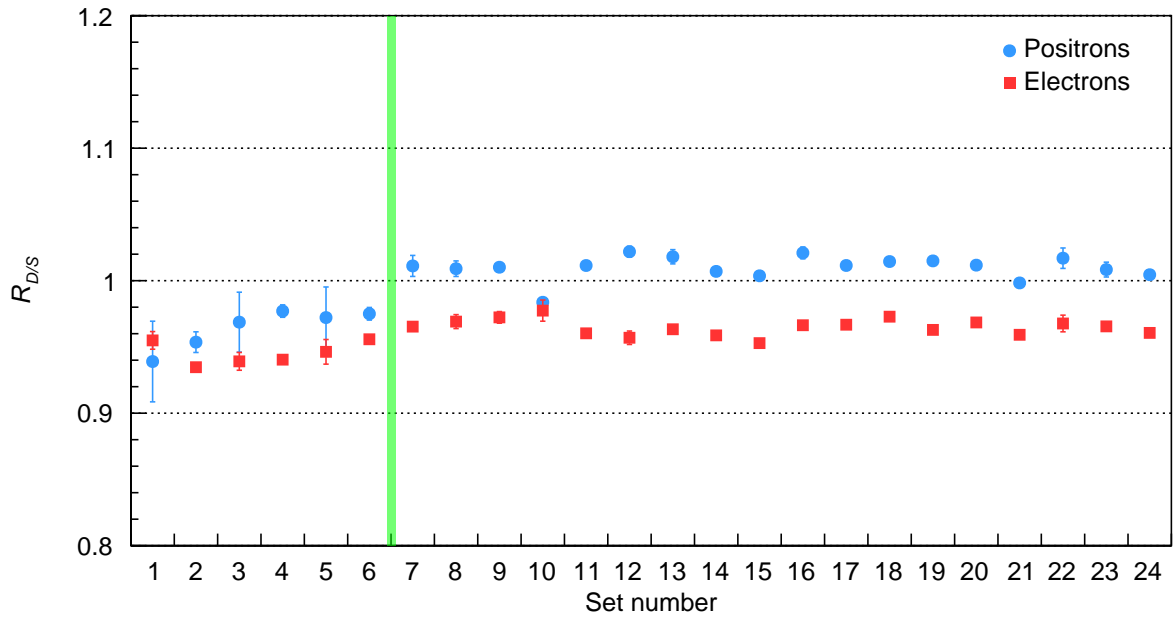


**Figure 8.32:** Data to simulation ratio dependence on a particular set of data collected within one consecutive period of time. Green line marks the beam scan.

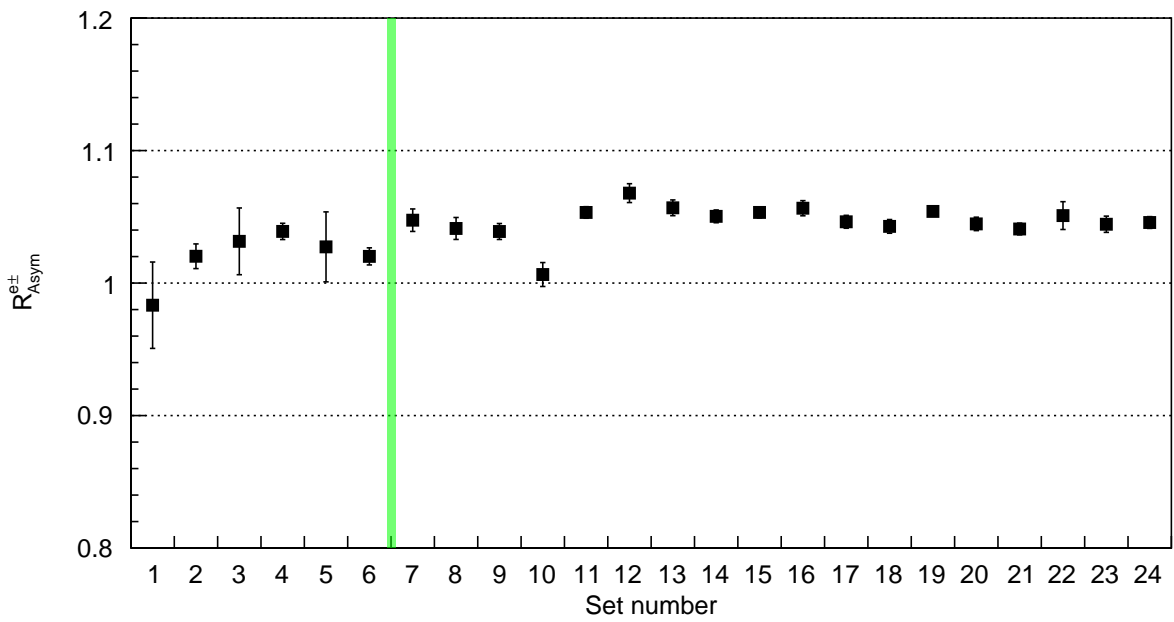


**Figure 8.33:** Asymmetry dependence on a particular set of data collected within one consecutive period of time. Green line marks the beam scan.

## 8.5 Conclusion

Unfortunately, due to an unknown systematic effect(s) it was impossible to determine the relative integrated luminosity as it was intended, *i.e.*, with elastic Møller/Bhabha scattering. As a result of this effect, the analysis shows a discrepancy between the electron and positron data. The observed Møller events are about 3.4% to 6.8% fewer in comparisons to what is expected based on the slow control luminosity while the Bhabha data have 3.4% fewer events in the first set and match that of the slow control in sets 2 and 3.

Table 8.6 summarizes investigated uncertainties and their total effect on the data to simulation count ratio for electron and positron data as well as interspecies asymmetry. Another unfortunate result is a very big uncertainty of the interspecies asymmetry. Assuming absence of the electron-positron discrepancy the asymmetry error of 4.4% renders the measurement as too inaccurate to determine whether the TPE effect is responsible for the difference between proton form factors extracted using Rosenbluth separation method and polarization technique.

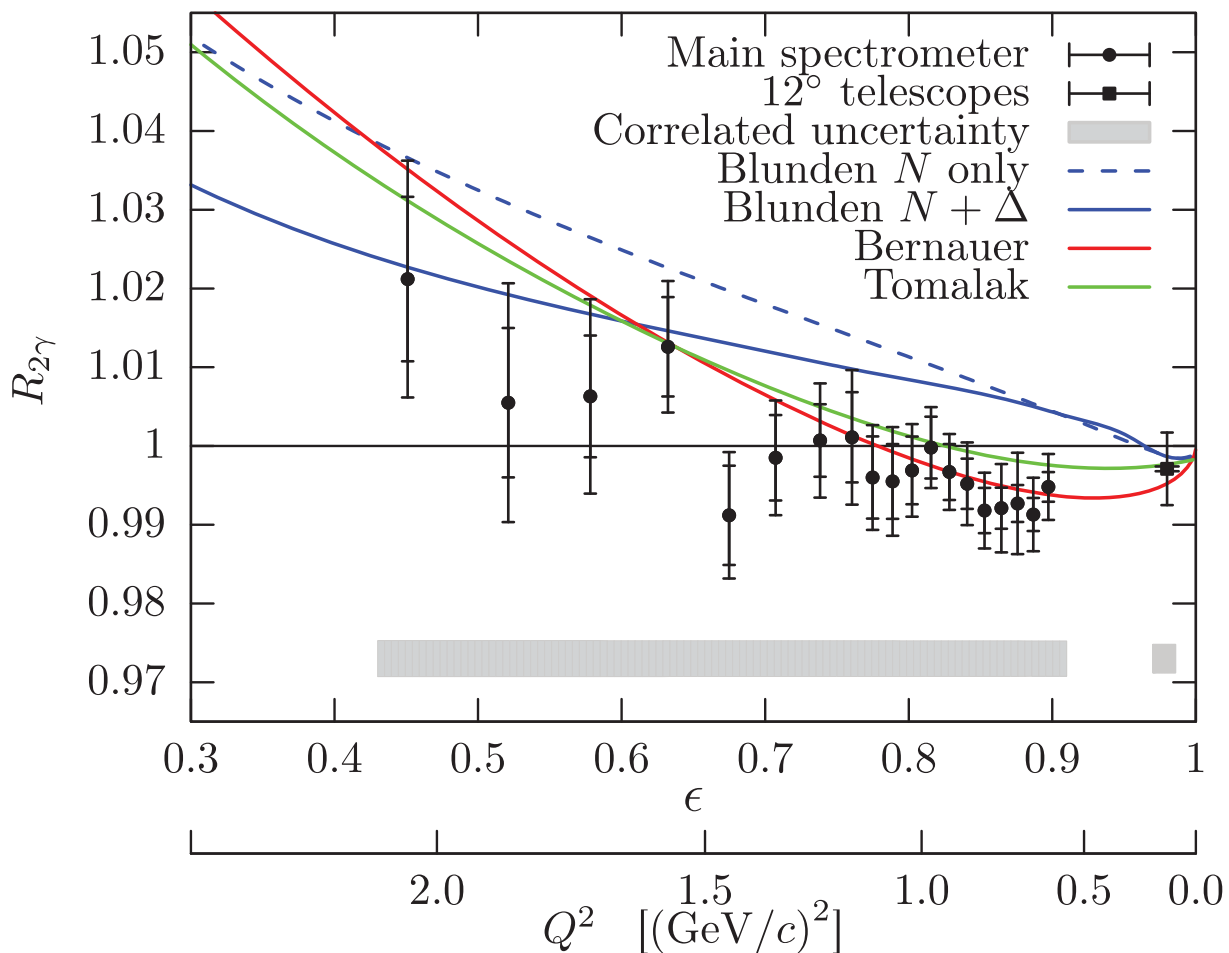
Another method of the luminosity determination, which was originally proposed as a cross check, was developed by a group of MIT students. This eventually made possible to use SYMB data and determine the relative integrated luminosity. The method uses multi-interaction events, where more than one lepton from the same bunch interacted with the target. More details can be found in the following theses [77, 108–110]. The combined result of these analyses [111] together with few theoretical calculations are shown in Fig. 8.34. As can be seen, the measured TPE contribution is very small at high  $\epsilon$  and only reaches 2% at  $\epsilon = 0.46$ . Thus, it seems that the proton form factor puzzle can not be explained by the two-photo exchange alone.

Fig. 8.35 shows a difference between the results from the OLYMPUS, CLAS [53], and VEPP-3 [54] experiments and newest calculations by Blunden ( $N + \Delta$ ). The theoretical values were calculated for each point individually taking experimental  $\epsilon$  and  $Q^2$  into account. All three experiments are consistent with each other and most data points lie below the theoretical prediction.

To quantify the size of the TPE effect at higher  $Q^2$  additional experiments are needed.

Effect	Effect uncertainty	$\frac{\Delta R_{D/S}^{e^+}}{R_{D/S}^{e^+}}$	$\frac{\Delta R_{D/S}^{e^-}}{R_{D/S}^{e^-}}$	$\frac{\Delta R_{e^+/e^-}}{R_{e^+/e^-}}$
Beam emittance	$\pm 20\%$	0.5%	0.5%	0.1%
Beam position monitors	0.2 mm along $X$	1.6%	3.5%	3.3%
	0.2 mm along $Y$	1.7%	0.5%	2.3%
Detector position	0.5 mm along $X$	2.0%	2.3%	1.0%
	0.5 mm along $Y$	1.7%	0.8%	1.0%
	0.5 mm along $Z$	0.1%	0.1%	0.1%
Detector rotation	$0.2^\circ$ about $X$	0.4%	0.2%	0.6%
	$0.2^\circ$ about $Y$	0.6%	0.7%	0.3%
	$0.2^\circ$ about $Z$	0.1%	0.1%	0.1%
Magnetic field	order of magnitude	0.5%	0.5%	0.3%
Event generator	model dependence	1.0%	1.0%	1.0%
Total		3.8%	4.5%	4.4%

**Table 8.6:** List of investigated systematic uncertainties which contributing to data to simulation ratios and electron to positron asymmetry.



**Figure 8.34:** OLYMPUS result for two-photon effect using the Mo-Tsai [112] prescription for radiative corrections to all orders. Uncertainties shown are statistical (inner bars), uncorrelated systematic (added in quadrature, outer bars), and correlated systematic (gray band). Note the  $12^\circ$  data point at  $\epsilon = 0.978$  is completely dominated by systematic uncertainties.

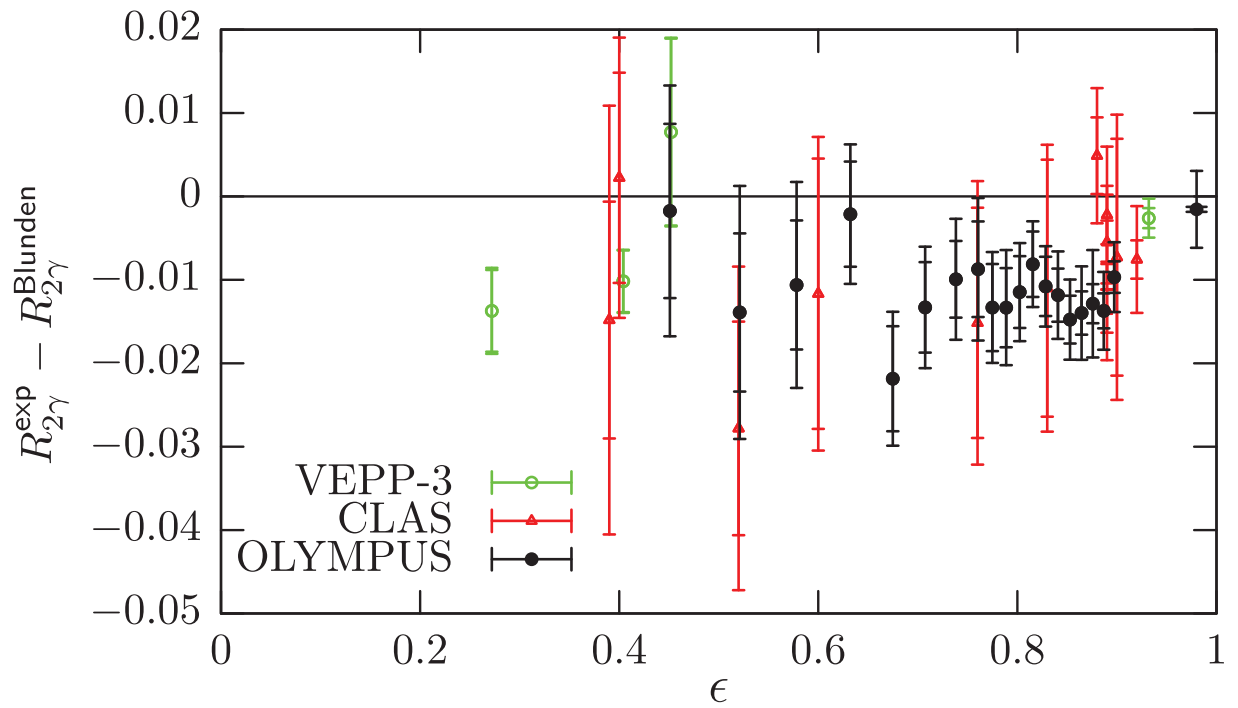


**Figure 8.35:** Comparison of the recent results to the calculation by Blunden. The data are in good agreement, but generally fall below the prediction. Please note that data at similar  $\epsilon$  values have been measured at different  $Q^2$ . Also note that the VEPP-3 data have been normalized to the calculation at high  $\epsilon$ .

## Part IV

# Form Factors at $\overline{\text{PANDA}}$

# Chapter 9

## Feasibility Study of $|G_E|$ and $|G_M|$ Extraction

### 9.1 Kinematics

The reaction of interest  $\bar{p}p \rightarrow e^+e^-$  has two-particles in the final state and can be generalized as:

$$\bar{p}(p_1)p(p_2) \rightarrow l^+(p_3)l^-(p_4), \quad (9.1)$$

where  $p_1$ ,  $p_2$ ,  $p_3$ , and  $p_4$  are the particle four-momenta. Let us consider this reaction in the lab. and c.m. frames.

In the lab. frame, shown in the Fig. 9.1a, the positive  $z$ -axis is aligned with the antiproton beam momentum and the target proton is at rest. The beam-target initial state kinematics can be fully defined by the antiproton beam momentum  $p_{beam}$ . Then, the antiproton beam and the proton target four-momenta can be written in the following form:

$$p_1 = (0, 0, p_{beam}, E_{beam}), \quad E_{beam} = \sqrt{m_p^2 + p_{beam}^2} \quad (9.2)$$

$$p_2 = (0, 0, 0, m_p), \quad (9.3)$$

where where  $m_p$  is the proton mass and  $E_{beam}$  is the antiproton beam energy. The invariant mass of the beam-target system, also the Lorentz invariant  $s$ , can be calculated knowing

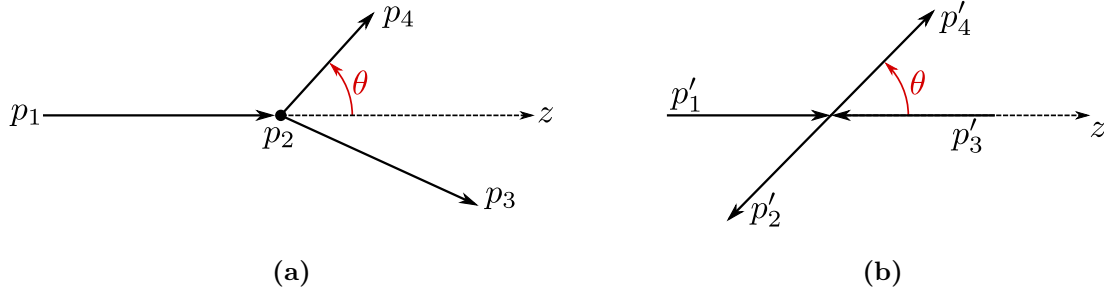


**Figure 9.1:** Two-particle final state kinematics in the lab. frame (a) and in the center-of-mass frame (b).

$p_1$  and  $p_2$ :

$$s = (p_1 + p_2)^2. \quad (9.4)$$

Considering the signal reaction  $\bar{p}p \rightarrow e^+e^-$ , in the one-photon exchange approximation, the four-momentum transfer carried by the virtual photon is equal to the Lorenz invariant:

$$q^2 = (p_1 + p_2)^2 = s. \quad (9.5)$$

In the c.m. frame the total momentum is zero, *i.e.*,  $p'_1 + p'_2 = 0$ . The four-momenta in the c.m. frame are defined as  $p'_1$ ,  $p'_2$ ,  $p'_3$ , and  $p'_4$ . Similar to the lab. frame, the beam four-momenta  $p'_1$  is defined as the positive direction of the  $z$ -axis. From the definition of the c.m. frame, both the antiproton beam and proton target collide with each other. The collision kinematics is illustrated in Fig. 9.1b.

Due to the equal final state lepton masses and conservation laws both leptons have the same energy and momentum:

$$p'_3 = -p'_4, \quad (9.6)$$

$$E'_3 = E'_4 = \frac{\sqrt{s}}{2}, \quad (9.7)$$

To complete the four-momenta of the outgoing leptons their polar  $\theta$  and azimuthal  $\phi$  angles have to be fixed in the c.m. frame. As in Eq. (3.9)  $\theta$  and  $\phi$  are the polar and azimuthal angles of the final state electron, respectively. The final state leptons are written in terms of  $\cos \theta(\cos \phi)$  and  $\sin \theta(\sin \phi)$ , where  $\theta$  and  $\phi$  can take any value in the interval  $[0, \pi]$  and  $[0, 2\pi]$ , respectively:

$$p'_3 = (p_{beam} \sin \theta \cos \phi, p_{beam} \sin \theta \sin \phi, p_{beam} \cos \theta, s/2), \quad (9.8)$$

$$p_3' = (-p_{beam} \sin \theta \cos \phi, -p_{beam} \sin \theta \sin \phi, -p_{beam} \cos \theta, s/2). \quad (9.9)$$

## 9.2 Signal Simulation

### 9.2.1 Signal Event Generator

An event generator for the signal process is developed and implemented into the EvtGen [113] package. EvtGen is part of the PandaRoot framework and it is used for primary particle generation.

The event generator requires a number of input parameters listed in Table 9.1. These parameters provide all necessary information to define the initial beam-target state, provide a FF model and constrain the kinematics of the final state particles. To simplify equations, in this chapter angle  $\theta$  is defined as an angle between the antiproton beam momenta and the final state electron in the  $\bar{p}p$  c.m. frame.

Parameter	Description
$p_{beam}$	Antiproton beam momenta
$\theta_{min}$	Minimum electron polar angle in the $\bar{p}p$ c.m. frame
$\theta_{max}$	Maximum electron polar angle in the $\bar{p}p$ c.m. frame
R	FF ratio
seed	Seed for the initialization of a random number generator

**Table 9.1:** Input parameters for the signal event generator.

As the event generation procedure does not require the exact cross section calculation, *i.e.*, only the shape of the distribution is important, Eq. (3.10) can be simplified in order to speed up the event generator operation. Discarding terms not included in the parenthesis, Eq. (3.10) can be rewritten as follows:

$$\frac{d\sigma}{d\cos\theta} = (1 + \cos^2\theta) + \frac{R^2}{\tau}(1 - \cos^2\theta), \quad (9.10)$$

Eq. (9.10) is used as probability density function  $f$  to generate correct angular distribution.

$$f(\cos\theta) = (1 + \cos^2\theta) + \frac{R^2}{\tau}(1 - \cos^2\theta), \quad (9.11)$$

Event generation is performed in a loop: 1) a random  $\cos\theta$  is generated between  $\cos\theta_{min}$  and  $\cos\theta_{max}$  with flat probability density and the corresponding value of  $f$  is calculated; 2) another random variable  $y$  is generated uniformly in the range  $[0,C]$ , where  $C$  is the upper bound of  $f$ ; 3) if  $y$  is larger than  $f$ , the event is rejected and the procedure goes back to step 1; otherwise 4) the event is accepted and  $\phi$  is generated uniformly in the range  $[0,2\pi]$  and 5) the four-momenta of the final electron-positron pair are calculated according to the kinematics described in Sec. 9.1. The sequence is repeated until the desired number of events is generated.

The four-momenta of accepted events and their particle types are passed to the PandaRoot framework which starts the propagation step described in Sec. 5.4.

### 9.2.2 Simulation Parameters

Angular distribution is generated according to the lepton differential cross section as in Eq. (3.9). Initial values of  $G_E$  and  $G_M$  are set using Eq. (3.12), assuming  $|G_E| = |G_M|$ . The expected number of events, given in Table 9.2, are generated within  $-0.8 < \cos\theta < 0.8$  range. This choice is motivated by the low detection efficiency at forward and backward angles. Fig. 9.2 shows the geometrical acceptance of the relevant  $\bar{P}$ ANDA sub-detectors as a function of  $q^2$ . A 100% detector efficiency and an integrated luminosity  $\mathcal{L} = 2 \text{ fb}^{-1}$  were assumed for each data point, which corresponds to four months of data taking. Angular distribution of generated electrons in the antiproton-proton c.m. system for different  $q^2$  is shown in Fig. 9.3. One can see that at higher energies the shape of the angular distribution is distorted due to the very low statistics, it is, therefore.

In addition to electron-positron pairs, final state radiation photons, are produced by PHOTOS [115] package. Photon emission does not induce any angular asymmetry, therefore the analysis does not require a correction of the reconstructed angular distribution. Fig. 9.4 illustrates electron-positron total energy distribution. As can be seen from Fig. 9.4, most produced photon have very low energies

The tail corresponds to events when a radiative photon is emitted.

$q^2$ (GeV/c) <sup>2</sup>	$p_{lab}$ (GeV/c)	signal		background	
		$\sigma_{int}$ (pb)	$N_{int}$	$\sigma_{int}$ (pb)	$N_{int}$
5.40	1.70	415	$830 \cdot 10^3$	$101 \times 10^6$	$202 \times 10^9$
7.27	2.78	55.6	$111 \cdot 10^3$	$13.1 \times 10^6$	$262 \times 10^8$
8.20	3.30	24.8	$496 \cdot 10^2$	$2.96 \times 10^6$	$592 \times 10^7$
11.12	4.90	3.25	6503	$0.56 \times 10^6$	$111 \times 10^7$
12.97	5.90	1.16	2328	$0.23 \times 10^6$	$455 \times 10^6$
13.90	6.40	0.73	1465	$0.15 \times 10^6$	$302 \times 10^6$

**Table 9.2:** Integrated cross section  $\sigma_{int}$  for the range  $|\cos\theta| \leq 0.8$  and number of counts  $N_{int}$  for  $\bar{p}p \rightarrow e^+e^-$ . The prediction was made according to the parameterization as in Ref. [114]. The corresponding values for the  $\bar{p}p \rightarrow \pi^+\pi^-$  channel are also listed. A 100% data taking efficiency and an integrated luminosity  $\mathcal{L} = 2 \text{ fb}^{-1}$  were assumed for each beam momentum value, which corresponds to four months of data taking.

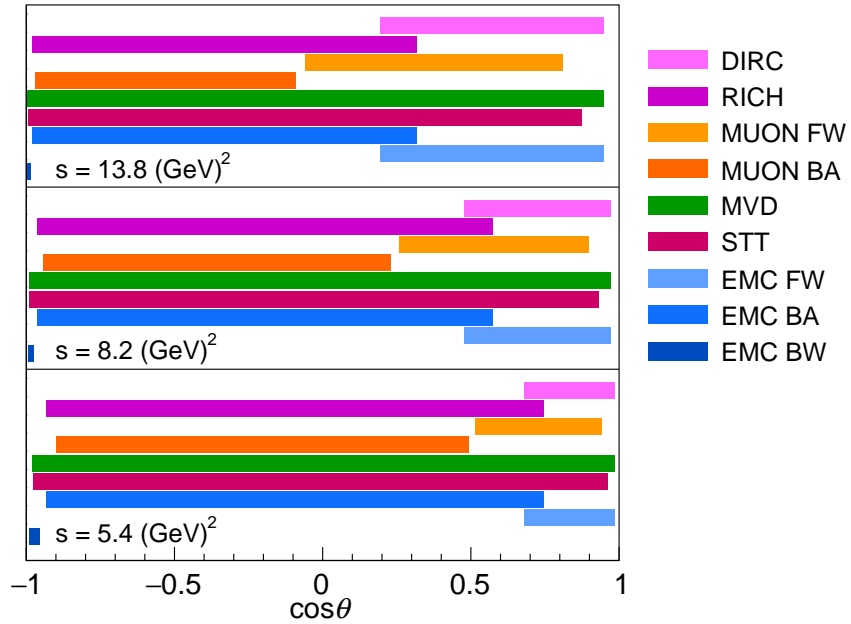


**Figure 9.2:** Geometrical acceptance of the relevant PANDA sub-detectors as a function of  $\cos\theta$ , where  $\theta$  is c.m. polar angle with respect to the beam momentum. The bars represent the angular coverage of a given sub-detector for different  $q^2$  values.

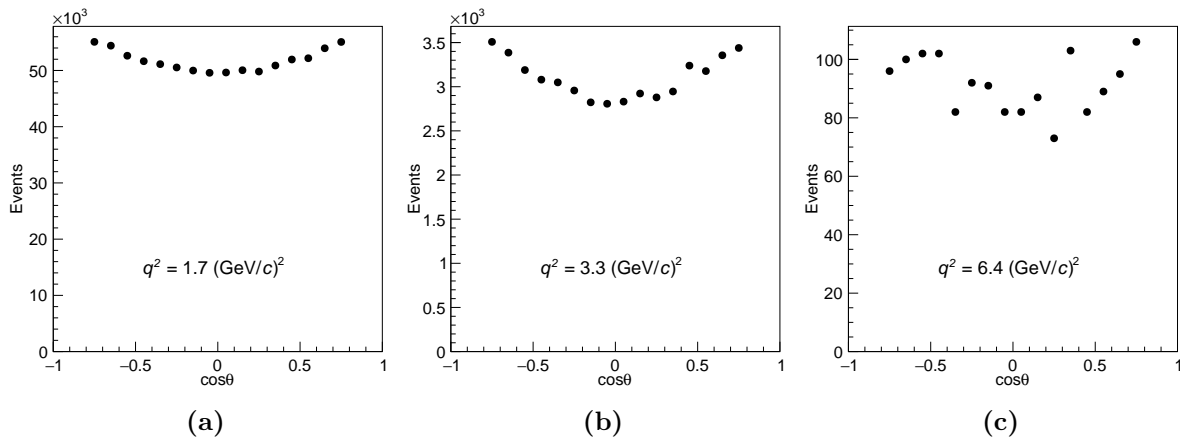


**Figure 9.3:** Angular distribution of generated electrons in the antiproton-proton c.m. system for different  $q^2$  values.

### 9.3 Background Study

Reactions with two or more hadrons in the final state constitute the most challenging background channels. Thanks to excellent tracking and PID capabilities of the  $\overline{\text{P}}\text{ANDA}$  detector, the suppression power of reactions with three or more hadrons in the final states is considered to be sufficient to achieve background free electron-positron signal.

Two-particle hadron final states as  $\bar{p}p \rightarrow \pi^0\pi^0$ ,  $\bar{p}p \rightarrow \pi^+\pi^-$ , and  $\bar{p}p \rightarrow K^+K^-$ , on the other hand, are harder to separate from the lepton signal. The production cross sections of neutral and charged pions are considered to be larger than that of the leptons by a factor of  $10^5 - 10^6$  [56, 116, 117] depending on the  $q^2$ . The double neutral pion production, where pions produce electron-positron pairs, will be suppressed using, among other cuts, kinematic constraints.

The charged hadron pair production can be easier misidentified as leptons. While kaons, due to their larger mass, can be more effectively rejected using kinematic constraints, the charged pions can yield detector response similar to that of the leptons. Therefore, double charged pion production is considered as the main background reaction.

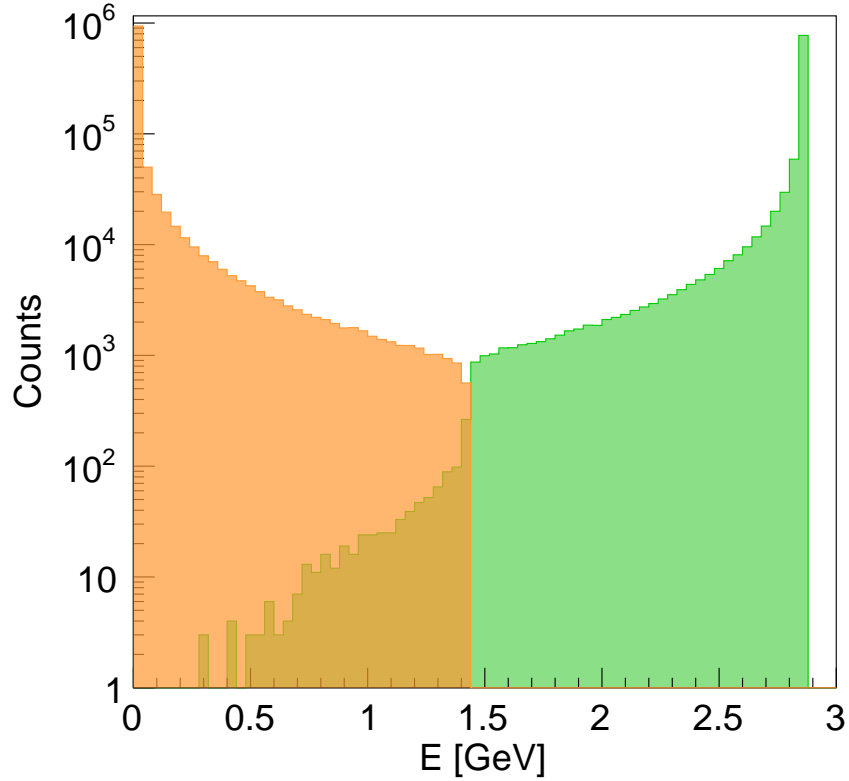


**Figure 9.4:** Total energy of electron-positron pairs (green) and emitted final state photons (orange).

### 9.3.1 Background Simulation

For a realistic background simulation an event generator based on Ref. [118] is employed. In the low energy region ( $q^2 < 6 \text{ (GeV}/c)^2$ ) the event generator uses the experimental data [116], while for the high energy domain ( $q^2 > 9 \text{ (GeV}/c)^2$ ) a combination of the experimental data [119–121] and theoretical calculations [117] is used. As there are neither data nor theory that would provide an information on  $\bar{p}p \rightarrow \pi^+\pi^-$  cross section in the intermediate energy region ( $6 < q^2 < 9 \text{ (GeV}/c)^2$ ), an interpolation between low and high energy regions is used.

The background was simulated at  $q^2 = 5.40, 8.20, \text{ and } 13.90 \text{ (GeV}/c)^2$  within  $-0.8 < \cos\theta < 0.8$  range. For each  $q^2$  a total of  $10^8$  events were generated. Therefore, if the suppression factor of  $10^8$  is achieved we ensure the background contamination of the

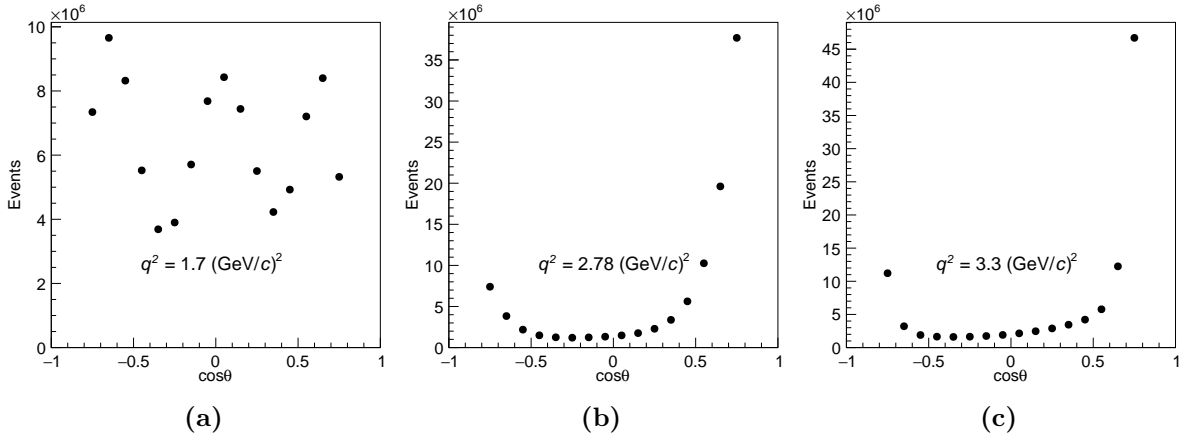


**Figure 9.5:** Angular distribution of generated negative pions at  $q^2 = 5.4$  (a),  $8.21$  (b), and  $13.8$   $(\text{GeV}/c)^2$  (c).

lepton signal on the level better than 1%.

Fig. 9.5 shows an angular distribution of generated negative pions at three different values of  $q^2$ . As one can see, the shape of the angular distribution strongly depends on the  $q^2$ . In the low energy region the cross section fluctuates with the scattering angle, while it's relatively smooth at intermediate and high energies with a maximum at forward and backward scattering angles. In all cases, due to the lack of data, it increases rapidly at extreme forward and backward angles.

## 9.4 Particle Identification

Particle identification (PID) is an essential part of the analysis. PandaRoot provides a number of tools which help to identify and distinguish between different particles based on the response of  $\bar{\text{P}}\text{ANDA}$  sub-detectors as well as particle identification algorithms. The later ones provide a probability of a particle being either an  $e$ ,  $\mu$ ,  $K$ ,  $\pi$ , or  $p$ .

### 9.4.1 Particle Identification Probabilities

In this work, the response of the EMC, DRC, DISC, STT, and MVD is used to calculate probabilities. For each track, a probability of it being a lepton (electron or positron) or

a charged pion is calculated. Probabilities given by each individual detector ( $\text{PID}_s$ ), as well as their combined probability ( $\text{PID}_c$ ), are used in the analysis. Figs. 9.6a and 9.6b show probability distributions for a particle to be an electron or a pion for the signal and background data set. One can see that for the signal sample most events, as expected, have a higher probability to be an electron rather than a pion. The opposite is true for the background sample, where the majority of events are identified as pions.

## 9.4.2 Detector Response

Additionally, a series of cuts are applied on the response of different  $\bar{\text{P}}\text{ANDA}$  sub-detectors.

The ratio of the energy deposited in the EMC to the reconstructed momentum ( $E_{\text{EMC}}/p_{\text{reco}}$ ) is proven to be one of the most effective lepton-pion separation method. Due to different interaction mechanisms of leptons and pions with matter the ratio allows effective separation of signal-background events. The signal and background  $E_{\text{EMC}}/p_{\text{reco}}$  distributions as a function of  $p_{\text{reco}}$  are shown in Figs. 9.8a and 9.8b. As can be seen, most signal events are distributed around  $E_{\text{EMC}}/p_{\text{reco}} = 1$  while the majority of background events lie below what allows an efficient signal-background separation. Narrow band visible in Fig. 9.8b corresponds to the Bethe-Bloch energy loss, while a broader areas around 1 GeV/ $c$  and 3.5 GeV/ $c$  are related to the photon production in the EMC.

In hadronic showers, most of the energy is typically contained in two to three crystals, while electromagnetic showers spread out over greater distances. The group of affected crystals is called a cluster. Typically, hadron showers have smaller lateral moment than electromagnetic showers as shown in Fig. 9.7a. Therefore, a cut on the EMC lateral moment (EMC LM) can be applied for the signal-background separation.

The center of a cluster is a crystal that has the highest energy among all other crystals. This energy (E1), shown in Fig. 9.7b, is also used for the PID.

Like the EMC, STT yields different signal depending on the type of the particle passing through its volume. Though electron and pion  $dE/dx_{\text{STT}}$  patterns are overlapped as can be seen in Figs. 9.8c and 9.8d the partial signal-background separation can still be performed.

As the ratio of the energy deposited in the EMC to the reconstructed momentum and

the energy deposited in the STT show the strongest dependence on  $q^2$  additional figures for  $q^2 = 5.4 \text{ (GeV}/c)^2$  and  $q^2 = 13.9 \text{ (GeV}/c)^2$  can be found in Appendix B.

### 9.4.3 Kinematic Cuts

Since all final state particles are detected, their total energy should be equal to that of the beam and target. Whereas these criteria does not contribute to the signal-background separation, it helps to remove events when one of the reconstructed particles was not a primary lepton. Figs. 9.9a and 9.9d illustrate the energy of a reconstructed pair of particles for the signal and background, respectively at  $q^2 = 8.2 \text{ (GeV}/c)^2$ .

Due to the two-body final state, the final particles have to be back-to-back in the c.m. frame, *i.e.*, a selection based on the sum of azimuthal angles ( $\theta + \theta'$ ) and the difference between polar angles ( $|\phi - \phi'|$ ), coplanarity criteria, can be performed. Figs. 9.9b and 9.9f show the sum of azimuthal angles and an absolute difference between polar angles of MC and reconstructed events at  $q^2 = 8.2 \text{ (GeV}/c)^2$ .

## 9.5 Extraction of Form Factors

### 9.5.1 Event Selection

The event selection is performed in two steps. First, events having exactly one positive and one negative reconstructed charged track are selected for further analysis. The number of reconstructed pairs of particles with an opposite charge are shown in Fig. 9.10. Note that only in 10% of the cases, the multiplicity is larger than one. If an event has *e.g.* one positive and two negative particles, it is considered to have a multiplicity of two, because the positive particle could be associated with either of the two negative particles.

Next, all events passing the selection scheme mentioned above are filtered through a set of additional criteria listed in Table 9.3. These criteria are chosen in order to maximize signal reconstruction efficiency while suppressing as many background events as possible. Some cuts are fixed for all values of beam momenta, whereas others are optimized to fit the response of the detector at each energy.

$q^2$	(GeV/c) <sup>2</sup>	5.4	7.3	8.2	11.1	12.9	13.9
PID <sub>c</sub>	(%)	>99	>99	>99	>99	>99	>99
PID <sub>s</sub>	(%)	>10	>10	>10	>10	>10	>10
$dE/dx_{STT}$	(a.u.)	>5.8	>5.8	>5.8	>5.8	>5.8	>6.5
$E_{EMC}/p_{reco}$	(GeV/(GeV/c))	>0.8	>0.8	>0.8	>0.8	>0.8	>0.8
EMC LM	-	<0.75	<0.75	<0.75	<0.75	-	-
EMC E1	(GeV)	>0.35	>0.35	>0.35	>0.35	>0.35	>0.35
$\theta + \theta'$	(degree)	175 < $\theta + \theta'$ < 185					
$ \phi - \phi' $	(degree)	175 < $ \phi - \phi' $ < 185					
$M_{inv}$	(GeV/c <sup>2</sup> )	-	-	>2.2	>2.2	>2.2	>2.7

**Table 9.3:** Criteria used to select the signal ( $e^+e^-$ ) and suppress the background ( $\pi^+\pi^-$ ) events for each  $q^2$  value.

Table 9.4 shows the reconstruction efficiency for the signal ( $e^+e^-$ ) selection and the background ( $\pi^+\pi^-$ ) suppression for each value of  $q^2 = 8.2$  (GeV/c)<sup>2</sup>.

$q^2$ (GeV/c) <sup>2</sup>	$e^+e^-$	$\pi^+\pi^-$
5.4	0.51	$6.8 \times 10^{-8}$
7.3	0.54	-
8.2	0.46	$2.0 \times 10^{-8}$
11.1	0.46	-
12.9	0.47	-
13.9	0.39	$2.9 \times 10^{-8}$

**Table 9.4:** Reconstruction efficiency for the criteria described in Sec. 9.5.1 for the signal and the suppression factor for the background for each value of  $q^2$ .

## 9.5.2 Determination of the Signal Efficiency

A significantly larger sample of  $e^+e^-$  pairs is simulated for each beam momentum. The signal efficiency is extracted from each sample and equals the ratio between the number

of reconstructed events passing the dedicated selection to the number of generated. The uncertainty of the efficiency was calculated in the following way:

$$\Delta\epsilon_i = \sqrt{\epsilon_i \frac{(1 - \epsilon_i)}{N_i^{reco}}}, \quad (9.12)$$

where  $\epsilon_i$  is the efficiency and  $N_i^{reco}$  is the number of reconstructed events in the  $i$ -th bin. The angular distribution of generated electrons, reconstructed and identified events, and the reconstruction efficiency at  $q^2 = 8.2 \text{ (GeV}/c)^2$  are presented in Fig. 9.11.

Thus, the angular distribution of reconstructed and identified electrons can be corrected using the reconstruction efficiency:

$$N_i^{corr} = \frac{N_i^{reco}}{\epsilon_i}, \quad (9.13)$$

where  $N_i^{corr}$  is the efficiency corrected number of events in the  $i$ -th bin.

### 9.5.3 Extraction of the Form Factor Ratio

To extract the FF ratio  $R$ , the reconstructed angular distributions first need to be corrected using the efficiency correction method described in Sec. 9.5.2. As a second step of this procedure, the corrected angular distribution is fit using the following equation:

$$\frac{d\sigma}{d\cos\theta} = \frac{\pi\alpha^2}{2\beta s} |G_M|^2 \left[ (1 + \cos^2\theta) + \frac{R^2}{\tau} \sin^2\theta \right], \quad (9.14)$$

where  $R$  is a free fit parameter. Equation (3.12) is used to calculate the value of  $|G_M|$  for each  $q^2$ . The reconstructed and acceptance corrected angular distribution for the electrons is shown together with the fitted curve in Fig. 9.12. For low  $q^2$ , where the cross section is higher, the fitted curve matches the shape of the angular distribution and the uncertainties are relatively small. At higher  $q^2$ , the reconstructed angular data points fluctuate and have larger statistical uncertainties. For  $q^2 = 13.9 \text{ (GeV}/c)^2$  the fit range is reduced to  $|\cos\theta| < 0.7$  because of the large uncertainties at  $\cos\theta = \pm 0.8$ . The reduced  $\chi^2$ , *i.e.*  $\chi^2/NDF$ , where  $NDF$  is the number of degrees of freedom, is close to unity for all  $q^2$ , except the largest one where  $\chi^2/NDF$  approaches 2.

### 9.5.4 Individual Extraction of $|G_E|$ and $|G_M|$

To extract  $|G_E|$  and  $|G_M|$  individually, the differential cross sections are calculated assuming an integrated luminosity of  $\mathcal{L} = 2 \text{ fb}^{-1}$ , and using:

$$\sigma_i = \frac{N_i^{corr}}{\mathcal{L}} \cdot \frac{1}{W_i}, \quad (9.15)$$

where  $W_i$  is the width of the  $i$ -th bin. The cross section uncertainty  $\Delta\sigma$  is calculated in the following way:

$$\Delta\sigma_i = \frac{1}{W_i} \frac{\Delta N_i^{corr}}{\mathcal{L}}. \quad (9.16)$$

Each differential cross section is fit using Eq. (3.9), which includes  $|G_E|$  and  $|G_M|$  as free parameters.

### 9.5.5 Results

After the fitting procedure, the ratio  $R$  and the individual values and the uncertainties of  $|G_E|$  and  $|G_M|$  are extracted from the fit. The extracted FF ratio is shown in Fig. 9.13 as a function of  $q^2$  together with results of other experiments. From this we conclude that the  $\overline{\text{PANDA}}$  experiment will be able to measure the FF ratio with a high statistical precision of around 1% at lower  $q^2$ . Furthermore,  $\overline{\text{PANDA}}$  will provide new measurements in the high  $q^2$  domain with a statistical precision of up to 50%.

The difference between the expected values and the extracted values of  $|G_E|$  and  $|G_M|$  are shown in Fig. 9.14 along with their statistical uncertainties.  $|G_M|$  can be measured with uncertainties within the range of 2% – 9%, whereas  $|G_E|$  has uncertainties of about 3%-45%. The difference in precision between  $|G_E|$  and  $|G_M|$  is due to the factor  $\tau$  in the fit function. Table 9.5 shows the expected values and uncertainties of the extracted  $|G_E|$ ,  $|G_M|$ , and  $R$ .

## 9.6 Systematic Uncertainties

Since a full systematic study requires both experimental data and MC, we are limited in our ability to estimate every possible source. Therefore, in the following we will discuss some of the sources of systematic uncertainties which can be tested with MC only. A

$q^2$ (GeV/c) <sup>2</sup>	$R \pm \Delta R$	$ G_E  \pm \Delta G_E $	$ G_M  \pm \Delta G_M $
5.40	1.0065±0.0129	0.1216±0.0010	0.1208±0.0004
7.27	1.0679±0.0315	0.0620±0.0013	0.0580±0.0004
8.21	0.9958±0.0523	0.0435±0.0017	0.0437±0.0005
11.12	0.9617±0.1761	0.0189±0.0029	0.0197±0.0006
12.97	1.1983±0.3443	0.0148±0.0033	0.0123±0.0007
13.90	1.0209±0.5764	0.0108±0.0051	0.0106±0.0010

**Table 9.5:** Expected values and uncertainties of the extracted  $R$ ,  $|G_E|$ , and  $|G_M|$ .

more precise estimation of systematic uncertainties will not be feasible until the design and construction of the detector is completed.

### 9.6.1 Luminosity Measurement

The  $\bar{P}$ ANDA experiment will use  $\bar{p}p$  elastic scattering for the luminosity measurement. Based on Ref. [90] the systematic uncertainty on the luminosity measurement might vary from 2% to 5%, depending on the beam energy, the  $\bar{p}p$  elastic scattering parameterization, and  $\bar{p}p$  inelastic background contamination. We considered the relative systematic luminosity uncertainty  $\Delta\mathcal{L}/\mathcal{L}$  to be 4.0% for all beam momenta. Table 9.6 shows the impact of the luminosity uncertainty on the precise extraction of  $|G_E|$  and  $|G_M|$ .

### 9.6.2 Detector Alignment

Thanks to the almost  $4\pi$  acceptance of the  $\bar{P}$ ANDA detector, misalignments of its different components will not affect the determination of proton FFs. Known displacements will be corrected for during the reconstruction of the raw data. The effect of small displacements up to a few hundred micrometers will give rise to spatial uncertainties that are much smaller than the foreseen uncertainties from the tracking resolution.

### 9.6.3 Pion Background

Using the achieved background rejection factor listed in Table 9.4, we can estimate the effect of misidentification of background events contaminating the signal. The analysis in Sec. 9.5 was repeated with signal and background events mixed together. The number of added background events was calculated in accordance with the achieved background suppression:

$$N_i^{Bg} = N_i^{MC} \times N_f \times S_f, \quad (9.17)$$

where  $N_i^{MC}$  is the number of generated background events in the  $i$ -th bin with a total number of events being equal to  $\sim 10^8$ ,  $N_f$  is the normalization factor which is necessary to get the number of expected events as in Table 9.2, and  $S_f$  is the background suppression factor as in Table 9.4. Reconstructed and efficiency-corrected angular distributions of generated electrons and electrons mixed with pions is shown in Fig. 9.15.

In addition, the cross section of the background channel  $\bar{p}p \rightarrow \pi^+\pi^-$  will be measured at  $\bar{\text{P}}\text{ANDA}$  with a very high precision due to its large cross section. Therefore, systematic uncertainties due to the model of the background differential cross section used in simulations are expected to be negligible. The impact of the background on the FFs precision is shown in Table 9.6.

### 9.6.4 Two-photon Exchange Contribution

The present analysis assumes even  $\cos\theta$  angular distribution if the final state leptons. The two-photon exchange contribution affects the symmetry if the angular distribution. The work presented in Ref. [122] shows that in case of a charge symmetric detection of electrons and positrons, the interference term between the one- and two-photon-exchange channels will not contribute to the differential cross section. Since the  $\bar{\text{P}}\text{ANDA}$  experiment will be able to detect both electrons and positrons (exclusive processes) and the contribution of TPE is symmetric between them, the TPE contribution can be eliminated by adding electron and positron angular distributions.

	$q^2$ (GeV/c) <sup>2</sup>	Statistical	Systematic		
			Pion	Lumi	Total
$\Delta G_E / G_E $	5.40	0.9%	0.3%	2.0%	2.2%
	8.21	4.1%	2.9%	2.0%	5.4%
	13.9	48%	3.1%	2.0%	48%
$\Delta G_M / G_M $	5.40	0.4%	2.8%	2.0%	3.5%
	8.21	1.2%	1.1%	2.0%	2.6%
	13.9	9.4%	1.0%	2.0%	9.7%
$\Delta R/R$	5.40	1.3%	2.9%	n/a	3.3%
	8.21	5.3%	4.0%	n/a	6.6%
	13.9	56%	4.1%	n/a	57%

**Table 9.6:** Effect of systematic and statistical uncertainties, as well as their total contribution, on the precision of  $|G_E|$ ,  $|G_M|$ , and R.

### 9.6.5 Contribution to Form Factors

The contributions of the luminosity and background to the precision of extracted values of FFs are reported in Table 9.6 together with the statistical contribution. The background contamination is on the level of a few percent for all values of  $q^2$ . The luminosity uncertainty affects only  $|G_E|$  and  $|G_M|$ , since the luminosity measurement is not needed for R determination. At lower  $q^2$  values, where the number of signal events is relatively large, the total uncertainty is dominated by the background contamination and luminosity contributions. In the intermediate energy domain, the statistics decreases and affects the total uncertainty on the same level as systematic uncertainties. At higher  $q^2$ , the main contribution to the total uncertainty is given by the statistical uncertainty due to the small signal cross section.

## 9.7 Comparison to Other Feasibility Studies

In parallel to this, two different analyses have been performed by my colleagues - Alaa Dbeyssi [26] and Iris Zimmermann [123].

The first analysis used the same signal  $\bar{p}p \rightarrow e^+e^-$  reaction to determine the proton form factor ratio  $R$ . The main difference in comparison to this work is the way the signal was generated. For each  $q^2$  approximately  $10^6$  electron–positron pairs were generated using flat distribution in the  $\bar{p}p$  c.m. frame and rescaled according to expected statistics for given  $q^2$ . This procedure effectively suppressed statistical fluctuations of the angular distribution of  $e^+e^-$  pairs at high  $q^2$ . Additionally, the  $R$  extraction was performed using an alternative fitting method. Instead of fitting electron  $\cos\theta$  distribution in the  $\bar{p}p$  c.m. frame, the  $\cos^2\theta$  distribution was fitted using a linear function.

Fig. 9.16 shows result of this work and the analysis of A. Dbeyssi where the most probable values of  $\Delta R$  were determined. The precision of the extracted form factor ratio is similar at lower and intermediate energies for the both analyses. At the highest  $q^2$  this work has a larger error due to the more realistic event generation procedure.

In contrast to this work, the analysis performed by I. Zimmermann employed an alternative signal reaction  $\bar{p}p \rightarrow \mu^+\mu^-$ . Similar to this work, the primary muon pairs were generated following expected angular distribution and statistics. Due to the much higher mass the muon signal in the EMC is very similar to that of the pion signal. What made this channel more challenging in the sense of the background rejection. The form factor ratio as well as individual  $|G_E|$  and  $|G_M|$  were extracted similarly to this work from the  $\mu^- \cos\theta$  event distribution in the  $\bar{p}p$  c.m. frame and differential cross, respectively.

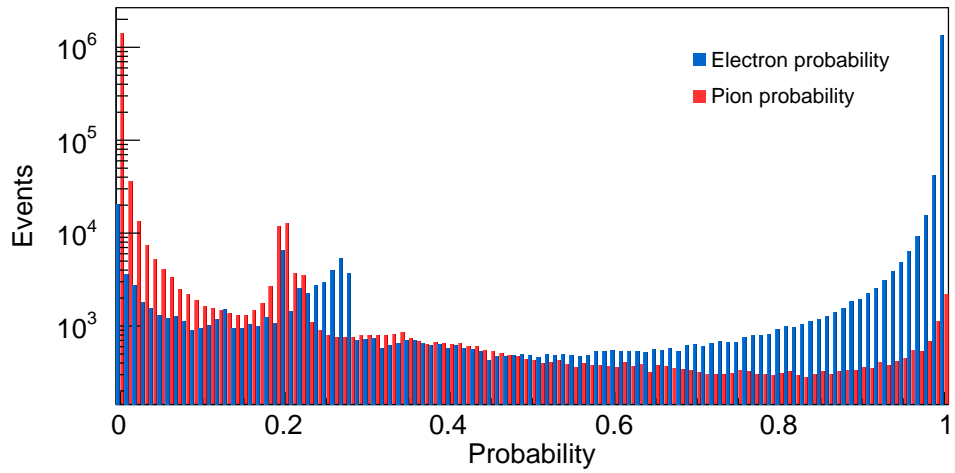
Fig. 9.17 shows result of this work and the analysis of I. Zimmermann. The precision of the muon and electron analyses are similar at the very low  $q^2$  while at the intermediate energies the former one has significantly bigger uncertainties due to the high background pollution. Although the precision of muon analysis is not as high as that of the electron one, the alternative independent measurement will be useful as a cross check for the electron–positron reaction.

## 9.8 Competitiveness of the $\bar{P}$ ANDA Experiment

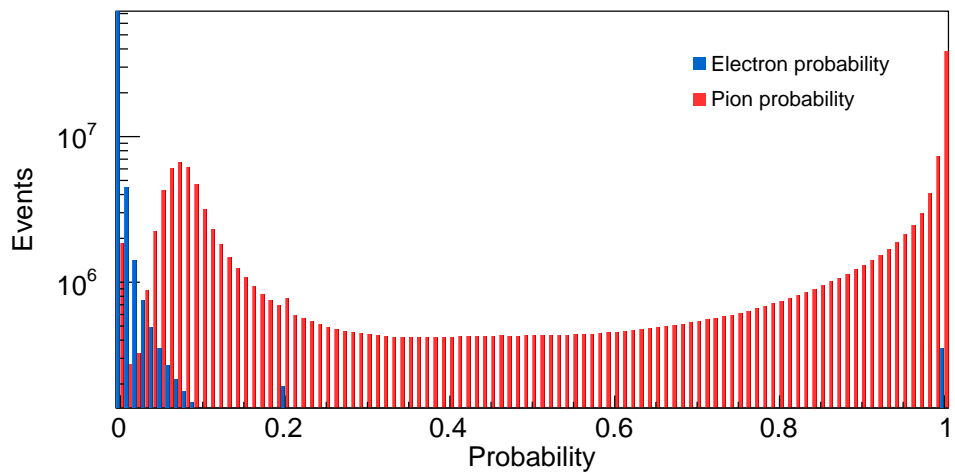
The moduli of the individual FFs,  $|G_E|$  and  $|G_M|$ , will be measured for the first time at BESIII using the data collected at 20 different  $q^2$  values between 4.0 and 9.5  $(\text{GeV}/c)^2$  [124]. A statistical precision on the FF ratio between 9% and 35% is expected.

Based on these numbers, it is clear that  $\overline{\text{PANDA}}$  will extend these measurements up to about  $q^2 = 14 \text{ (GeV}/c)^2$ , with a precision better than that expected at BESIII or comparable in the case of the reduced luminosity mode.

The modulus of the proton FFs ratio can also be measured at Belle [125], using the initial state radiation (ISR) technique, with a comparable accuracy to the BABAR data. The Belle detector was operating on the KEKB  $e^+e^-$  collider [126]. An integrated luminosity of about  $1040 \text{ fb}^{-1}$  was collected at KEKB between 1999 and 2010. Most of the data were taken at the  $\Upsilon(4S)$  resonance. The upgraded facility of the KEKB collider (SuperKEKB) aims to accumulate  $50 \text{ ab}^{-1}$  by about 2025 [127]. The Belle II experiment may provide the most accurate data on the proton FF ratio. So far, no estimation has been presented by the collaboration for the FF measurement at Belle and Belle II. One disadvantage of the ISR technique is that it only allows extraction of FFs in wide bins of  $q^2$ . This is in contrast to the formation reaction that  $\overline{\text{PANDA}}$  will use, where the precision of  $q^2$  is given, in general, by the very precise beam momentum resolution.



(a)



(b)

**Figure 9.6:** Probability distribution for the signal (a) and background (b) data sets.

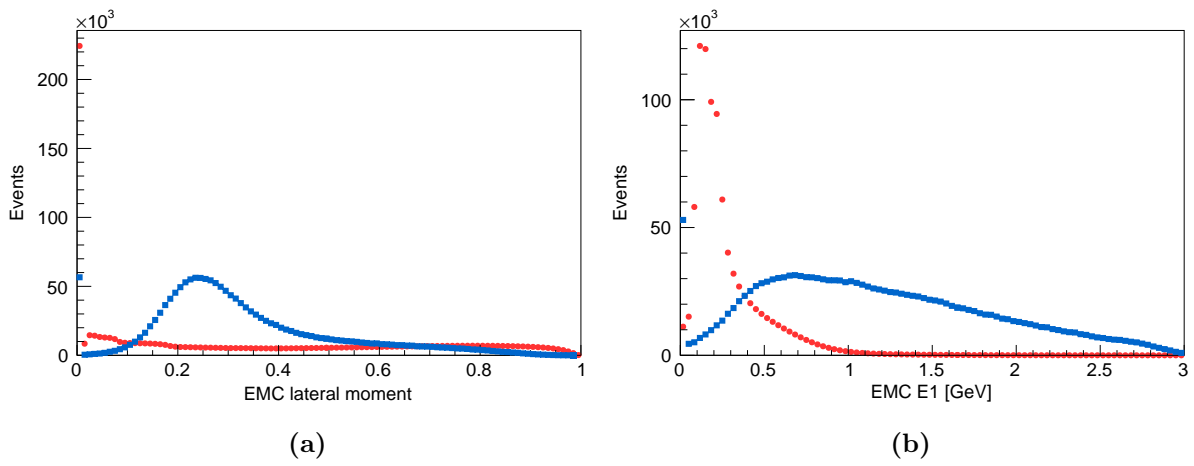


**Figure 9.7:** EMC lateral moment (a) and EMC E1 (b) for the signal (blue squares) and background (red circles) data sets at  $q^2 = 8.2 \text{ (GeV}/c)^2$ .

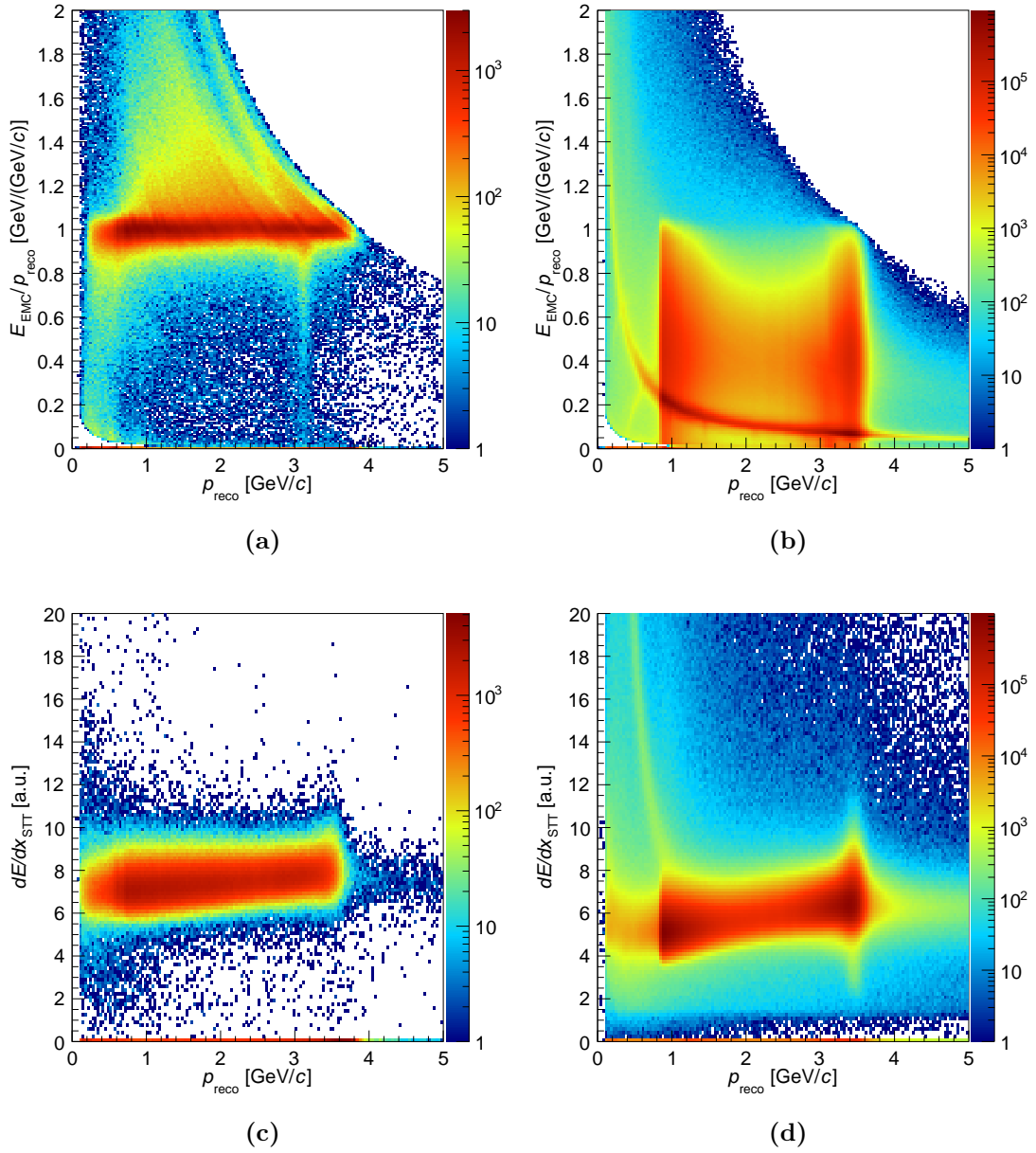


**Figure 9.8:** Detector response to the signal (left column) and the background (right column): (a, b) is the energy deposited in the EMC over the reconstructed momentum as a function of the reconstructed momentum; (c, d) is the energy loss per unit of length in the STT as a function of the reconstructed momentum at  $q^2 = 8.2 \text{ (GeV/c)}^2$ .

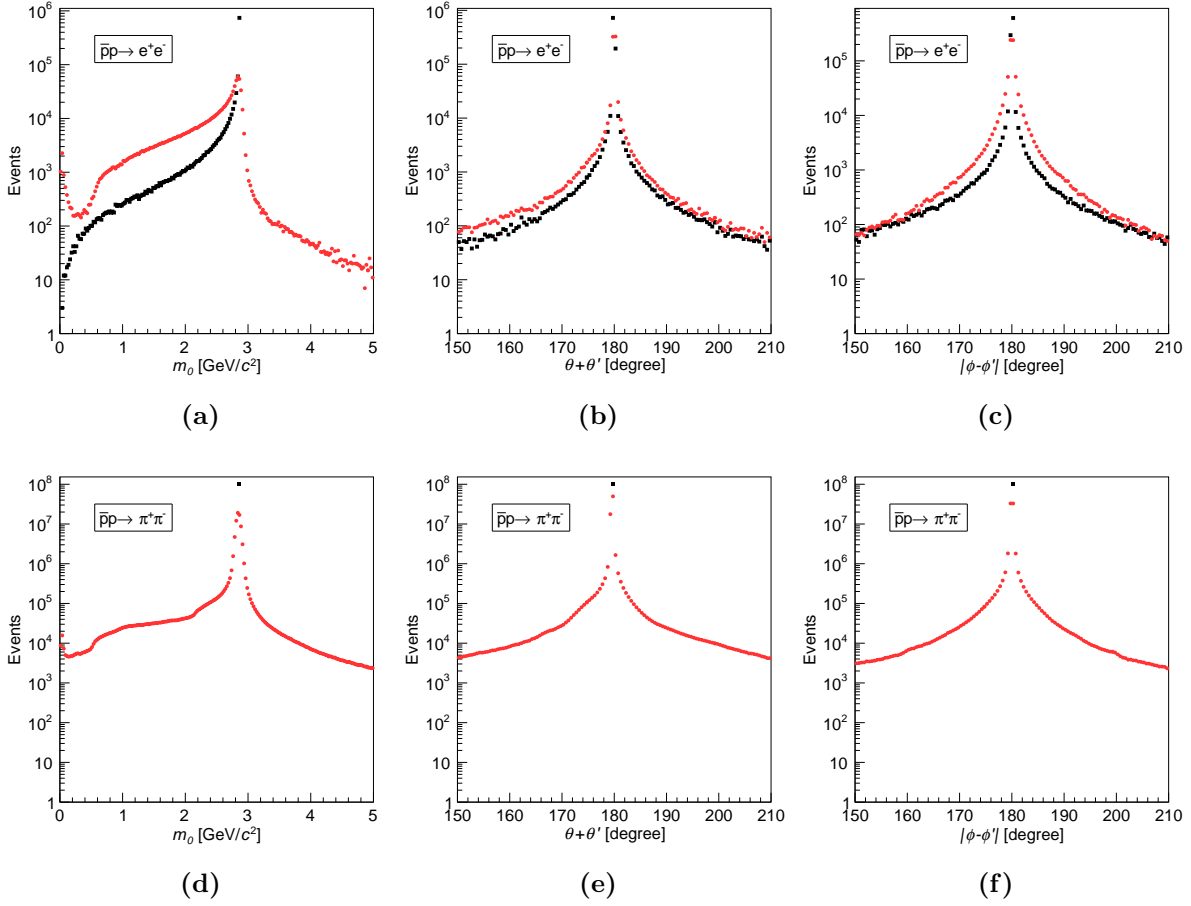


**Figure 9.9:** Spectra of generated (black) and reconstructed (red) events for different kinematic variables for the signal (top row) and the background (bottom row) at  $q^2 = 8.2 \text{ (GeV}/c)^2$ : (a, d) the sum of the polar angles in the c.m. frame; (b, e) the difference in the azimuthal angles in the c.m. frame; (c, f) the invariant mass of the reconstructed particles.

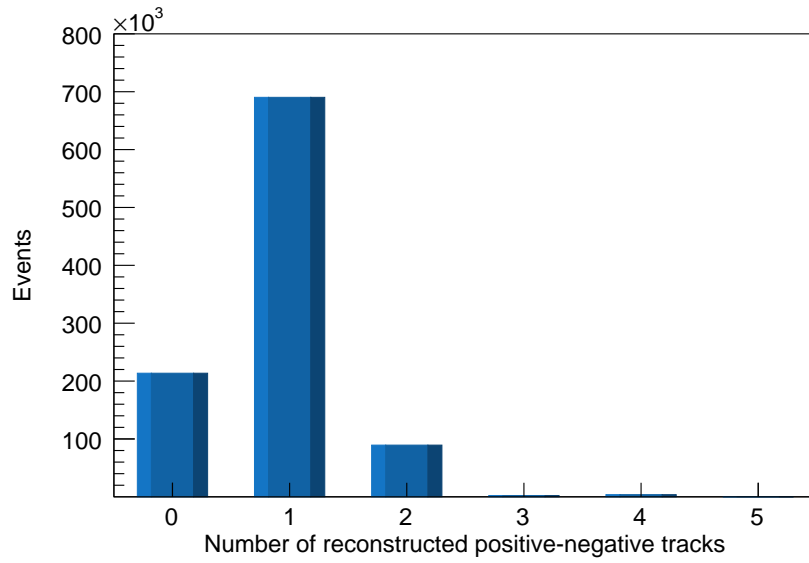


**Figure 9.10:** Multiplicity distribution or the number of reconstructed pairs of particles for the signal channel at  $q^2 = 8.2 \text{ (GeV}/c)^2$ .

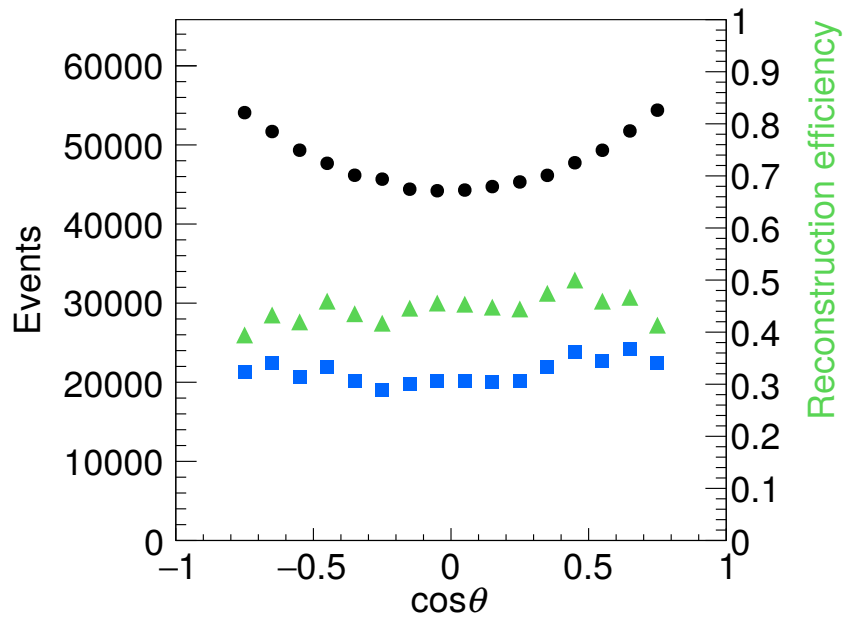


**Figure 9.11:** Angular distribution for  $\bar{p}p \rightarrow e^+e^-$  at  $q^2 = 8.2 \text{ (GeV}/c)^2$  of generated (black circles) and reconstructed and identified (blue squares) electrons. The reconstruction efficiency (green triangles) corresponds to the  $y$ -axis scale on the right.

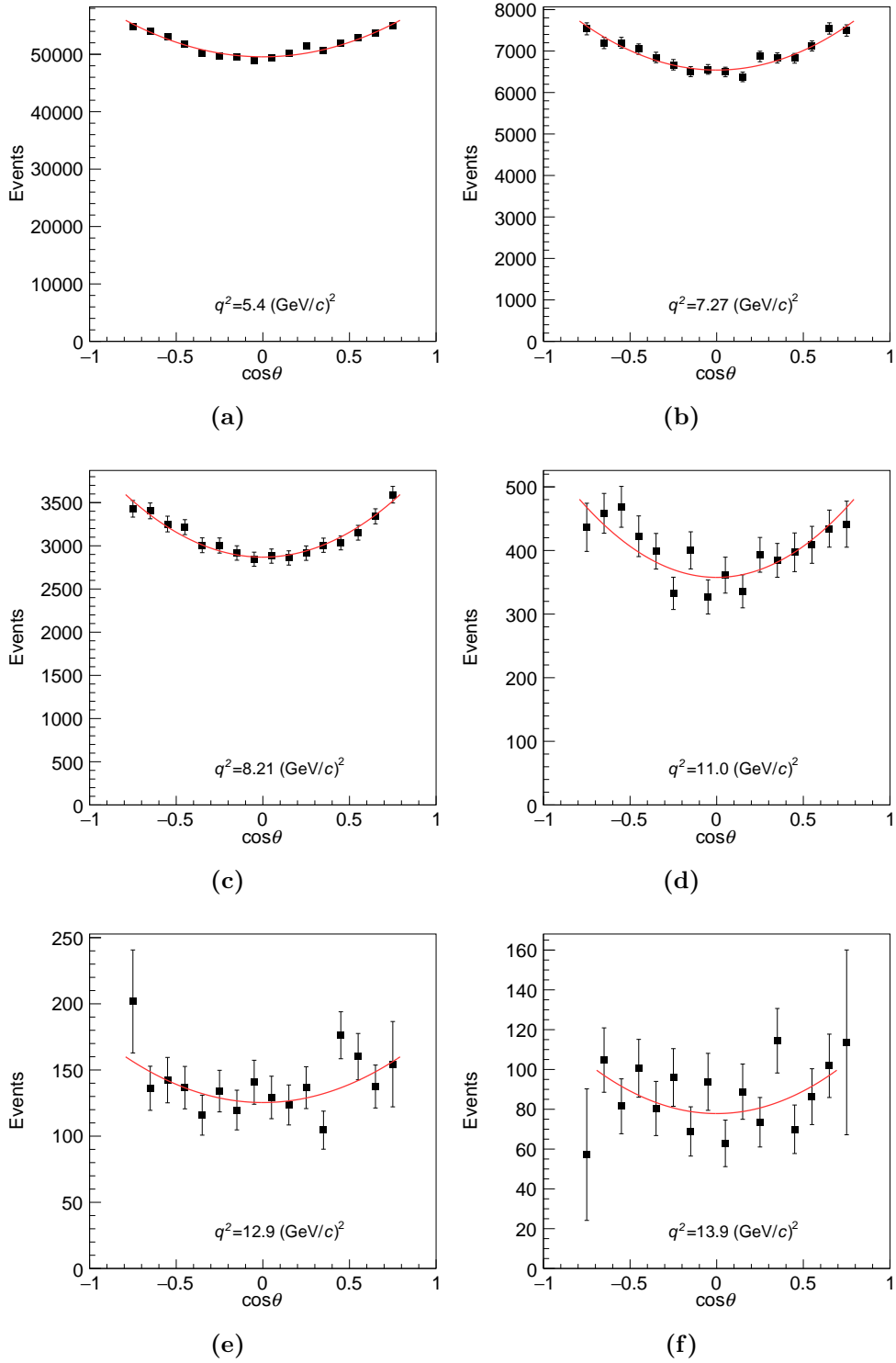


**Figure 9.12:** Reconstructed and efficiency-corrected angular distributions of generated electrons (black squares) and the fit (red line) for different  $q^2$  values: (a) 5.4, (b) 7.3, (c) 8.2, (d) 11.1, (e) 12.9, and (f) 13.9  $(\text{GeV}/c)^2$ .

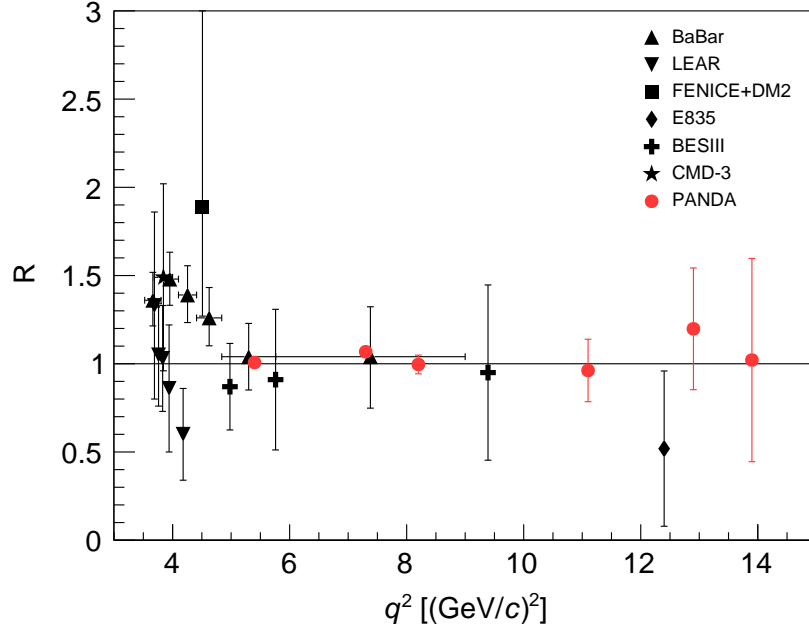


**Figure 9.13:** Form factor ratio as a function of  $q^2$ . The red circles show results of this work. The black symbols show the data from Refs. [12–16].

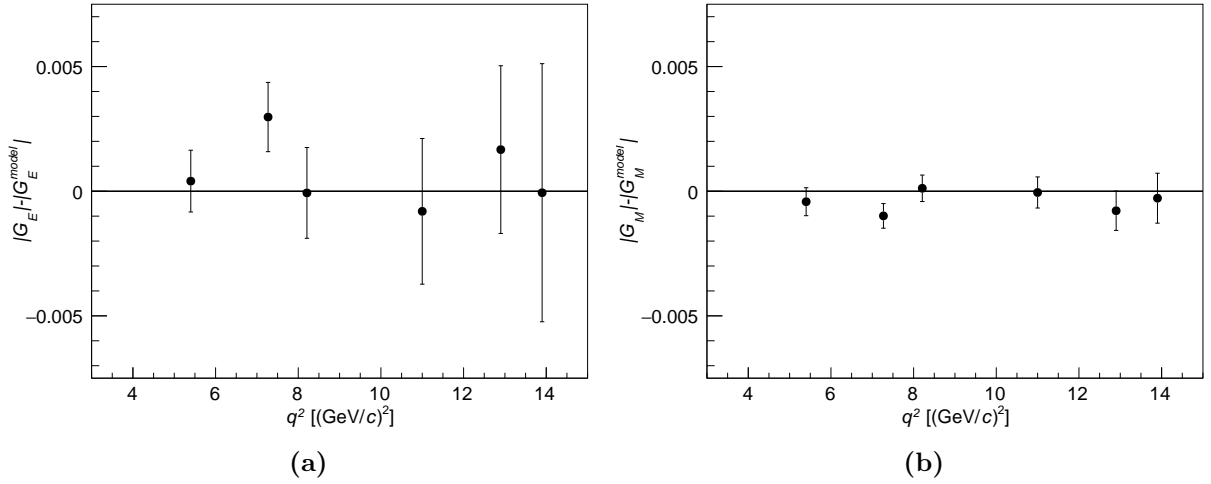
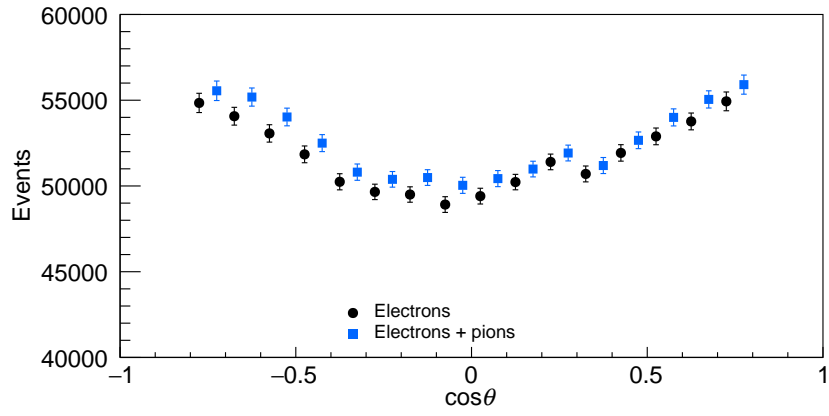
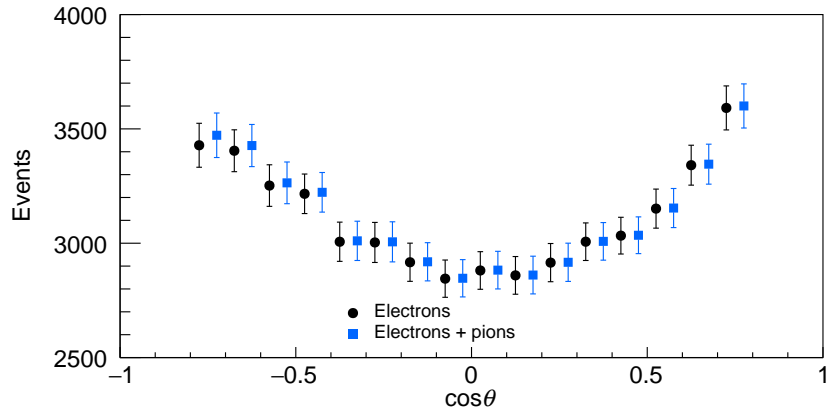


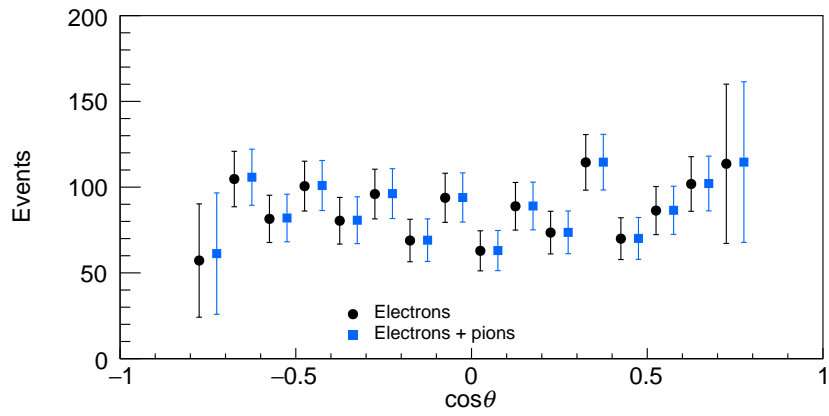
**Figure 9.14:** Residual values of  $|G_E|$  (a) and  $|G_M|$  (b) for different  $q^2$  values with statistical uncertainties only.



(a)



(b)



(c)

**Figure 9.15:** Reconstructed and efficiency-corrected angular distributions of generated electrons (black circles) and electrons mixed with pions (blue squares) for  $q^2$  values: (a) 5.4, (b) 8.2, and (c) 13.9 ( $\text{GeV}/c^2$ ).

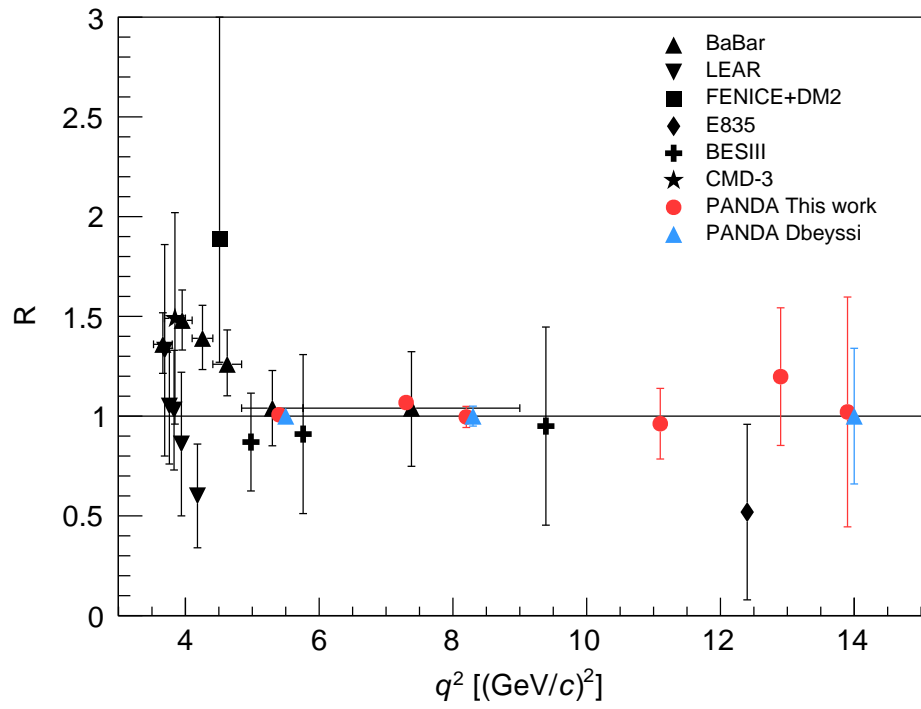


**Figure 9.16:** Form factor ratio as a function of  $q^2$  determined in this work (red circles), in the analysis of A. Dbeyssi (blue triangles), and in the past experiments (black markers).

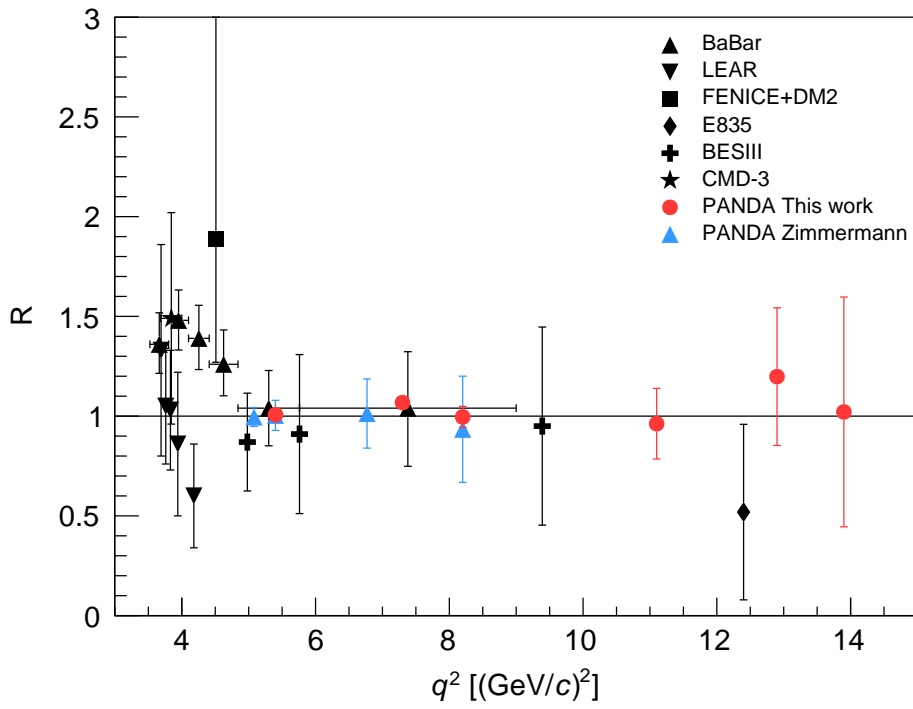


**Figure 9.17:** Form factor ratio as a function of  $q^2$  determined in this work (red circles), in the analysis of I. Zimmermann (blue triangles), and in the past experiments (black markers).

# Chapter 10

## Backward Endcap Calorimeter Performance Studies

The backward endcap of the electromagnetic calorimeter (BEMC) plays an essential role in the detection and identification of photons and leptons emitted at backward angles. It will be used for the proton FF measurement via  $\bar{p}p \rightarrow e^+e^-$ ,  $\bar{p}p \rightarrow \mu^+\mu^-$ , and  $\bar{p}p \rightarrow \pi^0e^+e^-$  reactions as all of them require an accurate particle identification and precise energy measurements of emitted leptons and photons.

The presence of an additional material (AM) between the interaction point and the BEMC in form of other detectors may have a negative impact on the energy resolution and efficiency of the BEMC. Particles emitted from the interaction point will need to cross these detectors, including their support structures, cooling systems, readout electronics, *etc.*, before reaching the BEMC. An analysis of the AM effect on the energy resolution and efficiency is presented in this chapter.

In order to measure the energy resolution and efficiency of the BEMC, a number of simulations are performed. In each simulation, photons are generated with a specific energy  $E$ , azimuthal  $\phi$ , and polar  $\theta$  angle. Two sets of simulations are performed. The first simulation includes only the BEMC geometry while the second one includes BEMC, MVD, and STT to evaluate the impact of the AM on the BEMC energy resolution and efficiency.

## 10.1 Geometry Description

For the purpose of this study, a new realistic geometry of the backward endcap calorimeter was implemented in PandaRoot using the ROOT framework. The BEMC consists of 524 lead tungstate ( $\text{PbWO}_4$ ) crystals assembled in a ring shape around the beam pipe. The geometrical characteristics of the BEMC are listed in Table 10.1. The crystals themselves are placed in alveoli of different sizes and shapes are shown in Fig. 10.1. Alveoli of different types "glued" together make up subunits of the BEMC. One quarter of the BEMC, illustrated in Fig. 10.2, consists of 14 subunits.

As the effect of the alveoli is considered to be insignificant, only crystals were implemented in the PandaRoot simulation as shown in Fig. 10.3.

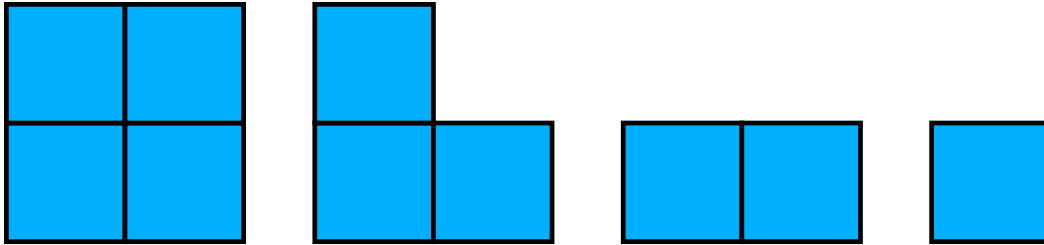


**Figure 10.1:** Different types of alveoli containing (left-to-right) four, three, two, and one crystal.

Number of crystals	524
Size (x,y,z)	$24.4 \times 24.4 \times 200$ mm
Inner radius	182 mm
Outer radius	406 mm
Angular acceptance	$146^\circ$ - $167^\circ$

**Table 10.1:** Characteristics of the backward endcap of the electromagnetic calorimeter.

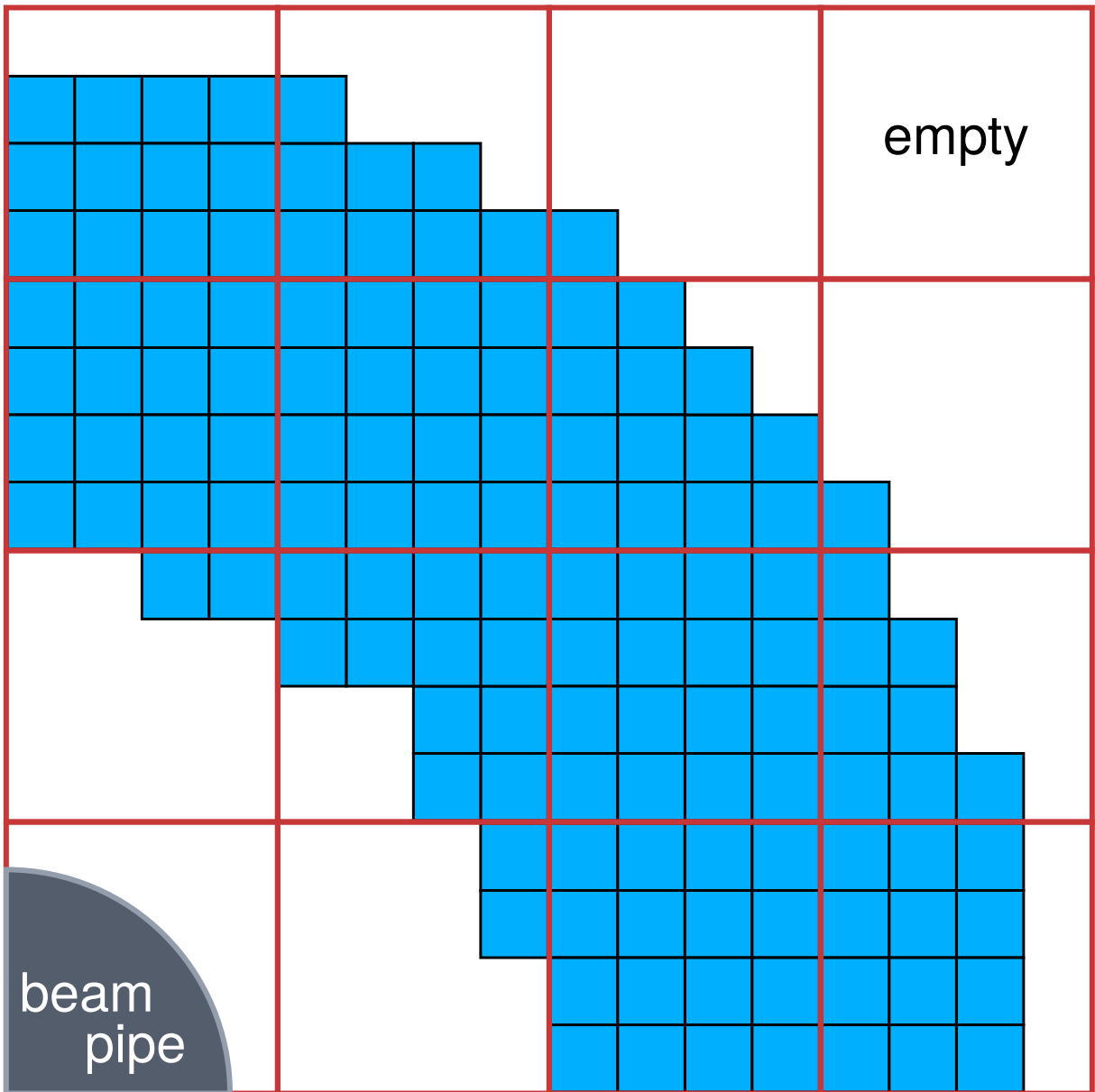


**Figure 10.2:** Schematic view of one quarter of the backward endcap of the electromagnetic calorimeter.

## 10.2 Simulation Settings

Fig. 10.4 illustrates two detector setups which are tested in this work. Fig. 10.4a shows the case where only the BEMC and the beam pipe are included in the simulation, while

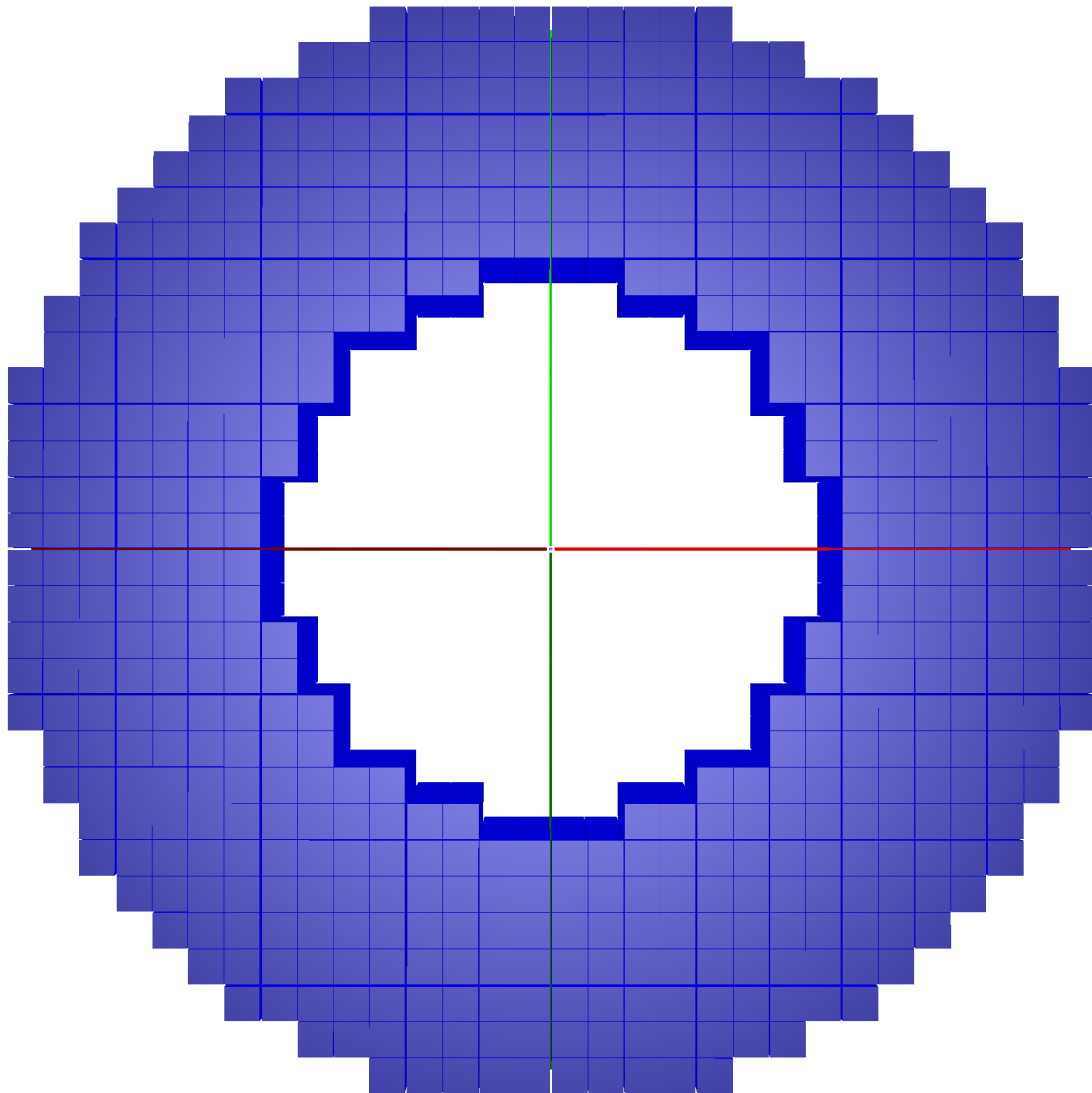


**Figure 10.3:** Front view of the backward endcap of the electromagnetic calorimeter as implemented in PandaRoot.

Fig. 10.4b shows an extended setup which includes the MVD and STT. At the time of this work, the MVD detector geometry included not only the detector itself but also the readout electronics, cooling, supporting structure, etc. The STT geometry, on the other hand, consisted only from the straw tubes tracker itself. In order to emulate the presence

of the STT's infrastructure, an aluminum disk with a thickness of 2 mm is placed between the STT and BEMC.

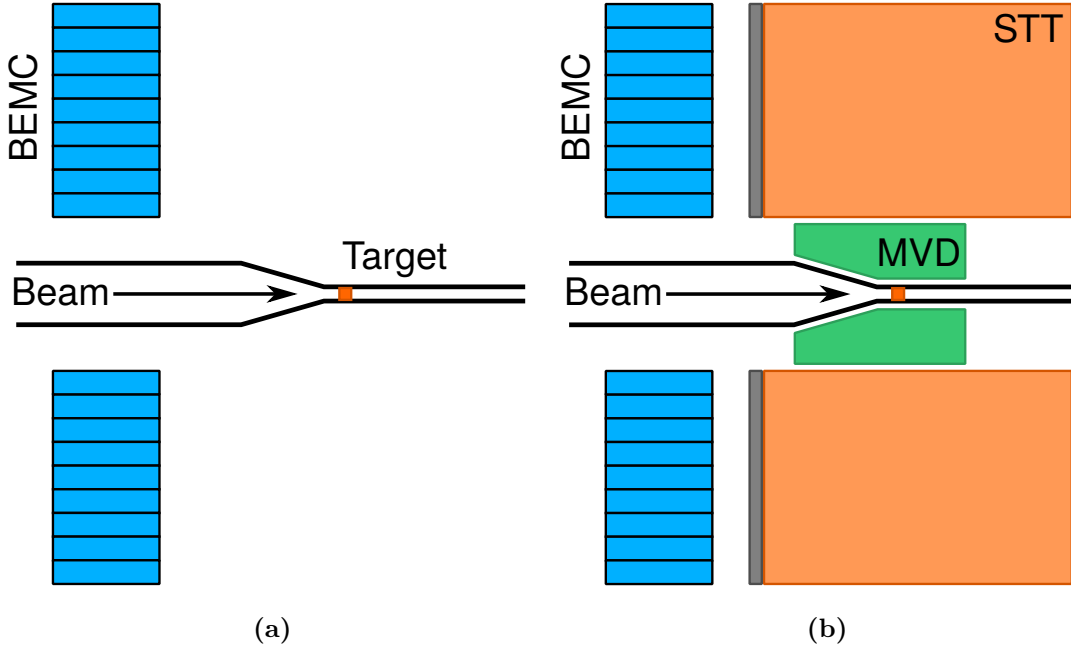


**Figure 10.4:** Side view of the detector setup with the BEMC only (a) and with the BEMC, STT, and MVD detectors (b).

A set of primary photon energies and angles, listed in Table 10.2, are chosen as an input for an event generator. The energy range corresponds to that of expected photons and leptons emitted at backward angles taken expected energies of the HESR antiproton beam. Azimuthal  $\phi$  and polar  $\theta$  angles are chosen to cover approximately 1/8 of the BEMC. Due to its symmetry, it is sufficient for the purpose of this study and can be extrapolated to the whole BEMC area.

For each combination of the energy,  $\phi$ , and  $\theta$  angles 50000 events are generated. Taking into account two data sets, *i.e.*, with the BEMC only and with the BEMC, STT, and MVD, 1000 data samples are produced. Geant3 is used for the event propagation and simulation of physics processes which occur when particles interact with matter, *e.g.*, pair production, bremsstrahlung, annihilation, *etc.*

$E(\text{MeV})$	$\phi$	$\theta$
30	314°	150°
100	319°	151.5°
250	324°	153°
500	329°	154.5°
700	334°	156°
	339°	157.5°
	344°	159°
	349°	160.5°
	354°	162°
	359°	163.5°

**Table 10.2:** Kinematic parameters used for the energy resolution and efficiency study.

### 10.3 Event Selection

In each event, a photon passing through the BEMC deposits its energy associated with an electromagnetic shower. Typically, the shower spreads among multiple crystals. The group of such crystals is called a cluster. One cluster can be formed by two particles if they hit the BEMC close enough. If it happens, the cluster is divided into areas which can be associated with individual particles. These areas are called bumps and defined by a local maximum of the deposited energy.

The bumps with the highest deposited energy are selected. An example energy spectra produced with and without the AM are shown in Fig. 10.5. In the latter case, the peak has a low energy tail, what can be explained by the energy loss caused by the AM. The peak width doesn't change much, though. Therefore the energy resolution is expected to be unaffected by the AM.

As a cross check, the bump position is projected on the XY plane. Fig. 10.6 shows that most primary photons that hit the BEMC do not deviate from their initial direction and form clearly visible dark-red areas in the right-bottom quarter of the BEMC. Additionally, a crescent-like distributions are visible around them. An investigation revealed, that these distributions originate in electron-positron pair production processes when the

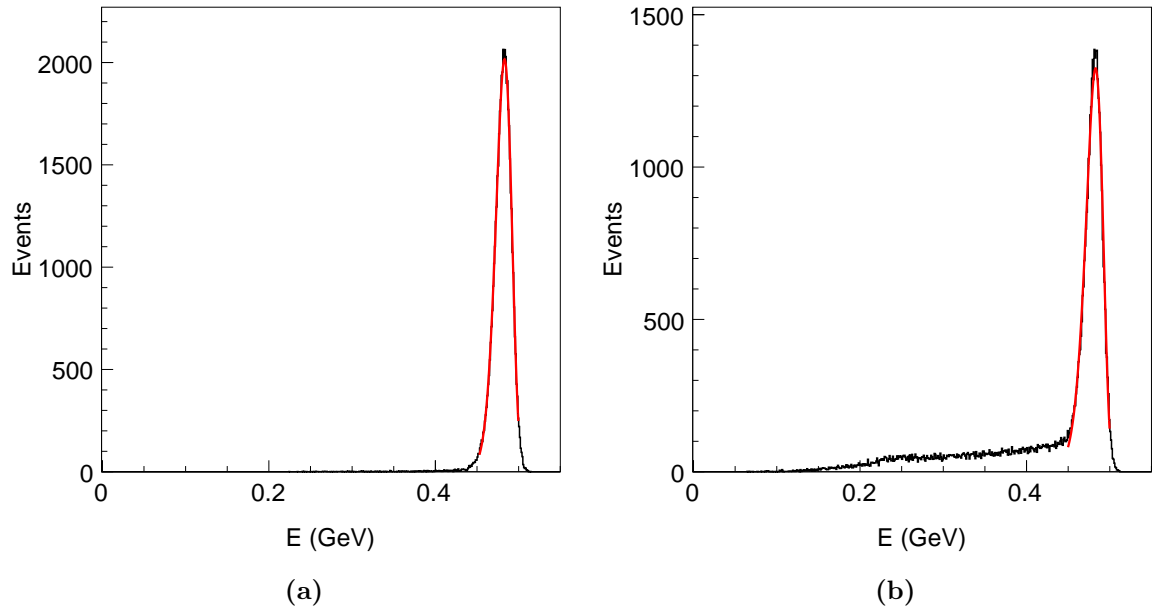


**Figure 10.5:** Bump energy containing the highest amount of deposited energy within a cluster for 500 MeV photons emitted at  $\theta = 156^\circ$  and  $\phi = 344^\circ$  with EMC alone (a) and with the additional material (b).

primary photon interacts with detectors before reaching the BEMC. Trajectories of produced electron-positron pairs are bent by the magnetic field in opposite directions what leads to an appearance of crescent-like distributions. Fig. 10.7 shows an example of such an event where the primary photon produces an electron-positron pair which in turn emits bremsstrahlung photons.

## 10.4 Energy Resolution and Efficiency Determination

The energy resolution can be determined from the width of the energy deposition peak while the detection efficiency can be estimated from the ratio of the reconstructed to generated events. All data sets with and without the AD are analyzed in the same way.

Novosibirsk function [107], which is fitted to each deposited energy spectra, has the following form:

$$f(E) = A \cdot \exp \left\{ -\frac{1}{2} \left[ \frac{\ln^2(1 + \Lambda\tau(E - E_0))}{\tau^2} + \tau^2 \right] \right\}, \quad (10.1)$$

where  $A$  is a normalization factor,  $E_0$  is the position of the maximum,  $\sigma$  is the standard deviation,  $\tau$  is a tail parameter, and  $\Lambda$  is:

$$\Lambda = \frac{\sinh(\tau\sqrt{\ln 4})}{\sigma\tau\sqrt{\ln 4}}. \quad (10.2)$$

The energy resolution is defined as the full width at half maximum divided by the maximum position:

$$E_{res} = 2\sigma\sqrt{\ln 4}/E_0, \quad (10.3)$$

where values of  $\sigma$  and  $E_0$  were extracted from the Novosibirsk fit function.

The efficiency is defined as the ratio of the reconstructed to generated events and was calculated in the following way:

$$E_{eff} = \frac{1}{N} \int_{E_0-3\sigma}^{E_0+2\sigma} f(E)dE, \quad (10.4)$$

where  $N = 50000$  is the number of generated events and the integral corresponds to the number of the reconstructed events in the range from  $E_0 - 3\sigma$  to  $E_0 + 2\sigma$ . T

## 10.5 Results

Figs. 10.8 and 10.9 show the energy resolution and detection efficiency of the backward endcap calorimeter for 500 MeV photons with and without AM. See Appendix C for energy resolution and detection efficiency figures for all investigated photon energies.

As expected, the detection efficiency is significantly lower, by about 20%, when the MVD and STT are included in the simulation. Some spots visible in Fig. 10.8 (bottom) show particularly lower efficiency due to the presence of a higher, than in average, amount of the AM, *e.g.*, supporting structure of the MVD. The uncertainty of the efficiency measurement is small (about 0.4%) throughout all  $\theta$ ,  $\phi$ , and photon energies combinations.

At the same time, the energy resolution is not affected so much by the presence of the AM. Comparing Fig. 10.9 (top and bottom) one can see that the energy resolution only slightly worse when more material is included in the simulation. The difference of 0.5% can be observed across most part of the angles covered. The energy resolution is worse at the extreme  $\theta$  angles as electromagnetic showers are not fully captured by the calorimeter.

The average energy resolution and detection efficiency with and without the AM are shown in Fig. 10.10. Fig. 10.10 (top) demonstrates that energy resolution has a strong correlation with the photon energy. The energy resolution of the backward endcap calorimeter is better for high energy photons and get worse by few percent only with the AM added. The average efficiency, shown in Fig. 10.10 (bottom), is strongly affected by the AM, though. With the BEMC only, the average efficiency stays constant for all photon energies and is higher by approximately 20%.

It must be mentioned that only statistical uncertainty was taken into account in the determination of the energy resolution and detection efficiency.

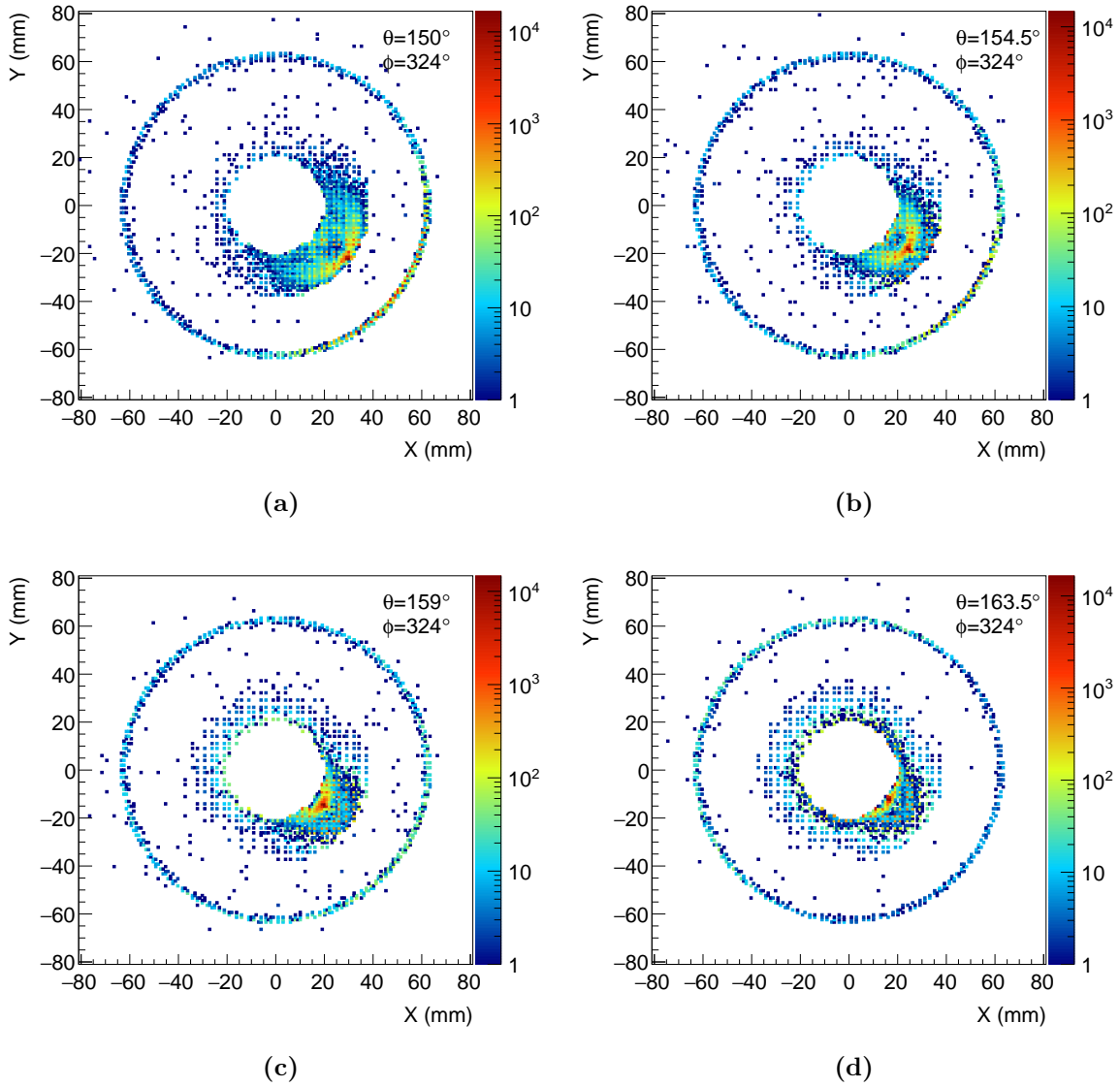


**Figure 10.6:** Reconstructed bumps positions projected on the XY plane for 500 MeV photons.

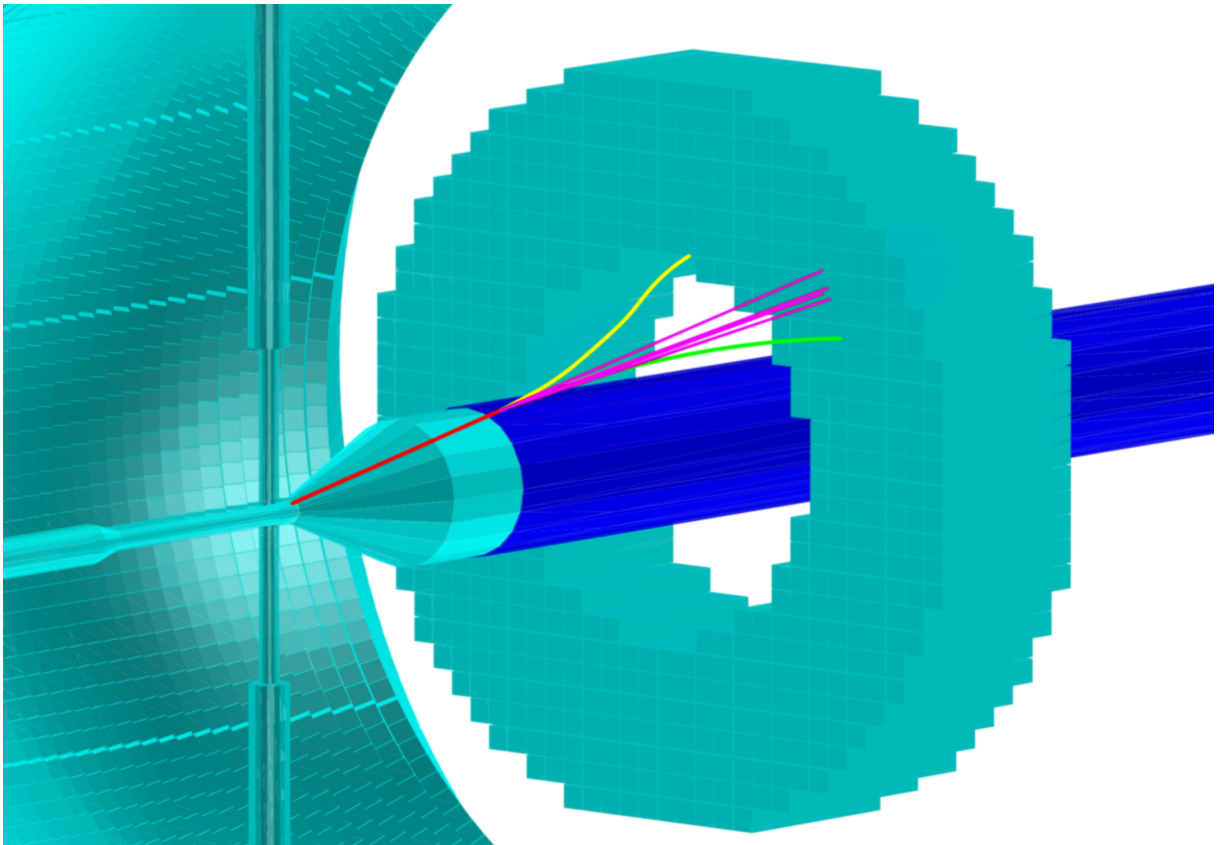


**Figure 10.7:** Visualized event from the simulation showing the case when the primary photon (red) produces an electron-positron (yellow-green) pair, which emits bremsstrahlung photons (pink). The MVD and STT are hidden for clarity.

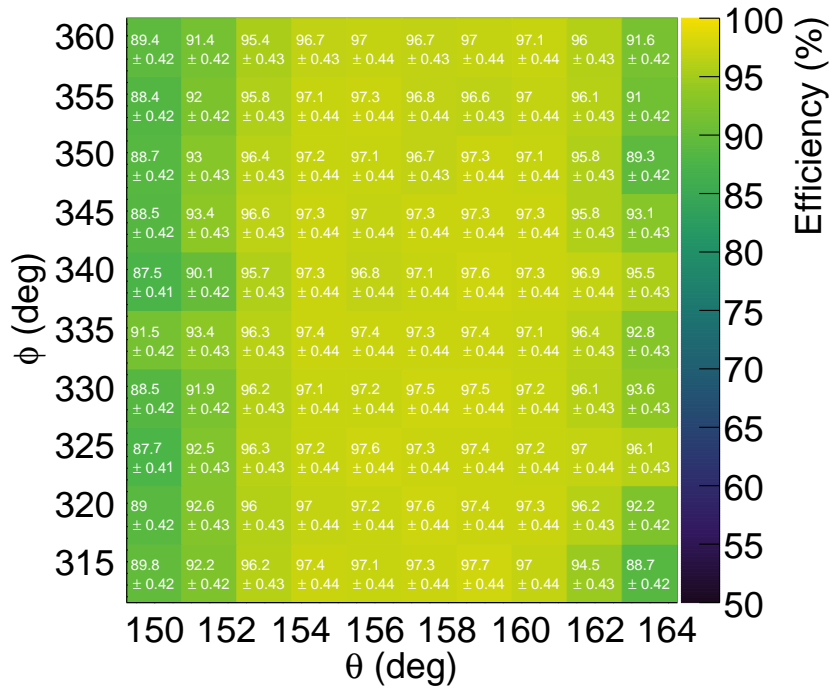
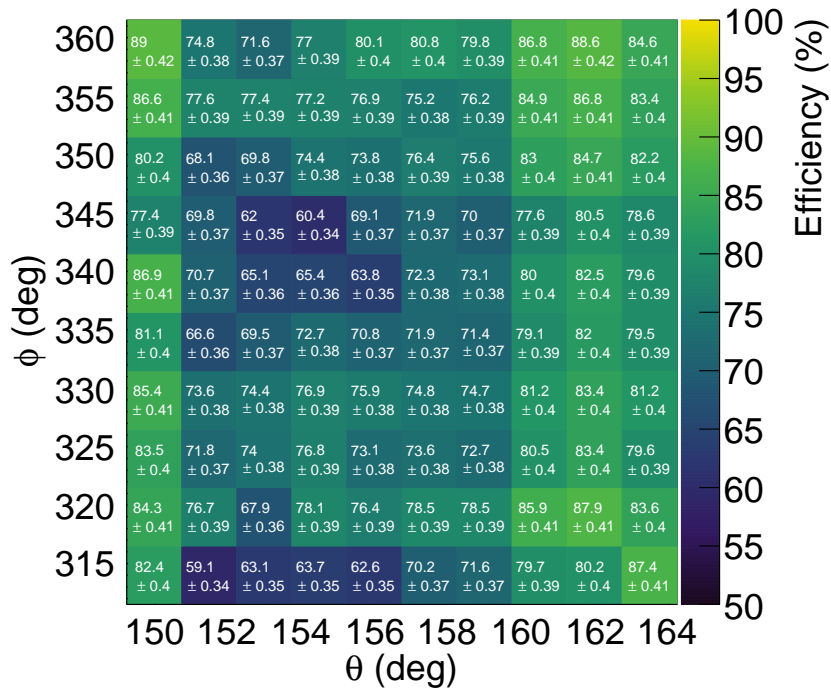


**Figure 10.8:** Detection efficiency for 500 MeV photons with (top) and without (bottom) the additional material.

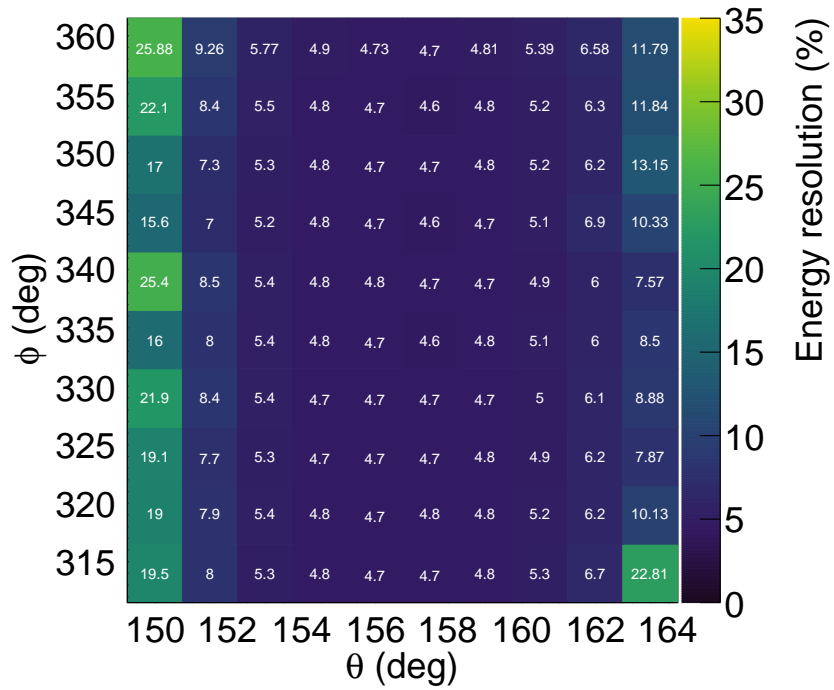
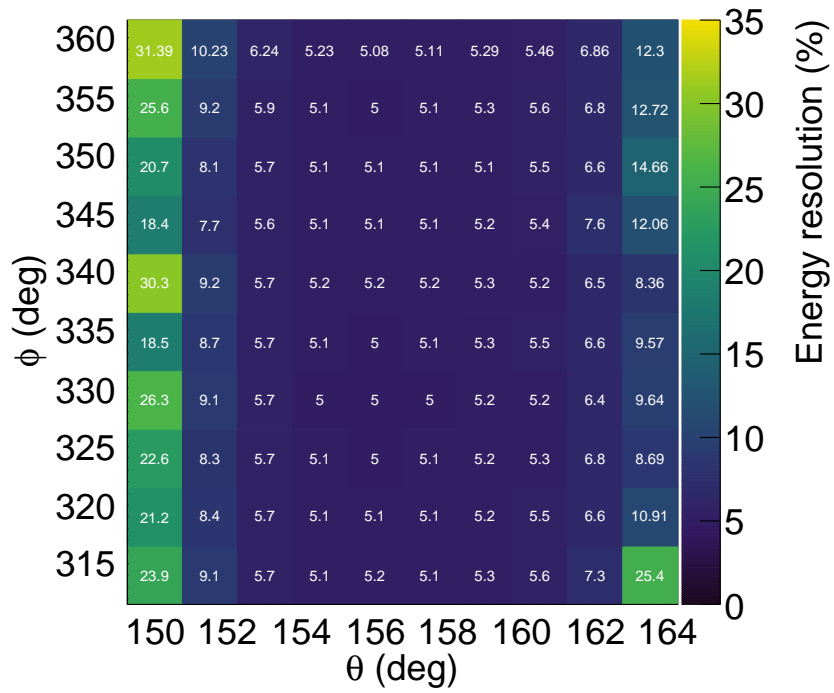


**Figure 10.9:** Energy resolution for 500 MeV photons with (top) and without (bottom) the additional material.

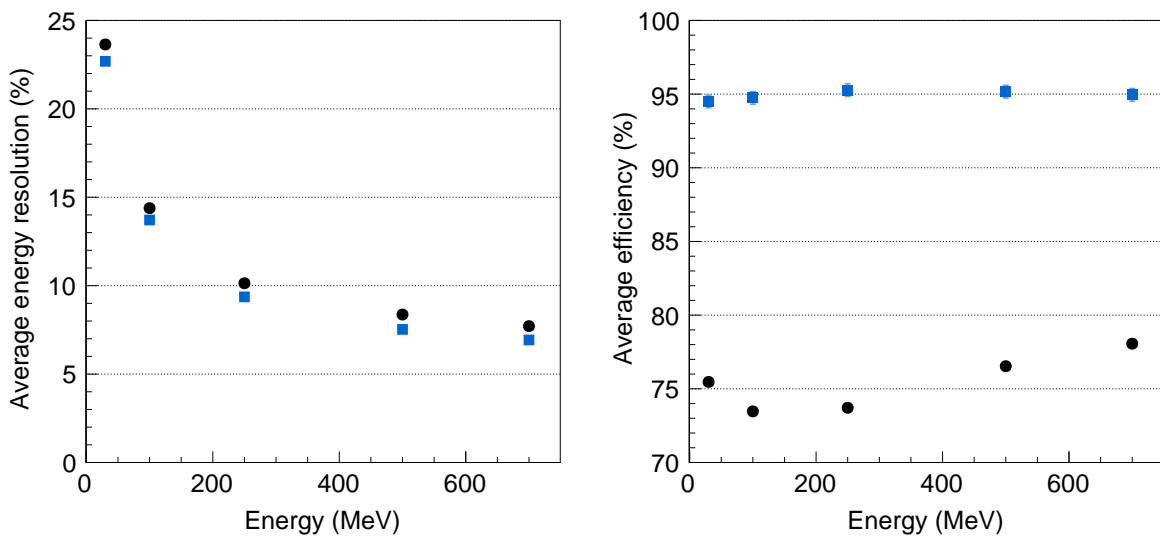


**Figure 10.10:** Average energy resolution (left) and detection efficiency (right) of the BEMC for different photon energies with (black circles) and without (blue squares) the additional material.

# Appendix A

## SYMB Calibration

In this appendix results of the SYMB PMTs gain calibration for all crystals in both detectors are shown. Dependencies of the ADC channel on the applied HV at a given energy of the incoming beam are shown. The exponential fit applied to the data points allowed to adjust HV to produce identical ADC outputs from all crystal for the same beam energy.

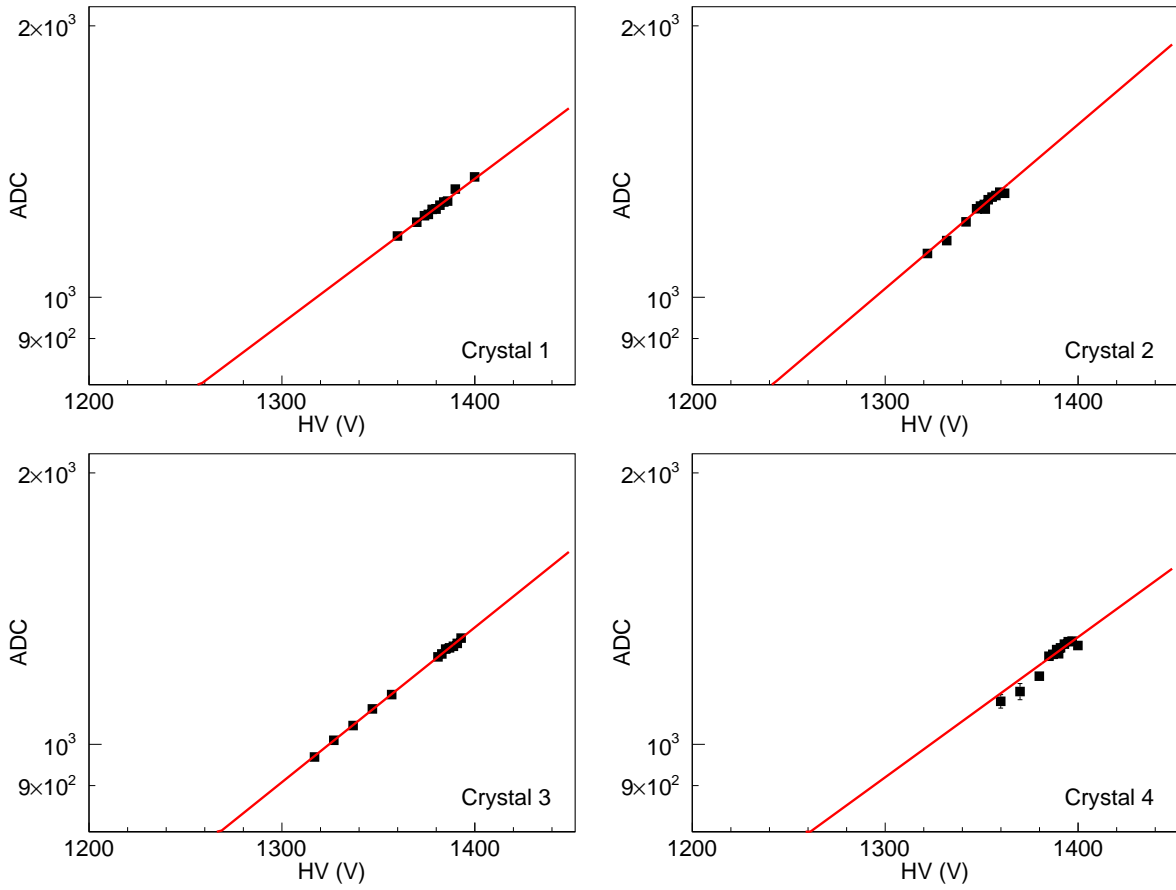


**Figure A.1:** Peak ADC channels dependence on HV (squares) in the left sector SYMB detector and an exponential fit (line).

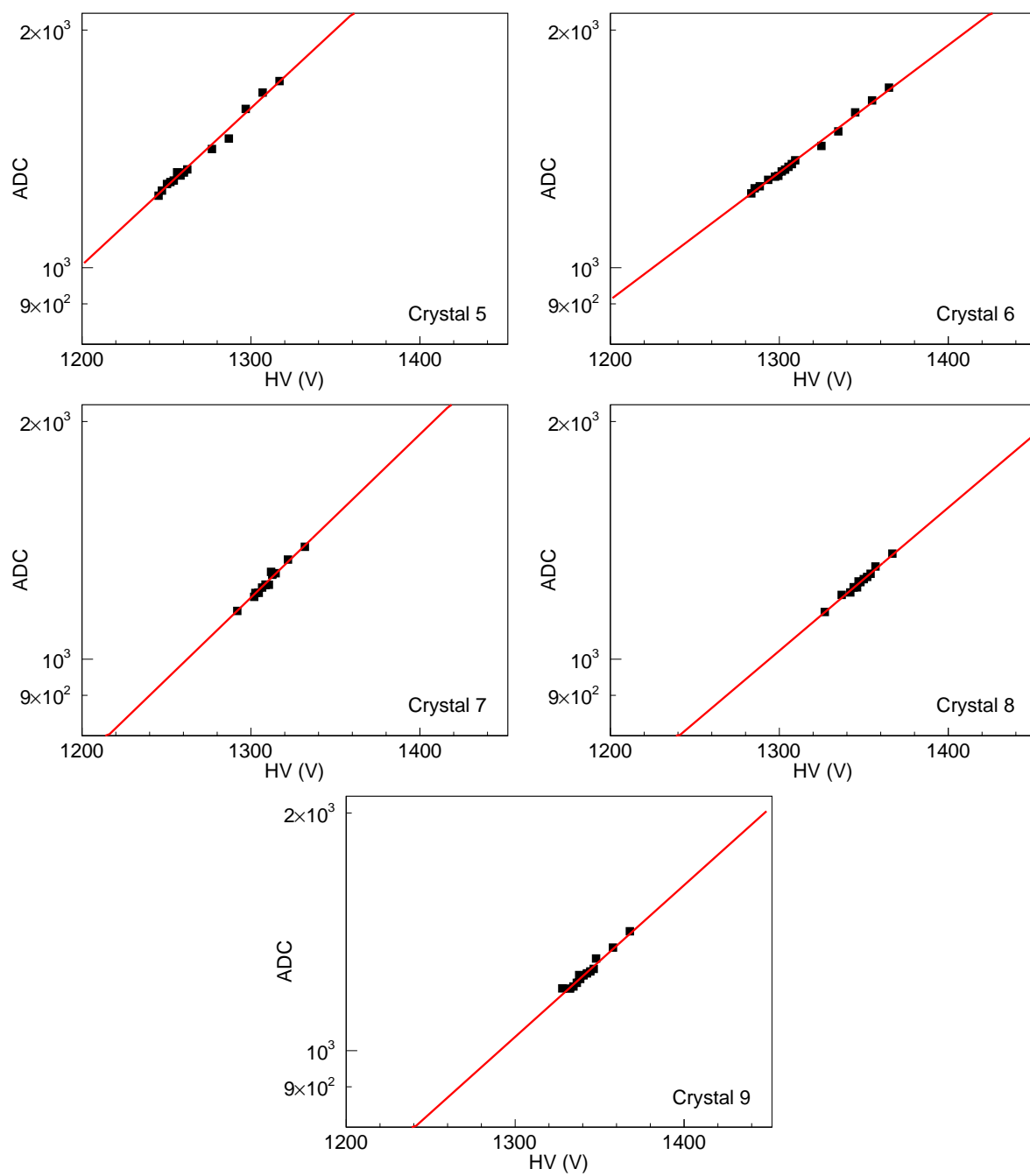


**Figure A.2:** Peak ADC channels dependence on HV (squares) in the left sector SYMB detector and an exponential fit (line).

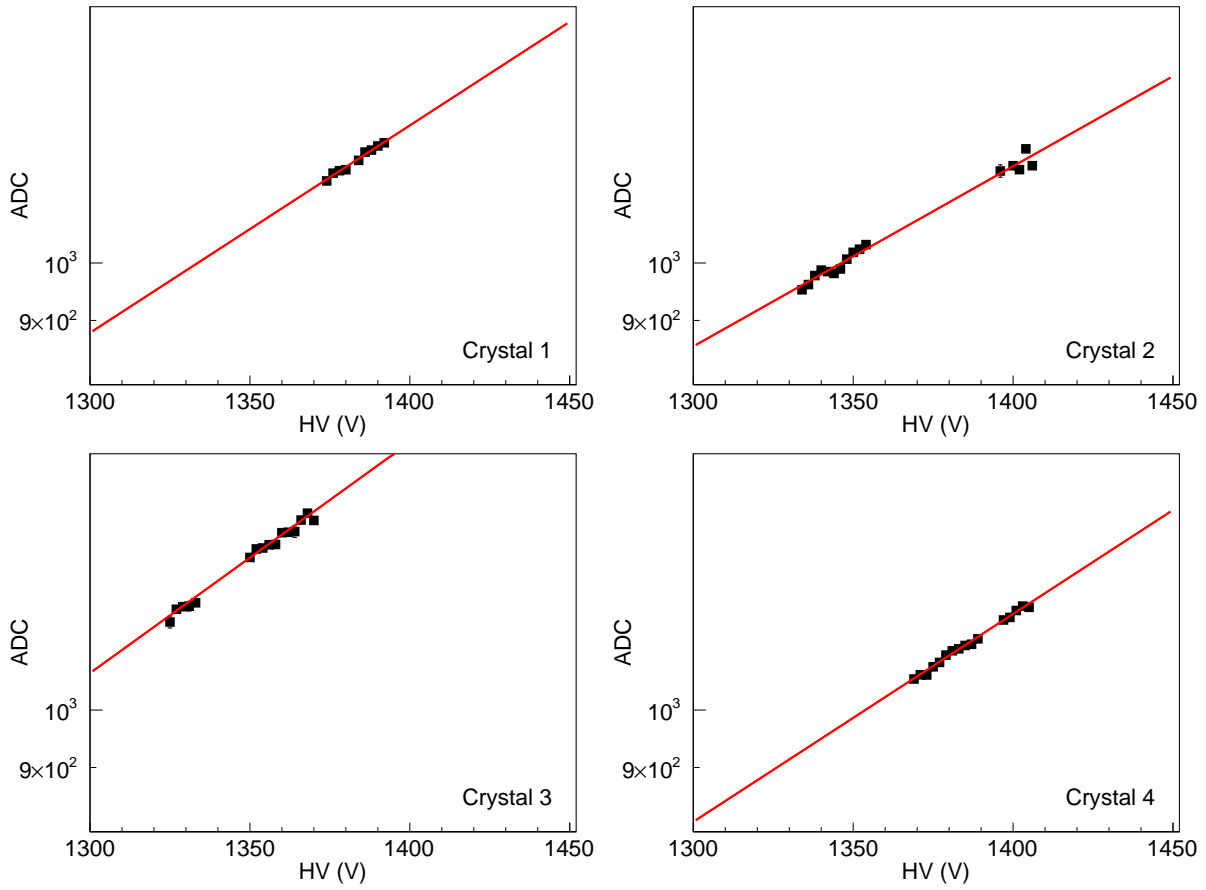


**Figure A.3:** Peak ADC channels dependence on HV (squares) in the right sector SYMB detector and an exponential fit (line).

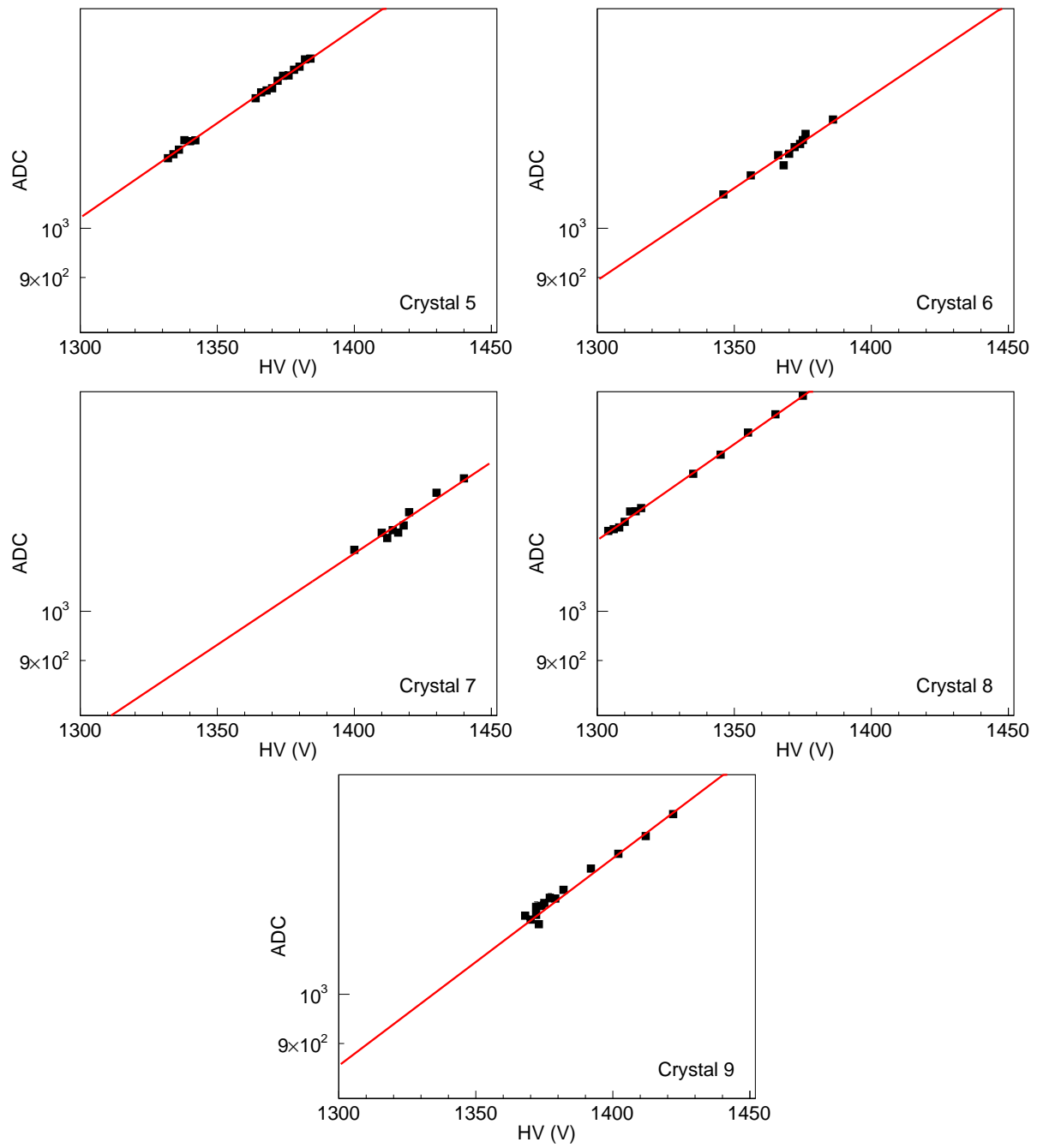


**Figure A.4:** Peak ADC channels dependence on HV (squares) in the right sector SYMB detector and an exponential fit (line).

## Appendix B

# Response of the EMC and STT detectors at $\overline{\text{PANDA}}$

The ratio of the energy deposited in the EMC to the reconstructed momentum and the energy deposited in the STT at  $q^2 = 5.4 \text{ (GeV}/c)^2$  and  $q^2 = 13.9 \text{ (GeV}/c)^2$  are shown in Fig. B.1 and Fig. B.2, respectively. At lower energy the pion cross section strongly fluctuates with the scattering angle (momentum) which is reflected by the three elliptical red areas are visible in Figs. B.1b and B.1d between  $p_{reco} = 0.7 \text{ GeV}/c$  and  $p_{reco} = 2.3 \text{ GeV}/c$ . At  $q^2 = 13.9 \text{ (GeV}/c)^2$  the cross section has to peaks at forward and backward scattering angles and a dip in between what is seen in Figs. B.2b and B.2d in a shape of two bigger red areas around  $p_{reco} = 1.2 \text{ GeV}/c$  and  $p_{reco} = 6.0 \text{ GeV}/c$ .

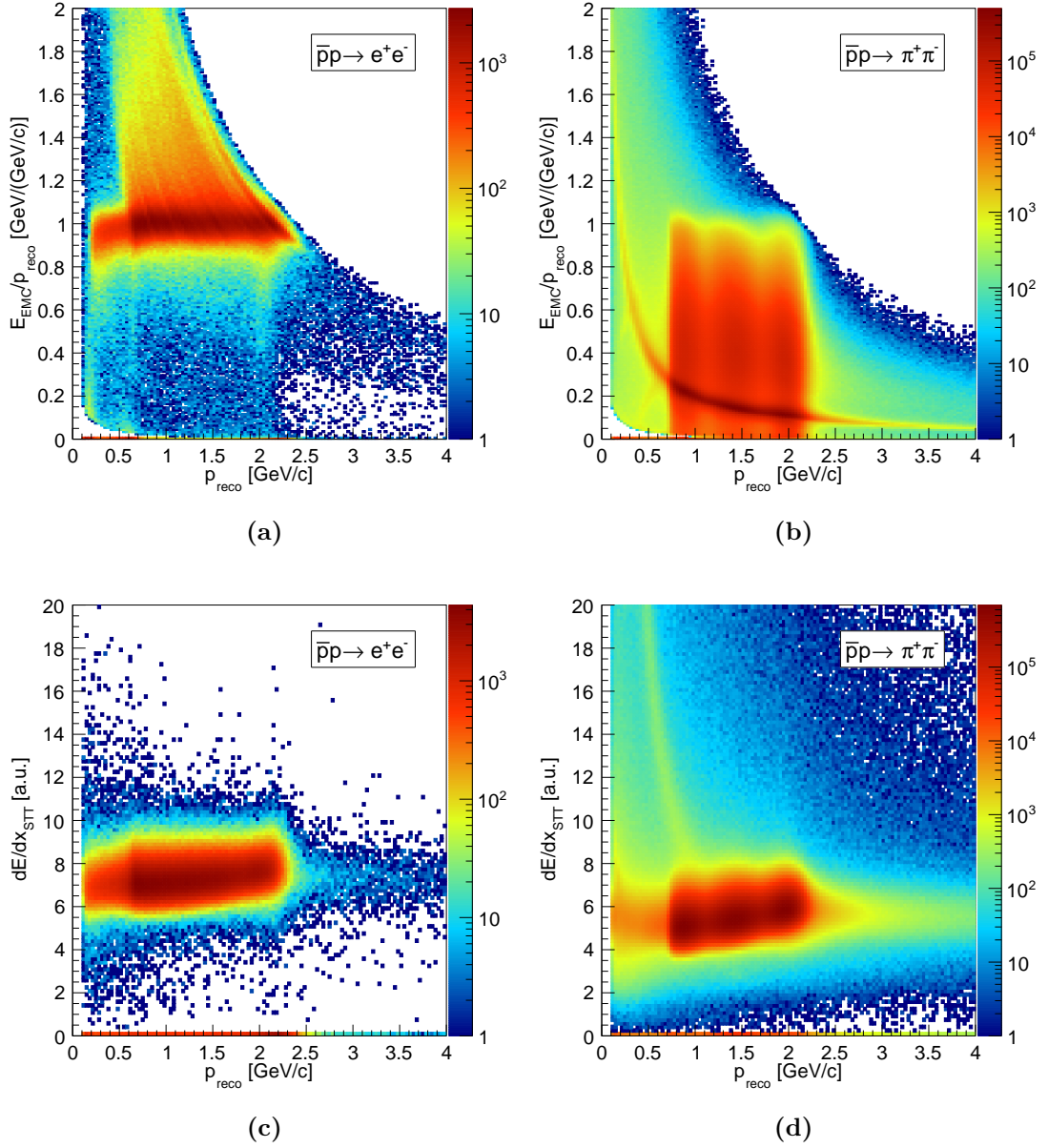


**Figure B.1:** Detector response to the signal (left column) and the background (right column): (a, b) is the energy deposited in the EMC over the reconstructed momentum as a function of the reconstructed momentum; (c, d) is the energy loss per unit of length in the STT as a function of the reconstructed momentum at  $q^2 = 5.4 \text{ (GeV}/c)^2$ .

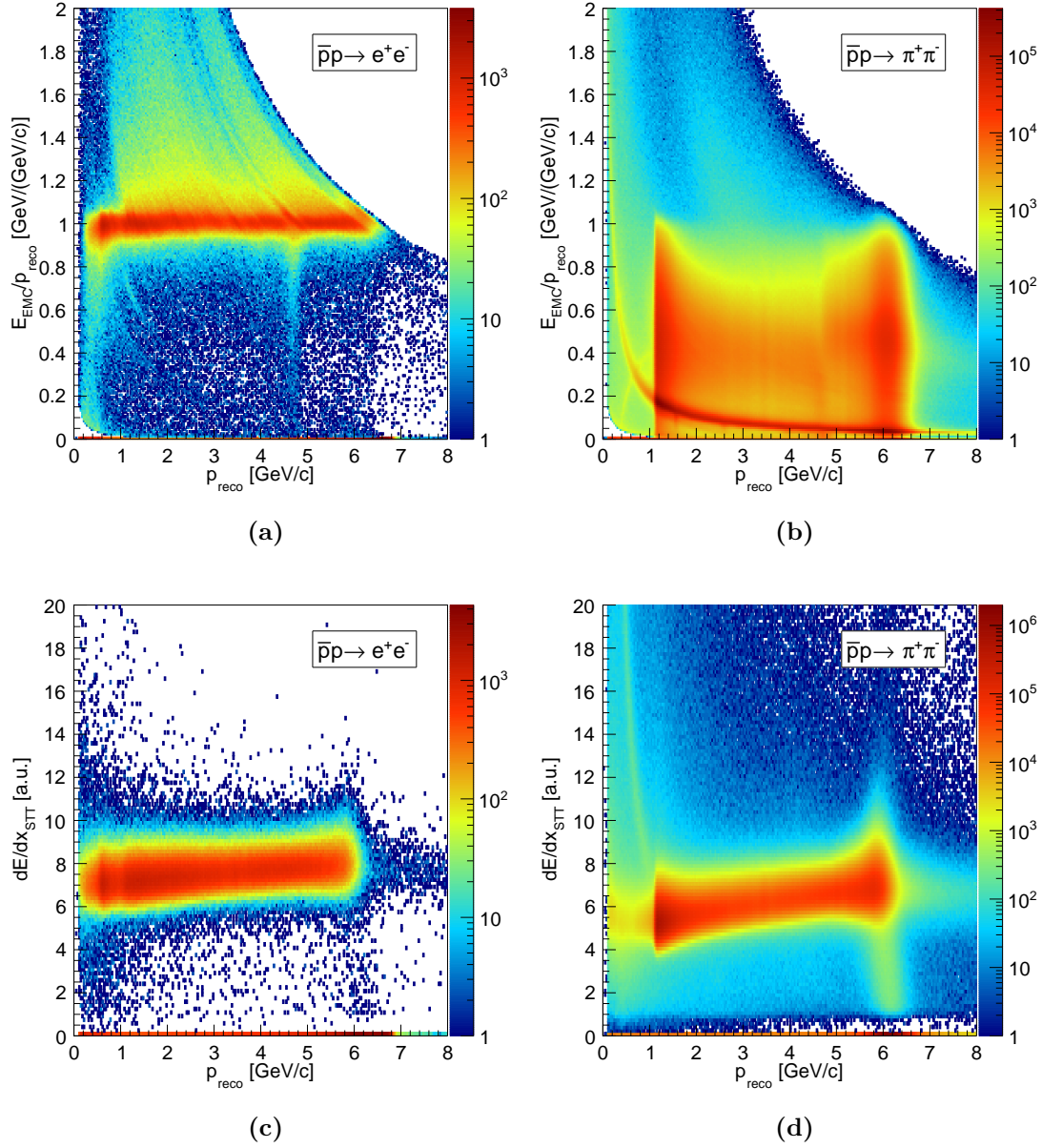
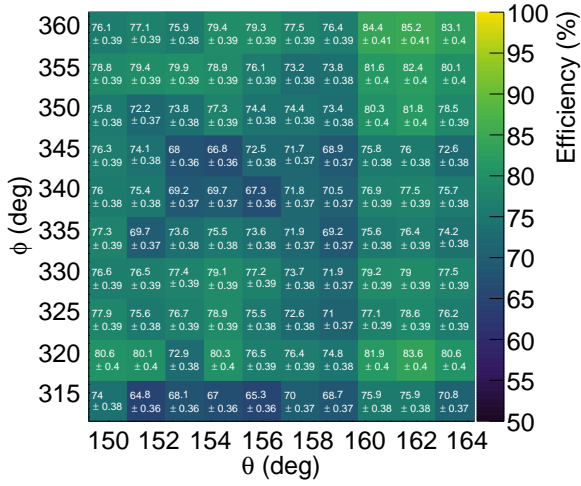


**Figure B.2:** Detector response to the signal (left column) and the background (right column): (a, b) is the energy deposited in the EMC over the reconstructed momentum as a function of the reconstructed momentum; (c, d) is the energy loss per unit of length in the STT as a function of the reconstructed momentum at  $q^2 = 13.9$  (GeV/c) $^2$ .

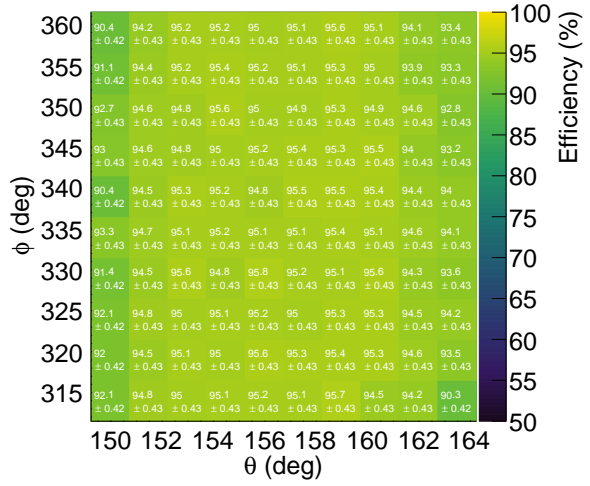
# Appendix C

## Backward EMC efficiency and energy resolution

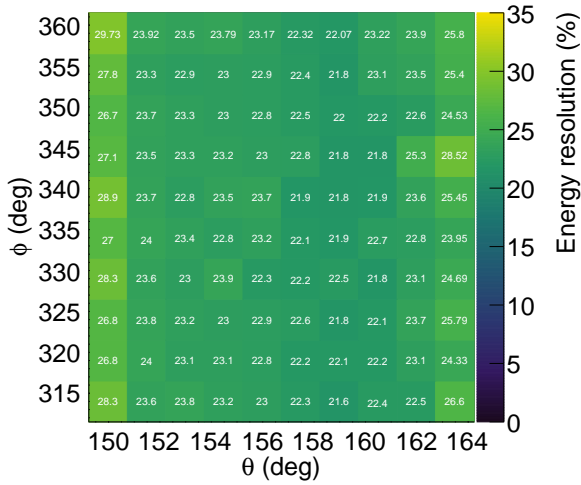
This appendix provide additional 2D histograms showing the energy resolution and efficiency of the  $\bar{\text{P}}\text{ANDA}$  backward endcap of the electromagnetic calorimeter.



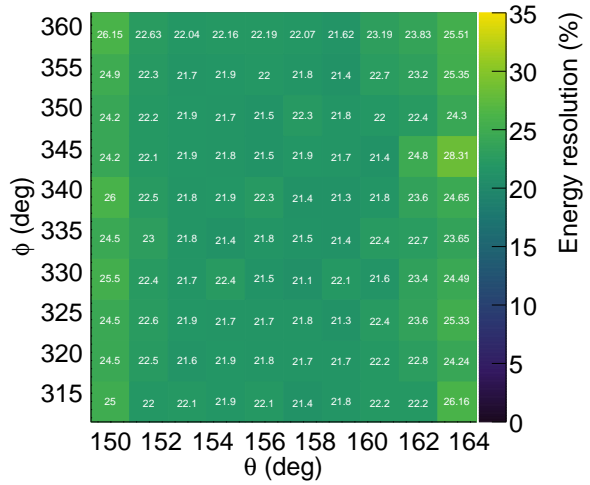
(a)



(b)



(c)



(d)

**Figure C.1:** Detection efficiency with (a) and without (b) the additional material and energy resolution with (c) and without (d) the additional material for 30 MeV photons.

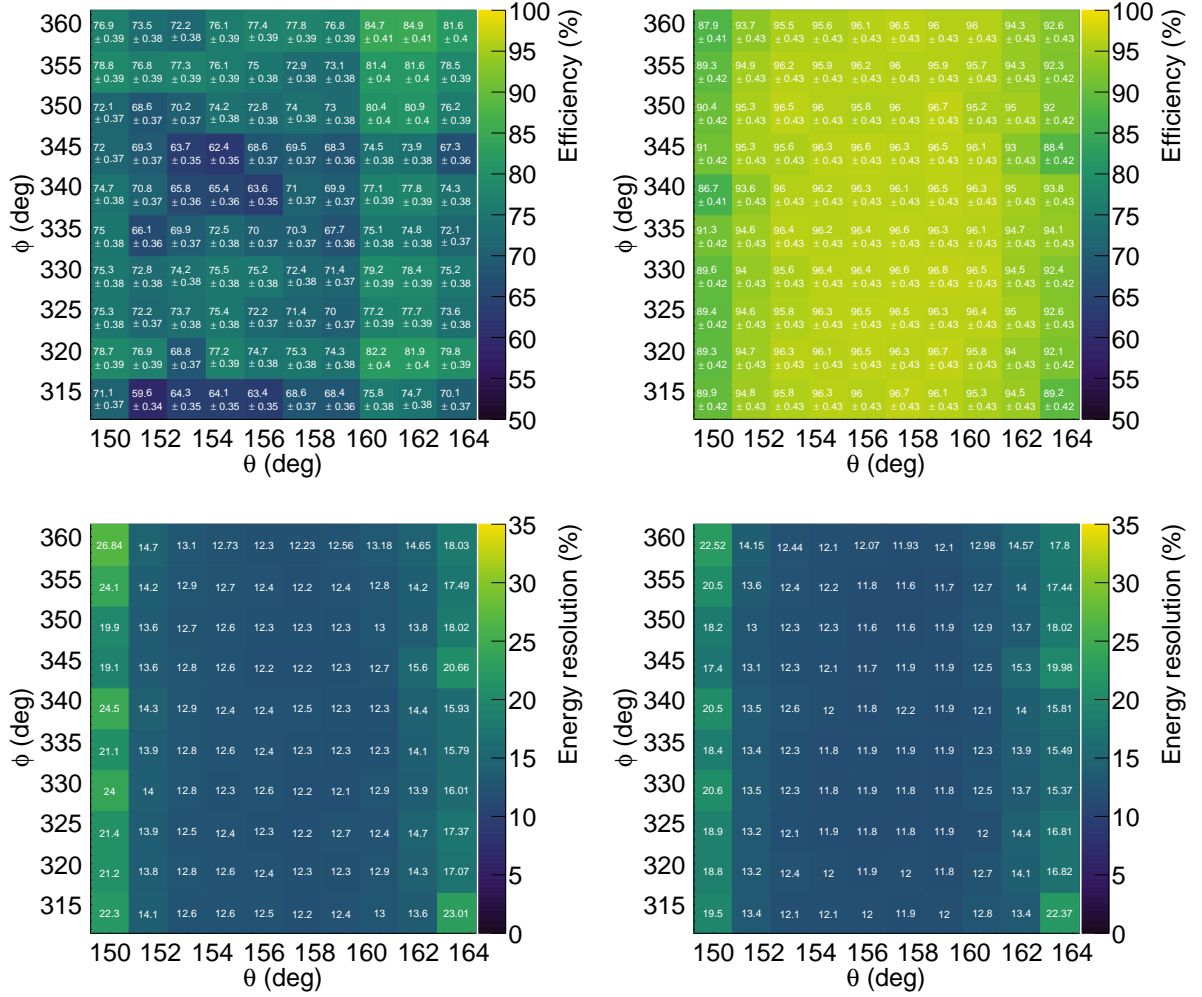


**Figure C.2:** Detection efficiency with (a) and without (b) the additional material and energy resolution with (c) and without (d) the additional material for 100 MeV photons.

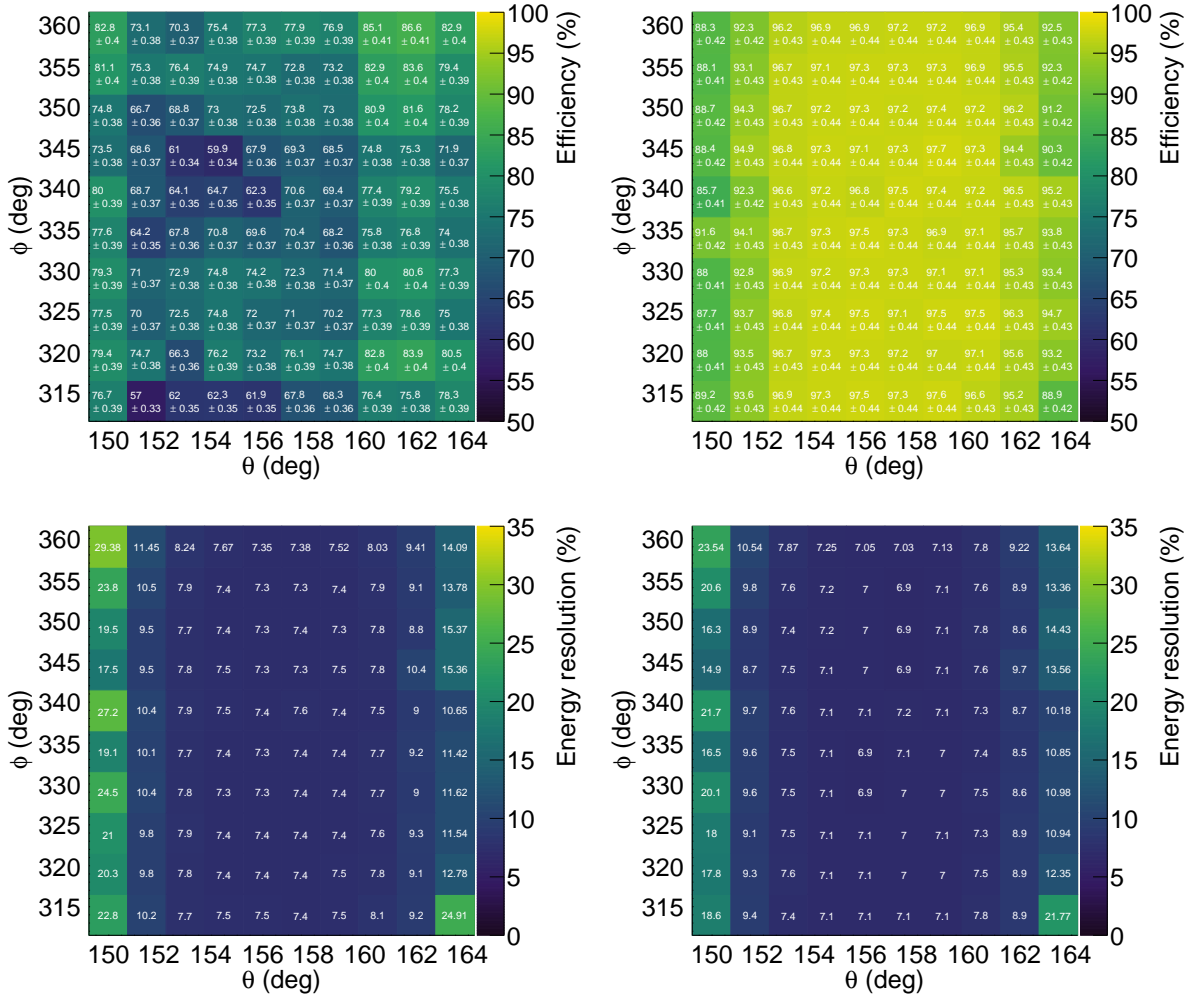


**Figure C.3:** Detection efficiency with (a) and without (b) the additional material and energy resolution with (c) and without (d) the additional material for 250 MeV photons.

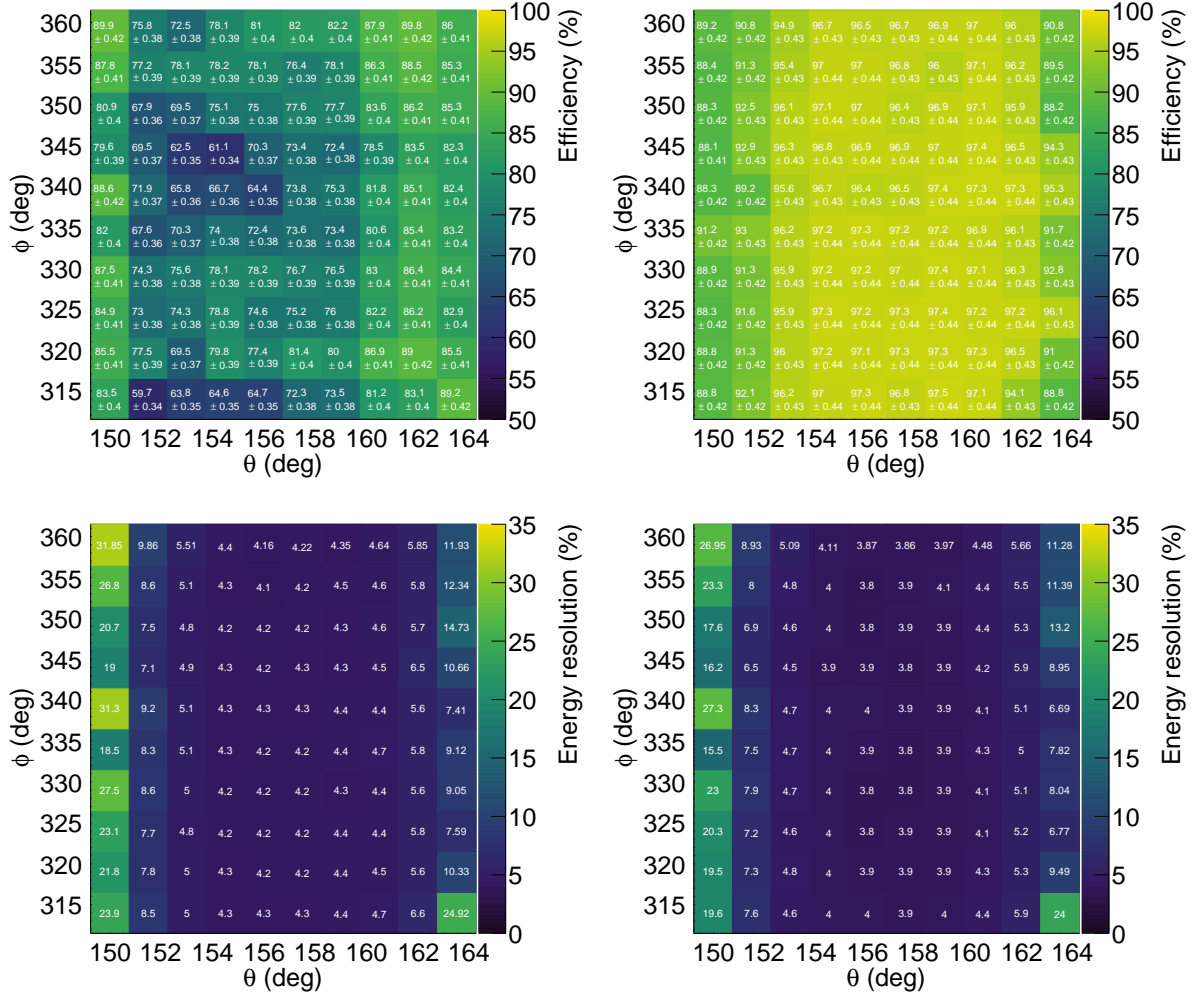


**Figure C.4:** Detection efficiency with (a) and without (b) the additional material and energy resolution with (c) and without (d) the additional material for 700 MeV photons.

# Bibliography

- [1] R. Hofstadter and R. W. McAllister. *Phys. Rev.*, 98:217–218, Apr 1955.
- [2] R. W. McAllister and R. Hofstadter. *Phys. Rev.*, 102:851–856, May 1956.
- [3] M. N. Rosenbluth. *Phys. Rev.*, 79:615–619, Aug 1950.
- [4] J. Litt et al. *Physics Letters B*, 31(1):40 – 44, 1970.
- [5] L. E. Price et al. *Phys. Rev. D*, 4:45–53, Jul 1971.
- [6] Ch. Berger et al. *Physics Letters B*, 35(1):87 – 89, 1971.
- [7] F. Borkowski et al. *Nuclear Physics A*, 222(2):269 – 275, 1974.
- [8] R. C. Walker et al. *Phys. Rev. D*, 49:5671–5689, Jun 1994.
- [9] L. Andivahis et al. *Phys. Rev. D*, 50:5491–5517, Nov 1994.
- [10] I. A. Qattan et al. *Phys. Rev. Lett.*, 94:142301, Apr 2005.
- [11] M. E. Christy et al. *Phys. Rev. C*, 70:015206, Jul 2004.
- [12] G. Bardin et al. *Nuclear Physics B*, 411(1):3 – 32, 1994.
- [13] M. Ablikim et al. *Phys. Rev. D*, 91:112004, Jun 2015.
- [14] J. P. Lees et al. *Phys. Rev. D*, 88:072009, Oct 2013.
- [15] R. Baldini et al. *Eur. Phys. J. C*, 46(2):421–428, 2006.
- [16] R.R. Akhmetshin et al. 2014. arXiv:1507.08013v2 [hep-ex].
- [17] M. K. Jones et al. *Phys. Rev. Lett.*, 84:1398–1402, Feb 2000.
- [18] O. Gayou et al. *Phys. Rev. Lett.*, 88:092301, Feb 2002.
- [19] V. Punjabi et al. *Phys. Rev. C*, 71:055202, May 2005.
- [20] C. B. Crawford et al. *Phys. Rev. Lett.*, 98:052301, Jan 2007.
- [21] A. J. R. Puckett et al. *Phys. Rev. Lett.*, 104:242301, Jun 2010.

- [22] G. Ron et al. *Phys. Rev. C*, 84:055204, Nov 2011.
- [23] X. Zhan et al. *Physics Letters B*, 705(1-2):59–64, 2011.
- [24] A. J. R. Puckett et al. *Phys. Rev. C*, 85:045203, Apr 2012.
- [25] R. Milner et al. *Nucl. Instrum. Meth. A*, 741:1 – 17, 2014.
- [26] B. Singh et al. *Eur. Phys. J. A*, 52(10):325, 2016.
- [27] I. Estermann, O. C. Simpson, and O. Stern. 132:169–170, 1933.
- [28] E. Clementel and C. Villi. *Il Nuovo Cimento (1955-1965)*, 4(5):1207–1211, 1956.
- [29] R Hofstadter. *Rev. Mod. Phys.*, 28:214–254, Jul 1956.
- [30] R. Hofstadter, F. Bumiller, and M. R. Yearian. *Rev. Mod. Phys.*, 30:482–497, Apr 1958.
- [31] L. N. Hand, D. G. Miller, and R. Wilson. *Rev. Mod. Phys.*, 35:335–349, Apr 1963.
- [32] G.G. Simon et al. *Nuclear Physics A*, 333(3):381 – 391, 1980.
- [33] E. Tomasi-Gustafsson and M. P. Rekaló. *Physics Letters B*, 504(4):291 – 295, 2001.
- [34] N. Dombey. *Rev. Mod. Phys.*, 41:236–246, Jan 1969.
- [35] A. I. Akhiezer and M. P. Rekaló. *Physics of Elementary Particles and Atomic Nuclei*, 4:662, 1973.
- [36] Raymond G. Arnold, Carl E. Carlson, and Franz Gross. *Phys. Rev. C*, 23:363–374, Jan 1981.
- [37] C.F. Perdrisat, V. Punjabi, and M. Vanderhaeghen. *Progress in Particle and Nuclear Physics*, 59(2):694 – 764, 2007.
- [38] T.W Donnelly and A.S Raskin. *Annals of Physics*, 169(2):247 – 351, 1986.
- [39] W. Bartel et al. *Nuclear Physics B*, 58(2):429 – 475, 1973.
- [40] A. V. Afanasev et al. *Phys. Rev. D*, 72:013008, Jul 2005.
- [41] A. V. Afanasev et al. *Physics Letters B*, 514(3–4):269 – 278, 2001.
- [42] J. Arrington et al. *Progress in Particle and Nuclear Physics*, 66(4):782 – 833, 2011.
- [43] P. G. Blunden et al. *Phys. Rev. C*, 72:034612, Sep 2005.
- [44] A. Browman, F. Liu, and C. Schaerf. *Phys. Rev.*, 139:B1079–B1085, Aug 1965.
- [45] R. L. Anderson et al. *Phys. Rev.*, 166:1336–1342, Feb 1968.
- [46] R. L. Anderson et al. *Phys. Rev. Lett.*, 17:407–409, Aug 1966.
- [47] J. Mar et al. *Phys. Rev. Lett.*, 21:482–484, Aug 1968.
- [48] D. Yount and J. Pine. *Phys. Rev.*, 128:1842–1849, Nov 1962.

- [49] W. Bartel et al. *Physics Letters B*, 25(3):242 – 245, 1967.
- [50] B. Bouquet et al. *Physics Letters B*, 26(3):178 – 180, 1968.
- [51] J. Guttman et al. *The European Physical Journal A*, 47(6):77, 2011.
- [52] D. Borisyuk and A. Kobushkin. *Phys. Rev. D*, 79:034001, Feb 2009.
- [53] D. Rimal et al. 2016. arXiv:1603.00315 [nucl-ex].
- [54] I. A. Rachek et al. *Phys. Rev. Lett.*, 114:062005, Feb 2015.
- [55] H.-Q. Zhou and N. S. Yang. *Eur. Phys. J. A*, 51(8):1–18, 2015.
- [56] A. Zichichi et al. *Il Nuovo Cimento (1955-1965)*, 24(1):170–180, 1962.
- [57] A. Antonelli et al. *Physics Letters B*, 334(3):431 – 434, 1994.
- [58] T. A. Armstrong et al. *Phys. Rev. Lett.*, 70:1212–1215, Mar 1993.
- [59] D. Bisello et al. *Nuclear Physics B*, 224(3):379 – 395, 1983.
- [60] B. Delcourt et al. *Physics Letters B*, 86(3):395 – 398, 1979.
- [61] M. Ablikim et al. *Physics Letters B*, 630(1-2):14–20, 2005.
- [62] J. P. Lees et al. *Phys. Rev. D*, 87:092005, May 2013.
- [63] D. Bisello et al. *Zeitschrift für Physik C Particles and Fields*, 48(1):23–28, 1990.
- [64] T. K. Pedlar et al. *Phys. Rev. Lett.*, 95:261803, Dec 2005.
- [65] M. A. Belushkin, H.-W. Hammer, and U.-G. Meißner. *Phys. Rev. C*, 75:035202, Mar 2007.
- [66] A. Denig and G. Salmè. *Progress in Particle and Nuclear Physics*, 68:113 – 157, 2013.
- [67] S. Pacetti, R. Baldini Ferroli, and E. Tomasi-Gustafsson. *Physics Reports*, 550-551:1 – 103, 2015.  
Proton electromagnetic form factors: Basic notions, present achievements and future perspectives.
- [68] J. Haidenbauer, X.-W. Kang, and U.-G. Meißner. *Nuclear Physics A*, 929:102 – 118, 2014.
- [69] I. T. Lorenz, H.-W. Hammer, and U.-G. Meißner. *Phys. Rev. D*, 92:034018, Aug 2015.
- [70] A. Bianconi and E. Tomasi-Gustafsson. *Phys. Rev. C*, 93:035201, Mar 2016.
- [71] G. Huang et al. Besiii proposal for data taking, internal note docdb-doc-127. 2014.
- [72] M. C. Mora Espí. PhD thesis, Johannes Gutenberg Universität in Mainz, 2012.
- [73] D. Hasell et al. *Nucl. Instrum. Meth. A*, 603(3):247 – 262, 2009.
- [74] J.C. Bernauer et al. The OLYMPUS internal hydrogen target. *Nucl. Instrum. Meth. A*, 755:20 – 27, 2014.

- [75] N. Bondar et al. Third Generation Coordinate ReadOut System CROS-3, PNPI High Energy Physics Division Main Scientific Activities 2002-2006, 2007, p. 334.
- [76] R. Perez Benito et al. *Nucl. Instrum. Meth. A*, 826:6 – 14, 2016.
- [77] B. S. Henderson. PhD thesis, Massachusetts Institute of Technology, 2016.
- [78] S. Agostinelli et al. *Nucl. Instrum. Meth. A*, 506(3):250 – 303, 2003.
- [79] U. Löring et al. *Eur. Phys. J. A*, 10(4):447–486, 2001.
- [80] P. Achenbach et al. *Hyperfine Interactions*, 209(1):99–104, 2012.
- [81] PANDA Collaboration (W. Erni *et al.*). 2009. arXiv:0903.3905 [hep-ex].
- [82] PANDA Collaboration (W. Erni *et al.*). Technical Design Report for the PANDA Internal Targets. 2012.
- [83] PANDA Collaboration (W. Erni *et al.*). 2012. arXiv:1207.6581v2 [physics.ins-det].
- [84] PANDA Collaboration (W. Erni *et al.*). *Eur. Phys. J. A*, 49:25, 2013.
- [85] O. Merle et al. *Nucl. Instrum. Meth. A*, 766:96–100, 2014.
- [86] PANDA Collaboration (W. Erni *et al.*). 2008. arXiv:0810.1216v1 [physics.ins-det].
- [87] L. Gruber et al. *Nucl. Instrum. Meth. A*, 824:104 – 105, 2016. Frontier Detectors for Frontier Physics: Proceedings of the 13th Pisa Meeting on Advanced Detectors.
- [88] PANDA Collaboration (W. Erni *et al.*). Muon Detectors Technical Design Report, unpublished.
- [89] PANDA Collaboration (W. Erni *et al.*). 2009. arXiv:0907.0169 [physics.ins-det].
- [90] PANDA Collaboration (W. Erni *et al.*). Luminosity detector technical design report, unpublished.
- [91] S. Spataro. *Journal of Physics: Conference Series*, 396(2):022048, 2012.
- [92] R. Brun and F. Rademakers. *Nucl. Instrum. Meth. A*, 389(1):81 – 86, 1997.
- [93] J. Allison et al. *IEEE Transactions on Nuclear Science*, 53(1):270–278, Feb 2006.
- [94] Chr. Möller. *Annalen der Physik*, 406(5):531–585, 1932.
- [95] L.P. Pitaevskii V.B. Berestetskii, E.M. Lifshitz. *Relativistic Quantum Theory*, volume 4. Pergamon Press, 1 edition, 1971.
- [96] H. J. Bhabha. *Proceedings of the Royal Society of London. Series A, Mathematical and Physical Sciences*, 154(881):195–206, 1936.
- [97] S. Baunack et al. 102:151803, Apr 2009.
- [98] J. Beringer et al. *Phys. Rev. D*, 86:010001, Jul 2012.

- [99] P. Achenbach et al. *Nucl. Instrum. Meth. A*, 465(2-3):318 – 328, 2001.
- [100] P. Achenbach et al. *Nucl. Instrum. Meth. A*, 416(2-3):357 – 363, 1998.
- [101] S. Köbis et al. *Nuclear Physics B - Proceedings Supplements*, 61(3):625 – 629, 1998. Proceedings of the Fifth International Conference on Advanced Technology and Particle Physics.
- [102] R. Kothe. PhD thesis, Johannes Gutenberg Universität in Mainz, 2008.
- [103] V.B. Berestetskii, E.M. Lifshitz, and L.P. Pitaevskii. *Quantum Electrodynamics*. Pergamon Press, 1982.
- [104] T. Benisch. PhD thesis, Universität Erlangen-Nürnberg, 2000.
- [105] C. S. Epstein and R. G. Milner. *Phys. Rev. D*, 94:033004, Aug 2016.
- [106] L. Capozza. PhD thesis, Johannes Gutenberg Universität in Mainz, 2010.
- [107] F. Cei et al. *Nuclear Physics B - Proceedings Supplements*, 169:44 – 49, 2007.
- [108] A. Schmidt. PhD thesis, Massachusetts Institute of Technology, 2016.
- [109] R. Russell. PhD thesis, Massachusetts Institute of Technology, 2016.
- [110] C. O'Connor. PhD thesis, Massachusetts Institute of Technology, 2017.
- [111] B. S. Henderson et al. *Phys. Rev. Lett.*, 118:092501, Mar 2017.
- [112] L. W. Mo and Y. S. Tsai. *Rev. Mod. Phys.*, 41:205–235, Jan 1969.
- [113] D. J. Lange. *Nucl. Instrum. Meth. A*, 462(1-2):152–155, 2001. BEAUTY2000, Proceedings of the 7th Int. Conf. on B-Physics at Hadron Machines.
- [114] M. Sudoł et al. *Eur. Phys. J. A*, 44(3):373–384, 2010.
- [115] Z. Wąs et al. *Nuclear Physics B - Proceedings Supplements*, 181-182:269–274, 2008. Proceedings of the International Workshop on  $e^+e^-$  Collisions from Phi to Psi.
- [116] E. Eisenhandler et al. *Nuclear Physics B*, 96(1):109 – 154, 1975.
- [117] J. Van de Wiele and S. Ong. *Eur. Phys. J. A*, 46(2):291–298, 2010.
- [118] M. Zambrana et al. 2014. Internal note.
- [119] A. Eide et al. *Nuclear Physics B*, 60:173 – 220, 1973.
- [120] T. Buran et al. *Nuclear Physics B*, 116(1):51 – 64, 1976.
- [121] C. White et al. *Phys. Rev. D*, 49:58–78, Jan 1994.
- [122] G.I. Gakh and E. Tomasi-Gustafsson. *Nuclear Physics A*, 761(1):120 – 131, 2005.
- [123] I. Zimmermann. PhD thesis, Johannes Gutenberg Universität in Mainz, 2017.

- [124] G. Huang et al. BESIII proposal for data taking, internal note DocDB-doc-127, 2014.
- [125] A. Abashian et al. *Nucl. Instrum. Meth. A*, 479:117–232, 2002.
- [126] K. Akai et al. *Nucl. Instrum. Meth. A*, 499:191–227, 2003.
- [127] T. Ferber. 2015. Towards First Physics at Belle II, DPG 2015.